Thèse de doctorat /
Dissertation zur Erlangung des akademischen Grades
Doctor rerum naturalium

préparée en co-tutelle au: /
Dissertation angefertigt in Zusammenarbeit von:

Laboratoire de Physique Nucléaire et des Hautes Energies (LPNHE),
Sorbonne Université,

Fakultät Physik, Technische Universität Dortmund,

École doctorale des Sciences de la Terre et de l'environnement et
Physique de l'Univers (STEP 'UP)

Standalone track reconstruction on GPUs in the first stage of the upgraded LHCb trigger system
&
Preparations for measurements with strange hadrons in Run 3

Lukas Calefice

né /geboren, 23.09.1996,
à Kempen, Allemagne / in Kempen, Deutschland

soutenue à Paris / verteidigt in Paris, 13.12.2022

Composition de jury /
Zusammensetzung der Prüfungskommission:

Johannes Albrecht (Technische Universität Dortmund)	Directeur de thèse / Betreuer der Doktorarbeit
Vladimir Gligorov (CNRS/LPNHE)	Directeur de thèse / Betreuer der Doktorarbeit
Carla Göbel Burlamaqui de Mello (PUC do Rio de Janeiro)	Rapportrice / Gutachterin
Delphine Hardin (CNRS/LPNHE/Sorbonne Université)	Membre du jury / Mitglied der Prüfungskommission
Kevin Kröninger (Technische Universität Dortmund)	Membre du jury / Mitglied der Prüfungskommission
Vincenzo Vagnoni (INFN/Università di Bologna)	Rapporteur / Gutachter

technische universität dortmund

SORBONNE UNIVERSITÉ

Abstract

The LHCb experiment is undergoing its first major detector upgrade to operate at a five times higher instantaneous luminosity during the Run 3 data taking period. It is equipped with a new set of tracking detectors (VELO, UT, SciFi) to match the conditions of an increased track multiplicity and radiation damage. The hardware trigger stage is removed. The first stage of the software trigger system is implemented to run on about 200 GPU cards with a throughput of 30 MHz. An alternative tracking algorithm called *Seeding & Matching* for the first trigger stage is developed and presented in this thesis. Other than the formerly used *forward tracking*, the presented algorithm performs the tracking without making use of the UT which allows to run in the early data taking of Run 3 before the UT will be installed. The *Seeding* is a standalone reconstruction of track segments in the SciFi, which is followed by a *Matching* step where the SciFi seeds are matched to VELO track segments reconstructed beforehand. The physics and computing performance of the *Seeding & Matching* is evaluated and found to be compatible with the *forward tracking*. The *Seeding & Matching* is now used as the new baseline algorithm and currently being commissioned on the first Run 3 data. Furthermore, preparations for an early Run 3 measurement of the ratios of the production cross-section of Λ^0 and K^0_S hadrons are presented in this thesis.

Résumé

L'expérience LHCb au CERN est en train d'effectuer son premier majeur upgrade (LHCb) afin de pouvoir prendre des données avec une luminosité cinq fois plus grande pendant le Run 3. Il sera équipé d'un nouvel ensemble de trajectographes (VELO, UT, SciFi) pour s'adapter aux conditions d'une multiplicité de traces et d'un rayonnement plus élevée. La première étape du système de trigger est mise en œuvre pour fonctionner sur 200 cartes GPU à un débit de données de 30 MHz. Une reconstruction de trace alternative, appelée *Seeding & Matching*, pour le premier niveau du trigger est développée et présentée dans cette thèse. Contrairement au *forward tracking* utilisé précédemment, l'algorithme présenté ici se passe de l'UT, de sorte qu'il peut être utilisé avant que l'UT ne soit complètement installé. Le *Seeding* est une reconstruction autonome de segments de trace dans le SciFi, suivie d'un *Matching* où les segments du SciFi sont associés aux segments de trace VELO reconstruits précédemment. Le *Seeding & Matching* montre une performance physique et informatique compatible avec le *forward tracking*. Il est maintenant utilisé comme nouvel algorithme principal et mis en service avec les premières données du Run 3. De plus, des études préparatoires pour une mesure avec les premières données du Run 3 LHCb des rapports des sections efficaces de production des hadrons Λ^0 et K^0_S sont présentées dans cette thèse.

Kurzfassung

Das LHCb-Experiment durchläuft sein erstes großes Detektor-Upgrade, um während Run 3 Daten mit einer verfünffachten instantanen Luminosität nehmen zu können. Es wird dafür mit einem neuen Satz an Spurfindungsdetektoren (VELO, UT, SciFi) ausgestattet, um sich an die Bedingungen der erhöhten Spurmultiplizität und Strahlungsschäden anzupassen. Der Hardware-Trigger wird entfernt. Die erste Stufe des Software-Triggers ist implementiert um auf 200 GPU-Karten bei einem Datendurchsatz von 30 MHz zu laufen. Eine alternative Spurrekonstruktion, genannt *Seeding & Matching*, für die erste Triggerstufe wird entwickelt und ist präsentiert in dieser Arbeit. Im Gegensatz zu dem vorher verwendeten *forward tracking* kommt der hier präsentierte Algorithmus ohne den UT aus, sodass er am Anfang von Run 3 verwendet werden kann bevor der UT vollständig installiert ist. Das *Seeding* ist eine eigenständige Rekonstruktion von Spursegmenten im SciFi, auf die ein *Matching* folgt, wo die SciFi-Segmente den vorher rekonstruierten VELO-Spursegmenten zugeordnet werden. Das *Seeding & Matching* zeigt ein physikalische und Computing-Performance kompatibel mit dem *forward tracking*. Es wird momentan als neuer Hauptalgorithmus verwendet und mit den ersten Run 3 Daten in Betrieb genommen. Zusätzlich werden vorbereitende Studien für eine Messung mit ersten Run 3 LHCb-Daten von Verhältnissen der Produktionswirkungsquerschnitte von Λ^0 und K^0_S Hadronen in dieser Arbeit vorgestellt.

Contents

Chapter 1

The Standard Model of particle physics

This chapter briefly describes the *Standard Model of particle physics* (SM), followed by an introduction to strange hadron physics at the LHCb experiment with particular focus on strange hadron production and rare decays of charged kaons. The introduction to the SM follows the descriptions in Ref. [1–3], which the reader of this thesis is encouraged to follow for further details.

1.1 Elementary particles

The SM is a relativistic quantum field theory that currently describes the elementary particles and their electromagnetic, strong and weak interactions most accurately. Figure 1.1 depicts the elementary particles and their interactions within the SM. They can be divided into twelve fermions with spin-1/2, five spin-1 gauge bosons ($\gamma, g^a, W^\pm, Z^0$) that are the force carriers of the electromagnetic, strong and weak interactions, and the spinless Higgs boson. The fermions are further divided into six quarks and six leptons. Their main difference is that quarks interact with all three fundamental forces of the SM whereas the leptons do not interact strongly. Quarks appear in six different flavours. In increasing order of quark masses they are called: *up* (u), *down* (d), *strange* (s), *charm* (c), *bottom* (b) and *top* (t) quarks. The b quark is also known as the *beauty* quark. The quarks can be further grouped into three generations of increasing quark masses.[1] They carry an electric charge q, a colour charge and a weak isospin τ. The weak isospin component $\tau^3 = \pm 1/2$ separates *up-type* quarks (u, c, t) with $q = +2/3$ from *down-type* quarks (d, s, b) with

[1] In the SM quark masses are free parameters that depend on the energy scale. The $\overline{\text{MS}}$ renormalisation scheme is commonly used to cite the quark masses. Details about the $\overline{\text{MS}}$ scheme can be found in Ref. [3, 4].

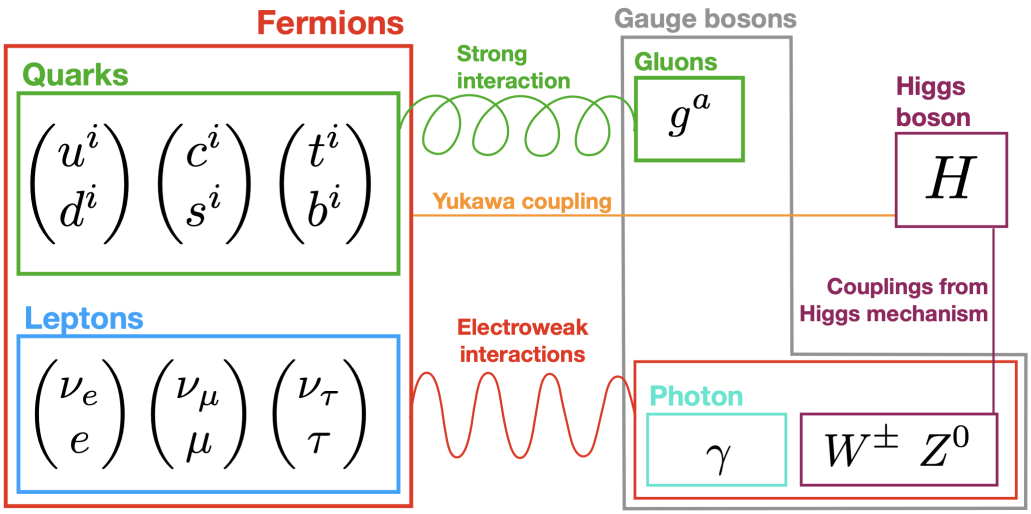

Figure 1.1: The elementary particles and their interactions within the Standard Model. The index $i = 1, 2, 3$ indicates the three possible colour charges for each quark, $a = 1...8$ stands for the eight colour charge configurations of gluons that generate the $SU(3)_C$ of the strong interaction (QCD). The Higgs mechanism provides the vector fields for the electroweak gauge bosons γ, $W^\pm$ and Z^0 and generates their masses and couplings. The Yukawa coupling describes the couplings of fermions to the Higgs field and generates the fermion masses.

$q = -1/3$.

Similarly to the quarks, the six leptons are also grouped into three generations of the different lepton flavours. Each generation contains a charged and an uncharged lepton that differ in their weak isospin. The charged leptons are the *electron* (e^-), the *muon* (μ^-) and the *tauon* (τ^-). Their associated uncharged partners are the so-called *neutrinos* (ν_e, ν_μ, ν_τ). Since they do not carry an electric charge they are not sensitive to the electromagnetic interaction. Furthermore, they are considered massless in the SM. The observation of neutrino oscillations [6] requires non-zero neutrino masses, so that they are added in some extensions of the SM. The number of leptons participating in an interaction is conserved which is known as *lepton number conservation*.

Table 1.1 summarises the fundamental properties of the fermionic elementary particles that make them unambiguously identifiable: the mass m and the electric charge q. In addition, the solutions of the Dirac equation [7] predict a counterpart to each of the twelve SM fermions with opposite charges and same mass. These are known as antiparticles. In the SM the number of leptons as well as the number of antileptons of each generation is conserved, i.e. lepton-flavour changing decays are not possible. Quark transitions between the generations are, however, allowed in

Table 1.1: Overview of the masses, charges and weak isospins of elementary fermions in the SM. Mass values are taken from Ref. [5] and are shown in in the $\overline{\text{MS}}$ renormalisation scheme. No uncertainties are shown for the masses if they are smaller than the last shown digit of the value.

gen.	τ^3	quarks			leptons		
		flavour	m	q	flavour	m	q
1.	$+1/2$	$\begin{pmatrix} u \\ d \end{pmatrix}$	$2.16^{+0.49}_{-0.26}\,\text{MeV}/c^2$	$+2/3$	$\begin{pmatrix} \nu_e \\ e^- \end{pmatrix}$	< 2 eV$/c^2$	0
	$-1/2$		$4.67^{+0.48}_{-0.17}\,\text{MeV}/c^2$	$-1/3$		$0.511\,\text{MeV}/c^2$	-1
2.	$+1/2$	$\begin{pmatrix} c \\ s \end{pmatrix}$	$1.27 \pm 0.02\,\text{GeV}/c^2$	$+2/3$	$\begin{pmatrix} \nu_\mu \\ \mu^- \end{pmatrix}$	$< 0.19\,\text{MeV}/c^2$	0
	$-1/2$		$93.4^{+8.6}_{-3.4}\,\text{MeV}/c^2$	$-1/3$		$105.66\,\text{MeV}/c^2$	-1
3.	$+1/2$	$\begin{pmatrix} t \\ b \end{pmatrix}$	$172.69 \pm 0.30\,\text{GeV}/c^2$	$+2/3$	$\begin{pmatrix} \nu_\tau \\ \tau^- \end{pmatrix}$	$< 18.2\,\text{MeV}/c^2$	0
	$-1/2$		$4.18^{+0.03}_{-0.02}\,\text{GeV}/c^2$	$-1/3$		$1776 \pm 0.12\,\text{MeV}/c^2$	-1

the weak interaction by exchanging $W^\pm$ bosons. Flavour-changing neutral currents (FCNCs) are not possible at tree-level and require higher-order loop processes and therefore highly suppressed.
In addition to the fermions of the SM, the five types of gauge bosons mediate the electromagnetic (γ), strong (g^a) and weak ($W^\pm, Z^0$) interactions between fermions. The Higgs mechanism generates the couplings of the weak gauge bosons to the Higgs field and their mass terms. The Yukawa term introduces the couplings between the fermion fields and the Higgs field and thereby generates also the fermion masses. More details about the interactions are given in the following section.

1.2 Fundamental interactions in the SM

The fundamental interactions of the SM can be described theoretically as a Lagrangian density

$$\mathcal{L} = \mathcal{L}_{\text{QCD}} + \mathcal{L}_{\text{EW}} + \mathcal{L}_{\text{Higgs}} + \mathcal{L}_{\text{Yukawa}}, \tag{1.1}$$

where the four terms represent the Quantum Chromodynamics (QCD) ($\mathcal{L}_{\text{QCD}}$) which is the quantum field theory that describes the strong interaction, the electroweak ($\mathcal{L}_{\text{EW}}$) interaction that unifies the electromagnetic and weak interactions, the Higgs term ($\mathcal{L}_{\text{Higgs}}$) that contains the potential of the Higgs field, and a term for the Yukawa coupling ($\mathcal{L}_{\text{Yukawa}}$). The SM Lagrangian is constructed to be gauge-invariant under local transformations of the $\text{SU}(3)_C \times \text{SU}(2)_L \times \text{U}(1)_Y$ symmetry group, where C stands for the colour charge in the QCD, L depicts the left-handed chirality and the Y the weak hypercharge.

1.2.1 Quantum Chromodynamics

The theory of Quantum Chromodynamics [8–12] is based on the $\mathrm{SU}(3)_C$ symmetry group. Every $\mathrm{SU}(N)$ gauge group comes with N^2-1 generators of the symmetry of the group. For the $\mathrm{SU}(3)_C$ these are the eight gluons (g^a) that mediate the strong force. The colour charge C is the charge of the QCD and it is conserved in strong processes. There is three values i of this charge (usually referred to as *red* (r), *green* (g) and *blue* (b)) as well as their anticolours ($\bar{r}, \bar{g}, \bar{b}$). Quarks carry one colour, whereas gluons carry one colour and one anticolour. The Lagrangian density of the QCD is given by

$$\mathcal{L}_{\mathrm{QCD}} = \bar{\psi}_i(i\gamma^\mu(D_\mu)_{ij} - m\delta_{ij})\psi_j - \frac{1}{4}G^a_{\mu\nu}G^{\mu\nu}_a, \tag{1.2}$$

with the gauge covariant derivative

$$(D_\mu)_{ij} = \partial_\mu\delta_{ij} - \frac{i}{2}g_s(\lambda_a)_{ij}A^a_\mu \tag{1.3}$$

and field strength tensor of the gluon fields A^a_μ

$$G^a_{\mu\nu} = \partial_\mu A^a_\nu - \partial_\nu A^a_\mu + g_s f^{abc}A^b_\mu A^c_\nu. \tag{1.4}$$

Here, the ψ_i stands for the quark wave functions with colour charge i, γ^μ for the the Dirac matrices, λ_a for the Gell-Mann matrices which represent the eight generators of the gauge group, $g_s = \sqrt{4\pi\alpha_s}$ with the coupling of the strong interaction α_s, and f^{abc} the structure constants for different combinations of the colour charge configurations of the gluon a, b and c.
The second term of the covariant derivative in equation 1.3 expresses the coupling between gluons and quarks, whereas the terms of the gluon field strength tensor in equation 1.4 generates the 3-vertex and 4-vertex self-couplings of gluons that become particularly relevant at low values of Q^2, the square of the transferred four-momentum in the process. The coupling α_s is not constant but depends on the Q^2. This dependency is commonly referred to as the *running coupling* of the QCD. Similarly, the quark masses have a dependency on the Q^2 scale. For small Q^2 or large distances (soft-QCD) the value of the coupling is large ($\alpha_s \sim \mathcal{O}(1)$), which makes a separation of quarks very difficult, so that only colourless bound states of quarks are observed, the so-called hadrons. This phenomenon is also known as *confinement*. For high Q^2 values, the coupling decreases. This phenomenon is known as *asymptotic freedom*. The two Q^2-regimes can be separated by the reference scale $\Lambda_{\mathrm{QCD}} \approx 300\,\mathrm{MeV/c^2}$-$1\,\mathrm{GeV/c^2}$ below which α_s becomes too large for the QCD to remain perturbative. Commonly known colourless bound states are the mesons ($q\bar{q}$), that are bosons build from a quark and an antiquark, as well as the fermionic

baryons (qqq) and antibaryons ($\bar{q}\bar{q}\bar{q}$) consisting of three quarks or antiquarks. In this thesis strange hadrons such $K^+(\bar{s}u)$, $\Lambda^0(uds)$, $\Xi^-(dss)$, $\Omega^-(sss)$ as well as the K^0_S, which is a superposition of $K^0(d\bar{s})$ and $\bar{K}^0(s\bar{d})$ states, are discussed in particular. The QCD also allows for states with a larger number of quarks, like tetraquarks or pentaquarks, an idea that was proposed by Gell-Mann in his quark model paper in 1964 [13]. The first confirmed tetraquark candidate $X(3872)$ has been observed in 2003 by the Belle Collaboration [14]. In 2015 and 2019 LHCb observed the first pentaquark candidates in $\Lambda^0_b \to J/\psi K^- p$ decays [15, 16]. Since then, various other tetra- and pentaquark states have been discovered and studied by the LHCb experiment [17].

1.2.2 Electroweak interaction and the Higgs mechanism

The remaining $\mathrm{SU}(2)_L \times \mathrm{U}(1)_Y$ gauge symmetry describes the electroweak interactions [18–20]. It is generated by the three massless vector boson fields $W^1_\mu, W^2_\mu, W^3_\mu$ from the $\mathrm{SU}(2)_L$ and the massless bosonic field B_μ from the $\mathrm{U}(1)_Y$. The electroweak terms of the SM Lagrangian are given by

$$\mathcal{L}_{\mathrm{EW}} = -\frac{1}{4}(W^{i\mu\nu}W^i_{\mu\nu} + B^{\mu\nu}B_{\mu\nu}) + \sum_{\substack{f=Q_L,u_R,d_R,\\ L_L,e_R}} \bar{f}_j i\gamma^\mu D_\mu f_j \tag{1.5}$$

with the covariant derivative

$$D_\mu = \partial_\mu - i\frac{g_w}{2}\tau^i W^i_\mu - i\frac{g'_w}{2}YB_\mu, \tag{1.6}$$

where the $W^i_{\mu\nu}$ and $B_{\mu\nu}$ of the first term stand for the field strength tensor of the electroweak gauge fields. The second term represents the couplings of the gauge fields to their associated charges, the components of the weak isospin described by the Pauli matrices τ^i and the weak hypercharge Y. They are related to the electric charge Q by the Gell-Mann-Nishijima-relation [21, 22]

$$Q = \tau^3 + Y. \tag{1.7}$$

The coupling strengths are given by the electroweak coupling constants g_w and g'_w. A fundamental property of the weak interaction is that the W^i_μ-boson fields only couple to the left-handed chirality components of the fermion fields that carry a weak isospin of $\tau = 1/2$. For their antiparticles they only couple to the right-handed components. The B_μ field, however, couples to fields with a weak hypercharge regardless of the weak isospin. The left-handed components of the fermionic fields can be written as ($\tau^3 = \pm 1/2$)-doublets $Q_L = (u_L, d_L)^T$ and $L_L = (\nu_{eL}, e_L)^T$ in the electroweak

interaction. This pairs the up-type and down-type quarks as well as the uncharged and charged leptons for each generation. The right-handed components with $\tau = 0$ exist as singlets u_R, d_R, e_R for all fermions except for neutrinos. Furthermore, neutrinos are massless in the SM which motivates the non-existence of singlets for them in the SM: this is confirmed by the lack of observed right-handed neutrinos. In addition to $\mathcal{L}_{\mathrm{EW}}$ there is a term $\mathcal{L}_{\mathrm{Higgs}}$ in the SM Lagrangian introduced by the *Higgs mechanism* [23] as

$$\mathcal{L}_{\mathrm{Higgs}} = |D_\mu \phi|^2 - \underbrace{(\mu^2 \phi^\dagger \phi + \lambda(\phi^\dagger \phi)^2)}_{=:V(\phi)} \tag{1.8}$$

with the scalar potential $V(\phi)$ of the $\mathrm{SU}(2)_L$ weak isospin doublet $\phi = (\phi^+, \phi^0)$ where the ϕ^+ and ϕ^0 are the two scalar fields in the minimal Higgs model and μ and λ are the free parameters of the mass term and the four-vertex Higgs field coupling term. For a mass term with $\mu^2 < 0$ the potential has an infinite set of degenerated minima invariant under the $\mathrm{SU}(2)_L$ symmetry at

$$\phi^\dagger \phi = -\mu^2/\lambda = \nu^2, \tag{1.9}$$

where ν stands for the non-zero *vacuum expectation value* of ϕ. The choice of specific vacuum state configuration among these minima induces a *spontaneous symmetry breaking* (SSB) of the $\mathrm{SU}(2)_L \times \mathrm{U}(1)_Y$ gauge symmetry, with a remaining $\mathrm{U}(1)_Q$ for the electromagnetic interactions. The vacuum state

$$\phi(x) = \frac{1}{\sqrt{2}} \begin{pmatrix} 0 \\ \nu + h(x) \end{pmatrix} \tag{1.10}$$

is chosen in a way that the photon field remains massless. Here, the $h(x)$ is the Higgs field. The SSB generates mass terms for the linear $W^\pm$-boson field combinations

$$W_\mu^\pm = \frac{1}{\sqrt{2}}(W_\mu^1 \mp i W_\mu^2) \tag{1.11}$$

and leads to a mixing

$$\begin{pmatrix} A_\mu \\ Z_\mu \end{pmatrix} = \frac{1}{\sqrt{g_w^2 + {g'_w}^2}} \begin{pmatrix} g'_w & g_w \\ g_w & -g'_w \end{pmatrix} \begin{pmatrix} W_\mu^3 \\ B_\mu \end{pmatrix} \tag{1.12}$$

that introduces the bosonic massless photon field A_μ as well as the Z-boson field Z_μ with a mass of $m_Z = g_w \nu / (2\cos(\theta_{\mathrm{W}}))$. The Weinberg angle θ_{W} is given by $\tan\theta_{\mathrm{W}} = {}^{g'_w}/_{g_w}$ and relates the masses of the $W^\pm$-bosons and the Z^0-boson by ${}^{m_W}/_{m_Z} = \cos\theta_{\mathrm{W}}$. They have been measured $m_W = (80.377 \pm 0.012)\,\mathrm{GeV}/c^2$ and $m_Z = (91.1876 \pm 0.0021)\,\mathrm{GeV}/c^2$ [5]. Another consequence of the SSB in the

electroweak theory is the mass term of the Higgs field which introduces a new particle, the Higgs boson at a mass of $m_H = \sqrt{2v^2\lambda}$. After its discovery by the ATLAS and CMS Collaborations in 2012 [24, 25] its mass has been measured to be $m_H = (125.25 \pm 0.17)\,\mathrm{GeV}/c^2$ [5].
The couplings of the $W^\pm$ and Z^0 to fermions in the weak interaction after the SSB are shown in Figure 1.2. The terms in the Lagrangian from the exchanges of

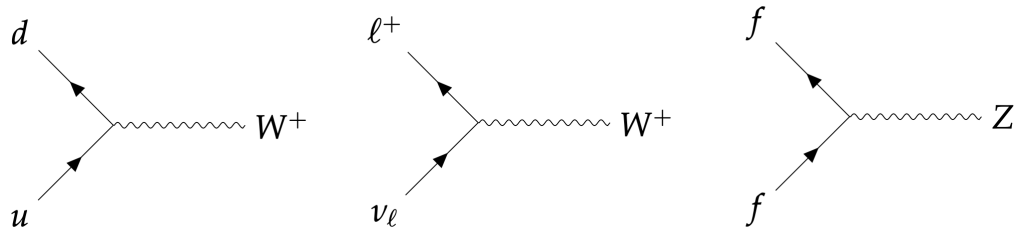

Figure 1.2: Feynman diagrams of the $W^\pm$ and Z^0-boson couplings to fermions in the weak interaction after SSB.

$W^\pm$-bosons (charged currents) and Z^0-boson exchanges (neutral currents) for the fermion fields f are given by

$$-\bar{f}' i\frac{g_W}{\sqrt{2}}\gamma^\mu\left(\frac{1-\gamma_5}{2}\right)f \qquad \text{and} \qquad -\bar{f} i\frac{g_Z}{2}\gamma^\mu\left(\frac{1}{2}\tau_f^3 - Q_f - \frac{1}{2}\tau_f^3\gamma_5\right)f, \tag{1.13}$$

where the coupling strengths are

$$g_W = \frac{e}{\sin\theta_\mathrm{W}} \qquad \text{and} \qquad g_Z = \frac{e}{\sin(\theta_\mathrm{W})\cos(\theta_\mathrm{W})} \tag{1.14}$$

and e is the elementary charge. Charged currents change the electric charge and the flavour of a fermion whereas neutral currents maintain both. For quarks, generations can be changed in charged currents, whereas for leptons they cannot. From the Lagrangian and the values in Table 1.1 it can be seen that for the leptons the coupling strength is independent of the lepton flavour since neither the flavour generation nor the fermion masses are part of the Lagrangian. The same is true for the electromagnetic interaction. This concept is better known as the *lepton flavour universality* (LFU) of the SM.

1.2.3 Yukawa coupling

The Yukawa coupling term of the SM Lagrangian $\mathcal{L}_\mathrm{Yukawa}$ consists of the couplings of the fermions to the Higgs field ϕ. It is given by

$$\mathcal{L}_\mathrm{Yukawa} = -Y_{ij}^D\bar{Q}_{Li}\phi d_{Rj} - Y_{ij}^U\bar{Q}_{Li}\phi^* u_{Rj} - Y_{ij}^L\bar{L}_{Li}\phi e_{Rj} + h.c., \tag{1.15}$$

where the Y_{ij} are the Yukawa couplings and the indices i and j run over the different quark and lepton generations. The couplings are represented by arbitrary 3×3 matrices that can be diagonalised and eliminated by transformations of the fermion fields. However, it is not possible to eliminate the couplings of the down-type quark sector Y_{ij}^{D} at the same time as the one of the up-type quark sector Y_{ij}^{U}, which leaves a unitary matrix, the so-called *Cabbibo-Kobayashi-Maskawa (CKM) matrix* V_{CKM}. It describes the mixing of the flavour eigenstates of quarks to their mass eigenstate and can be parametrised [26, 27] as

$$\mathrm{V_{CKM}} = \begin{pmatrix} V_{ud} & V_{us} & V_{ub} \\ V_{cd} & V_{cs} & V_{cb} \\ V_{td} & V_{ts} & V_{tb} \end{pmatrix} = \begin{pmatrix} c_{12}c_{13} & s_{12}c_{13} & s_{13}e^{i\delta_{13}} \\ -s_{12}c_{23} - c_{12}s_{23}s_{13}e^{i\delta_{13}} & c_{12}c_{23} - s_{12}s_{23}s_{13}e^{i\delta_{13}} & s_{23}c_{13} \\ s_{12}s_{23} - c_{12}c_{23}s_{13}e^{i\delta_{13}} & -c_{12}s_{23} - s_{12}c_{23}s_{13}e^{i\delta_{13}} & c_{23}c_{13} \end{pmatrix}, \quad (1.16)$$

where $s_{ij} = \sin(\theta_{ij})$ and $c_{ij} = \cos(\theta_{ij})$, θ_{ij} are the three CKM mixing angles and δ_{13} is the *CP*-violating phase. In charged currents of the weak interaction the $V_{ff'}$ element of the CKM matrix is added to the vertex factor. The elements on the diagonal, representing quark transitions within one generation, of the CKM matrix are the largest, whereas off-diagonal elements, i.e. quark transitions to another generation, are suppressed. Furthermore, the diagonalisation of the Yukawa couplings introduces the mass terms for the fermion fields. The hierarchy of the masses cannot be predicted by the SM.
In total, the SM has 18 free parameters: nine fermion masses, three CKM mixing angles, the *CP*-violating phase, three gauge couplings, the vacuum expectation value of the Higgs potential and the Higgs mass.

1.2.4 Open questions of the SM

The SM is the most precise theory to explain a majority of observed phenomena in particle physics. Nevertheless, there are some open questions that cannot be answered by the SM. They are briefly outlined in the following:

- As discussed above, the hierarchy of the quark and lepton masses is not explained, as the fermion masses are free parameters in the SM. In addition, the mass of the Higgs boson is another free parameter in the SM. It is also not explained why there is exactly three generations of fermions in the SM. A new theoretical model might be needed to explain these parameters [28].
- The observation of neutrino oscillations [6] proves the existence of lepton-flavour violating processes. This implies that neutrinos are required to have a mass. This mass term needs be incorporated in the SM Lagrangian, but the mechanism would depend on whether neutrinos are Majorana fermions, *i.e.* their own antiparticles, or not.

- The amount of *CP* violation observed in the quark sector of the SM is not sufficient to explain the matter-antimatter-asymmetry in the universe [29]. Searches for *CP* violation in the neutrino sector are ongoing. The vacuum structure of the QCD allows for additional *CP* violation in the SM. However, no evidence for *CP* violation in the strong interaction is observed. As shown by Peccei and Quinn [30], the problem can be resolved by introducing a spontaneously broken global U(1) symmetry. As a consequence, a new particle referred to as *axion* is required, which has not experimentally been observed to date.

- Studies of rotational curves of galaxies [31] indicate that other types of matter than the *ordinary matter* known to us have to exist. Furthermore, the observation of the accelerating expansion of the universe requires an extra source of energy. They are referred to as *dark matter* and *dark energy*, respectively. Axions or axion-like particles could be candidates for dark matter particles. Other dark matter candidates are postulated by models of supersymmetry. Up to now, no dark matter candidates and no evidence for supersymmetry have been observed in experiments.

The LHCb experiment among other flavour physics experiments performs indirect searches for physics beyond the SM (BSM) by looking at potential contributions of new particles in highly suppressed processes such as the flavour-changing $b \to s\ell\ell$ transitions. Recent measurements probing the SM predictions have shown tensions with the SM in branching fraction measurements [32–34], angular analyses [35] and LFU ratio measurements [36–39]. More tensions have been seen in LFU ratio measurements of tree-level $b \to c\ell\nu_\ell$ transitions by the BaBar, BELLE and LHCb Collaborations [40–46]. Similar measurements with more data from Run 3 of the LHC and the Belle II experiment will give further insights into the LFU of the SM. Extending the LFU measurements to charm and strange decays could give complementary insights. In addition, measurements of the anomalous magnetic moment of the muon have shown a large disagreement with the predicted value from the SM [47]. In contrast to the indirect searches in flavour physics experiments, direct searches for BSM particles are performed at ATLAS and CMS.

1.3 Strange hadrons at the LHCb experiment

The LHCb detector is designed primarily to study decays of heavy flavour hadrons containing c and b quarks. In pp collisions at the LHC at the centre-of-mass energy $\sqrt{s} = 13\,\text{TeV}$, $c\bar{c}$- and $b\bar{b}$-pairs are produced abundantly with cross-sections of $\sigma(p\bar{p} \to c\bar{c}) \approx 2400\,\mu\text{b}$ [48] and $\sigma(p\bar{p} \to b\bar{b}) \approx 140\,\mu\text{b}$ [49] in the LHCb acceptance.

The geometrical detector acceptance for the final state particles of typical c- and b-hadron decays can be as high as $\sim 25\,\%$ which allows for enormous c- and b-hadron data samples. While the knowledge in flavour physics has been greatly enhanced in the heavy-flavour sectors in the recent years, few measurements have been performed for the production of strange hadrons and their decays. Dedicated experiments such as NA48 [50], NA62 [51] or KOTO [52] have been built for the study of specific measurements of rare strange hadron decays. However, there is no flavour experiment with a comprehensive physics programme towards the strange sector. LHCb has so far made contributions to the sector of rare strange hadron decays by setting the world best upper limits on the branching fractions $\mathcal{B}(K^0_S \to \mu^+\mu^-)$ [53] and $\mathcal{B}(K^0_{S(L)} \to \mu^+\mu^-\mu^+\mu^-)$ [54], as well as by the search for the decay $\Sigma^+ \to p\mu^+\mu^-$ [55]. In Run 3 the LHCb experiment has the opportunity to further extend the already comprehensive physics programme more towards the strange sector.
Strange hadrons such as $K^\pm$, K^0_S and $\Lambda^0/\bar{\Lambda}^0$ are produced at the LHC with predicted cross-sections of $\sim$ 0.1-1 b, i.e. at a much larger amount than c or b hadrons. Figure 1.3b shows the average multiplicities per event of different hadron species inside the LHCb acceptance at 13 TeV for Run 2 conditions. It can be seen that on average there is at least one K^0_S or Λ^0 hadron produced in the pp-collision event that ends up in the LHCb acceptance, whereas there are multiple $K^\pm$ per event. The multiplicities for Run 3 are expected to scale with the luminosity increase. Although the number of available strange hadrons in LHCb is extremely high, collecting a large data sample of rare kaon decay candidates is complicated due to fundamental kinematic and topological differences of these decays with respect to decays of heavy-flavoured hadrons. Table 1.2 shows a comparison of the average mean lifetimes τ of strange

Table 1.2: Average mean lifetimes for different types of strange and heavy-flavour hadrons. All values are taken from Ref. [5].

hadron	τ in s
$K^\pm$	$(1.2380 \pm 0.0020) \cdot 10^{-8}$
K^0_S	$(0.8954 \pm 0.0004) \cdot 10^{-10}$
K^0_L	$(5.116 \pm 0.020) \cdot 10^{-8}$
Λ^0	$(2.632 \pm 0.020) \cdot 10^{-10}$
Ξ^-	$(1.639 \pm 0.015) \cdot 10^{-10}$
Ω^-	$(0.821 \pm 0.011) \cdot 10^{-10}$
D^0	$(410.3 \pm 1.0) \cdot 10^{-15}$
$D^\pm$	$(1033 \pm 5) \cdot 10^{-15}$
B^0	$(1.519 \pm 0.004) \cdot 10^{-12}$
$B^\pm$	$(1.638 \pm 0.004) \cdot 10^{-12}$

hadrons and heavy-flavour hadrons. Strange hadrons have a much larger average

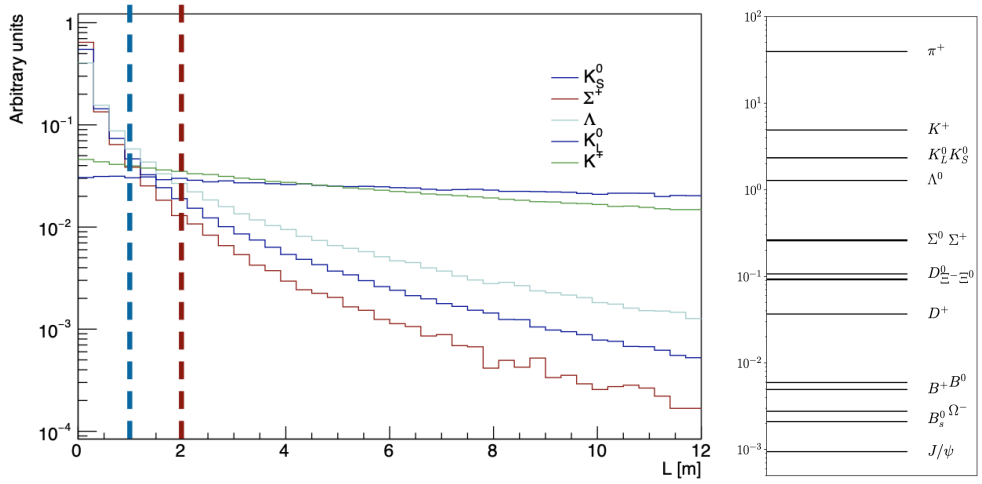

(a) decay lengths **(b)** multiplicities

Figure 1.3: (a) Distributions of the decay lengths for different species of strange hadrons. The blue and red dashed lines mark the 1 m and 2 m distances from the interaction point that roughly correspond to the end of the VELO and the beginning of TT/UT detectors. (b) Average multiplicities of different hadrons in the geometrical acceptance of the LHCb experiment produced in a single event. For both plots events are obtained from simulated pp-collisions at $\sqrt{s} = 13\,\text{TeV}$ and Run 2 conditions. Both plots are taken from Ref. [56].

mean lifetime than typical c or b hadrons. For example the average mean lifetime of a Λ^0 hadron is more than a factor 100 larger than the one of a $B^\pm$ or $D^\pm$. Figure 1.3a shows the distributions of decay lengths for different types of strange hadrons. It can be seen that a large fraction of the strange hadrons decays at $> 1\,\text{m}$ from the collision point, which is behind the first tracking detector of LHCb, the Vertex Locator (VELO) or even at $> 2\,\text{m}$, which is behind the last tracking detector before the magnet, TT/UT, as will be explained in the detector description in chapter 2.2. As a consequence, many of the decays cannot be reconstructed in the standard way that is used for c- and b-hadron decays. Moreover, the momentum and transverse momentum spectra of decay products of strange hadron decays are much softer compared to the ones from c- and b-hadron decays due to the smaller boost from the production processes and the small phase spaces in the decays. For example, the available energy in the rest frame of the decaying particle, the so-called phase space, in $K^0_S \to \pi^+\pi^-$ and $\Lambda^0 \to p\pi^-$ decays are

$$m(K^0_S) - 2 \cdot m(\pi^\pm) \approx 218\,\text{MeV/c}^2 \quad \text{and} \quad m(\Lambda^0) - m(p) - m(\pi^-) \approx 38\,\text{MeV/c}^2.$$

This makes it more difficult to discriminate them from random low-momentum tracks, especially pions, directly coming from the pp-collision and therefore also to efficiently trigger on them without picking up a large amount of random background tracks. In Run 2 the hardware stage of the trigger system selected events based on tracks with large transverse energy and transverse momentum. For strange hadrons decays with their soft momentum spectra this typically results in trigger efficiencies below 1 % as they can only be recorded as a byproduct of events that contained other c or b-hadron decays with such a signature. The abundance of K^0_S and Λ^0 hadrons from their large cross-section in the combination with the large branching fractions of $K^0_S \to \pi^+\pi^-$ and $\Lambda^0 \to p\pi^-$ decays enables them to overcome the trigger efficiency problem as they can be selected by a random trigger which will be explained later in chapter 4. Furthermore, the measurement of their production cross-section ratios will be discussed.

Chapter 2

The LHCb experiment at the Large Hadron Collider

This thesis uses data that were recorded by the *Large Hadron Collider beauty* (LHCb) experiment in 2018 during the second data taking period between 2015-2018 (Run 2) at the Large Hadron Collider (LHC) and presents developments for a track reconstruction algorithm that will enable to take data with the LHCb Upgrade I detector during the next data taking period (Run 3) starting in 2022. This chapter introduces briefly the LHC itself and how protons are accelerated in section 2.1 before they are brought to collision in the LHCb experiment followed by a more comprehensive description of the LHCb experiment in section 2.2 and its first major upgrade in section 2.3. Special focus will be given to the upgrade of the sub-systems that are particularly relevant for this thesis such as the tracking and trigger systems.

2.1 The Large Hadron Collider

The LHC [58] is a 27 km long circular particle accelerator located at CERN. Its main purpose is the acceleration of predominantly protons but also heavy ions (such as lead) and bringing them to collision. As final part of a chain of accelerators the LHC is designed to increase the energy of protons up to 7 TeV. Figure 2.1a depicts the accelerators at CERN during Run 2. Protons were obtained from hydrogen atoms coming from an hydrogen bottle after stripping off the electrons with the help of an electric field. Afterwards they were accelerated by the *Linear Accelerator 2* (LINAC 2) followed by the *Proton Synchrotron Booster* (PSB), the *Proton Synchrotron* (PS) and the *Super Proton Synchrotron* (SPS) with each of them gradually elevating the proton energy. Finally protons leaving the SPS are injected into the LHC at an energy of 450 GeV. For heavy ion runs the *Linear Accelerator 3* (LINAC 3) is used

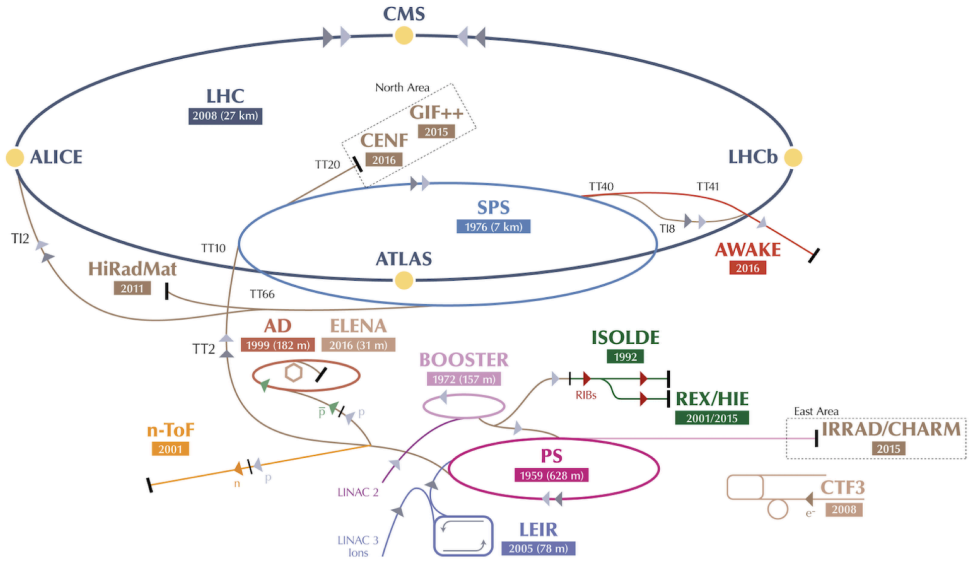

(a) Accelerator complex at CERN during Run 2

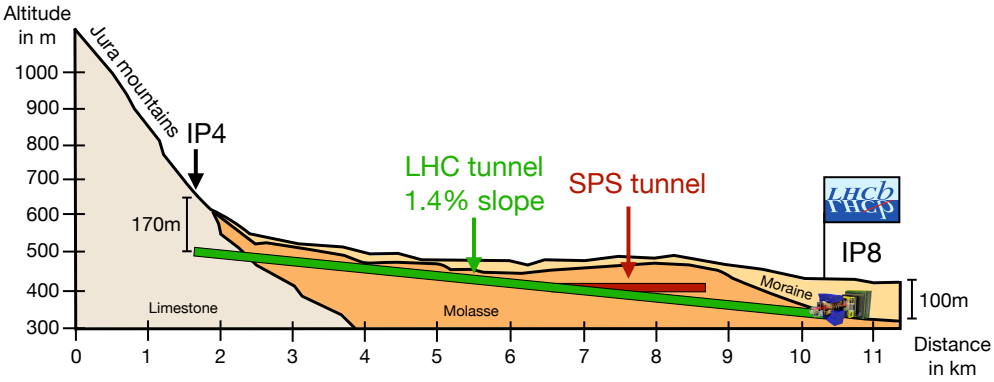

(b) Rock layers around the LHC tunnel

Figure 2.1: (a) Overview of the accelerator complex at CERN during Run 2. The years indicate when each machine started operation. Additionally for circular accelerator the circumferences are given. TT and TI are the *transfer lines* that are used to bring protons from one accelerator to the next. Taken from Ref. [57]. (b) Tilted position of the LHC ring in the rock layers of the Geneva area. IP8 where LHCb is located is the lowest point of the ring about 100 m below the surface.

to start the acceleration process from where ions are directly injected into the PS leaving out the PSB.
For Run 3 LINAC 2 is replaced by the *Linear Accelerator 4* (LINAC 4), that accelerates negatively charged hydrogen ions H^- up to 160 MeV before stripping off their electrons when injecting them to the PSB. The LINAC 4 exploits a new acceleration scheme that enables more densely packed proton beams which is a crucial element for the high-luminosity LHC (HL-LHC) envisioned for Run 4 that is planned for 2029. The LHC is filled with two beams consisting of up to 2808 bunches of 1.1×10^{11} protons each that turn around the ring in opposite directions through an ultra-high vacuum of 10×10^{-10} to 10×10^{-11} mbar. Such vacuum is needed to suppress beam-gas interactions. As shown in Figure 2.2 the LHC is

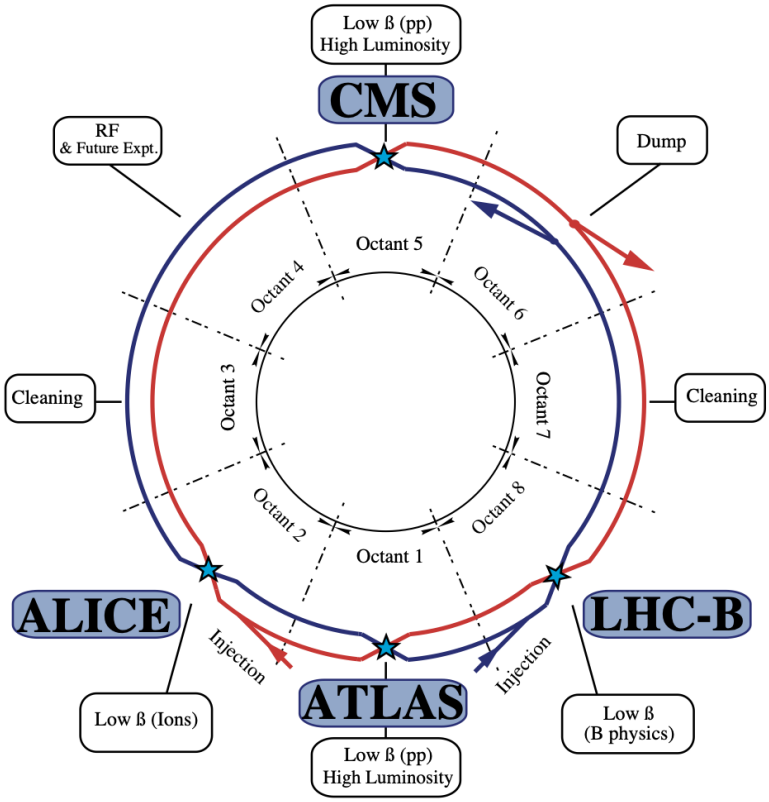

Figure 2.2: The eight sectors of the LHC dedicated to the LHC experiments, the RF cavities, the LHC collimation system (Cleaning) and the dumping. Beam 1 is depicted in red and beam 2 in blue. Low-β refers to the β-functions that define the transversal sizes of the beam $\sigma_{x,y}$ by $\sqrt{\beta_{x,y}\epsilon}$, where ϵ is the beam emittance. Taken from Ref. [59].

segmented into eight octants each consisting of an *arc* and an *insertion* sector. The arcs contain 23 cells each composed by a FODO magnet lattice[1] that consists of superconducting Niobium-Titanium dipoles with a magnetic field strength of 8.33 T bending the beams on the circular orbit, quadrupoles that focus the beam and higher order magnets to account for chromaticity[2]. In total, the LHC comprises 1232 dipoles that need to be cooled down to 1.9 K to enable their superconductivity which is realised with liquid helium. The insertion sectors are straight sections that contain octant-specific beam instrumentation. Four of them, the so-called interaction points (IP) are dedicated to the collision of the beams and host the experiments. Here, a more specialised set of magnets, the *Inner Triplet*, steers and further squeezes the beam to achieve maximal luminosity at the interaction point.

In the remaining sectors the beam is

- accelerated by eight superconducting radio-frequency (RF) cavities per beam for ramping up to the nominal LHC beam energy and compensate the energy losses due to synchrotron radiation, and kept tightly bunched in the longitudinal direction
- cleaned from outlier protons by the LHC collimation system.
- dumped into the 8 m long graphite dump block in case of unexpected irregularities in the beam operation or at the end of a LHC fill.

As shown in Figure 2.1b the LHC tunnel is tilted due to the geological conditions of rock layers in the Geneva area. The LHC is designed to collide two proton beams at a centre-of-mass energy of $\sqrt{s} = 14\,\text{TeV}$ (in Run 2 collisions at 13 TeV were achieved, for Run 3 $\sqrt{s} = 13.6\,\text{TeV}$ is foreseen) in four collision points. These are surrounded by the four major experiments at the LHC: ATLAS, ALICE, CMS and LHCb. The LHC experiments can be categorised into two classes: the general-purpose detectors (GDPs) and the detectors specialised to dedicated type of physics. The general-purpose detectors are the ATLAS [60] and CMS[61] experiments located in IP1 and IP5. They are nearly hermetic[3] detectors that are specialised in high-p_T physics, in measuring the properties of the top quark and the Higgs boson as well as in direct searches for physics beyond the standard model. In particular, the discovery of the Higgs boson in 2012 [24, 25] and the measurements of the Higgs couplings to beauty

[1] A FODO structure is an alternating lattice of focusing (F) and defocusing (D) quadrupule magnets interrupted by focus-wise neutral sections (O) where the dipole magnets are placed. Quadrupole magnets that have a focusing effect on the beam in one of the xz- and yz-planes are defocusing in the other one and vice versa.

[2] Chromaticity to pertubations of the beam dynamics by energy-dependent focusing of the beam in the quadrupole magnets which causes an unwanted spread of the beam.

[3] Instrumented in the full solid angle $\Omega = 4\pi$.

quark and top quark pairs are very important contributions to the understanding of the SM. The two large and more specialised LHC experiments are the ALICE and LHCb experiments. The ALICE experiment [62] located at IP2 studies the properties of the quark-gluon plasma in heavy ion collision. Relevant for this thesis are also the production cross-section measurements of strange hadrons in pp-collision that will be discussed in section 4. The LHCb experiment [63] located at IP8 is designed for precision measurements in the field of heavy-flavour physics. Its main purpose is the study of CP-violation and the indirect search for physics beyond the SM in decays of charm and beauty hadrons. The physics programme of LHCb has evolved in the two data taking periods more towards a general-purpose experiment making significant contributions to other fields such as hadron spectroscopy, heavy ion and electroweak physics. A detailed description of the LHCb experiment will be given in the following section 2.2.
Bunches at the LHC are separated from each other at a *bunch spacing* of 25 ns. During collisions, this results in a data rate of 40 MHz at which the detectors need to be read-out. Due to the filling scheme of the LHC and the position of the LHCb experiment in the LHC ring bunches are collided less often at LHCb, resulting in an effective collision rate of 30 MHz, which also corresponds to the data rate that the trigger system takes as input.

2.2 The LHCb experiment

This section introduces the LHCb detector and its trigger system as they were operated during Run 2. As discussed previously, protons are not fundamental particles but a compound of the uud valence quarks carrying the main part of the protons momentum, a sea of other low momentum quark-antiquark pairs as well as a large amount of strongly interacting gluons that bind the quarks together. When protons collide at the LHC it is most likely that not the proton itself but its constituents, referred to as partons, interact with each other. The leading processes for producing $c\bar{c}$ and $b\bar{b}$ pairs at the energy scale of the LHC are the gluon-gluon fusion and quark-antiquark annihilation. In these processes the momenta of the two colliding partons are very different, since inside the proton they can be found at a wide range of proton momentum fractions x as shown by the parton distribution functions in Figure 2.3a. Therefore, particles produced in the collision and with a mass much lower than the collision energy are boosted into the forward/backward region. This motivated the design of the LHCb detector as a single-arm forward spectrometer. It covers the pseudo-rapidity range between $2 < \eta < 5$, which translates to an angular acceptance of 10 to 300 mrad in the horizontal and 250 mrad in the vertical plane. Figure 2.3b shows the angular distribution of simulated $b\bar{b}$ pairs produced

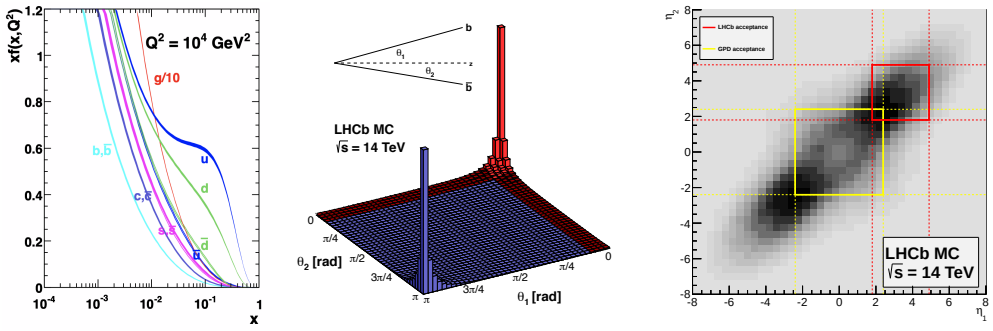

(a) **(b)** **(c)**

Figure 2.3: (a) Parton distribution function of protons at $Q^2 = 10^4\,\mathrm{GeV}^2$, x describes the fraction of the protons momentum that the parton carries and $f(x, Q^2)$ the probability of finding a parton with given x inside the proton. Taken from Ref. [64]. (b) Angular distribution of simulated $b\bar{b}$-pairs from gluon-gluon fusion and quark-antiquark annihilation at $\sqrt{s} = 14\,\mathrm{TeV}$. The events shown in red are covered by the geometrical acceptance of LHCb. Taken from Ref. [65]. (c) Comparison of the geometrical acceptance of produced $b\bar{b}$ pairs at $\sqrt{s} = 14\,\mathrm{TeV}$ between LHCb and the GPDs. Taken from Ref. [65].

via gluon-gluon fusion and quark-antiquark annihilation at $\sqrt{s} = 14\,\mathrm{TeV}$ and the fraction of these that are covered by the geometrical acceptance of LHCb, which is about 24 %. In Figure 2.3c this is compared to the acceptance of the GPDs at the LHC. It can be seen that the overlap of the geometrical acceptances is small which makes LHCb also an unique environment to study physics in the forward region. The layout of the LHCb detector is shown in Figure 2.4. The detector consists of various subdetectors that can be divided into two main classes: tracking and particle identification. They will be discussed in detail in sections 2.2.2 and 2.2.3. The reference frame that is used by LHCb is defined as follows:

- IP8 is the origin of the coordinate system.
- The z-axis is defined along the beam pipe in the direction of beam 1 (the beam that propagates clockwise through the LHC). As discussed above, the LHC tunnel is tilted by an angle of 3.601 mrad with respect to the LHCb cavern.
- The x-axis is horizontal, pointing outside of the LHC ring.
- The y-axis is pointing upwards, but tilted by an angle of 3.601 mrad with respect to the gravitational axis to form right-handed system. The subdetectors upstream of the magnet follow the direction of the beam, whereas downstream they follow the gravitational axis for mechanical reasons.

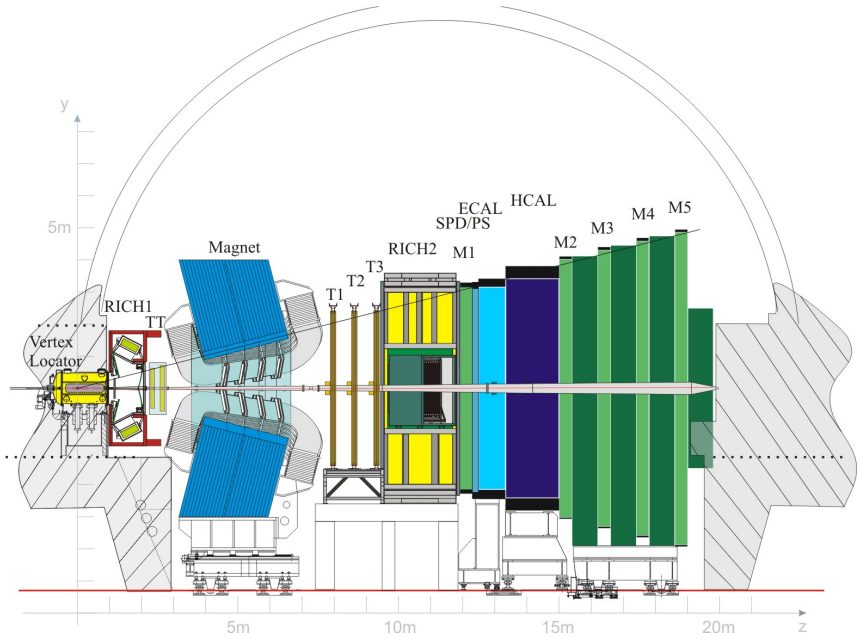

Figure 2.4: Schematic overview of the LHCb detector layout during the Run 1 (2011-2012) and Run 2 (2015-2018) data takings. Taken from Ref. [63].

Most of the subdetectors are divided into two halves called A-side ($x > 0$) and C-side ($x < 0$) to simplify their installation around the beam pipe. The majority of the read-out electronics are placed outside of the detector acceptance to minimise unwanted material interactions. The number of collisions per unit time taking place in LHCb is defined by the instantaneous luminosity $\mathcal{L}_{\text{inst}}$, whereas the recorded luminosity over time is defined by the integrated luminosity $\mathcal{L}_{\text{int}}$. Data have been acquired in the two data taking periods between 2010-2012 (Run 1) and 2015-2018 (Run 2). LHCb levels the luminosity to keep the data rate at a constant level which allows to run with the same trigger configuration throughout a fill of the LHC, enables a more precise reconstruction, and limits the ageing of the detectors in the high-multiplicity hadronic environment of the LHC. This is realised by introducing an offset between the beams in the horizontal plane and thereby avoiding head-on collisions. Figure 2.5 shows the evolution of the instantaneous luminosity at ATLAS, CMS and LHCb during a long lasting fill[4] of the LHC as well as a sketch of the introduced offset between the beams. As a result LHCb was operated in Run 2 at $\mathcal{L}_{\text{inst}} = 4 \times 10^{32}\,\text{cm}^{-2}\text{s}^{-1}$ and a constant average number of visible pp-interactions per bunch crossing of $\langle\mu\rangle = 1.1$. Figure 2.6 shows the amount of collected pp-collision data of LHCb split by year for the two physics data taking periods. In 2011 and 2012

[4]The typical length is about 8 h.

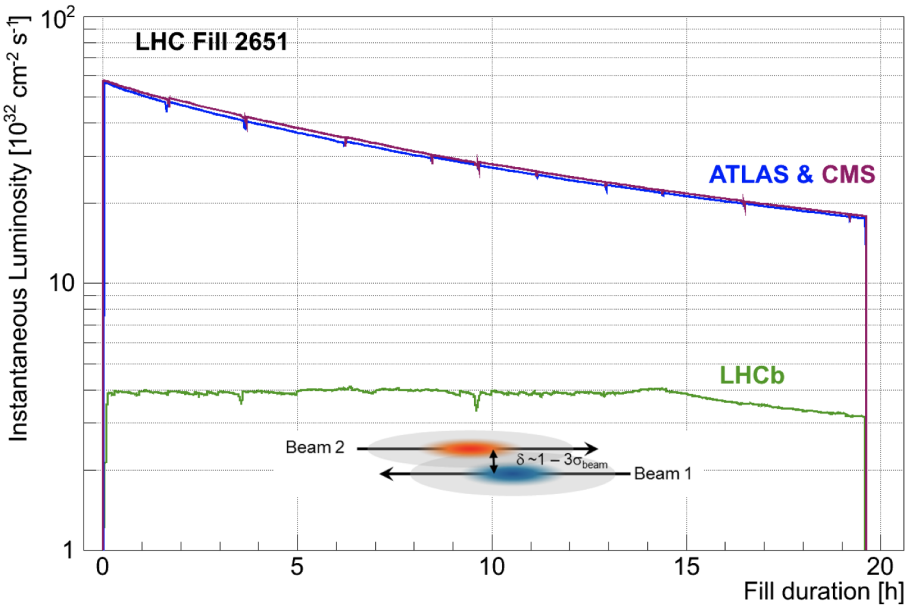

Figure 2.5: Instantaneous luminosity as a function of time at ATLAS, CMS and LHCb during a long lasting fill of the LHC. Taken from Ref. [66].

protons were collided at a centre-of-mass energy of $\sqrt{s} = 7\,\text{TeV}$ and $\sqrt{s} = 8\,\text{TeV}$, respectively, corresponding to about $3\,\text{fb}^{-1}$ of collected data in total, while for Run 2 $\sqrt{s}$ was increased to 13 TeV and about $6\,\text{fb}^{-1}$ of pp-data were collected. The total amount of collected pp-collision data corresponds to $\mathcal{L}_{\text{int}} = 9\,\text{fb}^{-1}$. The following sections describe in detail the different subdetectors, their operation principles and their performances.

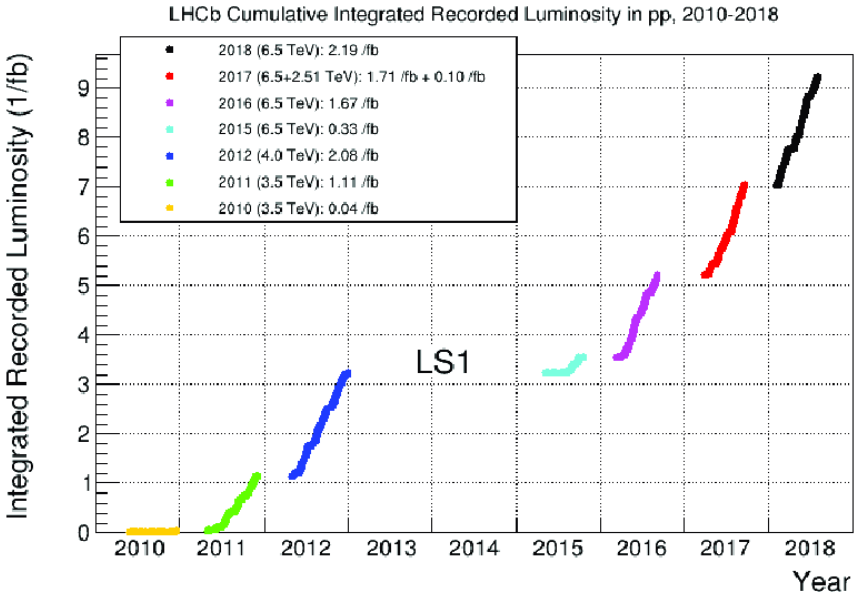

Figure 2.6: Overview of recorded physics data in pp-collisions at LHCb for the different years in the data taking periods Run 1 and Run 2. Taken from Ref. [67]

2.2.1 Crossing angle

When protons pass the LHCb detector they travel through the magnetic field of the LHCb dipole and get deflected in the horizontal plane. To compensate for the strength of this deflection there two compensator magnets (MBXWS and MBXWH) placed upstream of the LHCb dipole and one (MBXWS) downstream of the dipole. Nevertheless, a small orbit bump and hence a crossing angle is introduced.
In addition to this *internal crossing angle* there is a second *external crossing angle* applied by the D1 and D2 kicker magnets of the LHC that first separate and later recombine the two proton bunches to avoid parasitic bunch crossing in the horizontal plane outside the LHCb interaction region. This orbit correction cannot be equal between the two magnet polarities so that the effective crossing angle differs between the polarities. For Run 2 the crossing angles correspond to

$$\vartheta_{MagDown} = \mp 790\,\mu\text{rad}$$
$$\vartheta_{MagUp} = \mp 210\,\mu\text{rad}.$$

The signs apply to beam 1 and beam 2. For the K^0_S and Λ^0 production cross-section measurement presented in this thesis a correction of the p_T- and y-distributions will be applied to account for the crossing angle. More details about the origin of the crossing angles at LHCb can be found in Ref. [68].

2.2.2 Tracking system and vertex reconstruction

The tracking system is dedicated to the reconstruction of the trajectories of charged particles traversing the LHCb detector and leave hits in the sensitive layers of the detectors by depositing a fraction of their energy. The hits are used by tracking algorithms to find patterns that originated from a common traversing particle. Moreover, the tracking system provides a measurement of the momentum of charged particles and enables the reconstruction of primary and secondary vertices, crucial for identifying displaced signatures from c and b hadrons. The performance of a tracking system is characterised by its track and vertex reconstruction efficiencies as well as the momentum and impact parameter (IP) resolution. In order to achieve satisfactory performance good spatial resolution and low material budget are required. The LHCb tracking system has three main tracking detectors: the Vertex Locator (VELO) surrounding the interaction point, the *Tracker Turicensis* (TT) upstream of the LHCb dipole magnet and the three large-area tracking stations (T1-T3) downstream of the magnet consisting of the Inner Tracker (IT) close to the beam pipe and the Outer Tracker (OT) further outside. In addition, the LHCb dipole magnet bends charged particles on a curved trajectory in the horizontal plane which is crucial for the determination of their momenta. Figure 2.7 shows the five different track types that are reconstructed in LHCb:

- Long tracks: Tracks that traverse the full tracking system leaving hits in the VELO and the T stations. Additional hits from the TT can be added to improve the rejection of fake tracks. Long tracks are used for most of the physics analyses performed in LHCb.
- Downstream tracks: Tracks with hits in the TT and T stations only. They are mostly used for analyses involving decays of long-lived particles with a very displaced decay vertex such as K^0_S, Λ^0, Ξ^- and Ω^-.
- VELO tracks: Tracks that only leave hits in the VELO. They are used for the primary vertex reconstruction and can be used as starting point for a long track reconstruction by being extended to the tracking detectors further downstream and for the determination of tracking efficiencies.
- T tracks: Tracks that only leave hits in the T stations. They are rarely used for physics, only for very displaced topologies, but are important for the detector alignment and can be used for tracking efficiency determinations.
- Upstream tracks: Tracks that leave only hits in the VELO and TT and are bent out of the detector acceptance before reaching the T stations. They are mostly low-momentum tracks, rarely used for physics analyses but for flavour tagging algorithms.

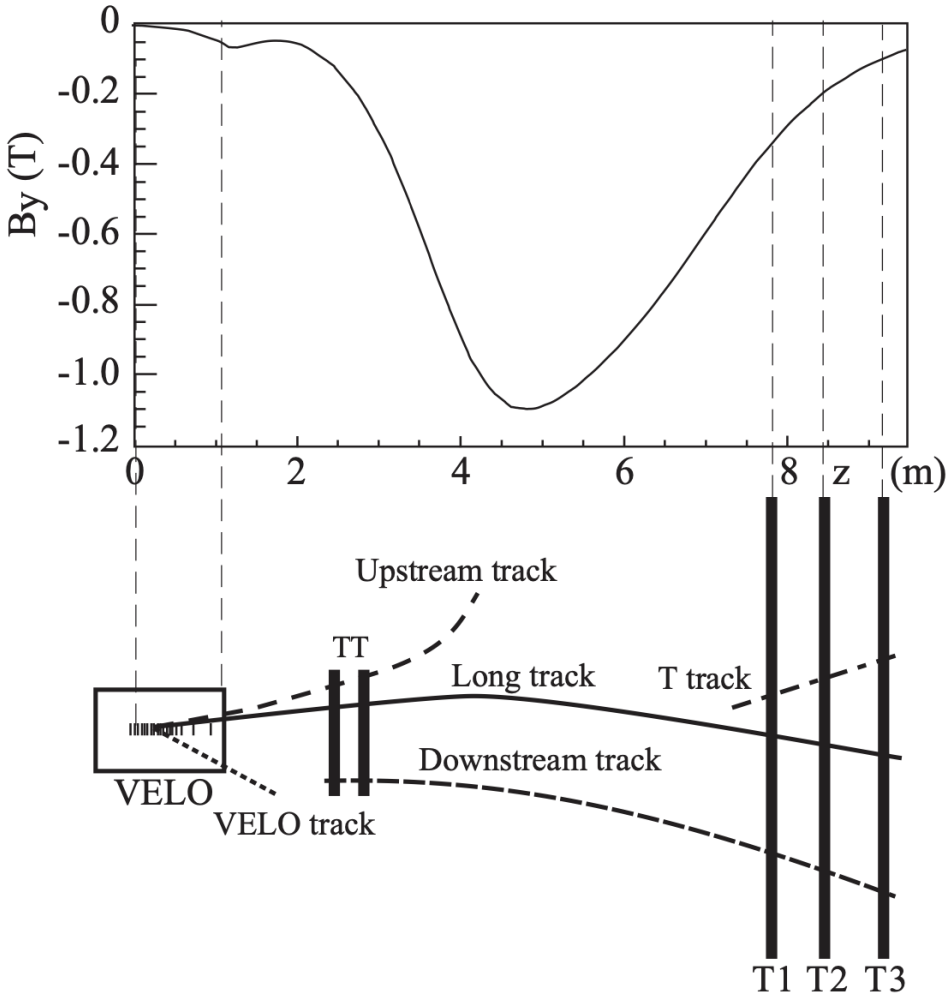

Figure 2.7: Strength of the magnet field component B_y in the different tracking detectors of LHCb and overview of the track types reconstructed in LHCb. Taken from Ref. [63].

The Λ^0 and K^0_S production cross-section analysis presented in this thesis makes use of long and downstream tracks. The tracking algorithms presented for HLT1 focus on long track reconstruction with extensions to downstream tracking and T tracks.

2.2.2.1 The LHCb dipole magnet

The LHCb dipole magnet is located between the TT and the T stations providing a magnetic field in the y-direction that bends charged particles on a curved trajectory in the horizontal plane and thereby enables measuring their momenta. The field strength in the y-direction as a function of the z-position is shown in Figure 2.7. Its integrated field strength corresponds to $B_y = 4\,\mathrm{T\,m}$. The field is designed in a way that it is maximal between the TT and the tracking stations but kept minimal at the position of RICH1 to not affect the performance of its photo multipliers. The magnet can be operated in two polarities *MagUp* and *MagDown* by inverting the direction of B_y, which is done to reduce systematic uncertainties in *CP*-violation measurements. Comparable amounts of data are taken in each configuration.

2.2.2.2 The Vertex Locator (VELO)

The Vertex Locator (VELO) is a silicon-strip based tracking detector consisting of two halves (A-side and C-side) that are equipped with 23 modules each, distributed around the interaction region over a total length of 1 m. Each module is composed of two semicircular 300 µm-thick sensors, the R- and the φ-sensor that measure the radial distance from the beam pipe and the azimuthal angle φ of the hits left by traversing particles at the z-position of the module. Their layout is shown in Figure 2.8. The silicon strips in the R-sensor are circularly aligned around the beam pipe

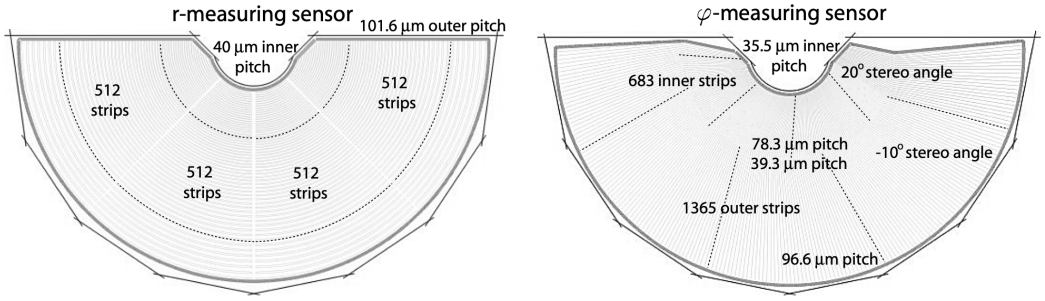

Figure 2.8: Sketch of R- and φ-sensors of a VELO module.

and structured in four segments of 45° each hosting 512 strips with a varying strip pitch from about 40 µm for the innermost strips to 100 µm for the strips furthest away from the beam. The strips of the φ-sensors are straight, pointing radially away from the beam pipe. They are divided into an inner region with 683 strips with an increasing pitch size from 39 µm to 78 µm and an outer region with 1365 strips with a pitch varying from 39 µm to 97 µm. The two VELO halves can be moved away

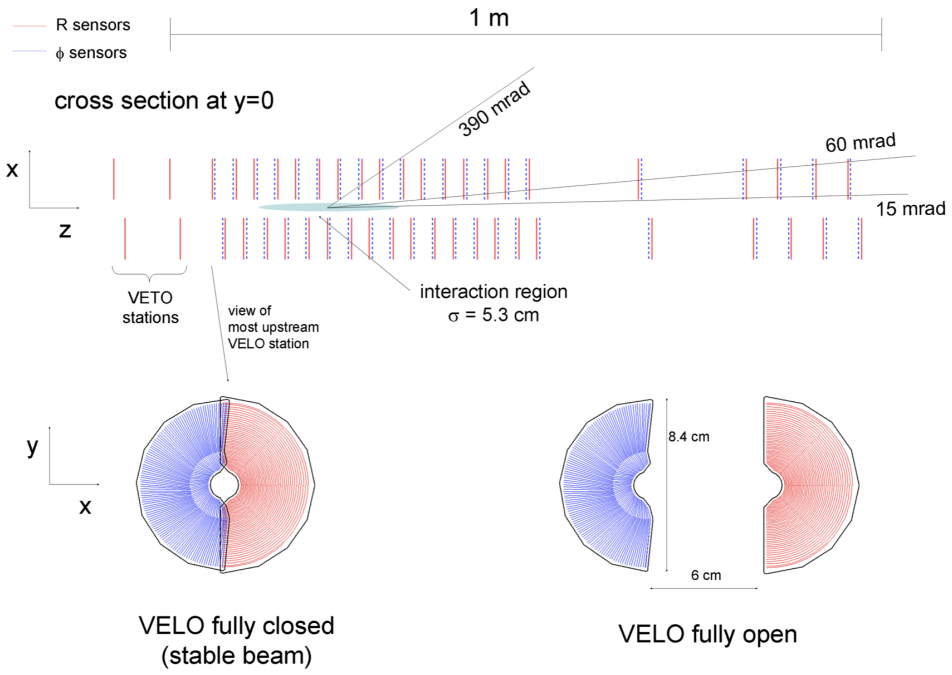

Figure 2.9: Layout of the VELO modules along the beam axis and closed and open position of the VELO. In addition to the regular VELO modules there is two VETO stations. Taken from Ref. [63].

from the interaction region to protect the modules from radiation damages during non-stable beam conditions such as the beam injection into the LHC and during the ramp of the beam energy. This is called the *VELO-open* position ($\sim 30\,\text{mm}$) in contrast to the *VELO-closed* position where the VELO encloses the beam at a distance of 8.2 mm. The positions of the VELO modules along the beam axis are chosen in a way that tracks coming from $z = 0$ with $2 < \eta < 4.5$ are ensured to have at least six hits in the VELO. They are sketched in Figure 2.9 as well as the *VELO-open* and *VELO-closed* positions. The VELO halves are placed in their own vacuum inside of two light-weight aluminum RF-boxes that separate them from the vacuum of the beam. This decouples the VELO modules from potential RF-wave pickups from the LHC beam which would lead to correlated noise among the VELO sensors. The surface that is facing the beam is also referred to as the RF-foil. For a track traversing the LHCb detector the RF-foil is significantly contributing to the material budget before it reaches the first VELO modules, causes elastic scatterings and therefore reduces the overall vertex reconstruction performance. The main tasks of the VELO are to reconstruct primary and secondary vertices with high

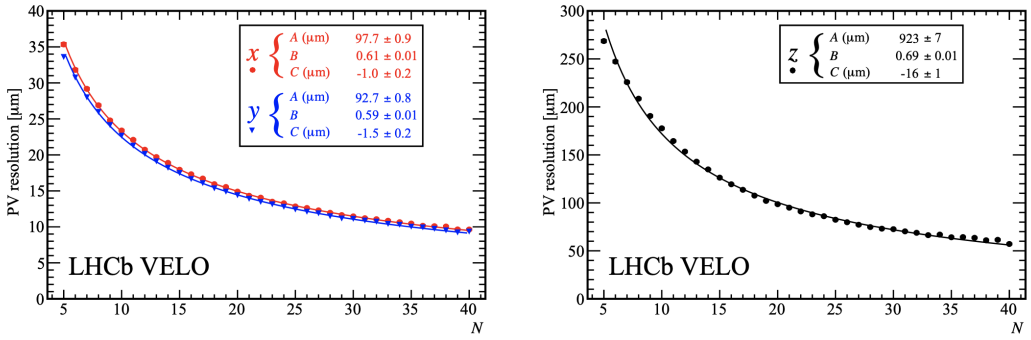

Figure 2.10: PV resolutions of the VELO for the x-, y- and z-directions as function of the number of VELO tracks forming the vertex determined with 2011 pp-data events that had exactly one PV. The minimal amount of VELO tracks for a reconstructed PV is five. Taken from Ref. [69].

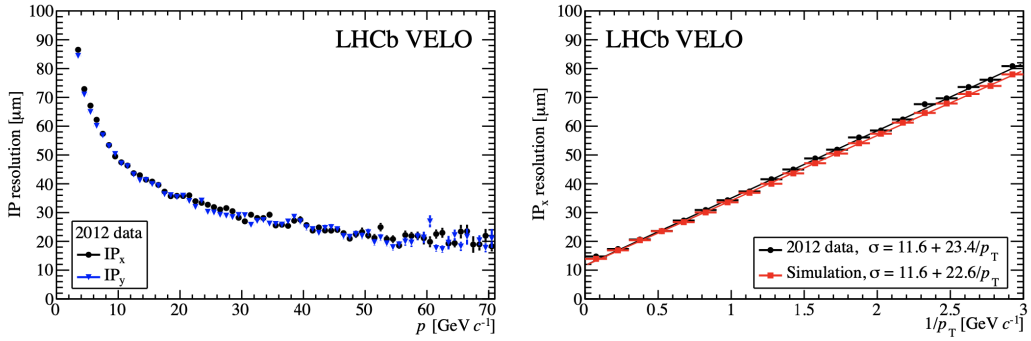

Figure 2.11: (left) $\mathrm{IP}_{x,y}$ resolution of the VELO as a function of p and (right) IP_x resolution as a function of $1/p_\mathrm{T}$. Both are obtained with 2012 pp-data. Taken from Ref. [69].

efficiency and good resolution, to provide a good impact parameter (IP) resolution and efficiently reconstruct high-quality VELO tracks that can be extended to the tracking stations to form long tracks. Figure 2.10 shows the PV resolution in the x-, y- and z-directions of the VELO as a function of the number of tracks used to build the vertex. The IP is defined as the minimal distance between the track and its associated PV. It can be used to efficiently discriminate b or c signal candidates from background. The IP resolution of the VELO as a function of p and $1/p_\mathrm{T}$ are shown in Figure 2.11. Finally, the tracking efficiency of the VELO is found to be about 99 % for the range of p and η usually relevant for LHCb analyses as shown in Figure 2.12.

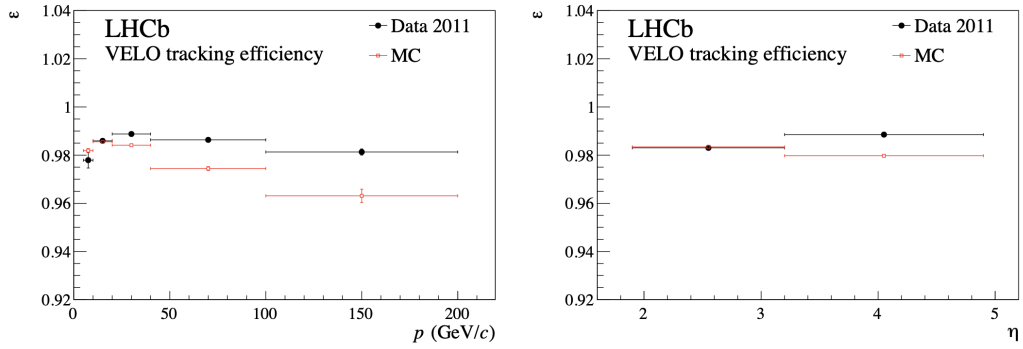

Figure 2.12: Track reconstruction efficiency of the VELO as a function of p and η. Taken from Ref. [69].

2.2.2.3 The Tracker Turicensis (TT)

The *Tracker Turicensis* (TT) is a silicon-strip sensor based tracking detector placed just behind RICH1 and upstream of the LHCb dipole magnet. The silicon sensors are arranged in four layers in two stations (TTa and TTb) that are separated by a gap of 27 cm along the beam axis. As shown in Figure 2.13 the layers follow a x-u-v-x stereo configuration, where the x-layers are aligned vertically and the u- and v-layers are tilted with respect to the x-layers by a stereo angle of $\pm 5°$. This layout allows to not only have a measurement of both the x- and y-position of a hit but also improves the rejection of fake tracks. Each silicon sensor has 512 silicon strips with a pitch size of 183 µm and a thickness of 500 µm. Seven silicon sensors are grouped together into a so-called half-module, with 30 half-modules forming a TT layer. The total active area in the xy-plane covered by the TT is 8.4 m^2. The sensors are further grouped into different read-out sectors (depicted as different colors in Figure 2.13) depending on the expected occupancy. The read-out sectors determine how many sensors are bonded to same wire-bond for the read-out that is performed at the top and bottom outside of the detector acceptance. The TT has a single hit positional resolution of 50 µm. Having a tracking detector upstream of the magnet like the TT is crucial for improving the momentum resolution of long tracks and reducing the amount of fake tracks, falsely reconstructed tracks by the pattern recognition, of the tracking algorithms. In addition, the TT enables the reconstruction of downstream tracks which is very important for decay modes involving long-lived particles.

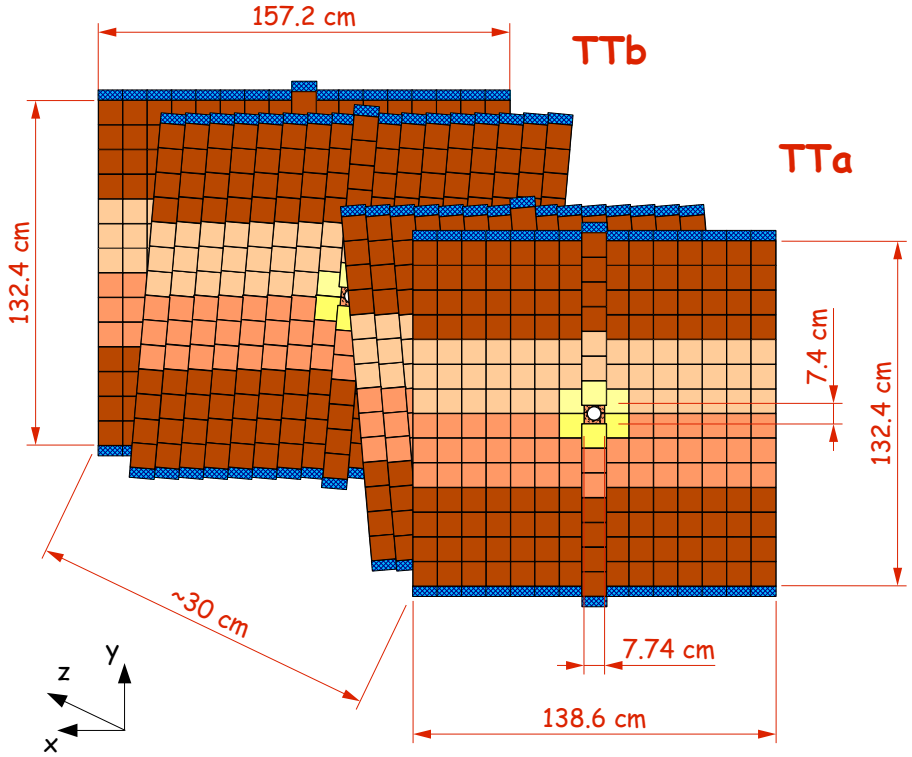

Figure 2.13: Layout of the four layers of the TT detector. The different colors depict the various read-out sectors. Taken from Ref. [70].

2.2.2.4 The T stations

The tracking stations T1-T3 are located downstream of the LHCb dipole magnet. They are composed of the *Inner Tracker* (IT) close to the beam pipe and the *Outer Tracker* (OT) further away from the beam. Each station consists of four layers that are organised in a x-u-v-x configuration in the same way as the TT. Two different detector technologies are used for the IT and OT. The IT is based on similar silicon sensors as used for the TT enclosing the high-multiplicity area (about 20 % of the track multiplicity while covering only 2 % of the LHCb acceptance) close to the beam pipe with a similar single hit resolution as achieved for the TT. A sketch of the detector layout is shown in Figure 2.14a. The IT comprises four detection boxes, where the top and bottom boxes are equipped with one row of seven silicon sensors each, whereas the left and right boxes are made of two rows. Each sensor contains

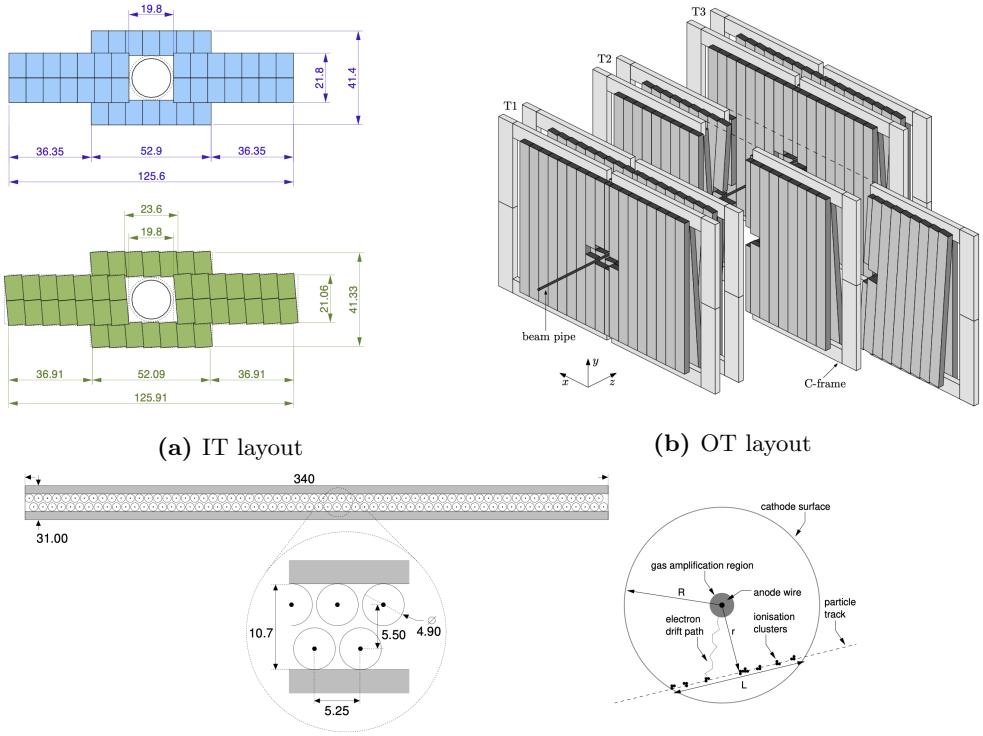

(a) IT layout **(b)** OT layout

(c) Structure of an OT module and sketch of the gas amplification.

Figure 2.14: (a) Detector layout of the x and stereo layers of the IT. Taken from Ref. [71]. (b) Detector layout of the OT assembled in the three T stations. OT modules are mounted into supporting structures called C frames each holding two layers. Taken from Ref. [72] (c) Arrangement of straw tubes and sketch of the gas amplification in the OT module. Taken from Ref. [72].

384 silicon strips with a pitch of 196 µm. The sensors are 7.6 cm wide (x-direction) and 11 cm long (y-direction) and have a varying thickness from 320 µm for the ones in the top and bottom boxes to 410 µm for the ones in the left and right boxes.
The multiplicity in the outer region of the T stations is much lower due to the distance from the beam pipe. Therefore, the OT can be instrumented with modules of straw gas drift tubes. The structure of an OT module is shown in Figure 2.14c. Each module contains 128 drift tubes with a pitch of 5.25 cm that are staggered into two rows shifted by half a pitch. They are electrically separated at $y = 0$ to distinguish signals in the upper and lower halves of the detector. 18 modules are forming together one layer of the OT. The outermost modules are 5 m long, whereas the ones in the inner region are slightly shorter to account for the space that is covered by the IT. The drift tubes have a diameter of 4.9 mm and consist of a gold-plated tungsten

anode with a diameter of 25 µm as well as an electrically conducting cathode. They are filled with a gas admixture of of $Ar/CO_2/O_2$ (70:28.5:1.5). Charged particles traversing the OT ionize the gas and free electrons that are drifting towards the anode wire which is put at a potential of 1550 V. Closer to the anode the electrons, encountering a higher electric field, further ionize the gas so that more electrons are drifting towards the anode and the signal gets amplified. This is visualised in Figure 2.14c. The gas admixture is chosen to have a drifting time below 50 ns where the exact time depends on the position where the particles traversed the tube. The achieved spatial resolution for the OT is about 170 µm [73].

2.2.2.5 Track reconstruction

Track reconstruction deals with the task of reconstructing trajectories of traversing charged particles from signals left in the various tracking detectors. Tracks in LHCb can occur in the various track types mentioned earlier in this chapter. The track reconstruction consists of three steps:

1. The *pattern recognition* is responsible for grouping together detector signals, usually referred to as hits, that are likely to have originated from the same traversing particle.
2. The *track fit* tries to match a track model to the hits found by the pattern recognition, estimate the parameters of the model and the quantities characterising the track such as its charge q and momentum p. Moreover, it is used to assign the quality of the track fit and filter out track candidates of poor quality that are likely to be fake tracks.
3. In the final step track candidates with a bad fit quality are discarded. Moreover, a dedicated algorithm removes duplicated tracks, which are tracks with a significant overlap of hits and are also known as clone tracks. They can be found by different steps in the pattern recognition or be a shorter track segment of the same track.

A track in LHCb is composed by a series of track states at different z-positions. A track state is given by a state vector $\vec{S} = (x, t_x, y, t_y, q/p)^T$, where

$$t_x = \frac{\partial x}{\partial z} \qquad \text{and} \qquad t_y = \frac{\partial y}{\partial z} \tag{2.1}$$

are the slopes in x and y of the track at the given z-position, and a 5×5 covariance matrix for the uncertainties. The goal of the track reconstruction is to determine this series of track states. VELO tracks are reconstructed by forming pairs of hits from the VELO modules furthest away from the interaction region which are then

extrapolated as straight lines to neighbouring modules to look for additional hits and form track seeds. Track seeds with at least three hits are stored and passed on to the track fit from which the VELO tracks are obtained. More details about the VELO tracking are given in Ref. [74]. Two different approaches of long track reconstruction are pursued for the pattern recognition: the *forward tracking* and the *Seeding & Matching*. The forward tracking [76, 77] is based on previously

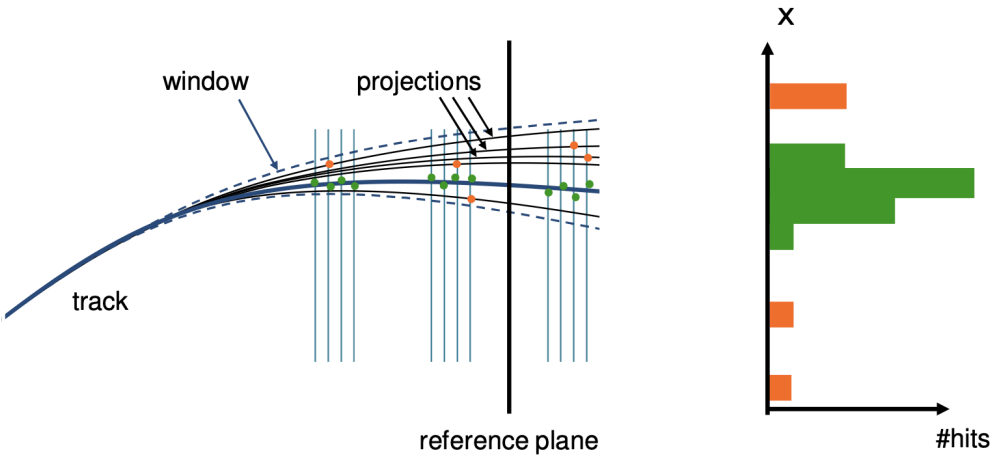

Figure 2.15: Projections of hits from the tracking stations to a common reference plane. The hits depicted in green originated from the same track and form a Hough clusters. Hits depicted in orange cannot be assigned to a Hough cluster. The considered hits are pre-filtered by a search window defined by the extrapolation of the VELO track. Taken from Ref. [75].

reconstructed VELO tracks that are extended to the tracking stations to look for additional hits. From the VELO track reconstruction (x, t_x, y, t_y) can already be determined at a reference z-position, *e.g.* at the end of the VELO, but not the q/p due to the lack of a magnetic field. Therefore, at least one x-position from hits in the tracking stations after the tracks have experienced most of the magnetic field, needs to be added.
A common approach here is to project the x-position of all hits in the tracking stations to a plane at a common z-position assuming a straight line for the trajectory by neglecting the residual magnetic field in the T stations. Afterwards, narrow clusters of hits with the same x-position can be identified as coming from the same track. Low momentum tracks for which the straight line approximation does not hold produce clusters with an enlarged width. This approach has its origin in the analysis of bubble chamber photographs [78, 79] and is today known as a generalised Hough-like transformation. Hits considered for the Hough-clustering are pre-selected

by extrapolating the VELO track via the model of the tracks' trajectory to the tracking stations to open a search window. Figure 2.15 shows an example of the projections of hits in the tracking stations to a common reference plane and the a resulting Hough cluster [80, 81] for a real track. For some use cases such as the HLT1 forward tracking in Run 2 VELO tracks are replaced with VeloTT tracks that were found with the *VeloTT tracking* algorithm described in Ref. [82].
The *Seeding* [83] approach starts from hits in the tracking stations to find seeds in the x-layers. T track seeds are obtained by building hit-combinations from hits of the different x-layers in predefined search windows, followed by a Hough-cluster search in t_y for the stereo layers. A dedicated matching algorithm then back-propagates the T track seeds to the VELO and tries to match them to previously reconstructed VELO tracks. This approach allows also for the reconstruction of downstream tracks by matching T track seeds with hits in the TT [84, 85]. Moreover, T tracks themselves can be used separately. Adaptations of the *Seeding & Matching* algorithms for the first stage of the trigger system of the LHCb Upgrade I detector are presented in chapter 3 of this thesis.
The track fit takes the track candidates found by the pattern recognition and fits them to the track model to obtain the best estimate of the track parameters. In LHCb this is done by applying a Kalman filter [86–88] to them. The Kalman filter tries to iteratively find the best estimate of the track states at different positions z_i that are usually chosen to be identical with the planes of the tracking detectors. More details about the working principle of a Kalman filter are given in Appendix A.

2.2.3 Particle identification

Particle identification (PID) aims at determining the type of particle that left signals in the LHCb detector. For LHCb this is a crucial task since the physics programme is based on studying exclusive decays that require to discriminate between different final state particles. The PID system is a combination of two ring-imaging Cherenkov (RICH) detectors RICH1 and RICH2 before and after the magnet, a calorimeter system and a set of muon chambers. The different systems are explained in more detail in the following sections.

2.2.3.1 The Ring Imaging Cherenkov (RICH) detectors

When a charged particle crosses a medium with a refraction index n and a velocity v higher than the phase velocity of light in the medium c_n, the particle emits photons that are called Cherenkov light. The produced Cherenkov light is emitted in a cone

in the direction of flight of the particle under the Cherenkov angle θ. The angle depends on the velocity of the particle given by the following equation

$$\cos(\theta) = \frac{1}{n\beta} \qquad \text{with} \qquad \beta = \frac{v}{c}. \tag{2.2}$$

A measurement of the Cherenkov angle with the RICH detectors combined with the information about the momentum from the tracking system can be used to determine the mass of the particle. LHCb is equipped with two RICH detectors

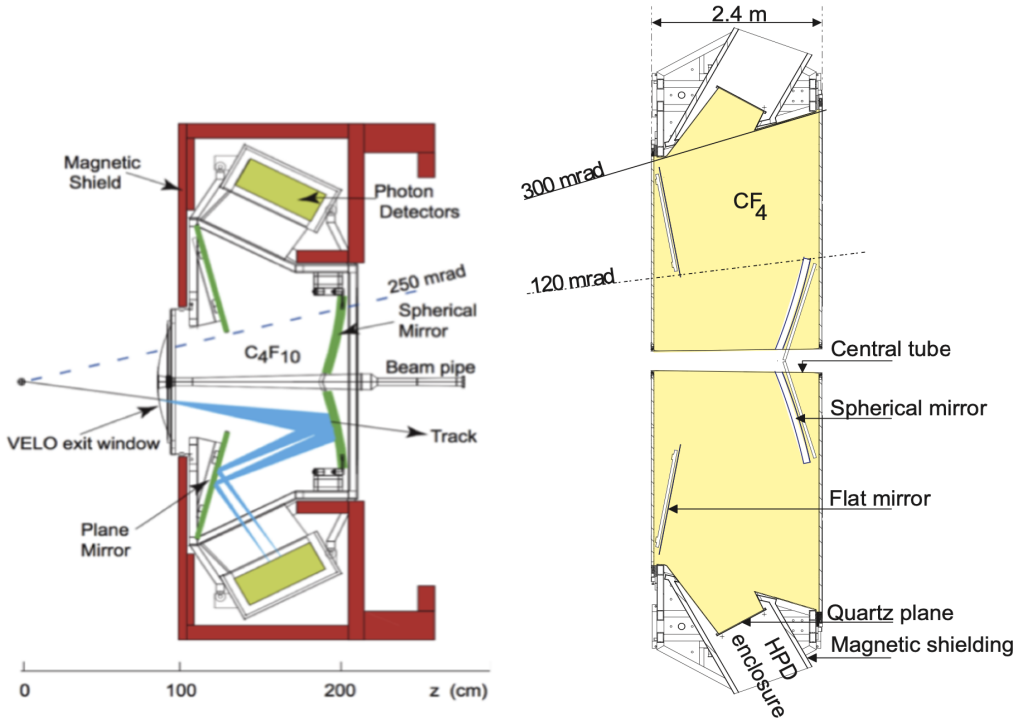

(a) RICH1 **(b)** RICH2

Figure 2.16: Schematic overview of the (a) RICH1 and (b) RICH2 detectors. RICH1 is shown in the yz-plane whereas RICH2 is shown in the xz-plane. Taken from Ref. [63]

RICH1 and RICH2 filled with gases of different refraction indices to cover a broader momentum range. RICH1 as it was operated in Run2 is shown in Figure 2.16a.[5]. The detector layout of the RICH2 is shown in Figure 2.16b. RICH1 uses C_4F_{10} gas

[5] In Run 1 the RICH1 detector was equipped with an additional Aerogel radiator that was removed for Run 2 due to its performance degradation in the high-multiplicity environment and to reduce the material budget.

($n = 1.0014$) as radiator for $\pi/K/p$-separation at momenta between 2 and 60 GeV/c. For RICH2 CF_4 gas ($n = 1.0005$) is used, providing good PID performance at a momentum range from 15 to 100 GeV/c. The RICH1 detector covers the full LHCb acceptance whereas RICH2 only covers the high-η region from 12 mrad to 120 mrad in the xz-plane and 12 mrad to 100 mrad in the yz-plane as the high momentum tracks to be identified by RICH2 have a strong boost into the forward region. The

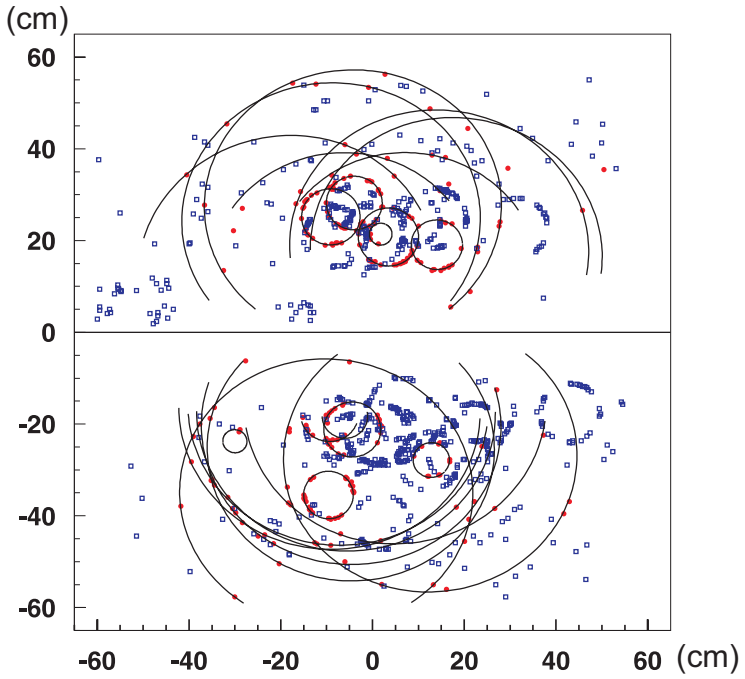

Figure 2.17: Reconstruction of Cherenkov rings in RICH1. Data points correspond to signals in the HPDs, ring segments are extracted from the reconstruction algorithm. Smaller radii are corresponding to the formerly used Aerogel radiator. Taken from Ref. [63]

produced Cherenkov cones are redirected and focused by a combination of spherical and planar mirrors which enables them to be detected by a matrix of Hybrid Photon Detectors (HPD) with a granularity of 2.5 mm × 2.5 mm. The hits in the HPDs from different photons are assigned to Cherenkov rings with dedicated reconstruction algorithms. From the reconstructed ring radii the Cherenkov angles can be derived. An example of the ring reconstruction in RICH1 is shown in Figure 2.17. Another advantage of the redirection is that the HPDs can be placed outside the LHCb acceptance so that they suffer less from radiation damage. Moreover, for RICH1 the HPDs are placed in the yz-plane where the residual magnetic field that could affect the HPD performance is smaller. In addition, for both RICH detectors a magnetic

shielding around the photo detectors is installed. From the reconstructed ring

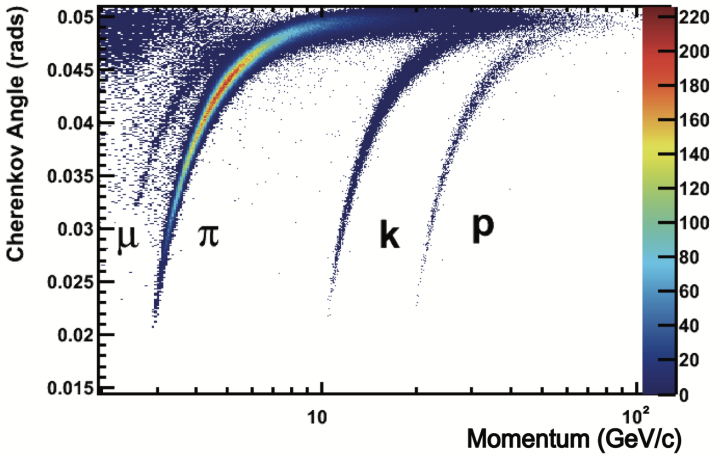

Figure 2.18: Separation power of the RICH1 detector for the various charged particles. Taken from Ref. [89].

segments likelihoods $\mathcal{L}_{\text{RICH}}$ for the different particle hypotheses (π, K, p, e, μ) are built. They can be combined with the PID information of the CALO and the muon systems as discussed later in this chapter. Figure 2.18 shows the discrimination power of RICH1 for the different types of particles.

2.2.3.2 The calorimeter system

The calorimeter system (CALO) is located downstream of RICH2 and the first muon chamber. It consists of an electromagnetic calorimeter (ECAL), a hadronic calorimeter (HCAL) as well as the *Scintillating Pad Detector* (SPD) and the *PreShower detector* (PS). The CALO is used for the identification of electrons, photons and hadrons and can provide a measurement of their energy and their position. All four subdetectors use scintillating material to detect traversing particles. The wavelength of the scintillation light is shifted by a wavelength shifters before it is brought to the Photo Multipliers (PMTs) in case of the ECAL and HCAL or to the *Multi-Anode Photo Multipliers* (MAPMTs) of the SPD and PS.
Two 18 mm thick vertical planes of scintillating tiles build the SPD/PS system. They are separated on the beam axis by 57 mm. In addition, a 15 mm thick lead plate is placed between them, corresponding to 2.5 electromagnetic interaction lengths (X_0) but only ~ 0.06 hadronic interaction lengths (λ_I). In this way electrons and especially photons start electromagnetic showers, while hadrons shower in the HCAL. Electrons produce additional hits in the SPD. This allows them to be distinguished

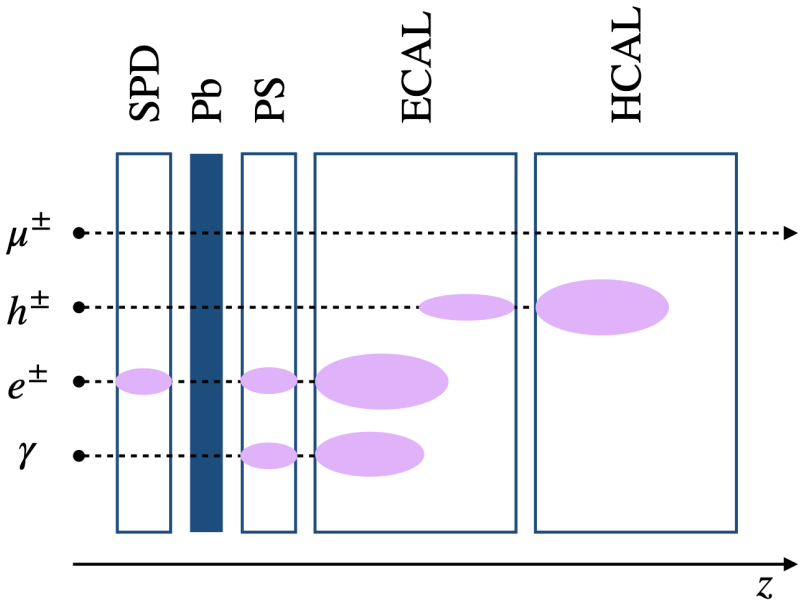

Figure 2.19: Sketch of the expected energy deposition in the various subdetectors of the CALO system by different species of particles. Taken from Ref. [90].

from photons. Figure 2.19 shows the expected energy deposition of muons, hadrons, electrons and photons in the CALO system.
The ECAL is a "shashlik"-type sampling calorimeter with alternating layers of 2 mm thick lead absorber plates and 4 mm thick scintillating tiles resulting in a total length of 83.5 cm and $25X_0$, so that even high-energetic electrons and photons can deposit all of their energy in the ECAL. The HCAL is made of 26 layers of thin iron plates and scintillation tiles and has a total length of 1.65 m with $\lambda_I = 5.6$ to absorb the energy of incoming hadrons. All four subdetectors are segmented into regions of laterally decreasing granularity dealing with the different hit densities close and far from the beam. The SPD, PS and ECAL detectors are split into three of these regions (inner, middle, outer) with cell sizes of about 4×4 cm, 6×6 cm and 12×12 cm whereas the HCAL has only two regions (inner, outer) with cell sizes of about 13×13 cm and 26×26 cm. They are shown in Figure 2.20. The energy resolutions [92] of the CALO system are

$$\frac{\sigma_E}{\sqrt{E}} = \frac{10\,\%}{\sqrt{E(\mathrm{GeV})}} + 1\,\%\ \text{(ECAL)} \qquad \text{and} \qquad \frac{\sigma_E}{\sqrt{E}} = \frac{69\,\%}{\sqrt{E(\mathrm{GeV})}} + 9\,\%\ \text{(HCAL)}. \tag{2.3}$$

The reason for the worse energy resolution of the HCAL lies in the nature of hadronic showers that have much larger Molière radii, i.e. a larger lateral shower profile,

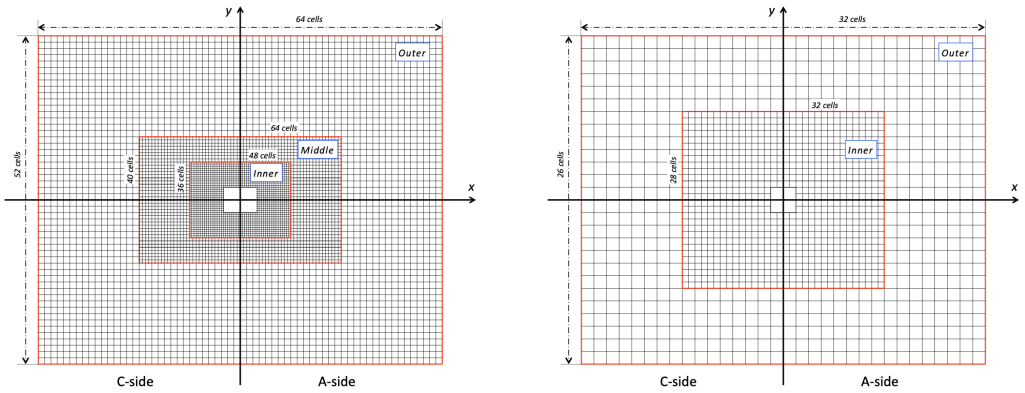

Figure 2.20: Segmentation regions of the ECAL and HCAL. The ECAL is divided into three regions of different granularity whereas the HCAL consists of two. Taken from Ref. [91].

with respect to electromagnetic showers.[6] The reconstruction and identification of electrons and photons in the calorimeter is performed by clustering algorithms that group together hits from neighbouring cells. Clusters that cannot be matched to tracks extrapolated to the ECAL or hits in the SPD are likely to come from photons, whereas clusters that can be matched are interpreted as electrons. The ratio of deposited energy in the ECAL over the momentum of the matched track, taken from the tracking system, gives a powerful discrimination between electrons that deposit most of their energy in the ECAL and hadrons that only leave small amounts in the ECAL and most of their energy in the HCAL. Electrons that are bent in the magnetic field can also lose energy by radiating bremsstrahlung photons that create clusters in the ECAL themselves. A dedicated bremsstrahlung recovery algorithm is responsible for attaching these clusters to reconstructed electron tracks to correct their measured momentum.
The CALO system is also crucial for the Level-0 (L0) hardware trigger. The hit multiplicity in the SPD is used to discard events with large track multiplicity that slow down the reconstruction in following software triggers. The energy in the transverse plane E_{T} provided by ECAL and HCAL is used to trigger on interesting events containing high-E_{T} electron, photon and hadron events. The trigger system is discussed in more detail in section 2.2.6.

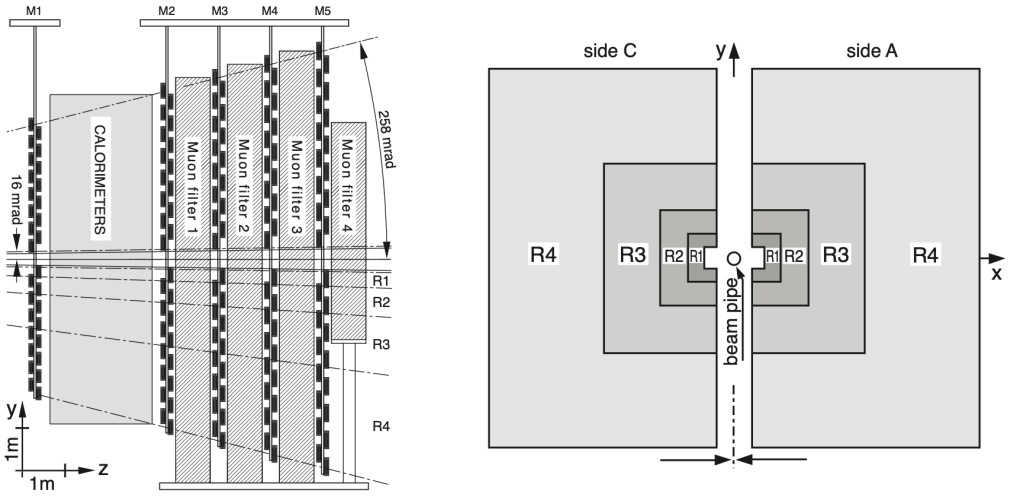

Figure 2.21: Detector layout of the muon chambers M2-M5 with different granularity regions R1-R4. Taken from Ref. [93].

2.2.4 The muon system

The muon system is made of five stations, where the first one (M1) is placed between RICH2 and the CALO system and the remaining four ones (M2-M5) downstream of the CALO. They are used to detect, identify and trigger muons that travel through the LHCb detector without depositing much energy before arriving at the muon chambers. The detector layout of the muon system is shown in Figure 2.21. M1 is particularly important for the L0 muon trigger that is based on a fast transverse momentum estimate in the muon stations. Its position is chosen to improve the p_{T} resolution in the trigger, by minimizing the effects of multiple scattering in the material of the calorimeter.
The muon stations M2-M5 are composed of four regions (R1-R4) of *multi-wire proportional chambers* (MWPC) with laterally decreasing granularity. The granularity in x is finer than in y. The first muon station however is equipped with triple *Gas Electron Multipliers* (GEM) to withstand the higher radiation caused by the stronger particle flux upstream of the calorimeter and thereby reduce the ageing of the detector. Both detector systems are operated with a $\mathrm{Ar/C0_2/CF_4}$ gas admixture in the ratios 45:15:40 for the GEMs and 50:40:10 for MWPCs. This gas admixture allows a fast read-out at about 20 ns and a significant signal yield that are needed for the L0 muon trigger. The MWPCs in M2-M5 are separated by 60 cm thick iron

[6] A Molière radius corresponds to the radius of a cone around the shower that contains 90 % of the energy deposition of a shower.

plate absorbers to force the muon to deposit its energy. The minimal momentum a muon needs for passing all stations is 6 GeV/c. In total there are 1360 MWPCs installed in the muon chambers corresponding to a total active area of 435 m^2 in xy-plane. The angular acceptance covered by the muon stations is 306 mrad in the bending and 258 mrad in non-bending plane.

2.2.4.1 PID variables

The RICH system provides a likelihood $\mathcal{L}_{\text{RICH}}$ for the different types of charged particles that is extracted from the fit of the Cherenkov rings.
The likelihood $\mathcal{L}_{\text{CALO}}$ provided by the CALO system takes into account the hit and showering information from the SPD/PS as well as the fraction of energy deposited in the ECAL and HCAL. An additional variable, in form of a confidence interval called photon `CL`, is used for the identification of photons and their separation from hadrons. It takes into account information from the SPD/PS system as well as the shower shape and energy distribution of ECAL clusters. For the muon identification `isMuon` is a commonly used variable. It is a binary variable constructed from the number of penetrated muon stations and iron absorbers for tracks of different momenta. The muon likelihood $\mathcal{L}_{\text{Muon}}$ is constructed from the average distance of muon station hits to the extrapolation of their associated track from the tracking system [94]. The likelihoods from the RICH, CALO and muon systems are combined to obtain a more powerful discriminant for the separation of (π, K, p, e, μ). Therefore, the likelihoods are multiplied which results in

$$\mathcal{L} = \mathcal{L}_{\text{RICH}} \cdot \mathcal{L}_{\text{CALO}} \cdot \mathcal{L}_{\text{Muon}}. \tag{2.4}$$

In practise, the differences of the hypothesis for a track being particle of type i and the hypothesis for being a pion

$$\Delta \ln(\mathcal{L}_i) = \ln(\mathcal{L}_i) - \ln(\mathcal{L}_\pi) \tag{2.5}$$

is used. They are called the `DLL` variables. Figures 2.22a, 2.22b and 2.22c show typical performances of the `DLL` variables for the separation of kaons and protons as a function of the momentum. An excellent separation between the charged hadrons can be seen for the majority of the momentum range relevant for LHCb. However, there are also regions, for example in the p-K separation at low momentum, where the RICH performance is limited.
In addition, another set of variables is obtained from training a Neural Network separately for each type of charged particle using the information of from all subdetectors. The output of the Neural Network returns the hypothesis for the particle type in form of a probability and is called `ProbNN`. In most cases the `ProbNN` have a stronger discrimination power than the `DLL` variables.

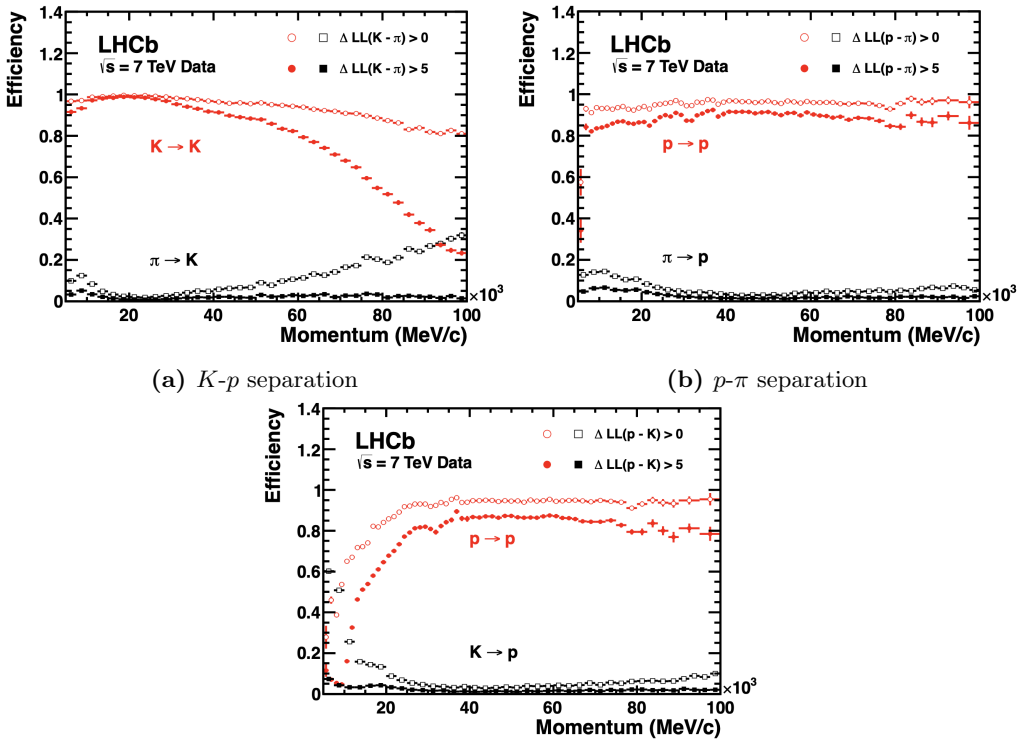

(a) K-p separation

(b) p-π separation

(c) p-K separation

Figure 2.22: Performances of the (a) K-π, (b) p-π and (c) p-K discrimination as a function of momentum. All figures are taken from Ref. [89].

2.2.5 Other systems

The *Beam Conditions Monitor* (BCM) [95] consists of two ring-like stations of eight diamond sensors that are distributed around the beam pipe. The stations are placed upstream of the VELO and downstream of the TT and monitor the particle flux by integrating the currents in the different sensors over predefined time intervals. If the average flux exceeds the tolerance threshold the BCM logic triggers a dump of the LHC beams. The BCM is particularly important to protect the sensitive VELO modules from unstable beam conditions. For LHCb it is especially relevant as the detector is close to transfer line T18, as shown in Figure 2.1a, from where beam 2 of the LHC is injected which might cause unsafe beam states.
The *System for Measuring Overlap with Gas* (SMOG) allows the LHCb experiment to run in a fixed-target mode by injection various gases in the vacuum chamber of the VELO. It was originally designed to perform a method for measuring luminosity

alternative to the van-der-Meer scans, called beam-gas [96–98] imaging, but has been further exploited for physics measurements.

2.2.6 The LHCb trigger system

The trigger system of LHCb consists of three stages. The first one is a Level-0 (L0) hardware trigger followed by a high-level software trigger (HLT) with two stages (HLT1 and HLT2). Figure 2.23 shows a schematic overview of the three trigger stages as they were operated in Run 2. The pp bunch crossing rate at LHCb corresponds

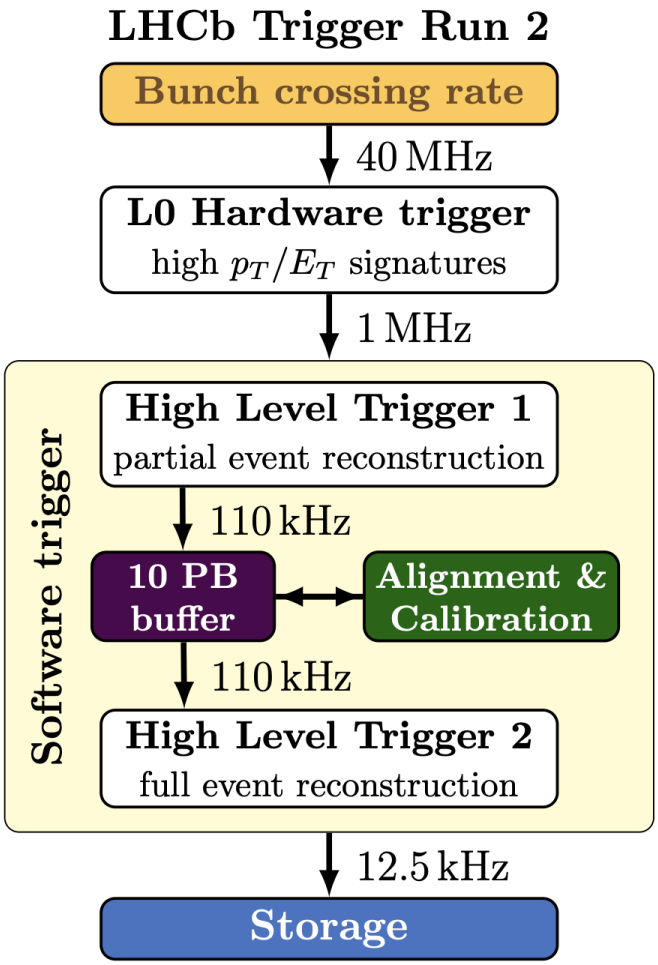

Figure 2.23: Stages of the LHCb trigger system and their event rates during Run 2. Taken from Ref. [99].

to 40 MHz. This also includes empty bunches so that the effective collision rate of visible interactions is reduced. In Run 2 it corresponded to about 30 MHz. The amount of event data resulting from colliding proton bunches at 30 MHz is by far too high to store every event. Moreover, many of the processes studied at LHCb are rare, so that many other events are not of interest. Therefore, the three stages of the trigger system are responsible for filtering out interesting events for the physics studied at LHCb while discarding a large amount of uninteresting events in order to decrease the rate down to 12.5 kHz. A set of trigger selection requirements for a specific process or type of physics is usually referred to as a *trigger line* in LHCb. The trigger stages are explained in more detail in the following sections.

2.2.6.1 L0 trigger

The L0 trigger is implemented in field-programmable gate arrays (FPGAs) with a fixed latency of 4 µs in the read-out electronics of the subdetectors. It is responsible for reducing the 40 MHz of raw data coming directly from the detector read-out by a factor of 40 down to 1 MHz. For this purpose a set of L0 trigger lines are implemented making requirements on the minimal amount of deposited transverse energy E_{T} in the calorimeter system or the minimal transverse momentum p_{T} of a track leaving hits in the muon stations as well as the maximal amount of hits left in the SPD. The calorimeter-based trigger lines use the E_{T} of a cluster of 2×2 cells in ECAL or HCAL. Here, the transverse energy of the cluster is given by

$$E_{\mathrm{T}} = \sum_i E_i \sin\theta_i, \tag{2.6}$$

where E_i describes the energy deposited in cell i and θ_i the angle between the beam axis an the centre of the cell. Information from the SPD/PS is used to distinguish among electrons, photons and hadrons and define the `L0Hadron`, `L0Electron` and `L0Photon` trigger lines. For the triggers based on the muon system straight tracks with hits in all five stations are searched for. The p_{T} of the track is then estimated from its direction assuming the particle originated from the interaction region. Thresholds on the minimal p_{T} are used to define the L0 single-muon trigger line `L0Muon` and the more specific di-muon `L0DiMuon` and high-p_{T} muon lines. Only one (pair of) track(s) in the event is needed to pass any of the trigger line requirements for the event to be accepted. In addition, for most of the lines events are required to have a maximum amount of hits in the SPD. This discards busy events with a high track multiplicity that require a lot of computing time for the reconstruction in the HLT. Table 2.1 shows typical selection requirements for the L0 trigger lines in 2016. Any event passing one of the L0 trigger lines is kept and further processed by the HLT system.

Table 2.1: Typical selection requirements of L0 trigger lines in Run 2. Values are taken for 2016 from [99]. Values for the kinematic thresholds slightly change among the years.

Trigger line	kinematic cut	SPD hits
`L0Hadron`	$E_{\mathrm{T}} > 3.7\,\mathrm{GeV}$	< 450
`L0Electron`	$E_{\mathrm{T}} > 2.4\,\mathrm{GeV}$	< 450
`L0Photon`	$E_{\mathrm{T}} > 2.78\,\mathrm{GeV}$	< 450
`L0Muon`	$p_{\mathrm{T}} > 1.8\,\mathrm{GeV/c}$	< 450
`L0DiMuon`	$p_{\mathrm{T}}^2 > 2.25\,\mathrm{GeV}^2/\mathrm{c}^2$	< 900
`L0Muon`, high p_{T}	$p_{\mathrm{T}}^2 > 6.0\,\mathrm{GeV}^2/\mathrm{c}^2$	-

2.2.6.2 High-level trigger (HLT)

The two stages of the high-level trigger are a set of algorithms fully implemented in software that are run on the Event Filter Farm (EFF). The first stage HLT1 reduces the incoming rate of 1 MHz by a factor of about 10 before events are transferred to the EFF buffer system with 10 PB of storage. HLT1 performs a partial event reconstruction which covers the track reconstruction and vertex reconstruction as well as the muon identification. The track reconstruction run in HLT1 is the forward tracking described previously in section 2.2.2.5. Other PID algorithms cannot be run in HLT1 due to tight timing constraints. HLT1 selections look for displaced vertices and tracks of certain quality as well as pairs of muon tracks. The selections are not decay channel specific but rather inclusive. Channels involving photons can only be triggered as byproduct of other signatures in the event, while electrons can be only triggered directly by fulfilling general track requirements in the trigger. Events surviving the HLT1 selections are stored in the buffer system, where automated alignment and calibration tasks, introduced in Run 2, are run in real-time for the different subdetectors before events are passed on to HLT2. They are necessary to improve the reconstruction quality in HLT2, which is crucial also for the LHCb Upgrade I as it will be discussed in section 2.4. For all alignment and calibration tasks samples of well-reconstructed tracks are taken by dedicated HLT1 trigger lines and the tasks are performed with a regular frequency. Figure 2.24 shows the typical time scales of the alignment and calibration tasks. The alignment of the VELO is performed by minimizing the residuals of a Kalman filter. The same strategy is used for the alignment of the other tracking detectors and the muon chambers. The alignment of the tracking detectors is crucial for the momentum resolution of charged tracks. Further alignment tasks are performed for the RICH mirrors by extracting their alignment constants from the fit of the Cherenkov rings to ensure a good performance of the PID. Finally, the global timing of the OT, the refraction

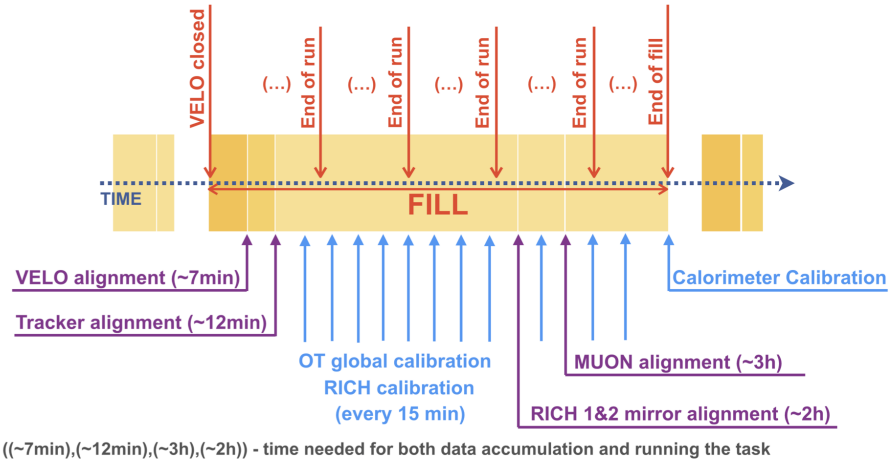

Figure 2.24: Sketch of the run time of the various alignment tasks in Run 2. Taken from Ref. [99].

indices of the gases in the RICH detectors, as well as the gains of the HPDs in the RICH and the PMTs in the ECAL need to be calibrated. Further details about the real-time alignment and calibration in Run 2 can be found in Ref. [99–101].
HLT2 performs a full event reconstruction, which means that also information of the RICH and CALO systems is exploited for the HLT2 selections. The reconstruction in HLT2 is also referred to as the *online* reconstruction in contrast to the *offline* reconstruction that is performed in the offline data processing after all trigger decisions are performed and the full raw data of selected events is saved to tape. The timing budget in HLT2 is much more flexible than in HLT1, which allowed in Run 2 to run the same reconstruction algorithms online and offline. Furthermore, selections for both inclusive and exclusive decay channels can be run. After passing the trigger selection events are packed into streams that contain all events that were triggered by trigger lines with similar physics. These are used offline for physics analyses. In Run 2 a novel real-time analysis technique called the *TURBO stream* [100, 102] was introduced for the HLT that writes offline quality signal candidates directly into storage without keeping the full raw data of the rest of the event. Special features of the TURBO stream are reduced event sizes that allow to save more events as well as a flexibility in the amount of raw and reconstructed event data that is saved for a trigger selection. This concept is called *selective persistence* and visualised in Figure 2.25. The success of the Turbo model is built on the high-quality online reconstruction ensured by the real-time alignment and calibration since an offline re-reconstruction is not possible.

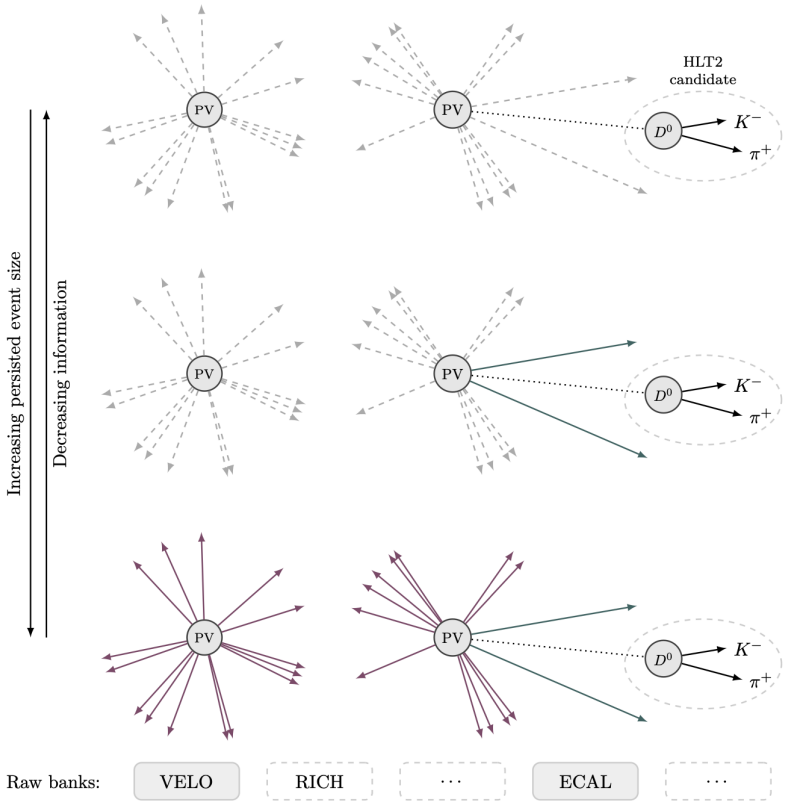

Figure 2.25: Sketch of the different level of persistence of a $D^0 \to K^-\pi^+$ candidate that triggered a selection line. Taken from Ref. [102].

2.2.6.3 Features of a trigger system

This section introduces concepts in the triggering strategy of LHCb that are relevant for the discussions later in this thesis.

- TIS and TOS: Signal candidates from events that survived the trigger selections can be assigned to different trigger categories with respect to a dedicated trigger line. They are classified as *Triggered on signal* (TOS) if the tracks of the signal candidate fired the trigger line and as *Triggered independent of signal* (TIS) if something else in the event fired that trigger line and the signal candidate is only kept as a byproduct. In addition, there is a third category *Triggered on both* if parts of both the signal candidate and the rest of the event are required. The classification is depicted in Figure 2.26.

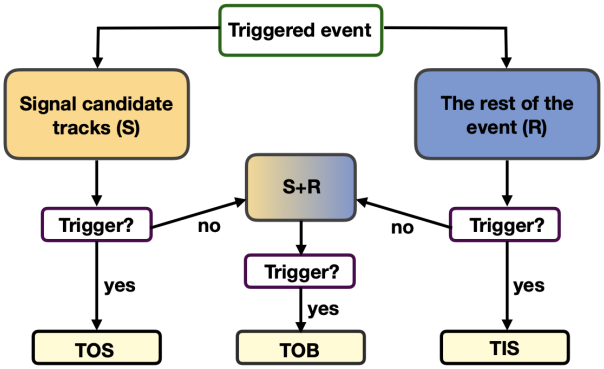

Figure 2.26: Trigger category assignment process for signal candidates to a dedicated trigger line. Adapted from Ref. [103].

- NoBias trigger: A NoBias trigger selects events pseudo-randomly without applying any trigger selection. The randomness is limited by only choosing events from non-empty bunch crossings. In Run 2 dedicated physics data samples were collected with NoBias triggers in all stages of the trigger system. The samples from the 2018 data taking are used in this thesis for the measurement of the Λ^0 and K^0_S production cross-section ratios. Simulated events with these conditions are referred to as *Minimum Bias* samples due to minimal requirements to the Monte Carlo generators.

- Trigger rates: The rate of a trigger line is defined as the amount of events per second that fire the trigger line. The rate is an important quantity when developing new trigger selections to see if they fit into the overall computing budget of the trigger system. For this purpose they can be measured on Minimum Bias simulation samples. Once the trigger is run on actual data the trigger rates can be measured directly.

- Prescale: If the rate of a trigger line is too high for the computing budget of the LHCb trigger system a so-called prescale can be applied to the line to further reduce its rate. The prescale randomly discards a predefined amount of events that fired the trigger line. Prescales can be varied during data taking if the trigger configuration is changed.

- Throughput: The throughput of a trigger system or one of its stages is defined as the amount of events that can be processed per second. For that all processes from the reconstruction to the trigger selections need to be taken into account. The minimal required throughput is determined by the computing structure used for the LHCb trigger system.

2.3 Upgrade I of the LHCb detector

Between 2018 and 2022 the LHC was in its second Long Shutdown that was used at IP8 to undergo the first major upgrade of the LHCb experiment, that goes under the name *LHCb Upgrade I* [104, 105]. LHCb Upgrade I is planned to be operated in Run 3 and 4 at an instantaneous luminosity of $\mathcal{L} = 2 \times 10^{33}\,\mathrm{cm}^{-2}\mathrm{s}^{-1}$ which is an increase of factor five with respect to Run 2 with a targeted $\langle\mu\rangle = 5.2$. As a consequence the detector has to be able to process a much higher data rate and withstand the radiation damage of the higher track multiplicity. Therefore, for LHCb Upgrade I the tracking system was fully replaced with a new set of detectors: the upgraded VELO, the Upstream Tracker (UT) upstream of the magnet replacing the TT and the Scintillating Fibre Tracker (SciFi) as the main tracking detector downstream of the magnet replacing the IT/OT. Another major change for the upgraded experiment is the redesign of the trigger system. The formerly used L0 hardware trigger is removed to allow for more flexibility in the trigger configuration and higher trigger efficiencies. This means that the first stage of the software trigger has to be operated at a throughput of 30 MHz. Moreover, all subdetectors need to be read-out at 40 MHz which requires a replacement of their front-end read-out electronics. This chapter is structured as follows:
The upgrade of the tracking system will be discussed in detail in sections 2.3.1-2.3.3 due to their relevance for the track reconstruction discussed in this thesis. Afterwards, the changes in the data processing chain with particular focus on the upgrade of the trigger system are discussed in section 2.4. Finally, major remaining changes of the subdetectors for the LHCb Upgrade I are highlighted in section 2.4.6

2.3.1 The upgraded Vertex Locator

The LHCb Upgrade I requires an upgrade of the VELO detector than can handle the higher track multiplicity and radiation dose from the increased luminosity and can be read-out at 40 MHz. At the same time the physics performances of the old VELO have to be maintained or even improved. For these reasons the silicon-strip based modules of the VELO are fully replaced by a modules based on silicon pixels to achieve a higher granularity than before and custom read-out ASIC called VeloPix [106]. The new VELO detector is planned to be operated during Run 3 and Run 4 with a foreseen amount of collected data of $50\,\mathrm{fb}^{-1}$. This means that the innermost sensors of the modules close to the interaction point will have been exposed to a fluence of $8 \times 10^{15}\,\mathrm{MeV}\,n_{\mathrm{eq}}\ \mathrm{cm}^{-2}$ at the end of their lifetime. The upgraded VELO is composed by two retractable halves (A-side and C-side) with 26 pixel

modules each that are arranged perpendicularly to the beam. Figure 2.27 shows the

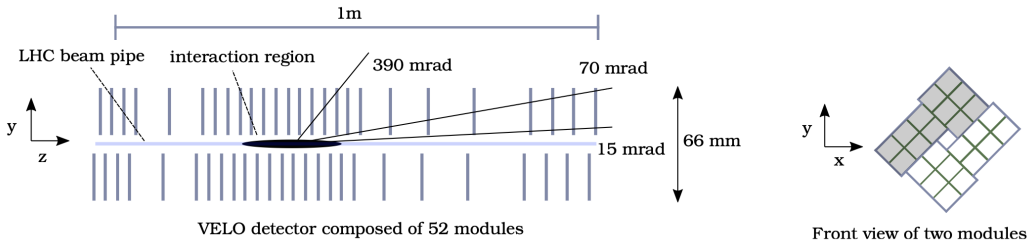

Figure 2.27: Positioning of the VELO modules along the beam axis and front view sketch of two VELO modules in closed position of the VELO. The squares depict the VeloPix read-out chips. Taken from Ref. [107].

layout of two VELO modules in the *VELO-closed* position and the positioning of the modules along the beam axis. The z-positions of the modules along the beam axis are optimized for IP resolution and track reconstruction performance. Figure 2.28a shows a comparison of the module positions for the old and the upgraded VELO. Tracks in the geometrical acceptance of the LHCb detector that originated from the interaction region have crossed at least four stations of the upgraded VELO detector. In comparison to the old VELO the two additional stations for $300\,\text{mm} < z < 500\,\text{mm}$ improve the acceptance for decays with displaced decay vertices such as the $K_S \to \pi^+\pi^-$ and $\Lambda^0 \to p\pi^-$ decays discussed in this thesis. A front and back side view of the VELO module is shown in Figure 2.28b. The modules consist of two assemblies that build a L-shape geometry. Each assembly contains two rows of tiles composed by one silicon sensor that is bump-bonded to three VeloPix read-out chips. The two rows are installed on the front and the back of the module with a sensor overlap of 110 µm to ensure the full coverage of the LHCb acceptance. The sensors closest to the beam start at a distance of 5.1 mm which is closer than for the previous VELO (8.2 mm). Each sensor consists of 768×256 pixels with a pitch of 55 µm. The thickness of the sensor is 200 µm. The tiles are then placed on a 500 µm thick silicon slab representing the microchannel cooling substrate. The cooling of the VELO modules is essential to avoid thermal runaway effects of the currents in the silicon sensor and read-out chip, which are likely to occur especially in the innermost region from higher leakage currents due to the increased radiation damage. In addition, there is heat generated from the VeloPix read-out chip that needs to be absorbed by the coolant to ensure a stable performance. As in Run 2 evaporative bi-phase CO_2 is used as coolant.[7] A key feature of the VELO upgrade is the integration of the bi-phase cooling directly into

[7] The heat is absorbed by the CO_2 at the phase transition from the liquid to the gaseous state. For more details see Ref. [109, 110].

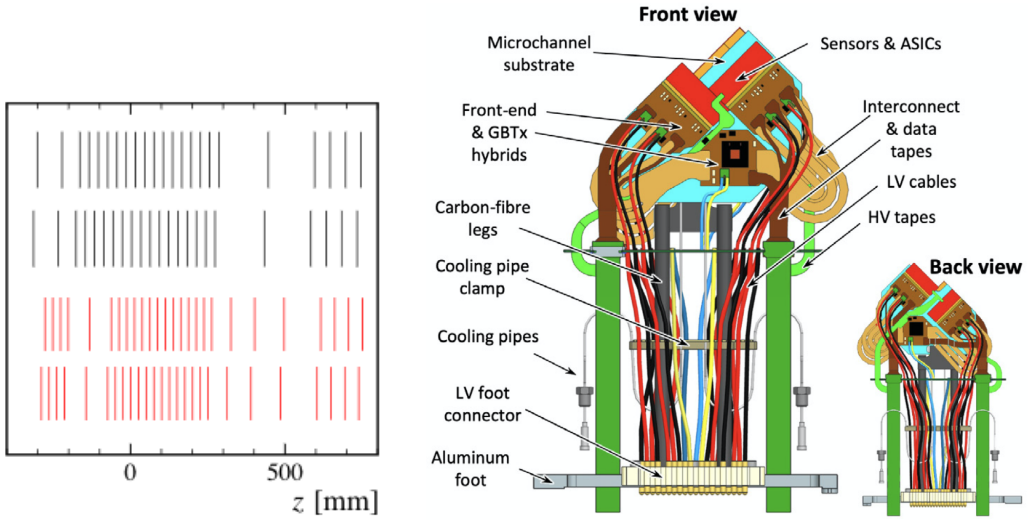

(a) positioning comparison **(b)** VELO module layout

Figure 2.28: (a) Comparison of the z-positions of the VELO modules for the old VELO (depicted in black) and the the upgraded VELO (depicted in red). Taken from Ref. [108]. (b) Front and back view of a VELO module. Two sensors bump-bonded to three VeloPix chips (ASICs) are installed on each side building an L-shape. The microchannel substrate supplied with bi-phase CO_2 via the cooling pipe is responsible for the cooling of the sensor and read-out chip. Cables for the read-out and high and low voltage supply are also shown. Taken from Ref. [109].

the module. This is realised by microscopic cooling channels in which the CO_2 is circulated.

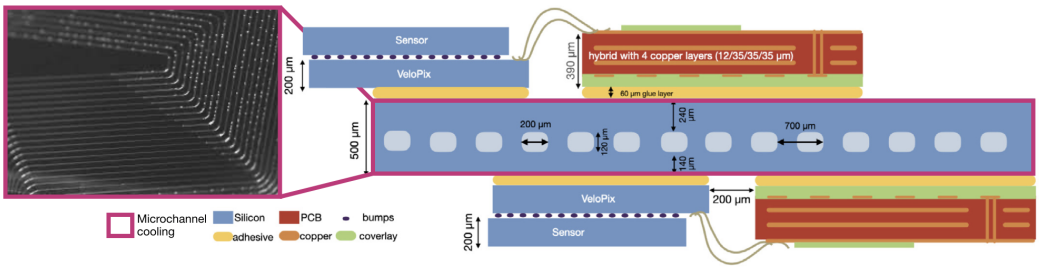

Figure 2.29: Cross-section of the VELO module and picture of the two phases of CO_2 in the cooling microchannels. Adapted from Ref. [109].

A similar technology has been used for high-energy physics applications previously

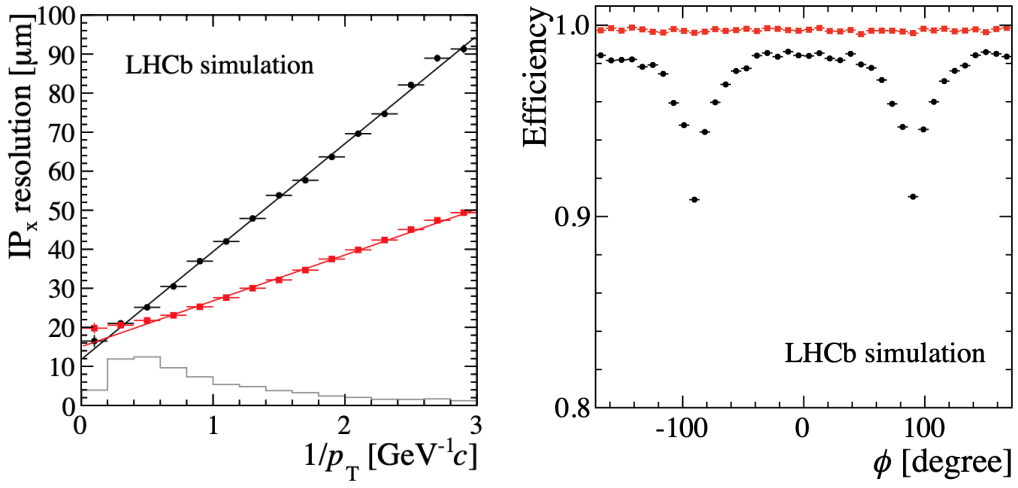

(a) IP$_x$ resolution

(b) Reconstruction efficiency

Figure 2.30: Comparisons of the performance of the old (black) and the upgraded VELO (red) detector showing (a) the IP$_x$ resolution for long tracks from decays of b-hadrons and (b) the track reconstruction efficiency of VELO tracks as a function of the azimuthal angle ϕ. Both plots are obtained from simulated events of b-hadron decays at 14 TeV and $\nu = 7.6$. Taken from Ref. [108].

only for the *GigaTracKer* by the NA62 experiment [111]. They are etched on the thin silicon substrates on the back of the silicon pixel sensors. Thereby, the silicon sensors are kept at a maximum temperature of $-20\,^{\circ}\mathrm{C}$. Figure 2.29 shows a cross-section of the VELO module and a picture of the bi-phase CO_2 flowing through the cooling microchannels. The expected IP resolution of the upgraded VELO detector is strongly improved with respect to the old VELO detector as can be seen on simulated data in Figure 2.30a. This mostly results from the instrumentation closer to the beam, in particular for the first measured hit to reduce the multiple scattering and the reduced distance between the stations of the VELO as shown in Figure 2.28a. From Figure 2.30b it can be seen that the overall VELO track reconstruction efficiency is also improved. Moreover, the dips in the track reconstruction efficiency for the old VELO at $\phi = \pm\pi$ are avoided with the overlapping design of the sensors of the new VELO module. Furthermore, slight improvements for the PV and decay time resolution are expected for the upgraded VELO.
A fast reconstruction of tracks and vertices in the upgraded VELO is crucial for the operation of the upgraded trigger system. A description of the *Search by triplet* algorithm [107] used for the VELO track reconstruction in HLT1 will be given in chapter 3.

2.3.2 The Upstream Tracker

The Upstream Tracker (UT) replaces the formerly used TT as the tracker upstream of the LHCb dipole magnet. As in the TT, the detector is based on silicon sensors, but optimized for the LHCb upgrade. This includes the need for a higher granularity especially close to the beam pipe because of the higher track multiplicity, an improved radiation hardness to enable the collection of $50\,\mathrm{fb}^{-1}$ of data and fast read-out of the detector at 40 MHz. The UT is composed of four layers in two stations (UTa,

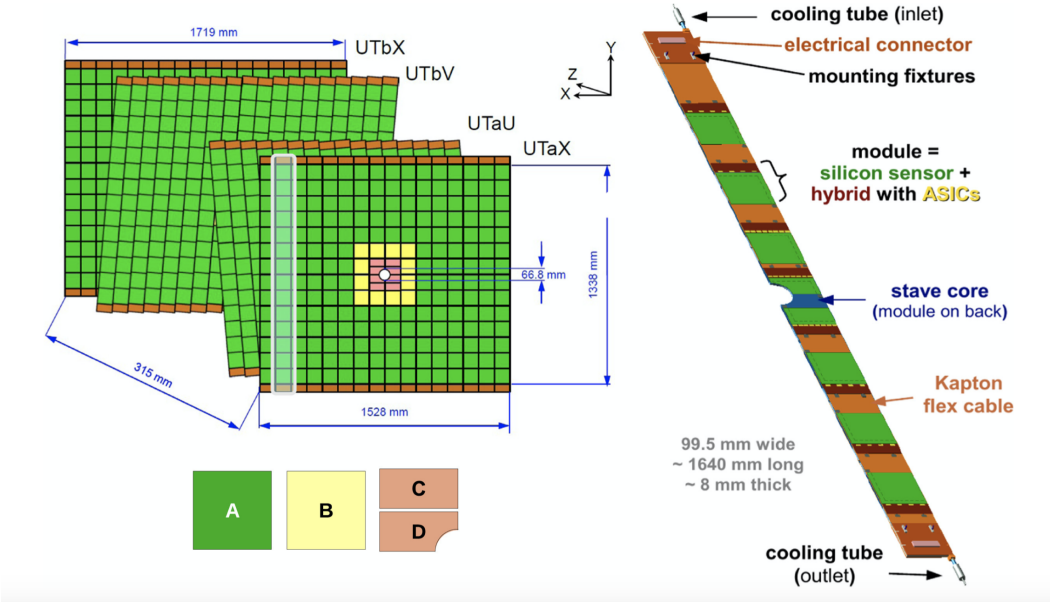

Figure 2.31: Arrangement of the four layers of the UT. The different sensor types are depicted in different colors. The structure of an UT stave is shown on the right. Taken from Ref. [112].

UTb) building a x-u-v-x configuration. Silicon micro-strip sensors are arranged in vertical columns, so-called *staves*, that cover the full vertical dimension of the detector. Figure 2.31 shows the geometry of the UT detector as well as the structure of a stave. The layers in the UTa station contain 16 of these staves, for the layers of the UTb station there are 18. Each stave is built from 14 sensors that are mounted together with their front-end read-out electronics (ASICs) on a custom hybrid that is placed alternately on the front and the back of the stave. In addition each stave has a cooling tube that keeps the sensors at a temperature below $-5\,^{\circ}\mathrm{C}$. Sensors within a stave have an overlap in the y-direction of about 3.8 mm. The stave supports are staggered by 1 cm in the z-direction to allow for sensor overlaps of 2 mm also in the

x-direction. The overlaps overcome any gaps in the detector acceptance that were present for the TT.
There are four classes of sensors (A, B, C, D) of different geometry and granularity used in every UT layer. Type A sensors are the default that are used for most of the active area of the UT. The sensors are quadratic with a dimension of about 10 cm containing 512 strips of 190 µm pitch. Type B sensors are used closer to the beam pipe where the track multiplicity is much higher. The sensor dimension is the same as for Type A sensors but the strip pitch size is halved to 95 µm, so that 1024 strips fit into one sensor. In addition there are Type C and Type D sensors that are used to instrument the area close to the beam pipe. The rectangular Type C sensors are identical to Type B sensors but with a reduced length of 5 cm. Type D sensors are the same as Type C sensors but with a cutout around the beam pipe. This design enables a larger geometrical acceptance of the UT compared to that of the TT. The active area of the innermost sensors starts at a distance of about 34.2 mm from the beam pipe. All sensors have a thickness of 320 µm which is significantly smaller than for the TT (500 µm). This reduces the material budget of the UT to $< 5\,\% X_0$. The angular coverage of the UTa (UTb) stations corresponds to ±317 mrad (±314 mrad) in the horizontal plane and ±279 mrad (±248 mrad) in the vertical plane.

2.3.3 The Scintillating Fibre Tracker

Similar to the previously operated IT/OT tracking stations the Scintillating Fibre detector (SciFi) consists of three tracking stations (T1-T3) with four layers each in a x-u-v-x configuration. Figure 2.32 shows the geometry of a SciFi station. Each layer is composed by two halves that are installed around the beam pipe. Each half contains five (six for T3) 5 m long and 54 cm wide SciFi modules that are read out at the bottom and the top of the detector where the SiPMs and front-end electronics are installed. Each module has 2×4 scintillating fibre mats that are separated in the centre of the module by a mirror to increase the scintillation light yield and separate the read-out of the lower and upper half of the detector. The fibre mats contain six stacked rows of 250 µm thick scintillating fibres that are embedded into two panels of 2 mm thick honeycomb layers laminated by a 0.2 mm thick carbon-fibre reinforced polymer layer. This ensures the stiffness of the module and hence its mechanical stability. The fibres consists of a scintillating core and two thin claddings with different refractive indices to ensure the guidance of the scintillation light through internal reflection as shown in Figure 2.33a. Figure 2.33b shows that on each side of the module there are 2 mm thick dead regions that are not covered with scintillating material. This leaves small gaps between the modules in the layer that are relevant to understand losses in the hit detection efficiencies. Overall, 99.2 % of a module is covered with active scintillation material and 11 000 km of scintillating

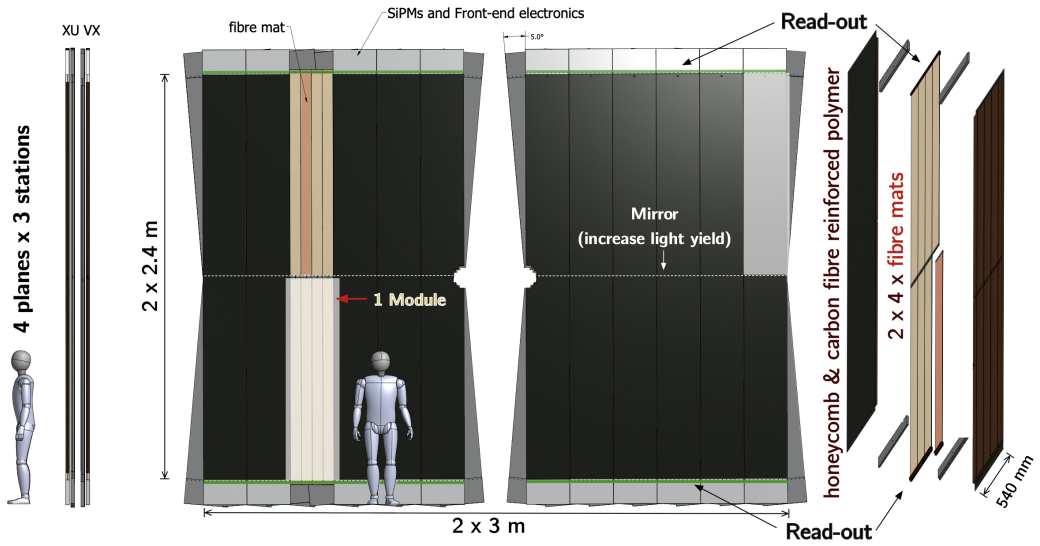

Figure 2.32: Geometry of the SciFi. Each station contains four layers in a x-u-v-x configuration with two halves of five SciFi modules. SciFi modules are sub-divided by eight scintillating fibre mats that are read-out at the top and bottom of each module. Taken from Ref. [113].

fibres are used for the entire SciFi detector. More details about the scintillating fibres of the SciFi are given in Appendix B. At the end of every SciFi module a read-out box containing the SiPMs and the front-end electronics can be found. Each fibre mat is connected to four SiPM with an array of 128 channels. Every channel contains a rectangular 250 µm (channel pitch) $\times$1.6 mm grid of 96 pixel with a size of 57 µm $\times$ 62 µm.

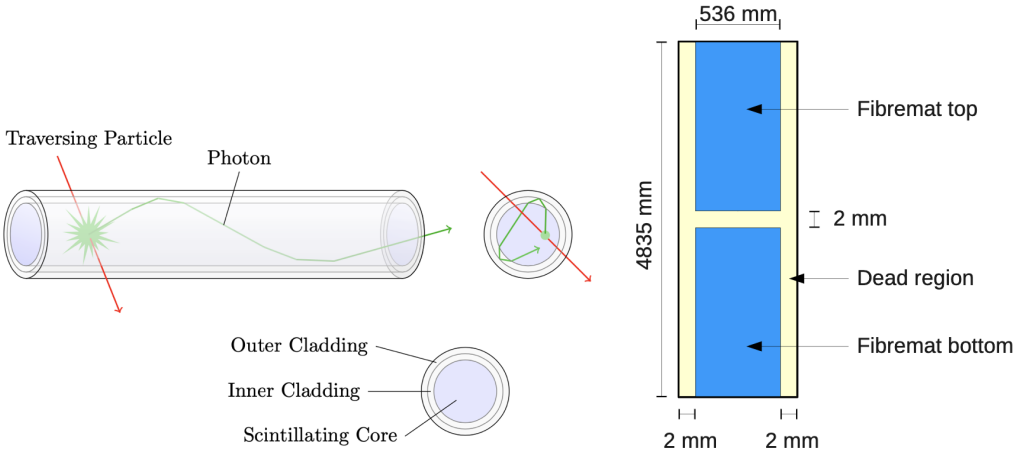

(a) Claddings **(b)** SciFi module dead regions

Figure 2.33: (a) Schematic structure of the scintillating fibres used for the SciFi composed of a core and two claddings with decreasing refractive indices for internal reflection. Taken from Ref. [114]. (b) Active and dead regions of a SciFi module. The two fibre mat regions (top, bottom) contain the scintillating fibres. They are separated by a mirror. Each module has 2 mm of inactive material on both sides. Taken from Ref. [112].

2.3.3.1 Signal detection and hit clustering

Charged particles propagating through a module of the SciFi detector are traversing several fibres of a fibre mat. The signals of the created photons in the different fibres are collected by the SiPM channels giving an information about the hit position. Depending on the initial angle of the particle multiple SiPM channels can be fired by only one passing particle. Therefore, the signals from the different channels have to be clustered for a precise estimation of the hit position. The clustering is illustrated in Figure 2.34. The clustering is performed on a Field Programmable Gate Array (FPGA) on the front-end electronics board. Three signal strength thresholds (low, middle and high) are set for clusters corresponding to 1.5, 2.5 and 4.5 photo-electrons. As a first step the clustering algorithm groups all neighbouring channels exceeding the low threshold into a cluster candidate. Figure 2.35 shows the different types of clusters. For clusters with a cluster size (number of neighbouring fired channels) $n_{\text{channel}} \leq 4$, so called unfragmented clusters, the cluster is kept if the sum of the collected charges in all channels exceeds the sum of the low and middle thresholds, *i.e* four photo-electrons. For clusters with only $n_{\text{channel}} = 1$ the high threshold has to be exceeded. For accepted clusters every channel is given a

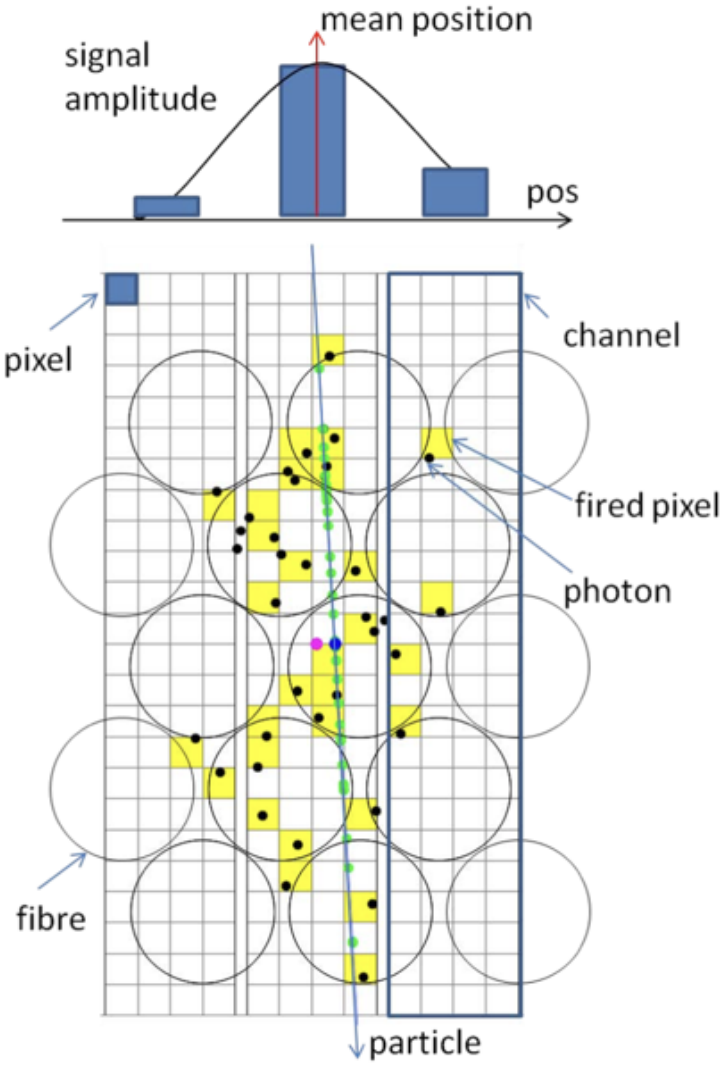

Figure 2.34: Sketch of a charged particle traversing a SciFi module and hitting fibres corresponding to three different SiPM readout channels. Hits are clustered by taking a weighted mean of the signals in the three channels. Taken from Ref. [112].

weight for its signal strength corresponding to the highest threshold it exceeded. The hit position x_{hit} is then obtained by taking a weighted mean of all contributing

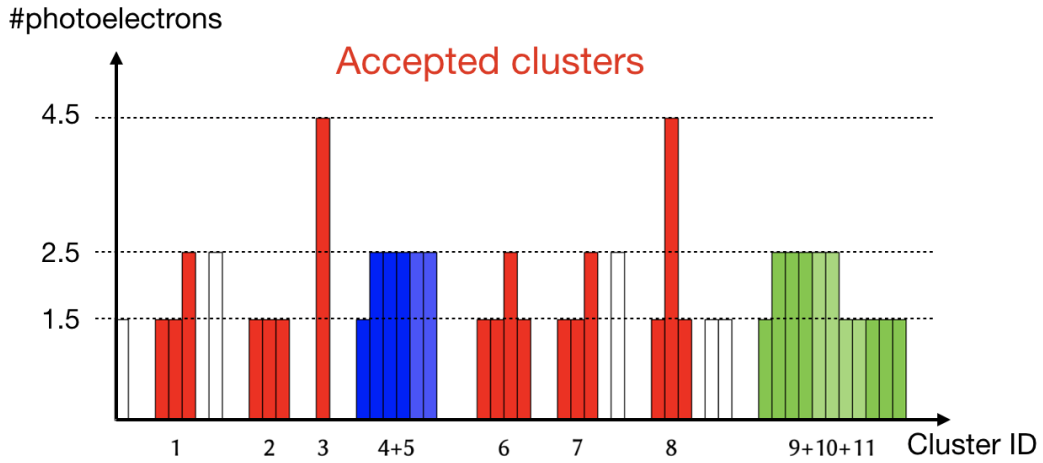

Figure 2.35: Sketch of the different cluster types. Red clusters show accepted clusters with less than 4 fired SiPM channels. Blue (green) clusters show large clusters that are fragmented before (partially) saved. White clusters are not passing the required thresholds and therefore are not saved. Adapted from Ref. [115].

channels

$$x_{\text{hit}} = \frac{\sum_{i=0}^{n_{\text{channel}}} x_i \omega_i}{\sum_{i=0}^{n_{\text{channel}}} \omega_i}, \tag{2.7}$$

where x_i is the x-position of the channel i and ω_i the assigned weight. Clusters of sizes $n_{\text{channel}} > 4$ are likely to have originated from not only one traversing particle. Therefore, they are split into multiple parts with $n_{\text{channel}} <= 4$ and referred to as *fragmented* clusters. The clusters of different cluster sizes mainly differ in their x-position resolution, also referred to as hit resolution σ, which can be used to build the track fit quality χ^2_{tr} in the track reconstruction. The typical hit resolution for a $n_{\text{channel}} = 4$ type cluster is about 70 µm. For the seeding in HLT1 all types of clusters are considered for the pattern recognition. However, in order to save memory the hit resolutions are not available in HLT1 and replaced by a constant average value that is determined from simulation. Further details on the clustering algorithm are given in reference [115]. The information about clusters found on the FPGAs in the front-end is send to the back-end readout TELL40 boards in the Event Builder (EB) nodes where they are further processed. Due to the limited bandwidth of the optical links between front-end and back-end, also the number of clusters that can be reconstructed for one SiPM is limited. In order to optimize this for the occupancy of the SciFi modules the SciFi follows a special TELL40 partitioning that is enabling a higher number of reconstructed clusters for the inner modules of the SciFi in the high-occupancy region.

2.4 Upgrade I of the LHCb trigger system

The LHCb trigger system for the Upgrade I is undergoing a complete redesign including a removal of the L0 hardware trigger stage and the partial event reconstruction in HLT1 on GPUs with the `Allen` project [116]. Events triggered by HLT1 are passed to the HLT buffer system where they are taken to run real-time alignment and calibration tasks for the different subdetectors. After that events are passed to HLT2 where a full event reconstruction and HLT2 selection is performed on CPUs within the `Moore` framework. Finally, events selected by HLT2 are then saved to tape and further processed offline. The upgraded online data flow is shown in Figure 2.36. The different steps of the online data processing chain are discussed in sections 2.4.1-2.4.4. Additionally, an introduction to GPUs will be given in section 2.4.3.2.

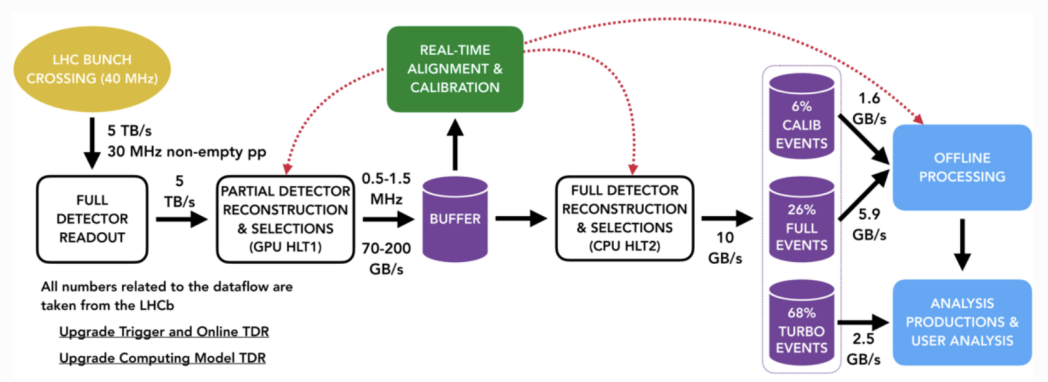

Figure 2.36: Online data processing chain of the LHCb Upgrade I. Events are reconstructed and selected online by two trigger stages (HLT1 and HLT2) on GPU and CPU architectures. In between them, real-time alignment and calibration tasks for the various subdetectors are run. After HLT2 events are then stored for offline analyses. Taken from Ref. [117].

2.4.1 Removal of the L0 hardware trigger

An essential change to the previously used trigger strategy is the removal of the L0 hardware trigger. This is mainly motivated by the large L0 trigger inefficiencies for most of the LHCb physics modes and especially for fully hadronic decay modes. They are usually the dominant part in the total trigger efficiency losses of a typical LHCb decay mode. Moreover, for many decay modes increasing the instantaneous luminosity, as it is done for the Upgrade I, does not increase the yield of triggered

events since the yield saturates with increasing luminosity. This is shown in Figure 2.37 for hadronic final states such $D_s^+K^-$ and $\pi^+\pi^-$.

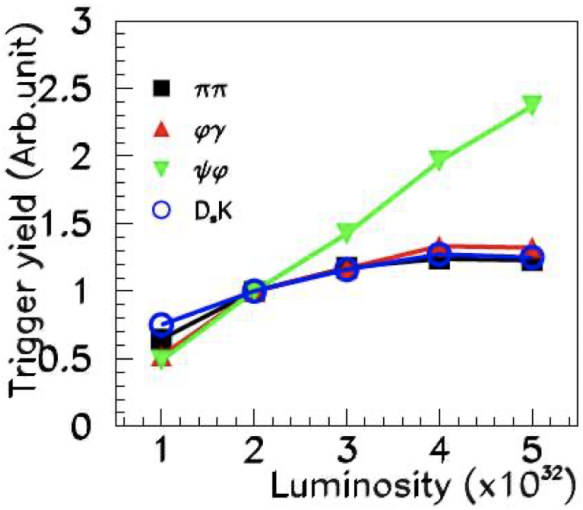

Figure 2.37: Trigger yield for typical reconstruction channels of LHCb analyses as a function of the instantaneous luminosity. Taken from Ref. [104].

As mentioned previously, it was necessary to have tight transverse energy E_{T} or transverse momentum p_{T} requirements in the L0 to reduce the event rate down to 1 MHz for the front-end read-out electronics. With the upgrade of the read-out electronics of all subdetectors data can directly be read-out at 40 MHz and be processed by HLT1 without the neccessity of a hardware trigger.

2.4.2 The event building infrastructure

Detector signals are read out by the front-end electronics (FEE) of the different subdetectors as fragments of the full data of the event. They are send via optical links to the back-end electronics consisting of several TELL40 FPGA readout boards. Here, the data fragments of several events received from the FEE are pre-processed, sorted and put into so-called *raw banks*. Each subdetector system has dedicated raw banks. They are then provided as so-called *Multi-Fragment Packets* (MFPs) to the Event Builder (EB) server nodes in which the TELL40 boards are hosted via PCI express (PCIe) slots. The EBs take the MFPs of all the subdetectors and group the detector raw banks with the same bunch crossing identifier into *Multi Event Packets* (MEPs). A MEP contains about 1000 events. The MEPs are then provided to the

Event Filter Farm (EFF) where they are processed and filtered by the high-level trigger system. For Run 3 it was chosen to use the remaining PCIe slots of the EBs

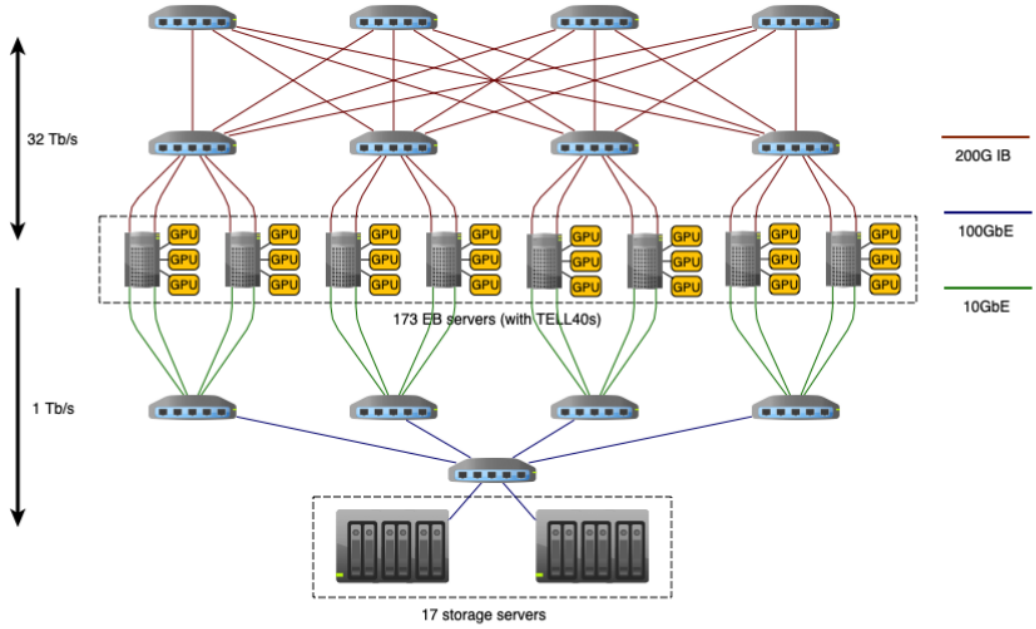

Figure 2.38: Server architecture of the Data Acquisition system and the Event Filter Farm for Run 3. GPUs are directly connected to the EB Nodes via PCIe slots. Taken from Ref. [118].

directly to also host the GPU cards for HLT1 in them [118]. Each EB node can host up to two GPU cards. This has the advantage of saving additional costs that are generated for the cooling and power supply when running the GPUs separately in the EFF and reduces the network size needed to send data from the EB nodes to the EFF as the output volume is decreased by a factor between 30 and 60. The data rate between the EB servers and the EFF is then about 1 TB/s instead of 30 TB/s. Figure 2.38 shows the architecture of the Run 3 data acquisition system with GPUs integrated into the EB nodes.
The budget saved to run HLT1 in the EFF[8] can be used to optimise the disk buffer size of the EFF and the number of CPU servers for HLT2 for LHCb's physics potential. The PCIe connection between EB node and GPU is sufficient to efficiently read and write raw events due to their small size of about 100 kB.

[8]The original budget plan had CPUs in mind for HLT1 that were part of the EFF.

2.4.3 HLT1

Removing the L0 trigger means that the first stage of the software-based high-level trigger (HLT1) has to be able to process and select interesting events out of the incoming data rate of 30 MHz. Furthermore, HLT1 has to reduce the rate by a factor of 30 down to 1 MHz before the selected events can be written to the HLT buffer system.
The detector information used in HLT1 is coming from the tracking detectors, the ECAL and the muon stations, whereas the RICH information is only used in the second stage of the high-level trigger (HLT2). Therefore, no PID information is available at this level. The partial event reconstruction comprises the reconstruction of the particle tracks, the primary and secondary vertices as well as the reconstruction of clusters in the ECAL and of track segments in the muon stations. Events are then selected by $\mathcal{O}(30)$ trigger selection requirements called *selection lines* covering different physics cases of interest such single- and di-muon or -electron events or inclusive multibody topologies.

2.4.3.1 Allen

The partial event reconstruction and event selection in HLT1 is implemented in the `Allen` project [116, 118] and will be operated in Run 3 on $\mathcal{O}(200)$ NVIDIA RTX A5000 Graphics Processing Unit (GPU) cards that are connected via PCIe slots directly to the EB CPU nodes. GPUs are well suited for HLT1 since most of the tasks to be performed in the partial event reconstruction have the following features:

- Events are mostly independent and can therefore be reconstructed in parallel.
- Event selection in HLT1 is based on information from tracking and vertex reconstruction, different tracks and vertices can be reconstructed independently $\rightarrow$ GPUs are designed for high-throughput applications to highly parallelisable problems.
- High computing load due to high combinatorics $\rightarrow$ GPUs can do many floating point operations per second (*TFLOPS*).
- Small raw event size (~ 100 kB) $\rightarrow$ GPUs have a large global memory that can fit a high number of events so that many events can be processed in parallel.

2.4.3.2 Graphics Processing Unit cards

Graphics Processing Unit (GPU) cards are dedicated graphics cards with a printed circuit board hosting a GPU chip as well as supporting hardware such as additional memory and PCIe connector slots that enable their integration into a CPU. The GPU itself is a many-core electronic circuit designed for parallel processing of large batches of data. The structure of a GPU card together with its different types of memory is illustrated in Figure 2.39. GPUs follow the *Single Instruction Multiple*

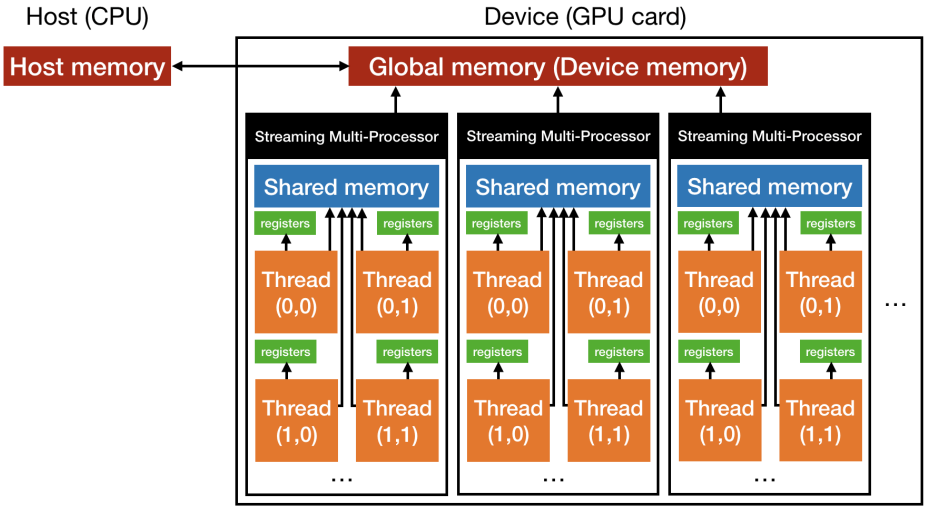

Figure 2.39: Simplified sketch of the different memories used for a GPU card (device) connected to a CPU (host). Each thread has its own registers assigned to it, whereas all threads in a Streaming Multi-Processor (SM) can read from the shared memory. Global memory from the GPU card can be accessed from all threads in all SMs and is used to copy data between the device and the host.

Threads (SIMT) paradigm where the same task (kernel) is executed in parallel on several processing units also known as *threads* and applied to different parts of the data set. The threads are organized in an array of *Streaming Multi-Processors* (SM) with a fixed amount of threads assigned to them. Each SM has a *shared memory* that can be read from and written to by all its threads. In addition, every thread has its own *registers*, a separate memory that cannot be used by other threads. Registers are the fastest memory to be read from and written to and all variables defined in a kernel are stored there. Apart from the shared memory and the registers, there is *global memory* from the graphic cards' board that can be used by all threads from all SMs. The global memory is also used to communicate to the CPU. In GPU programming the GPU is also referred to as the *device* while the CPU is

called *host*. Global memory has a huge latency which makes it much slower than shared memory. Therefore, data that is used by many threads of a block is often copied from the global to the shared memory for faster access. Since the amount of available shared memory is much smaller than for global memory, a common practice in GPU programming is the tiling of a large chunk of data into smaller tiles that can fit into the shared memory and process them one after another. This is only possible if not the full data is required by the algorithm that has to run on it. A correct handling of memory is an important part of an efficient GPU programming. Threads in a SM can be further grouped into *blocks* with the *block size* describing the number of threads assigned to it. The blocks are also defining the so called *grid* with the *grid size* standing for the number of blocks. From the software point of view only blocks are relevant, whereas for the hardware threads are only structured into SMs and blocks are artificial. The blocks of an SM also share its shared memory. The number of blocks should therefore be chosen in a way that data that should be copied in the shared memory fits in there.
Furthermore, for NVIDIA GPUs 32 threads are grouped into entities called *warps* that are used to start executing processes on threads in parallel.[9] Therefore, there cannot be less than 32 threads running at the same time. This means that the block size should always be multiples of 32 threads. It is an important constraint for architecture considerations, since the goal for a fast GPU performance is to keep threads always busy and not waste them due to a too large block size that is unnecessary for the execution of the algorithm. Nevertheless, the aim is to use as many blocks as possible given the needed size of shared memory per block. For most algorithms in Allen each event is assigned to an individual block so that they can be processed in parallel in batches of thousands. The threads are then used for an intra-event parallel processing of reconstruction tasks such track and vertex reconstruction or clustering in the ECAL.

2.4.4 HLT2

For events selected by the HLT1 trigger selections the full raw data information is kept and passed on to the HLT buffer system where the real-time alignment and calibration tasks are run. In Run 3 this is very important since for the full event reconstruction in HLT2 it is crucial to know the alignment and calibration constants precisely. The extended use of the Turbo model for Run 3 makes this even more important.
`Moore` is the framework to perform full event-reconstruction in HLT2 including also information of the RICH detectors. The bandwidth with which HLT2 can write

[9] For some AMD GPUs warps consist of 64 threads.

events to tape is limited to 10 GB/s. A major change for the upgrade of HLT2 is to get as much physics potential as possible out of this bandwidth by moving to the Turbo model as the default model to save events selected by the HLT2 selection lines. The Turbo model persists only the raw and reconstructed information of the particle candidate that triggered a HLT2 selection and its children particle. The advantage of this strategy is that the size of an event will be reduced which allows to save more events in total. In 2018 the average size of a Turbo event corresponded to 30 kB compared to 60 kB for an event with the full event information after the HLT2 selections [119]. In some cases the event size can even be reduced by an order of magnitude. As a consequence most of the physics data of LHCb used for offline analyses will rely on an online-only reconstruction that cannot be re-run offline.
Apart from the around 70 % of events that will be processed with the Turbo model, about 25 % of the events will be persisted with the full raw and reconstructed data information. This is necessary for example for analyses that perform flavour tagging or jet reconstruction. In addition, another 5 % of events will be saved for offline calibration purposes such as PID calibrations or tracking efficiency calculations. For these applications dedicated selection lines are implemented in HLT2 using decay channels that are well understood from previous measurements. To make the Turbo model more flexible in some cases a so-called *selective persistence* is performed. This means that selected extra information can be persisted, for example all additional reconstructed pion tracks or all ECAL clusters in the event. In this way the advantage of reducing the event size with respect to the full persistence is still there and the selections can take care of specific needs for offline analyses of certain decay modes. The different levels of persistence are illustrated in Figure 2.25.

2.4.5 Offline data processing

Figure 2.40 shows the data flow in Run 3 for the offline processing. The raw data of events that were selected by HLT2 are saved to tape and are then processed by the so-called *sprucing* framework that is sharing its code base with HLT2 in `Moore`. For events selected with the Turbo model, the sprucing stage works as a pass-through stage, but for fully persisted events an additional sprucing selection is applied. This is necessary because after the sprucing the data is written to disk at a limited bandwidth of about 2.8 GB/s.

Data that is written to the full stream will be further processed by sprucing selection lines. They share the code base of the `Moore` framework with the selections run in HLT2. This allows for a flexibility in the data processing change that enables to easily move selections from the offline data processing to the online processing

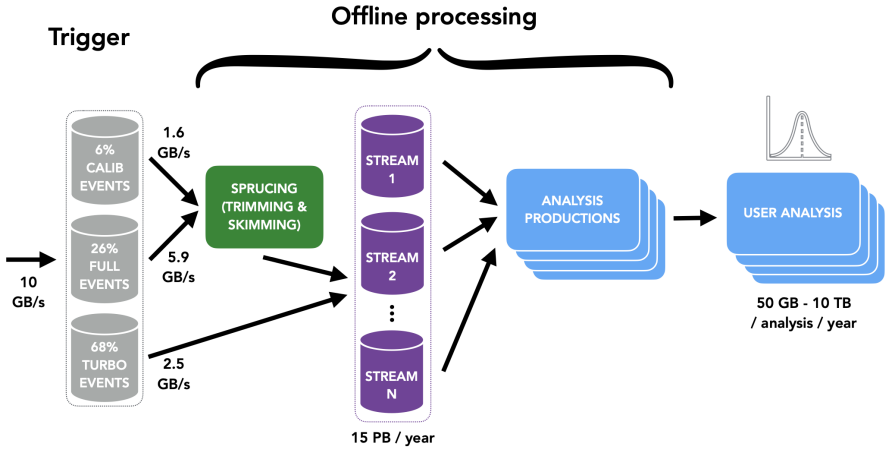

Figure 2.40: Offline data processing flow in Run 3. Events from HLT2 selected within the Turbo model pass through the sprucing step, whereas fully persisted events are further selected by the sprucing before they are stored to disk. Analysis Productions are used for tupling the data for offline user analyses. Taken from Ref. [117].

or vice versa if needed. Data that was processed via the sprucing selections can also be reprocessed in yearly resprucing campaigns since the full raw data of the event is saved to tape and accessible. This is not possible for events that were fully processed by the Turbo stream. The tupling application `DaVinci` was fully redesigned and replaced for the data processing in Run 3. The main improvements targeted with the redesign are a better handling of storage that avoids writing unnecessary information to the tuples as well as an adaption to the new event model by using the `ThOr` functor framework [120]. The tupling is then run in the `Analysis Productions` framework. `Analysis Productions` are a centralized and automated framework, that improves the management of computing resources, the monitoring and archiving of tupling tasks. The tupled data is then used for offline user analyses.

2.4.6 Other changes for LHCb Upgrade I

As previously mentioned the removal of the L0 hardware trigger requires that all subdetectors can be read out trigger-less at 40 MHz. For that, the front-end read-out electronics of all subdetectors are replaced. For the upgrade of the RICH detectors [121], the formerly used HPDs are replaced by MaPMTs to cope with the LHCb Upgrade I conditions. Furthermore, the focal length of the spherical mirrors in

RICH1 is increased by increasing the radius of its curvature to reduce the occupancy of the MaPMTs. The position of both the planar and spherical mirrors are changed accordingly. A new cell for the SMOG system separated from the VELO, SMOG2 [122], now consisting of two retractable halves is installed. A main feature of SMOG2 is the opportunity to operate it in parallel to the pp-collisions as the PVs originating from the beam-gas interactions can be fully separated in the z-direction from the PVs from the pp-collision inside the VELO. Moreover, additional sensors are installed in the SMOG2 cell to monitor the gas pressure. The BCM is equipped with a full new set of diamond sensors for LHCb Upgrade I. Additionally, a new luminometer called *Probe for LUminosity MEasurement* (PLUME) [123] has been installed upstream of the VELO detector to monitor the luminosity. Finally, the PS and SPD detectors as well as the first muon station that were predominantly used for the L0 hardware trigger have been removed to reduce the material budget of the detector.

Chapter 3

HybridSeeeding and matching on GPUs in HLT1

The track reconstruction is an essential part for the partial event reconstruction in HLT1. Tracks are used for the reconstruction of PVs and SVs as well as for the electron and muon reconstruction algorithms and the HLT1 event selection lines. This chapter gives a general introduction to the design of a tracking algorithm in LHCb in section 3.1 followed by a derivation of the analytical parameterisation of the track trajectory in the LHCb detector, also referred to as the *track model* in section 3.2. Afterwards the approaches used in the track reconstruction in HLT1 are explained in section 3.3 and the implementation of the *Hybrid Seeding* algorithm for the standalone track reconstruction in the SciFi is described in section 3.5-3.8. Finally, the matching of track segments from different subdetectors, in particular from the VELO and the SciFi, are discussed in section 3.9.

3.1 Design of a tracking algorithm

As discussed previously, a tracking algorithm usually consists of three major parts which are the pattern recognition, the track fit and the removal of bad track candidates. The pattern recognition tries to group together hits in the different layers of the tracking detectors that originated from same traversing particle. The track fit then determines how well this set of hits can be described by the assumed model for the particles trajectory and thereby gives a measure of how likely it is that the hits actually belong to the same track. In the final step track candidates are filtered by their track fit quality.
The physics performance of a tracking algorithm can be evaluated by a few key indicators that are used to tune free parameters of the tracking algorithm. The

following performance indicators are considered for the design of the *Seeding & Matching* algorithms in HLT1:

- **Track reconstruction efficiency**:

$$\varepsilon_{\text{tr}}^{\text{MC}} = \frac{N^{\text{reconstructed \& matched}}}{N^{\text{reconstructible}}} \tag{3.1}$$

  The fraction of reconstructible MC particles that can be reconstructed as a track by the tracking algorithm. The reconstructibility of a particle is defined by being in the geometrical acceptance of LHCb and traversing a sufficient amount of layers in the tracking stations. A reconstructed track is succesfully matched to its associated MC particle if they share at least 70 % of their hits.

- **Ghost rate**:

$$\text{ghost rate} = \frac{N^{\text{ghosts}}}{N^{\text{reconstructed}}} \tag{3.2}$$

  Fake tracks are tracks that are falsely found by the pattern recognition and not discarded by the track fit, thus reconstructed tracks that cannot be matched to a reconstructible MC particle. In the LHCb terminology they are often referred to as *ghosts*. The ghost rate is defined as the fraction of ghosts among the reconstructed tracks.

- **Clone rate**: Reconstructed tracks that share the majority of their hits are called *clone tracks*. For the algorithms designed here at least 70 % of the hits have to be shared for two tracks to be considered as clones. The clone rate is defined as the number of clones divided by the total number of reconstructed tracks. A dedicated clone killing algorithm described in section 3.8 is implemented to remove the duplicated tracks.

- **Hit purity**:

$$\text{hit purity} = \frac{N_{\text{hits}}^{\text{reconstructed \& matched}}}{N_{\text{hits}}^{\text{reconstructed}}} \tag{3.3}$$

  The hit purity is defined as the fraction of hits of the reconstructed and matched track that are can also be found in the corresponding MC particle. It is a measure for the number of wrongly assigned hits to tracks.

- **Hit efficiency**:

$$\text{hit efficiency} = \frac{N_{\text{hits}}^{\text{reconstructed \& matched}}}{N_{\text{hits}}^{\text{MC particle}}} \tag{3.4}$$

  The hit efficiency defines the fraction of hits from the MC particle that were also found in the reconstructed track that was matched to the MC particle.

The track reconstruction efficiency and ghost rate strongly depend on kinematic properties of the particle such as the momentum p, the transverse momentum p_{T} and the pseudorapidity η. These dependencies have also be taken into account during the development of the *Seeding & Matching* algorithms.

3.2 Track model

The force $\vec{F}$ acting on a charged particle with charge q and velocity $\vec{v}$ that propagates through the electromagnetic fields $\vec{E}$ and $\vec{B}$ is given by the Lorentz force law

$$\frac{\mathrm{d}\vec{p}}{\mathrm{d}t} = \vec{F} = q(\vec{E} + \vec{v} \times \vec{B}). \tag{3.5}$$

Writing the time-dependence as a z-position dependence and assuming that there are no relevant electric fields present in the LHCb detector this leads to three coupled differential equations for the momentum components p_x, p_y, p_z:

$$\frac{\mathrm{d}p_x}{\mathrm{d}t} = q(t_y B_z - B_y) \tag{3.6}$$

$$\frac{\mathrm{d}p_y}{\mathrm{d}t} = q(B_x - t_x B_z) \tag{3.7}$$

$$\frac{\mathrm{d}p_x}{\mathrm{d}t} = q(t_x B_y - t_y B_x), \tag{3.8}$$

where the $t_i = p_i/p_z$ define the slopes of the track trajectory in the x- and y-directions. This can also be written for t_x and t_y as

$$\frac{\mathrm{d}t_x}{\mathrm{d}z} = \frac{q}{p}\sqrt{1 + t_x^2 + t_y^2}\left(t_x t_y B_x - (1 + t_x^2)B_y + t_y B z\right) \tag{3.9}$$

$$\frac{\mathrm{d}t_y}{\mathrm{d}z} = \frac{q}{p}\sqrt{1 + t_x^2 + t_y^2}\left(-t_x t_y B_y - (1 + t_y^2)B_x - t_x B z\right) \tag{3.10}$$

which define the trajectories in the xz- and yz-planes. Tracks in the LHCb acceptance are highly boosted forwardly into the z-direction so that $t_{x,y}$ can be assumed to be small and only the first-order terms are considered. Moreover, the magnetic field components in the central region are negligible except for B_y which results in a bending of the tracks in the xz-plane. These two assumptions are used to simplify the track equations to

$$\frac{\mathrm{d}x^2}{\mathrm{d}z^2} = \frac{\mathrm{d}t_x}{\mathrm{d}z} \approx -\frac{q}{p}B_y \tag{3.11}$$

and

$$\frac{\mathrm{d}y^2}{\mathrm{d}z^2} = \frac{\mathrm{d}t_y}{\mathrm{d}z} \approx 0. \tag{3.12}$$

For the y-position of the trajectory this translates to a simple linear function

$$y(z) = a_y + b_y(z - z_0), \tag{3.13}$$

where a_y is the starting position of y at a reference position z_0 and $b_y = t_y$. For the x-direction the strong z-dependence of the magnetic field component B_y shown in Figure 2.7 has to be taken into account, which is done as a first order approximation

$$B_y(z) \approx B_0 + B_1(z - z_0), \tag{3.14}$$

where B_0 and B_1 represent the coefficients of the constant and linear terms in the magnetic field parametrisation. The dependence of the magnetic field component B_y as a function of the x- and z-position is shown in Figure 3.1. The equation for

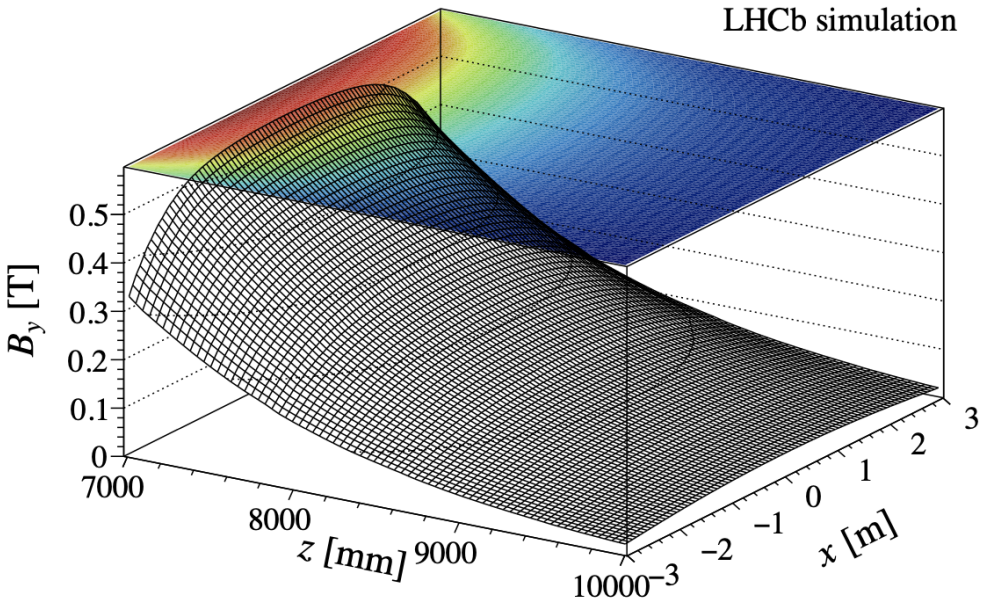

Figure 3.1: Dependence of the magnetic field component B_y on the x- and y-position. The decrease of the magnetic field with z can be modelled in first approximation as linear. Taken from Ref. [124].

the x-position can then be written as

$$x(z) = a_x + b_x(z - z_0) + \frac{q}{p}\left(\frac{B_0}{2}(z - z_0)^2 + \frac{B_1}{6}(z - z_0)^3\right) \tag{3.15}$$

$$= a_x + b_x(z - z_0) + c_x \underbrace{(z - z_0)^2(1 + \texttt{dRatio}(z - z_0))}_{:=d\eta}, \tag{3.16}$$

where a_x stands for the x-position at a reference point z_0 and the parameter $\texttt{dRatio} = B_1/3B_0$ is a constant correction for the z-dependence of the magnetic field B_y which is only a good approximation in the central region of the detector. The optimal value $\texttt{dRatio} = -0.00028$ is determined from simulation.

3.2.1 Track fit

The track fit is performed by solving a linear system of equations obtained when minimising the χ^2_{tr} which defines a measure for the track quality. It can be written as

$$\chi^2_{\text{tr}} = \sum_{i=0}^{N_{\text{hits}}} = \left(\frac{(\tilde{x}_i - x(z_i))}{\sigma_i}\right)^2, \tag{3.17}$$

where $\tilde{x}$ corresponds to the measured x-position of the hit i, $x(z_i)$ to the position of the reconstructed track at z_i and σ_i to the hit resolution discussed earlier in section 2.3.3.1 of the hit i. In HLT1, a constant value σ is assumed for the latter one as the hit resolution is not stored to save memory. The measured position $\tilde{x}_i$ is determined by

$$\tilde{x}_i = \tilde{x}_i(y = 0) + \alpha_i^{\text{stereo}} y(z_i), \tag{3.18}$$

where α_i^{stereo} is the stereo angle of the layer in which the hit i was found and $y(z_i)$ its y-position from the track model in the y-direction. As discussed previously α^{stereo} is 0 for the x-layers and $\pm 5°$ for the u/v-layers. In order to minimise χ^2_{tr} considering all parameters of the track model

$$\vec{\xi} = (a_x, b_x, c_x, a_y, b_y)^T \tag{3.19}$$

the gradient $\vec{\nabla}_\xi$ of χ^2_{tr} has to vanish, which can be expressed as:

$$\vec{\nabla}_\xi \chi^2_{\text{tr}} = \frac{\partial \chi^2_{\text{tr}}}{\partial \xi_i} \stackrel{!}{=} 0. \tag{3.20}$$

Writing the equation system as matrices this leads to:

$$\begin{pmatrix} \langle 1 \rangle & \langle dz \rangle & \langle d\eta \rangle & \langle -\zeta \rangle & \langle -\zeta dz \rangle \\ \langle dz \rangle & \langle dz^2 \rangle & \langle d\eta dz \rangle & \langle -\zeta dz \rangle & \langle -\zeta dz^2 \rangle \\ \langle d\eta \rangle & \langle d\eta dz \rangle & \langle d\eta^2 \rangle & \langle -\zeta d\eta \rangle & \langle -\zeta d\eta dz \rangle \\ \langle -\zeta \rangle & \langle -\zeta dz \rangle & \langle -\zeta d\eta \rangle & \langle \zeta^2 \rangle & \langle \zeta^2 dz \rangle \\ \langle -\zeta dz \rangle & \langle -\zeta dz^2 \rangle & \langle -\zeta d\eta dz \rangle & \langle \zeta^2 dz \rangle & \langle \zeta^2 dz^2 \rangle \end{pmatrix} \begin{pmatrix} a_x \\ b_x \\ c_x \\ a_y \\ b_y \end{pmatrix} = \begin{pmatrix} \langle \Delta x \rangle \\ \langle dz \Delta x \rangle \\ \langle d\eta \Delta x \rangle \\ \langle -\zeta \Delta x \rangle \\ \langle -dz\zeta \Delta x \rangle \end{pmatrix}$$

with

$$\begin{aligned} dz_i &= z_i - z_0, \\ d\eta_i &= (dz_i)^2(1 + \texttt{dRatio} \cdot dz_i), \\ \zeta_i &= \alpha_i^{\text{stereo}}, \\ \Delta x_i &= \tilde{x}_i - x(z_i), \end{aligned} \tag{3.21}$$

and the notation $\langle v \rangle$ for a variable v corresponding to

$$\langle v \rangle = \sum_i^{n^{\text{Hits}}} \frac{v_i}{\sigma_i}. \tag{3.22}$$

The system derived from equation 3.20 describes a full 5-dimensional track fit using both hits from the x-layers and the uv-layers. The fit can be simplified to the fits in the xz- and yz-projections by solving equation 3.20 only for (a_x, b_x, c_x) and (a_y, b_y), respectively. This results in the following matrix sub-systems for the

- 3-dimensional fit of the xz-projection:

$$\begin{pmatrix} \langle 1 \rangle & \langle dz \rangle & \langle d\eta \rangle \\ \langle dz \rangle & \langle dz^2 \rangle & \langle d\eta dz \rangle \\ \langle d\eta \rangle & \langle d\eta dz \rangle & \langle d\eta^2 \rangle \end{pmatrix} \begin{pmatrix} a_x \\ b_x \\ c_x \end{pmatrix} = \begin{pmatrix} \langle \Delta x \rangle \\ \langle dz \Delta x \rangle \\ \langle d\eta \Delta x \rangle \end{pmatrix} \tag{3.23}$$

  For the fit of the xz-projection only hits from the x-layers are used.

- 2-dimensional fit of the yz-projection:

$$\begin{pmatrix} \langle \zeta^2 \rangle & \langle \zeta^2 dz \rangle \\ \langle \zeta^2 dz \rangle & \langle \zeta^2 dz^2 \rangle \end{pmatrix} \begin{pmatrix} a_y \\ b_y \end{pmatrix} = \begin{pmatrix} \langle -\zeta \Delta x \rangle \\ \langle -dz\zeta \Delta x \rangle \end{pmatrix} \tag{3.24}$$

  For the fit of the yz-projection only hits of the uv-layers are used.

The fits of the xz- and yz-projections are used for the adaption of the *HybridSeeding* algorithm for HLT1, whereas the full 5-dimensional fit is not, to save computing time. A full 5-dimensional fit would be beneficial to further reduce the ghost rate.

3.3 Track-reconstruction in HLT1 at the LHCb experiment

As discussed previously in section 2.2.2.5 long track reconstruction in LHCb can be performed with two orthogonal approaches: the *forward tracking* where the pattern recognition is started in the VELO and the reconstructed VELO tracks are extrapolated to the tracking detectors further downstream to look for additional hits, and the *Seeding & Matching* where the tracking is started from a standalone track reconstruction in the tracking stations downstream of magnet and back-propagated to the tracking detectors further upstream. The seeding is designed to perform better at low p or p_T whereas the forward tracking is better at high p or p_T. For Run 3 a redundancy of running both approaches in parallel for an overall higher tracking efficiency is not fitting into the timing budget for HLT1, so that the forward tracking is considered as the baseline approach for the long track reconstruction in HLT1 [116] as it was already in Run 2 [99]. However, during Run 2 both approaches were run at the same time in HLT2. In order to increase the throughput in HLT2 for Run 3 the redundancy of running both the forward tracking and the *Seeding & Matching* for all reconstructible long tracks was removed. The *Seeding & Matching* approach is used as the default, whereas the forward tracking is run only on residual VELO tracks that are not matched to T tracks [125].
Due to delay of the UT installation an alternative approach for a VeloSciFi track reconstruction needed to be developed. Therefore, also the *Seeding & Matching* approach is considered for HLT1 besides a *forward tracking without UT* [126]. For the start of Run 3 running both algorithms in parallel with an adaption of the *forward tracking without UT* for high momentum ($p > 5\,\mathrm{GeV/c}, p_\mathrm{T} > 1\,\mathrm{GeV/c}$) is considered. Figure 3.2 shows the integration of the *Seeding & Matching* into the HLT1 algorithm sequence.

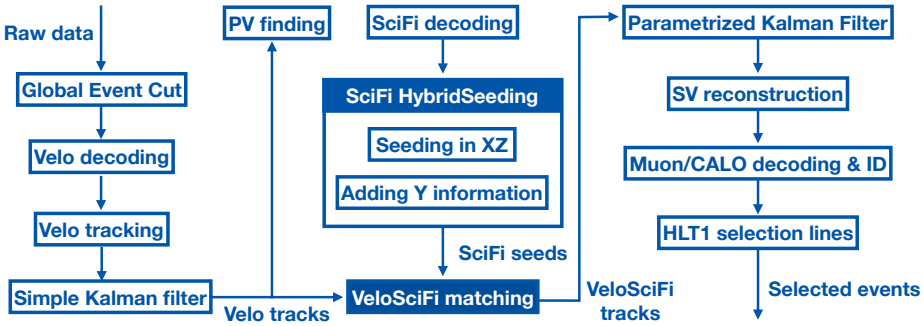

Figure 3.2: Sketch of the HLT1 algorithm sequence run for the *Seeding & Matching* approach.

3.4 HybridSeeding in the Scintillating Fibre Tracker

The *HybridSeeding* algorithm [124] is originally designed to run on CPU in HLT2. This section briefly introduces the concepts of the baseline developments whereas the following sections describe the algorithm in detail and the adaptions made for running on GPUs in HLT1. The *HybridSeeding* is run in iterations that are defined by the underlying minimal momentum assumption p_{min} and the choice of the initial layers of each SciFi station. The initial layers are varied to account for inefficiencies in the hit detection and clustering which results in a higher tracking efficiency of the seeding. The underlying momentum assumption defines the minimal momentum of charged particles that the seeding algorithm aims to reconstruct by determining the size of the search windows. For the CPU version three iterations of the SciFi seeding are run with $p_{\text{min}} > [5, 3, 1.5]\,\text{GeV/c}$ starting with the highest momentum first. Between iterations the SciFi hits are *flagged* which means that the hits used for tracks in the previous iteration are not considered for reconstruction in the next step anymore. This helps to reduce the combinatorics for the iteration step at low momentum where the search window sizes are enlarged.
The SciFi `Hybrid Seeding` is performed in two algorithms, one looking for seeds in the xz-plane where the tracks are bent due to the magnetic field, the second is adding the y-information from the u/v-layers of the SciFi. Figure 3.3 shows a sketch of the iterations in the xz-part of the SciFi seeding designed for the CPU architecture. Combinations of two hits from the initial x-layers in the first and last station of the SciFi are build. The straight line connecting the two hits of a two-hit combination is back-propagated to (0,0,0) for a rough momentum estimate.

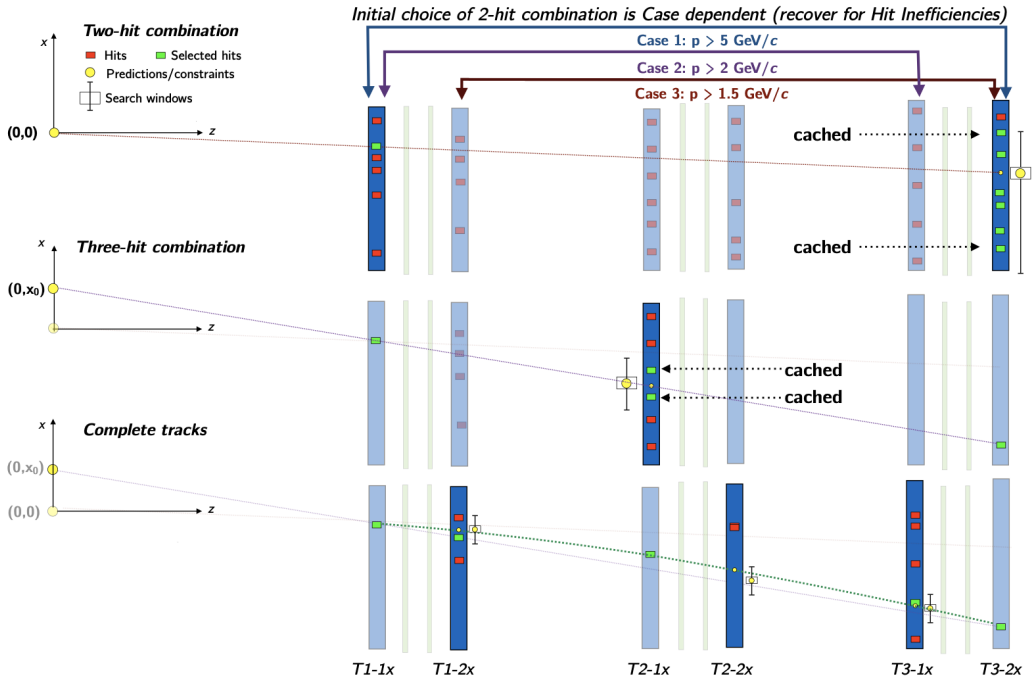

Figure 3.3: Sketch of the three cases in the CPU implementation of the seeding in the xz-plane. The minimal momentum assumption as well as the initial layers for the first three hits are varied per case. Taken from Ref. [113].

With that momentum estimate a search window is opened in the initial layer of the second SciFi station to look for a third hit building a parabola with previous two hits. Afterwards, search windows for hits in the remaining x-layers are defined based on extrapolations from the found parabola and hits within the search windows are added. Seeds in xz with at least five found hits are fitted and filtered by their track fit quality. An outlier hit removal is applied to discarded track candidates, before they are refitted and again filtered by their track fit quality. Surviving xz-seeds need to have at least four hits and are then considered for the second part of the SciFi seeding where the y-information is added. Finally, clone tracks are removed by a dedicated clone killing algorithm. The details of the algorithm and its adaption to HLT1 for Run 3 are discussed in the following sections.
The algorithm adding the hits from the stereo layers is based on a binned Hough cluster search in the slope t_y of the y-direction. For that, hits from the u/v-layers are projected to a common plane at reference z-position z_{ref}. Clusters of hits contributing to the same bin can then be identified as originating from the same track. For HLT1 an alternative approach for the adding of y-information is exploited to match better

with the GPU architecture. This is discussed in section 3.7. Seeds from the stereo layers are first fitted with a linear model in the yz-plane. Afterwards a full xyz-fit is performed, outlier hits are removed and clone tracks are killed. Finally, SciFi seeds with at least ten hits and a sufficient track quality are maintained.

3.5 HybridSeeding on GPUs in HLT1

For the HLT1 adaption of the *HybridSeeding* algorithm the number of cases is reduced to two with equal minimal momentum assumption of $p = 3\,\text{GeV}$. This simplifies the algorithm structure for the GPU application, avoiding the implementation of a hit flagging after each iteration. Table 3.1 shows the configuration of the two iterations that the seeding is run with in HLT1. The search window sizes for the building of two-hit and three-hit combinations are derived from p_{min} and are described in sections 3.6.1.1 and 3.6.2.

Table 3.1: Configuration of the two iterations run in the SciFi seeding in HLT1.

Iteration	p_{min}	T1 layer	T2 layer	T3 layer
0	3 GeV	T1x1	T2x1	T3x1
1	3 GeV	T1x2	T2x2	T3x2

3.6 Seeding in the horizontal plane

The seeding starts in the horizontal plane, the xz-plane in the LHCb coordinate system, by iterating over all hits in the initial T1 layer of the SciFi. Each iteration consists of the following steps:

1. Finding two-hit combinations with hits from the initial T1 and T3 layers
2. Adding a third hit from the initial T2 layer
3. Looking for hits in the three remaining layers and accepting tracks with more than five found hits
4. Fitting the track model to the accepted tracks

Figure 3.4 shows a sketch of the first two steps.

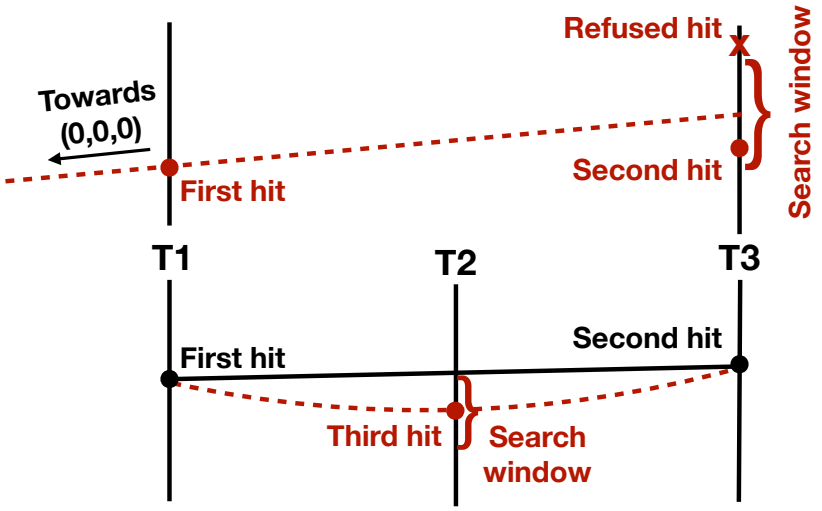

Figure 3.4: Sketch of finding two- and three-hit combinations in the Scintillating Fibre Tracker.

3.6.1 Building two-hit combinations

In the first step particle trajectories are assumed to originate from $(x, y, z) = (0, 0, 0)$ and to be straight lines, which corresponds to particles with infinite momentum or a non-existing magnetic field. For a found hit at a measured x-position $\tilde{x}_1$ in the T1 layer the slope t_x of the trajectory can then be defined as

$$t_x^{\infty} = \frac{\tilde{x}_1}{z_1}, \tag{3.25}$$

where z_1 stands for the z-position of the initial T1 layer. The straight line is extrapolated to the initial T3 layer, so that

$$x_3^{\infty} = x_1 + t_x^{\infty}(z_3 - z_1) = t_x^{\infty} z_3 \tag{3.26}$$

corresponds to the predicted position in T3 assuming infinite momentum of the particle. A search window for hits in the initial T3 layer is defined around the predicted x-position. Only hits that are within the bounds of the search window $x_{\text{tol}}^{\text{lower/upper}}$ are considered to belong to the same track as $\tilde{x}_1$. This translates to the constraints for the measured position $\tilde{x}_3$ of the hit in T3,

$$x_{\text{tol}}^{\text{lower}} < \tilde{x}_3 < x_{\text{tol}}^{\text{upper}}. \tag{3.27}$$

All T3 hits fulfilling this condition are used to build two-hit combinations with the initial hit in T1.

3.6.1.1 Defining second-layer tolerances

The straight line connecting $\tilde{x}_1$ and $\tilde{x}_3$ can be propagated back to $z = 0$ to calculate the offset x_0 in the x-position with respect to $x = 0$. The difference Δx_3 of the x-position of a measured T3 hit $\tilde{x}_3$ to the predicted position x_3^{∞} can be related to x_0 by

$$k\Delta x_3 = k(\tilde{x}_3 - x_3^{\infty}) = x_0, \tag{3.28}$$

with

$$k = \frac{z_1}{z_3 - z_1}. \tag{3.29}$$

Figure 3.5 shows a scatter plot of the q/p as a function of x_0 of simulated events. The relation between $1/p$ and x_0 can be modeled with a second-order polynomial

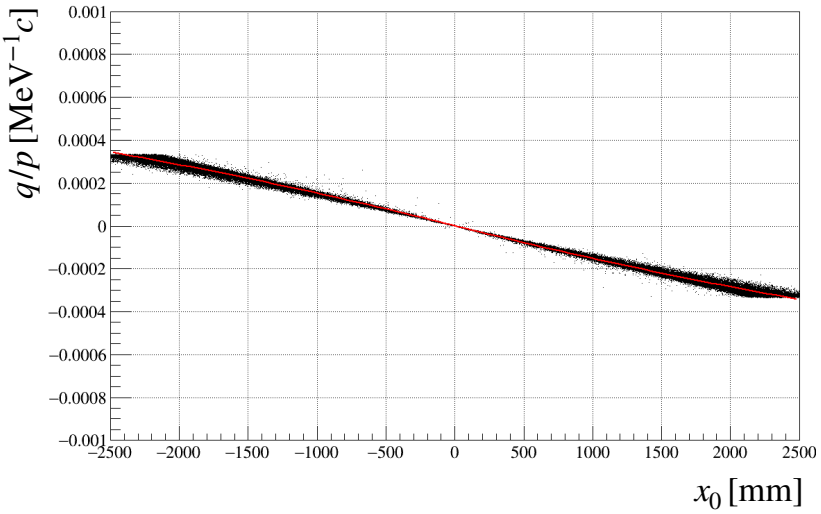

Figure 3.5: Fitted scatter plot of the q/p as a function of x_0 for long tracks taken from simulated $B_s^0 \to \phi\phi$ events. p corresponds to the true momenta reconstructed of the simulated particles.

$$\frac{1}{p} = f(x_0) = \alpha|x_0| + \beta x_0^2 \tag{3.30}$$

and the parameters α and β can be determined by fitting the model to the distribution in the scatter plot. Knowing the relation between x_0 and $1/p$ a tolerances $x_0^{\max}$ for x_0, *i.e.* how much tracks are allowed to bend given an assumption for the minimal

momentum p_{min}, can be obtained by requiring

$$\alpha|x_0^{\text{max}}| + \beta(x_0^{\text{max}})^2 = \frac{1}{p} < \frac{1}{p_{\text{min}}}, \tag{3.31}$$

which can also be written in the quadratic form

$$\alpha|x_0^{\text{max}}| + \beta(x_0^{\text{max}})^2 - \frac{1}{p_{\text{min}}} < 0. \tag{3.32}$$

Replacing x_0 according to equation 3.28 this translates to

$$\alpha|k\Delta {x_3}^{\text{max}}| + \beta(k\Delta {x_3}^{\text{max}})^2 - \frac{1}{p_{\text{min}}} < 0. \tag{3.33}$$

After solving this equation for $\Delta {x_3}^{\text{max}}$ the tolerances are determined by

$$\Delta {x_3}^{\text{max}} = \frac{1}{2k\beta}\left(-\alpha + \sqrt{\alpha^2 + \frac{4\beta}{p_{\text{min}}}}\right) \tag{3.34}$$

The values of α and β obtained from the the fit shown in Figure 3.5 and correspond to

$$\alpha = 1.6322 \times 10^{-7}\,(\text{GeV/c})^{-1}\text{mm}^{-1} \quad \text{and} \quad \beta = -5.0217 \times 10^{-12}\,(\text{GeV/c})\text{mm}^{-2}. \tag{3.35}$$

3.6.1.2 Correction for the two-hit tolerance values

The parametrisation $f(x_0)$ of the q/p distribution as a function of x_0 is not analytical and fully data-driven. It assumes that tracks are originating from the (0,0,0) and a constant B_y component of the magnetic field in the horizontal plane. Therefore, it is likely that the tolerance windows obtained with this parametrisation are not ideal for all tracks propagating through the detector.
A strong not-considered t_x^{∞}-dependence of the momentum is known for $f(x_0)$. This is shown in Figure 3.6a. An alternative parametrisation of the q/p distribution

$$f(x_0, t_x^{\infty}) = (a_1 + a_2 t_x^{\infty})x_0 + q(b_1 + q t_x^{\infty}(b_2 + b_3 t_x^{\infty}))x_0^2 \tag{3.36}$$

takes into account the t_x^{∞} dependence which leads to a much more precise q/p estimation. This is clearly visible from the q/p resolution in shown in Figure 3.7. However, the complexity of this parametrisation introduces further parameters in the seeding that have to be tuned on simulation. Since the improvement in the relative resolution is not huge (from 4.4 % to 2.8 %), the alternative parametrisation

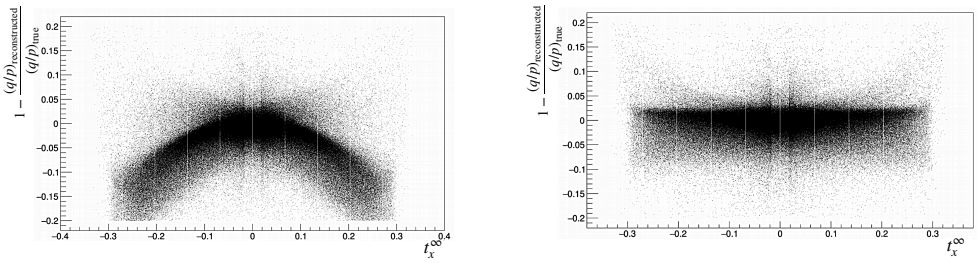

(a) $f(x_0)$ parametrisation **(b)** $f(x_0, t_x^\infty)$ parametrisation

Figure 3.6: Scatter plot of the relative q/p error as a function of t_x^∞ for the (a) $f(x_0)$ and (b) $f(x_0, t_x^\infty)$ parametrisations.

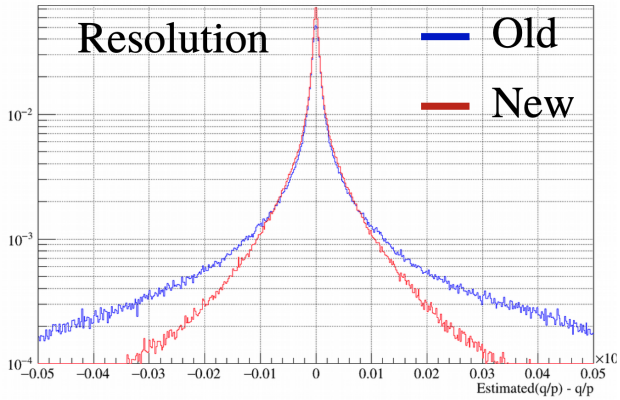

Figure 3.7: Distribution of the absolute q/p error of the $f(x_0)$ (old) and $f(x_0, t_x^\infty)$ (new) parametrisations. The absolute resolutions are calculated as the rms-values of the distributions.

is not used in the HLT1 seeding. Instead, a p_{min}-dependent correction factor α_{corr} for the central position of the search window is calculated. Figure 3.8a shows the tolerances obtained from the $f(x_0)$ and from a fit to tolerance windows that contain 99 % of the hits of simulated tracks. The correction factor is parametrised as

$$\alpha_{\text{corr}}(p_{\text{min}}) = \frac{\alpha_0}{k p_{\text{min}} \alpha_1}, \tag{3.37}$$

where the coefficients $\alpha_0 = 2.18 \times 10^6$ and $\alpha_1 = -1073$ are obtained from the fit shown in the right plot of Figure 3.8b. The tolerance window for the second hit in the T3 x-layer is then given by

$$x_{\text{tol}}^{\text{lower/upper}} = \frac{z_3 + \alpha_{\text{corr}}}{z_1} x_1 \mp \Delta x_3{}^{\text{max}}. \tag{3.38}$$

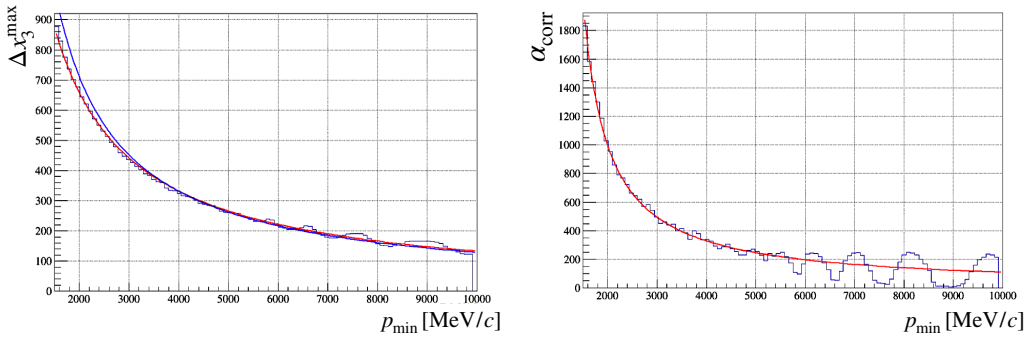

(a) tolerance vs. $p_{\min}$

(b) α-correction vs. $p_{\min}$

Figure 3.8: Comparison between the (a) tolerance $\Delta x_3^{\max}$ for the T3 hit as a function of $p_{\min}$ obtained from the $f(x_0)$ parametrisation (blue) and from the windows that contain 99 % of the hits of simulated tracks (red). (b) Fit to the correction factor α_{corr} as a function of $p_{\min}$.

3.6.2 Building three-hit combinations

The second step of the seeding in the xz-plane iterates over all two-hit combinations found in the previous step. The tolerances for the third hit in the initial T2 layer can be derived from the difference Δx_2 from the measured hit position $\tilde{x}_2$ to the predicted position in T2 x_2^{pred} assuming a straight line between the hits found in T1 and T3. Having now three hits, a parabola can be used as the underlying track model. Depending on the charge and the momentum of the particle there can be 4 different scenarios (per magnet polarity) for the Δx_2. These are illustrated in Figure 3.9. They can be distinguished by the signs of x_0 and Δx_2.

a) $x_0 > 0, \Delta x_2 < 0$: positive charge

b) $x_0 < 0, \Delta x_2 < 0$: positive charge, mostly high-momentum tracks since low-momentum tracks will bend out of acceptance

c) $x_0 > 0, \Delta x_2 > 0$: negative charge

d) $x_0 < 0, \Delta x_2 > 0$: negative charge, mostly low-momentum tracks since high-momentum tracks are less likely to bend back into the SciFi acceptance

Additionally, when flipping the magnet polarity scenario a) becomes c) and b) becomes d). Similar to how the tolerances for the T3 hit are defined, the tolerances Δx_2 for the T2 hit can be derived from inserting the momentum estimate obtained

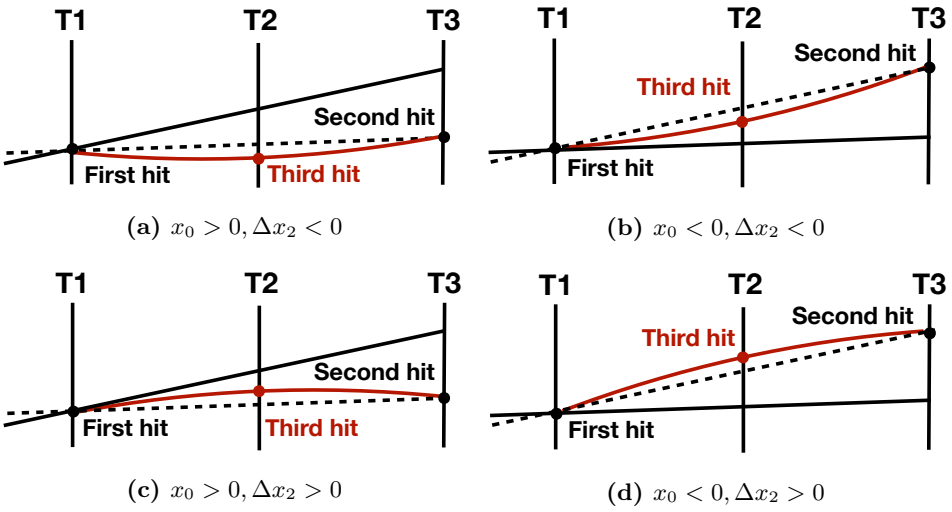

(a) $x_0 > 0, \Delta x_2 < 0$ **(b)** $x_0 < 0, \Delta x_2 < 0$

(c) $x_0 > 0, \Delta x_2 > 0$ **(d)** $x_0 < 0, \Delta x_2 > 0$

Figure 3.9: Sketches illustrating the four different scenarios for the third hit in T2 classified by the signs of x_0 and Δx_2. The solid black line corresponds to the straight line built from the T1 hit and (0,0,0), the dashed black line to the straight line from the two-hit combination of the T1 and T3 hit and the solid red line to the parabola built by the three hits. All scenarios are shown for magnet polarity MagDown.

from x_0 into the track model from equation 3.16 and comparing it to the predicted position

$$x_2^{\text{pred}} = \tilde{x}_1 + \frac{\tilde{x}_3 - \tilde{x}_1}{z_3 - z_1}(z_2 - z_1) \tag{3.39}$$

in T2 from the straight line between the T1 and T3 layer hits. Writing down the difference between $x(z_2)$ and x_2^{pred} results then in

$$\Delta x_2 = x(z_2) - x_2^{\text{pred}} = a_x + b_x z_2 + c_x \bar{z}_2^2 - \tilde{x}_1 - \frac{\tilde{x}_3 - \tilde{x}_1}{z_3 - z_1}(z_2 - z_1). \tag{3.40}$$

For $\tilde{x}_1$ and $\tilde{x}_3$ equation 3.16 can now be used again so that the expression for Δx_2 simplifies to

$$\Delta x_2 = c_x \underbrace{(\bar{z}_2^2 - \bar{z}_1^2 - (z_2 - z_1)\frac{\bar{z}_3^2 - \bar{z}_1^2}{z_3 - z_1})}_{:=k_{\text{corr}}}. \tag{3.41}$$

As c_x is describing by how much a track bends in the magnetic field, also the tolerances are given by this. Knowing that the bending depends on the initial

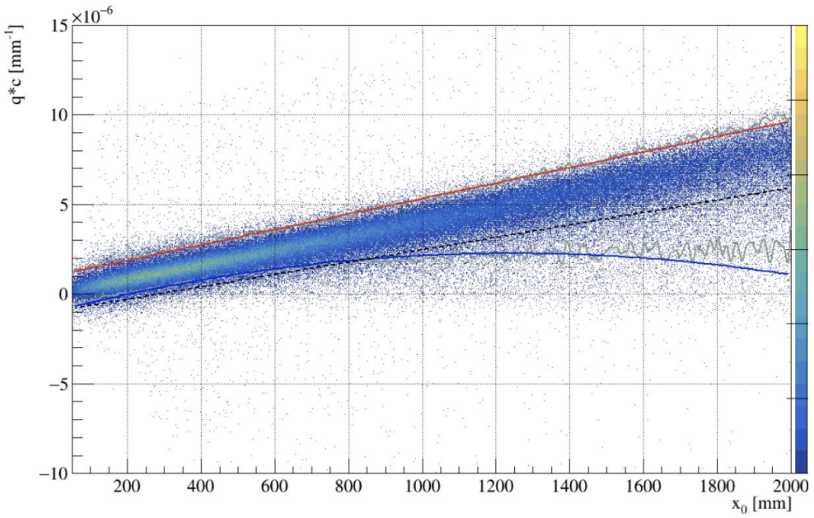

Figure 3.10: Distribution of qc_x as a function of x_0. Parabolic Fits (red and blue) to intervals that contain 99 % of simulated hits for each x_0 as a function of $1/p_{\text{min}}$ are performed to obtain the lower and upper thresholds for the third hit tolerances. The black curve is a simplification to reduce the amount of fake tracks from the large search windows for large x_0 due to the loose lower bound.

momentum of the particle and $1/p$ is related to $|x_0|$ by equation 3.30 we can define the tolerance window size as a function of $|x_0|$ by plotting c_x as a function of $|x_0|$.

Multiplied by the electric charge q, obtained from the direction in which the track bends. This is illustrated as 2D histogram in Figure 3.10. Afterwards, for each x_0-bin the qc_x-interval containing 99 % of all three-hit combinations is calculated, so that for each bin both a lower and upper threshold is obtained. In addition, all lower (upper) thresholds are fitted with a linear (parabolic) function which is shown in the Figure 3.10 as red and blue solid lines. Since for large x_0 the distributions spread out for low qc_x the used lower limits are parametrised by another straight line depicted by the black dashed line. This choice suppresses the number of ghosts while not loosing a lot of efficiency. The obtained thresholds for c_x can be re-converted afterwards to Δx_2 via equation 3.41 and hence be used to define the tolerances for the third hit. All three-hit combinations with T2 hits that fulfill

$$\Delta x_2^{\text{lower}} < \tilde{x}_2 < \Delta x_2^{\text{upper}} \tag{3.42}$$

are kept to look for hits in the remaining x layers.

3.6.3 Adding remaining hits

For each three-hit combination the track model can be written down for each measured hit so that the system of the three equations

$$\begin{aligned}\tilde{x}_1 &= a_x + b_x z_1 + c_x \bar{z}_1^2 \\ \tilde{x}_2 &= a_x + b_x z_2 + c_x \bar{z}_2^2 \\ \tilde{x}_3 &= a_x + b_x z_3 + c_x \bar{z}_3^2\end{aligned}$$

can be solved to obtain the track parameters a_x, b_x and c_x. Using these parameters the x-positions in the remaining x-layers can be predicted. All hits within a tolerance window of 0.5 mm from the predicted position are kept to build xz-seed candidates. The size of the tolerance window for the remaining hits is a free parameter of the seeding that is tuned on simulation. The seed candidate must have at least five found hits, *i.e.* only one remaining x-layer can be skipped when no hit is found. All accepted xz-seed candidates are then forwarded to the track fit in the xz-plane.

3.6.4 Track fit in the xz-plane

For xz-seeds with at least five hits a track fit in the xz-plane is performed by following equation 3.23. The linear system of equations is solved by building determinants and applying Cramer's rule. Seeds for which the resulting χ^2_{tr} from equation 3.17 is larger than 6 are discarded and not considered in the next step of the seeding that adds the y-information from the uv-layers. A clone killing for the xz-seeds is applied before y-information is added to them. The clone killing algorithm is described in section 3.8.

3.7 Adding y-information

The algorithm that performs the pattern recognition in the vertical plane (y-direction) from hits in the uv-layers starts from the predicted x-position $x^{\text{pred}}(z)$ in the first u-layer. The predicted position is obtained by evaluating the track model in x-direction at the z-position of the u-layer using the track parameters obtained from the final fit in the xz-plane. Due to the stereo angle in the uv-layers the predicted position is ambiguous when assigning it to a certain fibre.[1] Therefore, a large tolerance window for the x-position of the first hit has to opened, so that all fibres that could have

[1] A fibre is here taken as a simplified way to think about this problem. In reality, hits always come from various fibres and even various SiPM channels.

been hit are included. This is illustrated by Figure 3.11. All fibres depicted in black that cross the predicted hit position can potentially be the fibre that actually got hit. This means that for each predicted x-position there can around 820 different measured positions from different SiPM channels in the SciFi.[2] For every SiPM

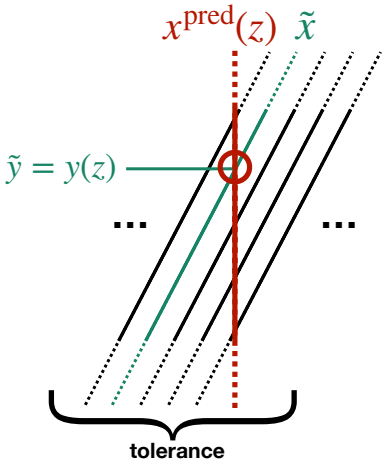

Figure 3.11: Sketch of the tolerance window for the pattern recognition in the uv-layers starting from the first hit.

channel inside the tolerance window the measured x-position can then be related to a measurement $\tilde{y}$ in the y-direction. The considered channel is depicted with the green line. The slope in the y-direction t_y can then be obtained as

$$t_y = \frac{\tilde{y}}{z} \tag{3.43}$$

assuming the track originated from $y = z = 0$. Since the magnetic field is negligible for the track trajectory in the y-direction this slope is now used to search for hits in the next uv-layer. This is done by extrapolating t_y to the z-position of the next layer and opening a tolerance window around this position. At the same time the initial constraint from the predicted x-position in each layer still exists. Only hits fulfilling both criteria can be considered for the seed candidate. With a found hit in the second layer the t_y measurement can be updated by now using the straight line between the two hits and the process can be repeated for the remaining uv-layer. Finally, only seed candidates with

$$n^{xz}_{\text{Hits}} + n^{uv}_{\text{Hits}} > 10 \tag{3.44}$$

[2] $n^{\text{per } x^{\text{pred}}(z)}_{\text{channels}} \approx \text{n}^{\text{per mat}}_{\text{SiPMs}} n^{\text{per SiPM}}_{\text{channels}} l_{\text{module}} \tan(\alpha_{\text{stereo}})/w_{\text{mat}} = 4 \cdot 128 \cdot 2500\,\text{mm} \cdot 0.086/134\,\text{mm}$

are accepted as candidates for the SciFi seeds. Here n^{xz}_{Hits} corresponds to number of hits found in the horizontal plane, whereas n^{uv}_{Hits} corresponds to the number of hits found in the uv-layers.
After the hits from all layers are added the track model in the y-direction from equation 3.13 is fitted to the candidate to obtain the track parameters a_y and b_y.

3.8 Clone killing

Clone tracks as described in section 3.1 are likely to occur in the seeding due to the iterative procedure of building all possible combinations of hits in predefined search windows. In addition, the approach of using two cases with the same momentum assumption but different initial layers increases the tracking efficiency but also the amount of clone tracks. Therefore, it is crucial to run a dedicated clone killing step after the pattern recognition and track fit. The clone killing algorithm implemented for the seeding in HLT1 brings the clone rate to 0 % by definition since it compares the hits of pairs of found SciFi seeds and discards the seed with the larger χ^2_{track} if the two seeds share more than 70 % of their hits.
For the HLT1 computing performance it is important that the clone killing step is implemented in a time-saving way. Instead of a doubly nested $\mathcal{O}(N^2_{\text{tracks}})$ loop over the the hits of the two tracks comparing the hits a novel $\mathcal{O}(N_{\text{tracks}})$ shared-memory-based clone killing algorithm is run to avoid iterating over a huge number of track combinations in the global memory.
Conceptually it is still possible to have surviving clone tracks that share less than 70 % of their hits. Therefore, in some offline analyses other methods such as selection requirements on the angle between two potential clones are applied. For the tracking in HLT1 this is not needed since the clone rate is at a minimal level and computing resources need to be saved. The remaining clone tracks are contributing to the final ghost rate since only one of seeds can be matched to a MC particle.

3.9 Matching track segments

The different track types for physics and performance studies shown in Figure 2.7 can be obtained as the output of the standalone tracking algorithms directly or by combining track seeds from different subdetectors. While high-quality VELO tracks and T tracks can be extracted from the VELO tracking and SciFi seeding after applying a track fit via a Kalman filter, the more complex long, downstream and upstream tracks require a matching of seeds. This thesis focuses on the matching of VELO tracks with SciFi seeds, the *VeloSciFi matching*, in the absence of the

UT as it will be used for data taking in the early period of Run 3 of the LHC. The matching algorithm can be adapted for a downstream tracking in HLT1 by matching SciFi and UT seeds. For the non-UT scenario the *VeloSciFi matching* is an alternative track reconstruction approach to the *forward tracking without UT*.

3.9.1 VeloSciFi matching

As depicted in Figure 3.2, for the *VeloSciFi matching*, VELO tracks after the simplified Kalman filter and SciFi seeds directly from the *HybridSeeding* in the SciFi are used as input.[3] The matching is performed in both the x- and y-directions by iterating over SciFi seeds and matching Velo tracks to them. The average amount of tracks considered for the matching for both the VELO and the SciFi is about 100 per event. Here, VELO tracks are pre-filtered to point into the forward direction and to be in the geometrical acceptance of the SciFi.[4] This reduces the ghost rate and computing performance significantly.

3.9.1.1 Matching in the yz-plane

Figure 3.12 illustrates the matching of VELO tracks and SciFi seeds in the yz-plane. For the VELO track the track state highest in z is extrapolated as a straight line to the matching position z_y^{match}=10 m where the matching in the yz-plane is performed. The position is just behind the last SciFi station, to integrate over potential bending of the track. Similarly this is done for the SciFi seed by taking its last state. Matching candidates should have a similar extrapolated y-position at z_y^{match} as well as a similar t_y. Before matching them, a pre-selection for the differences t_y in y at z_y^{match} between VELO tracks and SciFi seeds is applied that requires candidates to fulfill

$$|\Delta t_y| = \left|t_y^{\text{VELO}} - t_y^{\text{SciFi}}\right| < 0.02 \tag{3.45}$$

and

$$|\Delta y| = \left|y^{\text{VELO}} - y^{\text{SciFi}}\right| < 150\,\text{mm}. \tag{3.46}$$

The selection requirements are derived from the comparison of VeloSciFi tracks associated to a true MC particle with combinations of VELO tracks and SciFi seeds that were matched falsely. The corresponding distributions for Δy are shown in Figure 3.13. For the remaining candidates, the differences in y and t_y will be used

[3] In the current implementation of Allen, Kalman filters are only applied to VELO track candidates. A Kalman fitting of SciFi seeds or forward tracks would require to load the magnetic field map into memory which is computationally too expensive for HLT1.

[4] Backwardly pointing VELO tracks are relevant for the reconstruction of PVs.

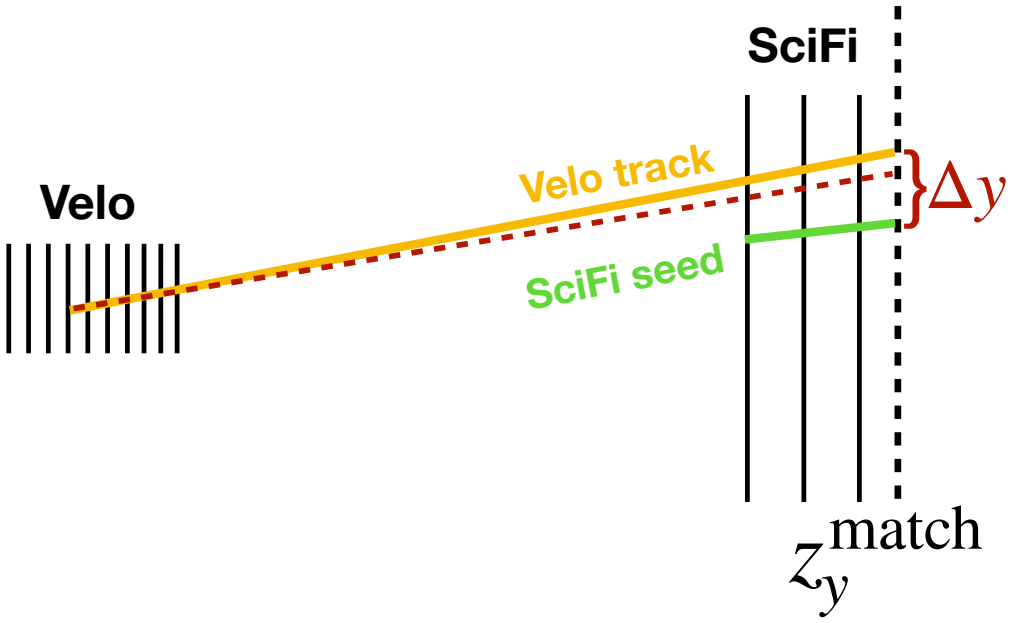

Figure 3.12: Sketch of the *VeloSciFi matching* in the yz-plane.

to build the total χ^2 of the *VeloSciFi matching* in section 3.9.2.

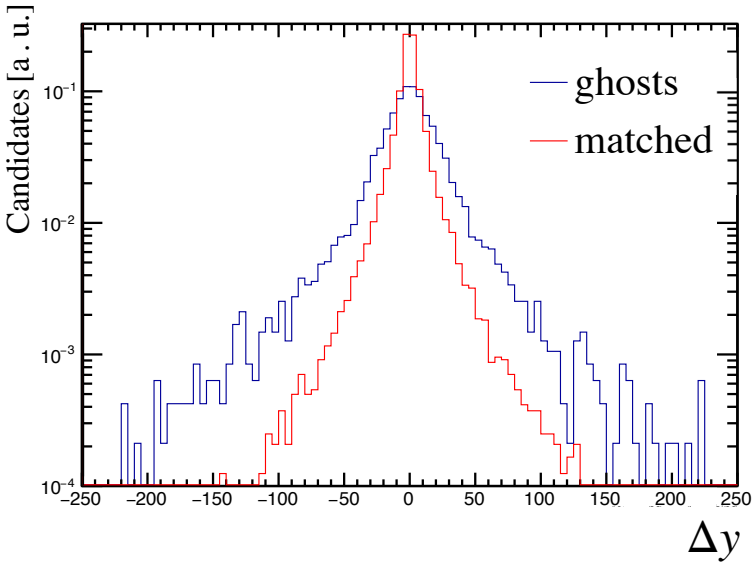

Figure 3.13: Distributions of $\Delta y = y^{\text{VELO}} - y^{\text{SciFi}}$ at z_y^{match} for fake tracks (ghosts) and truth-matched VeloSciFi tracks. A pre-selection for the matching candidates is derived from these distributions.

3.9.1.2 Matching in the xz-plane

Figure 3.14 illustrates the matching in the xz-plane. Due to the presence of the magnetic field component $B_y(z)$ the extrapolation of VELO tracks and SciFi seeds in the xz-plane is not as trivial as in the yz-plane. Loading the map of the measured magnetic field strengths into the memory requires a tremendous amount of storage and is computationally very expensive. Therefore, this is not feasible for HLT1 and the extrapolation of VELO tracks and SciFi seeds to a common matching position z_x^{match} is simplified with the so-called *kink approximation*. Here, VELO tracks and SciFi seeds are extrapolated as straight lines to an optimal matching position z_x^{match} where their intersection builds the most obtuse kink. The z_x^{match} is obtained from a parametrisation of the magnetic field. The parameters a_{i} of the parametrisation are extracted by taking true hits from simulated particles and passing them through the reconstruction to find where the kink approximation works best. The matching position is then obtained via

$$z_x^{\text{match}} = a_0 + a_1|\Delta t_x| + a_2 t_x^2 + a_3\left|x^{\text{SciFi}}\right| + a_4\left(t_x^{\text{Velo}}\right)^2, \tag{3.47}$$

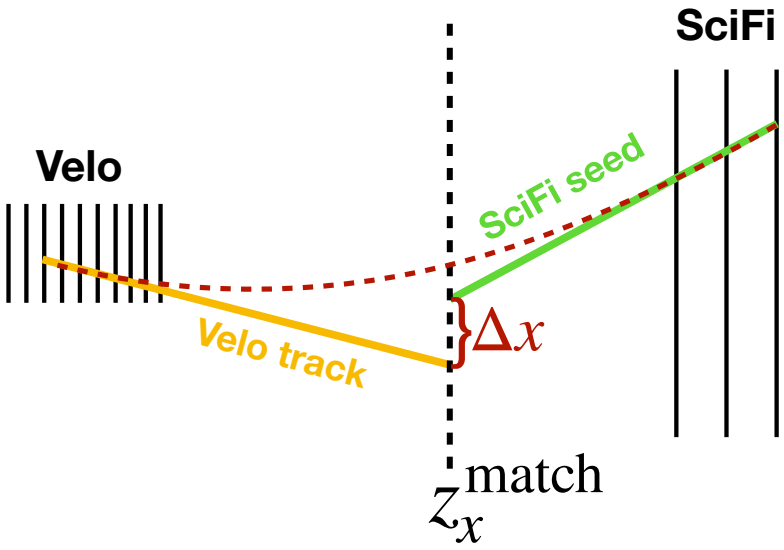

Figure 3.14: Sketch of the VeloSciFi matching in the x-direction.

where the a_i with i = 0...4 are the coefficients shown in table 3.2. Since the parametrisation depends on x^{SciFi} and t_x^{Velo} the matching position in x is different for each matching candidate. As for the matching in the yz-plane matching candidates

Table 3.2: Coefficients of the magnetic field parametrisation determined from simulation.

i	a_i
0	5287.6 mm
1	−7.988 78 mm
2	317.683 mm
3	0.0119379
4	−1418.42 mm

are pre-selected based on their difference in x and t_x with the following requirements at z_x^{match}:

$$|\Delta t_x| = \left|t_x^{\mathrm{VELO}} - t_x^{\mathrm{SciFi}}\right| < 1.5 \tag{3.48}$$

and

$$|\Delta x| = \left|x^{\mathrm{VELO}} - x^{\mathrm{SciFi}}\right| < 20\,\mathrm{mm}. \tag{3.49}$$

The selection requirements for x can be chosen more tightly with respect to the one for y since in the SciFi seeding the resolution of the position is much better for the x than for y-direction. For the differences in the slope the y-direction can be constrained more strictly while for the x-direction the bending in horizontal plane requires less tight constraints.

3.9.2 Constructing a matching variable

The variable used to decide if a VELO track matches to a SciFi seed is the χ^2_{match}. It is constructed from the variables Δy, Δt_y at z_y^{match} and Δx, Δt_x and z_x^{match}. They describe the absolute differences in the positions and slopes of the extrapolated track states in the x- and y-directions. In addition, the scaling factors $f_{\Delta t_y} = 0.0625 \cdot 10^5$ and $f_{\Delta t_x} = 10$ are introduced to obtain a good performance in the matching efficiency and ghost reduction. Moreover, the contributions of Δx and Δy are further normalised by the constant tolerances parameters $\text{tol}_{\Delta x} = 8\,\text{mm}$, $\text{tol}_{\Delta t_x} = 80\,\text{mm}$, $\text{tol}_{\Delta y} = 6\,\text{mm}$ and $\text{tol}_{\Delta t_y} = 300\,\text{mm}$. They can be interpreted as the resolutions of the extrapolated positions and slopes in x and y. Finally, the χ^2_{match} is obtained by

$$\chi^2_{\text{match}} = \cdot f_{\Delta t_y} \cdot (\Delta t_y)^2 + f_{\Delta t_x} \cdot (\Delta t_x)^2 + \frac{(\Delta x)^2}{(\text{tol}_{\Delta x})^2 + (\text{tol}_{\Delta t_x} \cdot \Delta t_x)^2} + \frac{(\Delta y)^2}{(\text{tol}_{\Delta y})^2 + (\text{tol}_{\Delta t_y})^2 \cdot [(t_y^{\text{VELO}})^2 + (t_x^{\text{VELO}})^2]}$$

For each SciFi seed an iteration over all VELO tracks is performed in order to determine the best matching VELO track, *i.e.* the one with smallest χ^2_{match}. If the χ^2_{match} of the best VELO track is smaller than the required $\chi^2_{\text{match, cut}} = 2.5$ the combination of the SciFi seed and the Velo track are saved as a VeloSciFi track and a momentum for the track is calculated. The $\chi_{\text{match, cut}}$ is obtained from Figure 3.15 that compares correctly matched candidates that could be associated to a simulated particle and ghost tracks. The *Seeding & Matching* approach has the advantage with respect to the *forward tracking* that SciFi seeds where no matching VELO track was found for can be used independently for T track studies.

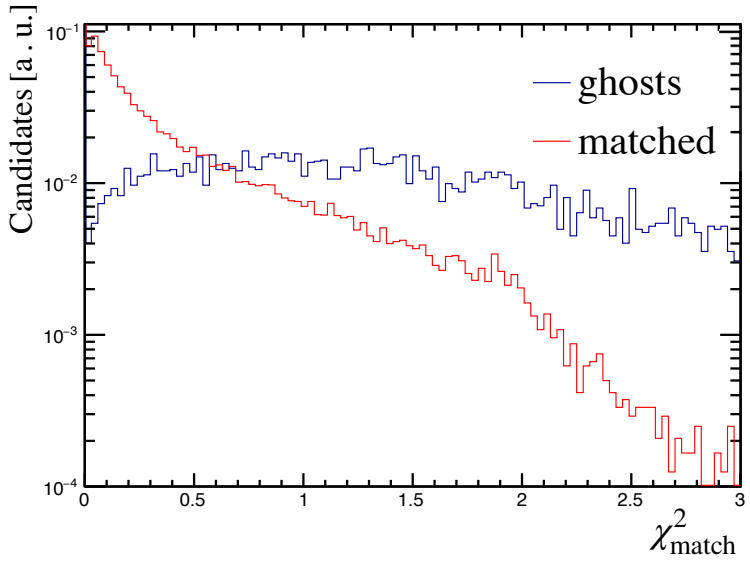

Figure 3.15: Comparison of the χ^2_{match} distributions for truth-matched VELOSciFi tracks and ghost tracks.

3.10 Physics performance of the *Seeding & Matching*

The physics performance of the SciFi *HybridSeeding* and *VeloSciFi matching* is evaluated with the performance indicators described earlier in section 3.1 for different track categories. Apart from the classification of reconstructed tracks into track types as done in Figure 2.7 further categories can be introduced for simulated particles where the true origin of the particle and its momentum are known. The categories that will be used introduced in the following. Simulated tracks categorised as

- `long` are required to have at least three hits in the VELO, three hits in the UT and ten hits in the SciFi detector. This ensures their reconstructibility.
- `from B` are required to have originated from a *b*-hadron decay. They are identified via the MC particle ID
- `from strange` are required to have originated from a *s*-hadron decay.
- `electrons` are required to have the MC particle ID of an electron.

The two main indicators of interest are the track reconstruction efficiency and the ghost rate as functions of p, p_{T} and η. They are discussed in sections 3.10.1 and 3.10.2. In addition, the momentum resolution of the VeloSciFi tracks is discussed in 3.10.3.

3.10.1 Track reconstruction efficiency

The track reconstruction efficiencies $\varepsilon_{\mathrm{tr}}^{\mathrm{MC,\ VELO}}$ for the VELO tracking, $\varepsilon_{\mathrm{tr}}^{\mathrm{MC,\ SciFi}}$ for the SciFi seeding and $\varepsilon_{\mathrm{tr}}^{\mathrm{MC,\ VeloSciFi}}$ for the *VeloSciFi matching* algorithms are obtained from running over 5000 simulated events including $B_s^0 \to \phi\phi$ decays and are shown in Table 3.5. For the *VeloSciFi matching* previous inefficiencies from the VELO tracking and SciFi seeding need to be taken into account. Figure 3.16 and

Table 3.3: Integrated track reconstruction efficiencies of the VELO tracking, the SciFi seeding and the VeloSciFi matching for different track categories. Numbers are obtained from running over 5000 simulated $B_s^0 \to \phi\phi$ events.

track category	$\varepsilon_{\mathrm{tr}}^{\mathrm{MC,\ VELO}}$	$\varepsilon_{\mathrm{tr}}^{\mathrm{MC,\ SciFi}}$ in %	$\varepsilon_{\mathrm{tr}}^{\mathrm{MC,\ VeloSciFi}}$ in %
`long`	99.36	76.35	70.32
`long`, $p_{\mathrm{T}} > 5\,\mathrm{GeV/c}$	99.62	92.63	87.59
`long from B`	99.22	85.69	81.99
`long from B`, $p_{\mathrm{T}} > 5\,\mathrm{GeV/c}$	99.46	93.50	90.60

3.17 show the track reconstruction efficiencies after the VELO tracking, the SciFi seeding and the *VeloSciFi matching* as functions of p, p_{T} and η for the track category `long from B`. For the VELO the plots are done before filtering out backward tracks and the ones that do not point into the SciFi acceptance. It can be seen that the track reconstruction efficiency is close to 100 % for the full range of p, p_{T} and η. The plots for the SciFi seeding show that tracks can be reconstructed at a high efficiency of above 80 % down to around $p > 3\,\mathrm{GeV/c}$ and $p_{\mathrm{T}} > 500\,\mathrm{MeV/c}$. Below the tracking efficiency decreases due to the choice of the minimal momentum in both cases of the seeding. Nevertheless, events relying on tracks with even lower momentum are still being reconstructed at a decent efficiency which enables to run HLT1 trigger selections with low momentum tracks which was not possible during Run 2 due to the tight constraints from the L0 trigger stage. Moreover, it can be observed that the efficiency drops for tracks with low η. The reason for that can be a more displaced topology of the decaying b hadron since the seeding is assuming that tracks originated from the interaction point. The tracking efficiencies after the *VeloSciFi matching* are further reduced by around 3-5 % depending on the track category. More insight about the matching is given when looking at the matching

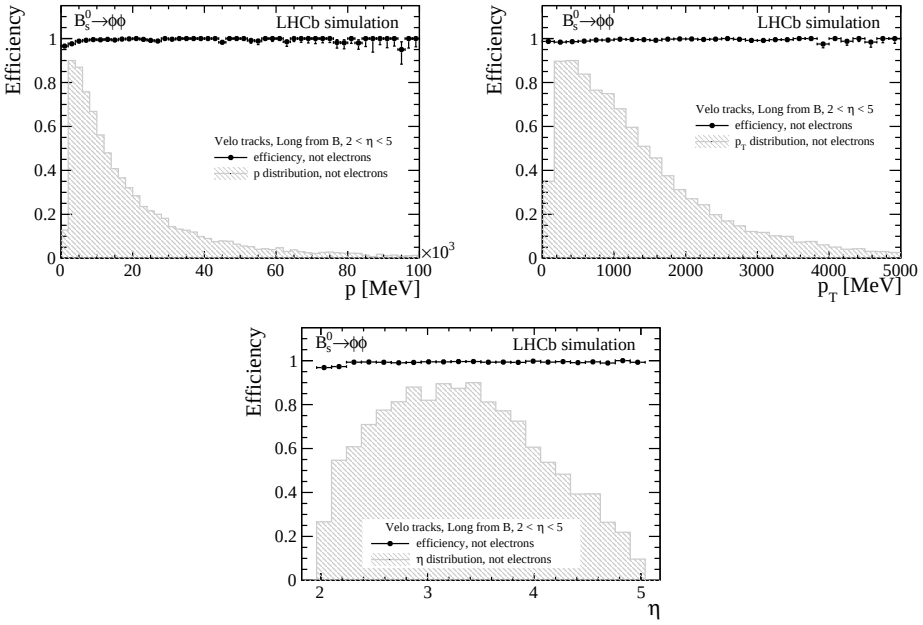

Figure 3.16: Tracking efficiency for VELO tracks as a function of p, p_{T} and η. The histograms show the p, p_{T} and η distributions of reconstructed VELO tracks in these variables. The plots were obtained by running over 5000 simulated $B_s^0 \to \phi\phi$ decays and show the performance for VELO tracks that originated from b-hadron decays inside the LHCb acceptance. Taken from Ref. [127].

efficiencies directly. The left column of Figure 3.18 shows the comparison between the track reconstruction efficiency after the *VeloSciFi matching* (black) and the product of the track reconstruction efficiencies of the standalone VELO tracking and the SciFi seeding algorithms (blue) as a function of p, p_{T} and η. The ratio of the two distributions is shown in the right column of Figure 3.18 and depicts the efficiency of the matching procedure itself. The matching efficiency is close to 100 % for the full p, p_{T} and η ranges except for a slight decrease for low (transverse) momenta where the kink approximation is sub-optimal. Another important indicator of the matching performance is the ghost rate that is being discussed in the next section.

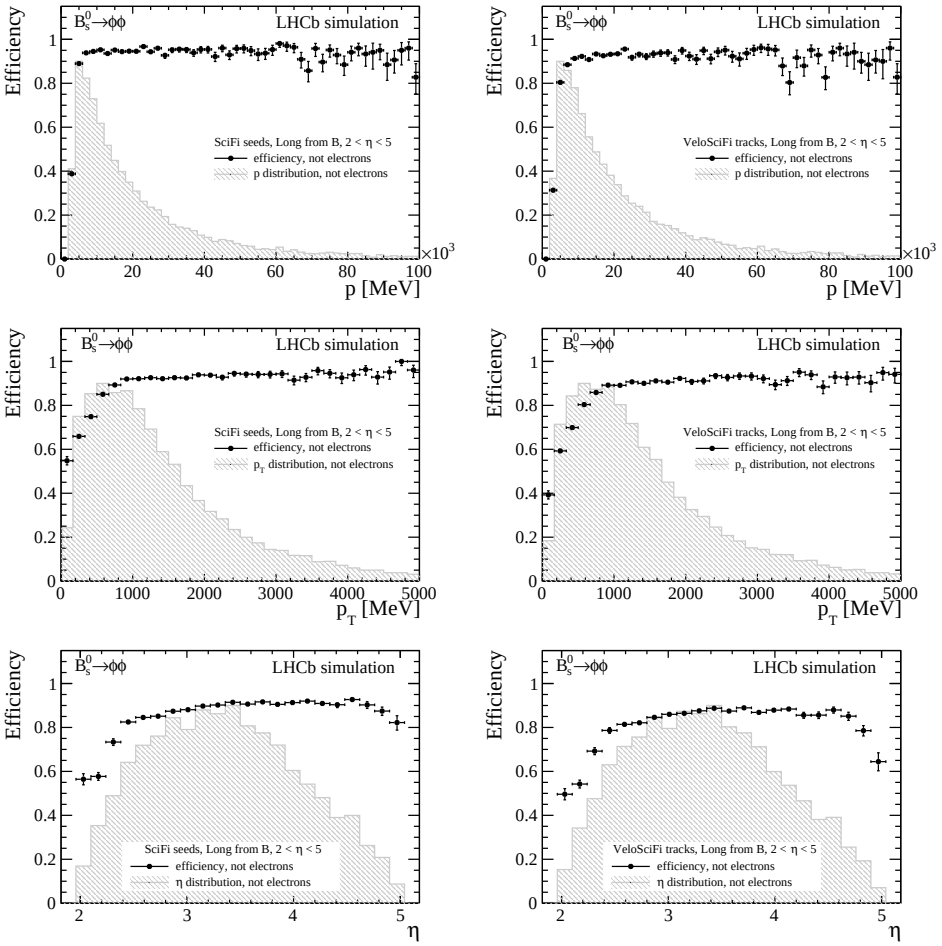

Figure 3.17: Tracking efficiency for SciFi seeds (left) and VeloSciFi tracks (right) as function of p, p_{T} and η. The histograms show the p, p_{T} and η distributions of reconstructed VeloSciFi tracks in these variables. The plots were obtained by running over 5000 simulated $B_s^0 \to \phi\phi$ decays and show the performance for VeloSciFi tracks that originated from b-hadron decays inside the LHCb acceptance. Taken from Ref. [127].

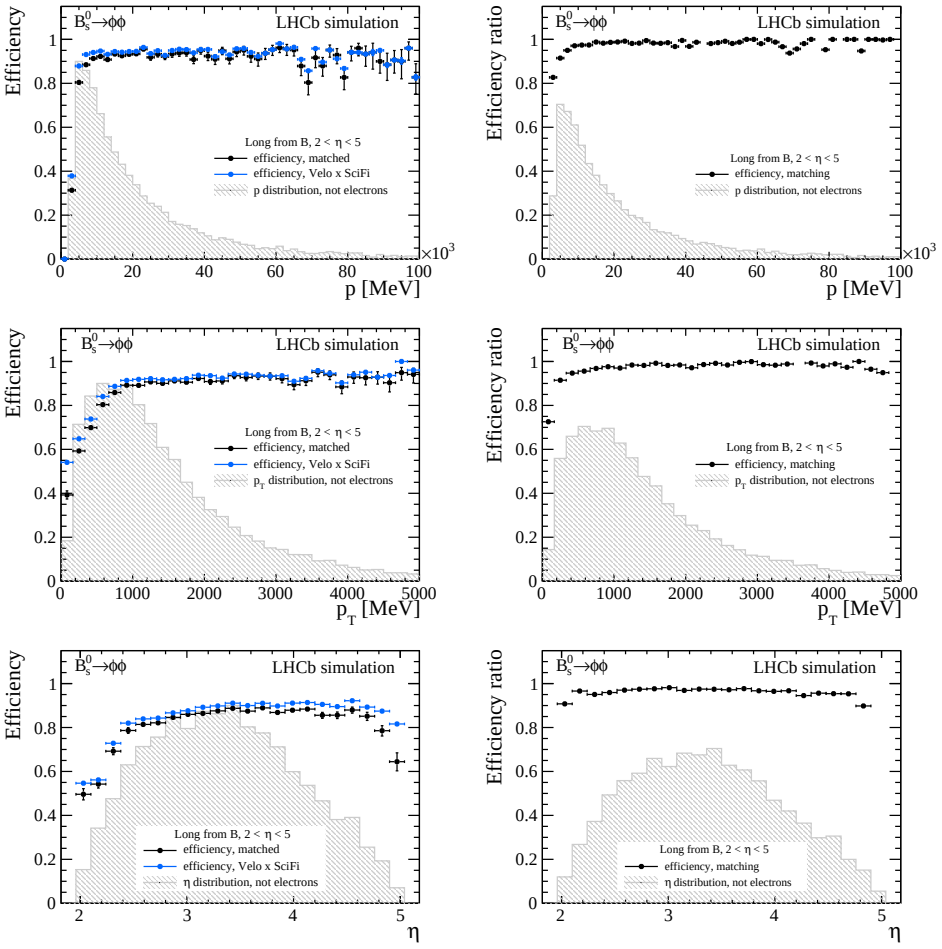

Figure 3.18: Comparison of the tracking efficiency for VeloSciFi tracks to the product of the tracking efficiencies of Velo tracks and SciFi seeds (left) as well the efficiency of the VeloSciFi matching algorithm (right) as function of p, p_{T} and η. The histograms show the p, p_{T} and η distributions of reconstructed VeloSciFi tracks in these variables. The plots were obtained by running over 5000 simulated $B_s^0 \to \phi\phi$ decays and show the performance for VeloSciFi tracks that originated from b-hadron decays inside the LHCb acceptance. Taken from Ref. [127].

3.10.2 Ghost rates

Figure 3.19 shows the ghost rate after *VeloSciFi matching* as defined in equation 3.2 as a function of p, p_{T} and η. The total ghost rate for the *VeloSciFi matching* matching obtained from 5000 simulated $B_s^0 \to \phi\phi$ events is about 9 % while the total ghost rate for the SciFi seeding is 11 % and 1 % for the Velo tracking. From the plots it is visible that the ghost rate is particularly high for low p and p_T and slightly increased at high p and p_T with respect to the average. For highly forwarded boosted tracks it is hard for the matching to discriminate between real and fake tracks since the variables that build the χ^2_{match} have more discrimination power for low-momentum. High momentum tracks are also likely to have high η. For low momentum the main contribution to the ghost rate comes from the SciFi seeding. In addition, the kink approximation performed in the *VeloSciFi matching* is not working perfectly for low momentum.

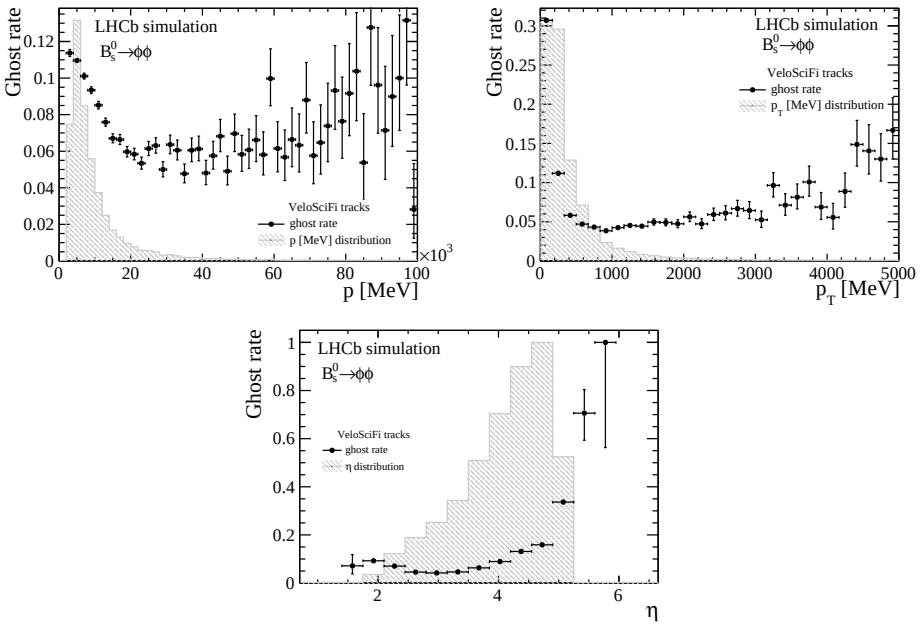

Figure 3.19: Ghost rates of VeloSciFi tracks as function of p, p_{T} and η. The histograms show the p, p_{T} and η distributions of ghost tracks in these variables. The plots were obtained by running over 5000 simulated $B_s^0 \to \phi\phi$ decays and show the performance for VeloSciFi tracks that originated from b-hadron decays inside the LHCb acceptance. Taken from Ref. [127].

For the *VeloSciFi matching* there are four potential sources where ghost tracks can originate from.

1. Both the SciFi seed and the VELO track are ghosts and they were matched.
2. The SciFi seed is real and matched to a ghost VELO track.
3. The SciFi seed is a ghost track and matched to a real VELO track.
4. The SciFi seed and the VELO track are both real but did not originate from the same track, *i.e.* the ghost track originated from the matching.

Since the ghost rate of the VELO tracking is very low the first two cases are very unlikely and negligible for further investigations. A high ghost rate from the matching indicates a sub-optimal matching parameter that could be replaced by using a multivariate classifier. A high ghost rate from the seeding would require a better track fit and selection based on the track fit quality parameters.

3.10.3 Momentum resolution

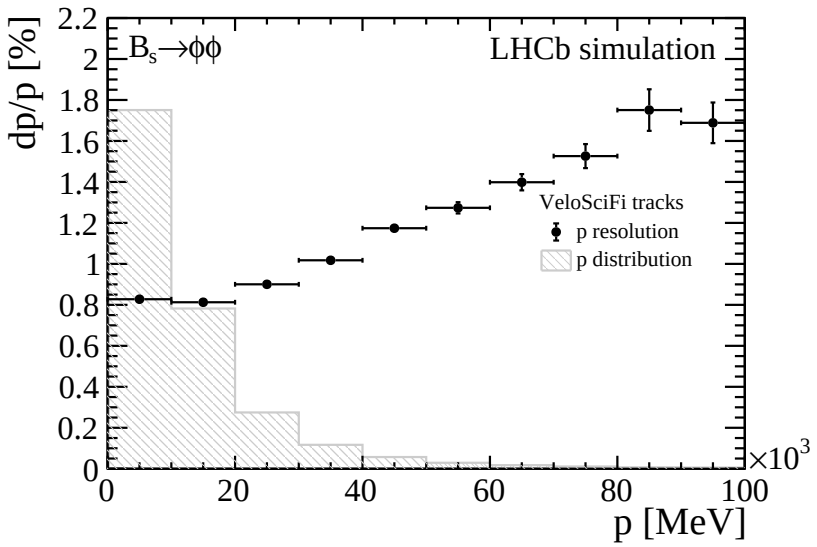

Figure 3.20: Momentum resolution of VeloSciFi tracks as a function of p. The histograms show the p distribution of reconstructed VeloSciFi tracks. The plot was obtained by running over 5000 simulated $B_s^0 \to \phi\phi$ decays and shows the performance for VeloSciFi tracks that originated from b-hadron decays inside the LHCb acceptance. Taken from Ref. [127].

The relative momentum resolution of VeloSciFi tracks

$$\frac{dp}{p} = \left| \frac{p_{\text{reconstructed}} - p_{\text{true, MC}}}{p_{\text{true, MC}}} \right|, \tag{3.50}$$

where $p_{\text{reconstructed}}$ stands for the momentum of track reconstructed by the VeloSciFi matching and $p_{\text{true, MC}}$ for the momentum of its associated MC particle is shown Figure 3.20 as a function of p. The momentum resolution lies between 1-2 % which is slightly worse than the baseline HLT1 reconstruction with the *forward tracking* with UT [116]. The reason for that is mostly the lack of hits closely before the LHCb dipole magnet from the UT. A more detailed comparison to the forward tracking is given in section 3.10.6.

3.10.4 Hit purity and hit detection efficiency

Table 3.4 shows the hit purity and hit detection efficiency of the three tracking algorithms for the different track categories. The hit purity is above 99 % for tracks from all algorithms in all track categories. For the VELO tracks it is slightly higher than for SciFi seeds and VeloSciFi tracks. In the HLT1 implementation of the SciFi

Table 3.4: Hit purity and hit detection efficiencies for VELO tracks, SciFi seeds and tracks from the VeloSciFi matching. All number are obtained by running over 5000 simulated $B_s^0 \to \phi\phi$ decays.

track category	hit purity in %			hit efficiency in %		
	VELO	SciFi	Matching	VELO	SciFi	Matching
`long`	99.70	99.02	99.48	97.75	95.98	96.27
`long`, $p_{\text{T}} > 5\,\text{GeV/c}$	99.73	99.04	99.49	98.30	96.63	96.84
`long from B`	99.54	99.13	99.49	97.92	96.71	96.94
`long from B`, $p_{\text{T}} > 5\,\text{GeV/c}$	99.58	99.16	99.51	98.23	97.00	97.19

seeding two important changes with respect to HLT2 have been done that have an impact on the hit purity. The first is the changed minimal number of hits in the x-layers and the total number of hits in the SciFi that a SciFi seed needs to have. In addition, the removal of outlier hits for tracks with a bad track fit quality and refitting of these after the removal is not performed for the HLT1 version of the seeding to save computational time. While the first improves the hit purity, the second degrades it. Overall, no significant differences for the different track categories are observed.
The hit detection efficiencies are above 96 % for tracks from all three algorithms. For the SciFi seeding they are slightly decreased with respect to the VELO tracking.

The hit detection inefficiencies of the SciFi seeding mainly arise from the tight search windows when looking for two-hit and three-hit combinations. In the current implementation they are necessary to control the ghost rate. Adding a removal of outlier hits and tighten the track fit quality parameter, while loosen the search window sizes would allow for a higher hit efficiency. For the SciFi seeding the hit detection efficiencies also vary within 1 % among the track categories. For the reconstruction of low momentum tracks it is more likely to miss a hit, especially when the momentum is below the minimal momentum the seeding is tuned for.

3.10.5 Tracking efficiencies for electrons

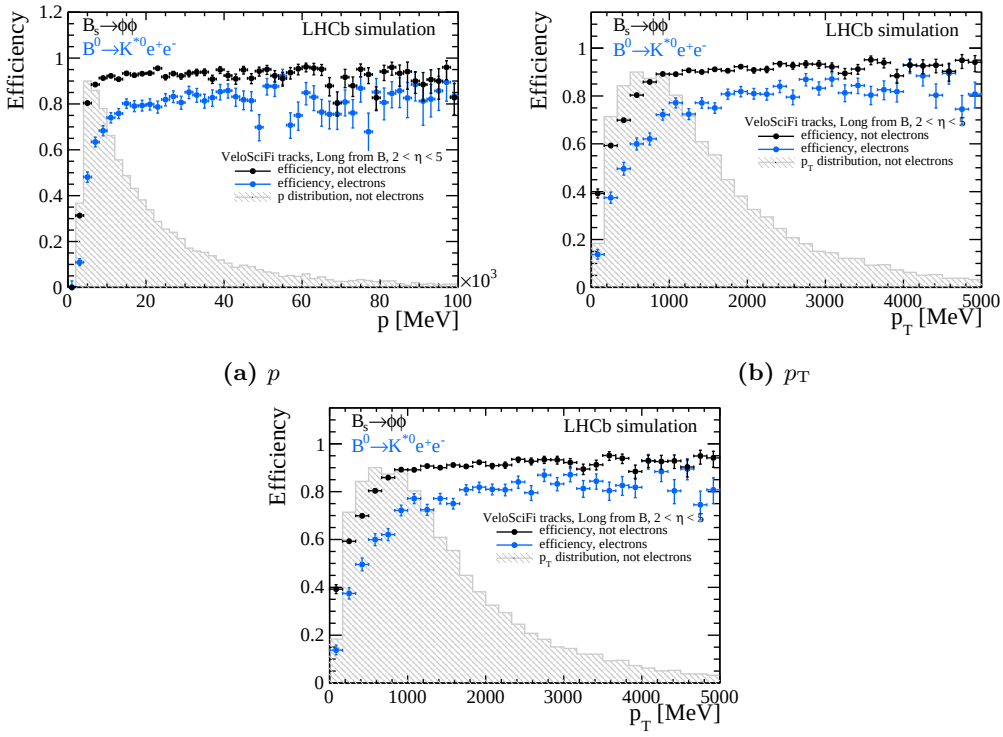

(a) p **(b)** p_{T}

(c) η

Figure 3.21: Comparison of the track reconstruction efficiency as a function of (a) p, (b) p_{T} and (c) η for VeloSciFi tracks that are matched to a MC particle identified as (non-)electrons. All plots are obtained from running over 5000 simulated $B_s^0 \to \phi\phi$ (non-electrons) or $B^0 \to K^{*0} e^+ e^-$ (electrons) events. Taken from Ref. [127].

The tracking efficiencies as functions of p, p_{T} and η are compared between `long electrons from B` and `long from B` particles reconstructed as VeloSciFi tracks in Figure 3.21. It can be observed that the tracking efficiencies for `long electrons from B` are about 10-20 % lower for the full ranges of the p, p_{T} and η with respect to non-electrons. This is an effect that is caused by the bremsstrahlung radiated by electrons before the SciFi. In the seeding the momentum estimate from the x_0 is obtained from back-propagated straight line from the two-hit combination. This momentum is then used to to open the search window for the third hit. If the electron looses momentum due to the radiation of bremsstrahlung photons, the electron track bends stronger than expected from the momentum estimate and therefore the search window for the third hit is more likely to be too tight.

Table 3.5: Integrated track reconstruction efficiencies of the VELO tracking, the SciFi seeding and the VeloSciFi matching for `long electrons` from different track categories. Numbers are obtained from running over 5000 simulated $B^0 \to K^{*0}e^+e^-$ events.

track category	$\varepsilon_{\mathrm{tr}}^{\mathrm{MC,\ VELO}}$[%]	$\varepsilon_{\mathrm{tr}}^{\mathrm{MC,\ SciFi}}$[%]	$\varepsilon_{\mathrm{tr}}^{\mathrm{MC,\ VeloSciFi}}$[%]
all	96.76	58.17	44.07
$p_{\mathrm{T}} > 5\,\mathrm{GeV/c}$	-	78.69	62.14
`from B`	96.98	79.09	70.93
`from B`, $p_{\mathrm{T}} > 5\,\mathrm{GeV/c}$	97.74	84.42	76.53

3.10.6 Performance comparison to the forward tracking

The physics performance shown in the previous section are compared to the performances of the *forward tracking* tracking. The comparisons of the track reconstruction efficiencies and ghost rates as a function of p and p_{T} as well as the momentum resolution are shown in Figure 3.22. The track reconstruction effiencies are very similar between the *Seeding & Matching* and *forward tracking* for most of the p/p_{T} range. Only for low p/p_{T} the *Seeding & Matching* performs better. At the same time the total ghost rates of the *Seeding & Matching* are about twice as high as the one of the *forward tracking* with increased values for low and high p/p_{T}. Although the *Seeding & Matching* is not using any hits from the UT detector the momentum resolution is slightly worse but in a similar range compared to the one of the *forward tracking*.

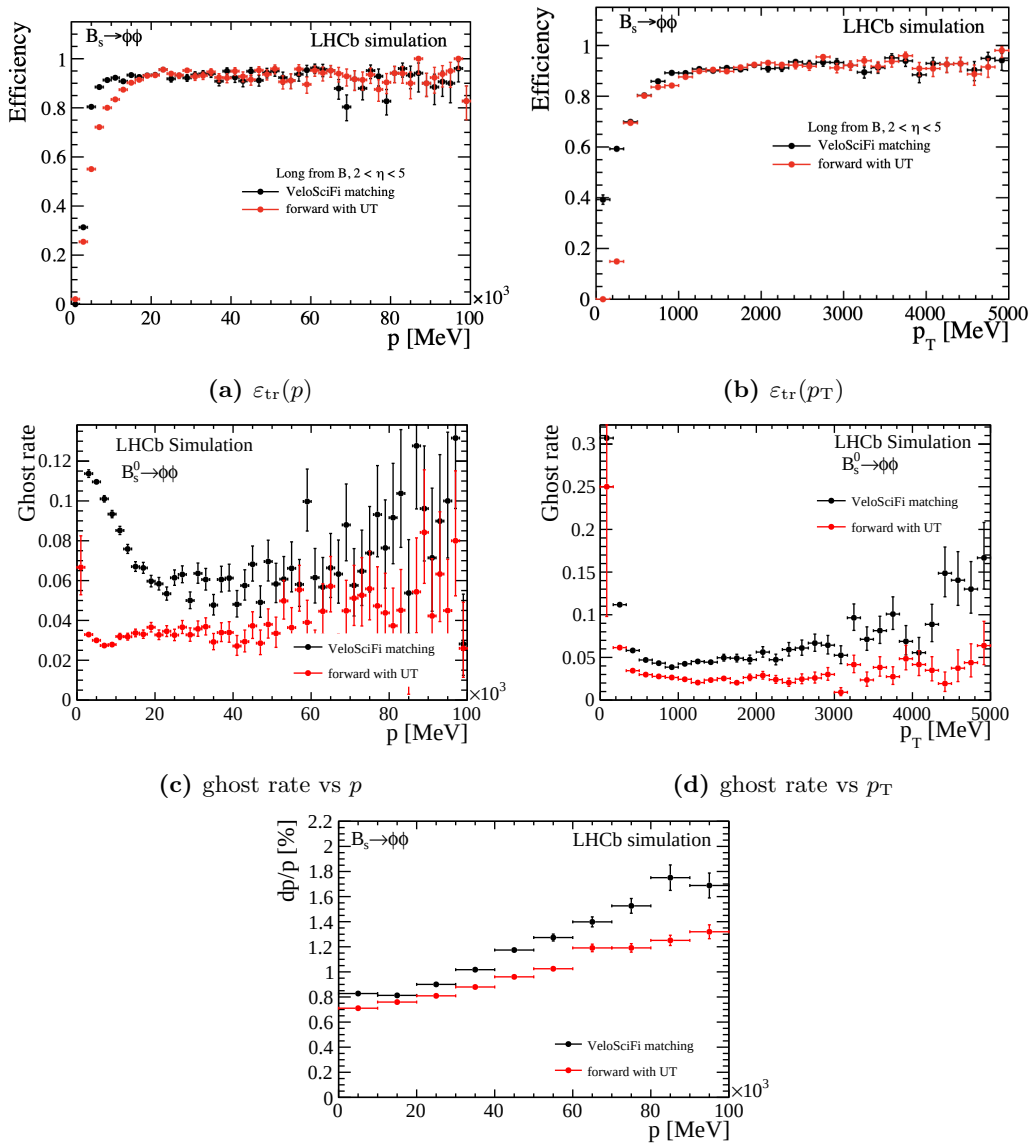

(a) $\varepsilon_{\mathrm{tr}}(p)$

(b) $\varepsilon_{\mathrm{tr}}(p_{\mathrm{T}})$

(c) ghost rate vs p

(d) ghost rate vs p_{T}

(e) dp/p

Figure 3.22: Comparison of the track reconstruction efficiency as a function of (a) p and (b) p_{T}, the ghost rates as a function of (c) p and (d) p_{T} as well as (e) the momentum resolution for VeloSciFi tracks (black) and long tracks from the forward tracking with UT. All plots are obtained from running the HLT1 sequence with either the VeloSciFi matching or the forward tracking with UT over 5000 simulated $B_s^0 \to \phi\phi$ events. Taken from Ref. [127].

3.11 Features of the *Seeding & Matching* on GPUs

The handling of memory is a key challenge for the computational performance of the *Seeding & Matching*. In the following the way the different types of memory in a GPU card are used for the seeding are described. Since the different steps of the seeding requires multiple accesses of the hit data, loading them into the shared memory and keeping them there for all iterations in all steps of the seeding, reduces the amount of redundant slow accesses to the global memory. The execution time of the seeding is about 1.5 times faster when accessing hits via the shared memory instead of the global memory.
The seeding is split into an algorithm looking at the xz-part and an algorithm that adds y-information. That means, that the hits of six layers need to be considered at the same time. Furthermore, the pattern recognition treats the upper and lower halves of the detector completely independently.
Therefore, the hit data is tiled into chunks of hits of the upper and lower detector halves and into x-layer and u/v-layer hits. In that way only data that need to be accessed by each algorithm of the pattern recognition are loaded into the shared memory. This reduces the needed amount of shared memory per block, so that more blocks can be used and the computation is accelerated. Temporary intermediate variables or arrays that are created for calculations in an algorithm can be stored into the registers that are associated to the thread executing that algorithm. This is beneficial time-wise since the registers are the fastest memory that can be accessed in a GPU. In order to do that the size of them as well as their indices in the array needs to be known at the compile time. Moreover, there need to be sufficient registers for all variables that need to be stored. The number of available registers per thread is constrained by the number of threads per block. If there is not enough registers available variables need to be stored in the global memory which slows down the execution. Therefore, the number of threads for the algorithms of the seeding is also optimised to match the number of registers with the requirements. For that, the choice of the block size is crucial.
Both algorithms of the seeding need a shared memory of around 8 kB per block to store the relevant hits of an event. This corresponds to four warps and 128 threads per block which is large enough to efficiently process hits and seed candidates. A profiling of the memory usage is performed to identify potential flaws in the occupancy. This also confirms the choice of the block size to have enough but not too many registers per thread. A check for very busy events where the hits do not fully fit into the shared memory is performed. In these infrequent cases, hits need to be accessed from the global memory.

Since the fixed size of intermediate and final arrays where track candidates are stored needs to be known at compile time, it is essential to make them not too small. A problem of non-determinism that can arise from that lies in the nature of how processes are launched in the GPU. The order in which threads are launched is non-controllable and non-deterministic. If the number of *e.g.* reconstructed tracks is larger as their output container, not only the efficiency of the track reconstruction decreases but also the exact tracks that will be reconstructed changes since the order of threads that write to the output array will also be non-deterministic.
Another important feature of the GPU implementation of the *Seeding & Matching* is the way it is parallelised. For the seeding in the xz-plane an important aspect of the GPU implementation is the in-depth processing of candidates in one thread. This means that the building of two-hit and three-hit combinations as well as adding remaining hits is performed in the same kernel. This avoids saving the enormous amount of combinatorics of two-hit and three-hit combinations into memory. Moreover, due to the tight search window sizes the amount of combinatorics for hits to be considered rapidly decreases with every added hit. While there are around 300 first hits in the initial layer, around 20-40 two-hit combinations per first hit and 0.05-0.3 three-hit combinations per two-hit combination need to be iterated over. Therefore, an extra parallelisation for *e.g.* the adding of the remaining hits would not necessarily give improvement in the throughput as threads will be less occupied.

3.11.1 Computing performance

The throughput of the HLT1 sequence with the track reconstruction performed by the *Seeding & Matching* approach is evaluated by running over 1000 simulated minimum bias events and shown in Figure 3.23 for different GPU and CPU cards. On the NVIDIA RTX A5000 GPU cards, which are installed in the EB nodes of the LHCb data acquisition system, the throughput is around 170 kHz. Since there are about $\mathcal{O}(200)$ of these cards used for HLT1 in Run 3 this matches well with the total throughput requirement of 30 MHz for HLT1. Figure 3.24 shows a breakdown of the throughput into the three tracking algorithms and additional other algorithms of the sequence for the same GPU and CPU cards. It is clearly visible that the SciFi Seeding has the largest contribution which is mainly given by the hit combinatorics in xz-part of the seeding.

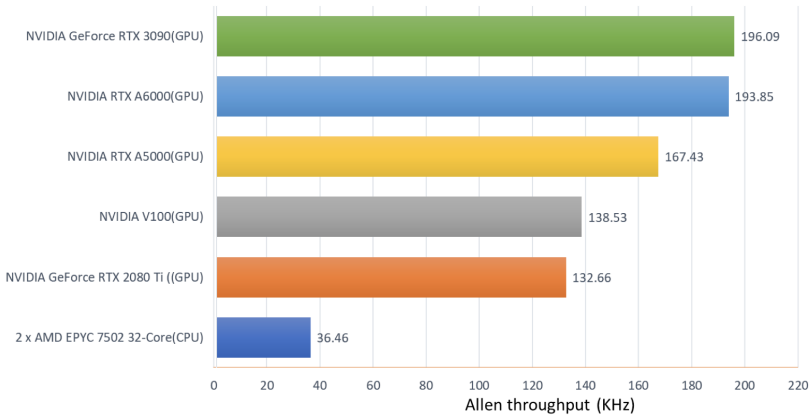

Figure 3.23: Throughput of the HLT1 sequence with the *Seeding & Matching* approach as the VeloSciFi track reconstruction algorithm for different GPU and CPU architectures. The GPU block and thread configuration is optimised for the NVDIA RTX A5000 GPU card. Taken from Ref. [127].

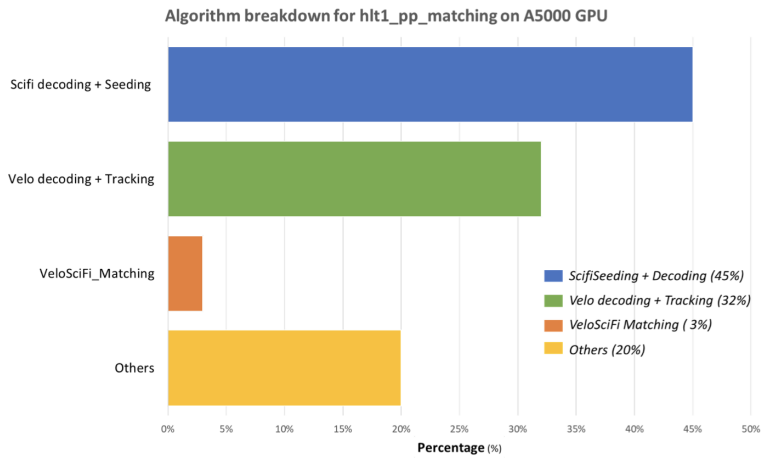

Figure 3.24: Breakdown of throughput into the three main tracking and other algorithms of the HLT1 sequence with the *Seeding & Matching* approach as the VeloSciFi track reconstruction algorithm for different GPU and CPU architectures. Taken from Ref. [127].

3.12 Conclusions and Outlook

As part of this thesis the *Seeding & Matching*, a new long track reconstruction, has been developed for the first trigger stage of the upgraded LHCb trigger system, HLT1. It is an alternative to the baseline track reconstruction, the *forward tracking*, and runs without hits from the UT detector, whose installation is delayed for the start of Run 3. The algorithm is based on the *Seeding & Matching* for HLT2 [124] and adapted for HLT1. The key differences to the HLT2 implementation lie in

- the reduced number of iterations that are run for the pattern recognition for the seeding in the xz-plane.
- only considering one minimal momentum for the pattern recognition, which avoids a hit flagging between the iterations.
- a redesign of the seeding in the yz-plane based on search windows in t_y instead of a Hough cluster search.
- a simplification of the matching algorithm that does not use a neural network to decide on the best matching candidate between SciFi seeds and VELO tracks.

Further minor changes have been made to increase the throughput of *Seeding & Matching* algorithm sequence to meet the available budget for HLT1. In addition, the memory handling and parallelisation of the *Seeding & Matching* algorithms have been optimised by using of shared memory and a deep processing, *i.e.* building all the intermediate hit combinations, of a track seed with same thread instead. The physics and computing performances are compatible with the baseline *forward tracking* algorithm for HLT1 [116] that can make use of hits from the UT detector. The total track reconstruction efficiencies are found at about 83 (92) % for long tracks (with $p > 5\,\mathrm{GeV/c}$) from b-hadron decays and about 70 (75) % for electrons (with $p > 5\,\mathrm{GeV/c}$) from b-hadron decays reconstructed as long tracks. With respect to the *forward tracking* tracking the *Seeding & Matching* is a bit more efficient at low-p and p_T. The total ghost rate is with about 10 % about twice as high as for the *forward tracking*. Efforts for improving the ghost rate are currently ongoing by looking for better parameter configuration of the χ^2_match. For the future studies of a neural network approach for the matching, similar to the one used in HLT2, is foreseen. A simplification of the neural network used in HLT2 is necessary to match the memory resources of HLT1. The *Seeding & Matching* is currently being commissioned with Run 3 data as the main tracking algorithm in HLT1.
Extensions of the *Seeding & Matching* towards track reconstructions for SM measurements (*e.g.* branching fractions of $K^0_\mathrm{S} \to \mu^+\mu^-$, $\Lambda^0_b \to \Lambda^0\gamma$, electric dipole

moment of baryons from polarized Λ^0, Λ_c^+ or Ξ_c^+ hadrons) and BSM searches (such as Higgs extensions as dark matter portals in $B \to H'(\to \ell + \ell -)K^{(*)}$ decays [128]) involving long-lived particle decays are currently being made [129]. They would extremely profit from having a downstream or standalone T track reconstruction.
Efforts for a downstream track reconstruction, once the UT detector is installed, with unmatched SciFi seeds is ongoing. Two approaches, depicted in Figure 3.25, are investigated. The first performs a standalone UT track reconstruction by looking for seeds with four hits in the layers of the UT. The UT seeds can then be matched to SciFi seeds with a matching algorithm similar to the one used for matching SciFi seeds and VELO tracks discussed above. Preliminary tests of this implementation show promising tracking efficiencies for particles that have originated from a vertex downstream of the VELO, but the throughput of the algorithms is far from a possible application in HLT1. A possible solution for this could be to run the UT seeding

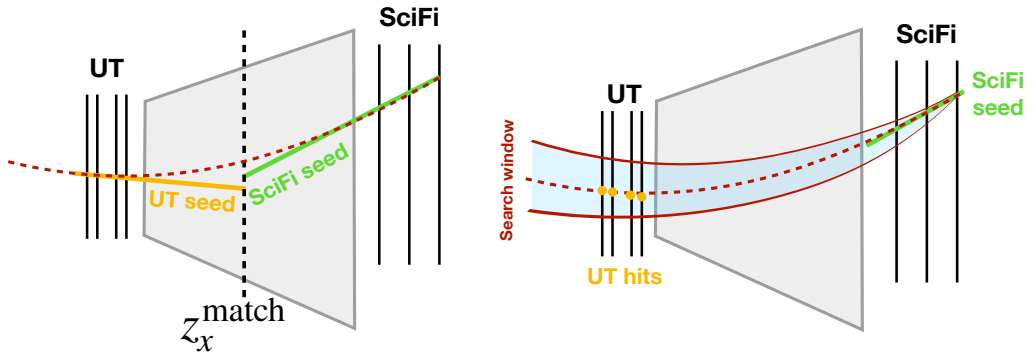

(a) Seeding approach **(b)** HLT2 approach

Figure 3.25: Sketches of the two possible approaches for a downstream track reconstruction in HLT1.

after the long track reconstruction (either the *Seeding & Matching* or the *forward tracking*) and only use UT hits that have not been used previously for long tracks. A second approach is motivated by the downstream tracking in HLT2, where SciFi seeds are propagated upstream of the magnet and additional hits from the UT are looked for by predefined search windows. Also here, only previously unused UT hits are considered.
In addition, SciFi seeds that have neither been used for long tracks nor for downstream tracks can be used as standalone track type, a T track. The major challenge for reconstructing decays from multiple T tracks is the vertexing far from the interaction point, that is currently been developed both for HLT1 and HLT2.

Chapter 4

Strangeness production in Run 3

This chapter describes the preparations performed for early Run 3 measurements of production cross-section ratios with K^0_S and $\Lambda^0/\bar{\Lambda}^0$ hadrons that are based on performing an equivalent analysis on Run 2 data. The chapter is structured as follows. The strategy of the measurement is introduced in the sections 4.1-4.3. Sections 4.4-4.6 explain the used data and simulation samples. They are followed by a description of the fitting procedure and the development of a candidate selection in sections 4.7 and 4.8. Section 4.9 describes the crossing angle correction applied to V^0 candidates. Finally, sections 4.10-4.14 cover the final steps of the analyses such as the fits to the invariant mass distributions and the efficiency calculations before the results for the production cross-section ratios are calculated. Section 4.15 then concludes the chapter and gives an outlook for the Run 3 measurement.

4.1 V^0 particles

Neutral hadrons that decay into two charged hadrons and have a significant lifetime such that the vertex built by their decay products is often found to be very displaced from the collision region are called V^0 particles due to their V-shaped signature in the detector. The most common V^0 particles are K^0_S, Λ^0 and $\bar{\Lambda}^0$ hadrons. As discussed previously in section 1.3, V^0 particles are produced very abundantly at the LHC due to their large cross-sections. Furthermore, they can be reconstructed with a simple selection in the tree-level weak decay channels $K^0_S \to \pi^+\pi^-$ and $\Lambda^0 \to p\pi^-$ that have large branching fractions [5]: $\mathcal{B}(K^0_S \to \pi^+\pi^-) = 0.6920 \pm 0.0005$ and $\mathcal{B}(\bar{\Lambda}^0 \to \bar{p}\pi^+) = 0.639 \pm 0.005$. Therefore, they are ideal candidates to perform early calibration studies with the upgraded LHCb detector in Run 3. In addition, LHCb has an unique geometrical acceptance in the forward region ($2 < \eta < 5$) and is therefore well suited to perform measurements of V^0 production at the LHC complementary to those of the central detectors. Production cross-section

measurements of forwardly produced particles are an important input for astroparticle studies of cosmic ray showers. In particular, measurements of strangeness production can help in understanding the *muon puzzle* which refers to the observed discrepancy on the amount of produced muons when high-energetic ($E > 1\,\text{TeV}$) cosmic rays interact with the earth's atmosphere with respect to what is expected by current air shower models [130]. Knowing precisely the abundance of muons in these shower events is essential to estimate the total mass of the cosmic ray shower. The discrepancy could potentially be explained by higher production cross-sections for strange hadrons in the forward region than what is modeled by current QCD generators. Since the effect of the muon deficit is observed from the TeV scale onwards, the LHC, and particularly LHCb, is ideal to better understand the production cross-section of strange hadrons in the forward region. Moreover, studying ratios of V^0 production cross-sections is of interest for soft-QCD predictions and can help to model the measured baryon-meson suppression [131], that is defined as the production cross-section ratio of a baryon over a meson of same charge with the same amount of (s, c, b) quarks but different amount of u, d quarks.

4.2 Analysis strategy

The analysis described here is designed to understand the early data that will be taken with the new detector and to accurately measure ratios of V^0 production cross-sections. The production cross-section for a V^0 can be calculated using

$$\sigma(pp \to V^0 X) = \frac{N(V^0 \to h^+ h^{(\prime)-})}{\varepsilon_{V^0 \to h^+ h^{(\prime)-}} \mathcal{B}(V^0 \to h^+ h^{(\prime)-}) \mathcal{L}}, \tag{4.1}$$

where $N(V^0 \to h^+ h^{(\prime)-})$ defines the yield of found $V^0 \to h^+ h^{(\prime)-}$ decays, $\varepsilon_{V^0 \to h^+ h^{(\prime)-}}$ the total efficiency of reconstructing and selecting them, $\mathcal{L}$ the integrated luminosity of the used data sample and $\mathcal{B}(V^0 \to h^+ h^{(\prime)-})$ the branching fraction of a V^0 decaying to the two charged hadrons $h^+ h^{(\prime)-}$ ($\pi^+\pi^-$ in case of the K^0_S, $p\pi^-$ in case of the Λ^0 and $\bar{p}\pi^+$ in case of the $\bar{\Lambda}^0$). Constructing the ratios of the Λ^0, $\bar{\Lambda}^0$ and K^0_S cross-sections, one obtains

$$R(\bar{\Lambda}^0, K^0_\text{S}) = \frac{\sigma(pp \to \bar{\Lambda}^0 X)}{\sigma(pp \to K^0_\text{S} X)} = \frac{N(\bar{\Lambda}^0 \to \bar{p}\pi^+) \varepsilon_{K^0_\text{S} \to \pi^+\pi^-} \mathcal{B}(K^0_\text{S} \to \pi^+\pi^-)}{N(K^0_\text{S} \to \pi^+\pi^-) \varepsilon_{\bar{\Lambda}^0 \to \bar{p}\pi^+} \mathcal{B}(\bar{\Lambda}^0 \to \bar{p}\pi^+)} \tag{4.2}$$

and

$$R(\bar{\Lambda}^0, \Lambda^0) = \frac{\sigma(pp \to \bar{\Lambda}^0 X)}{\sigma(pp \to \Lambda^0 X)} = \frac{N(\bar{\Lambda}^0 \to \bar{p}\pi^+) \varepsilon_{\Lambda^0 \to p\pi^-}}{N(\Lambda^0 \to p\pi^-) \varepsilon_{\bar{\Lambda}^0 \to \bar{p}\pi^+}} \tag{4.3}$$

since the integrated luminosity cancels. Measuring the ratios of cross-sections therefore has the advantage to be independent of a precise luminosity measurement which will not be available immediately at the beginning of the data taking in Run 3. The strategy for the preparation of the measurement with early Run 3 data is to find a minimal selection for the V^0 candidates for which the efficiency can be reliably estimated once the data is taken. Therefore, the analysis framework is fully developed on the 2018 NoBias data set that has been introduced previously in section 2.2.6.3 and has the most similar run conditions of all previously taken data sets to the ones for Run 3. The measurement on Run 2 also delivers a reference that the Run 3 results can be cross-checked to.

4.3 Previous measurements

Production cross-sections of V^0 particles and ratios of them have been previously measured in pp-collision at LHCb with Run 1 data at $\sqrt{s} = 0.9\,\text{TeV}$ and $\sqrt{s} = 7\,\text{TeV}$ [97, 131]. In addition, the ALICE collaboration measured cross-sections of various strange hadrons at 13 TeV [132]. In both cases, the measurements were performed as function of the transverse momentum p_T and rapidity y. The ALICE collaboration also studied the multiplicity dependence of multi-strange hadron (K^0_S, Λ^0, Ξ, Ω) production cross-sections [133]. The ratios $R(\bar{\Lambda}^0, K^0_\text{S})$ and $R(\bar{\Lambda}^0, \Lambda^0)$ measured on the Run 1 LHCb data at $\sqrt{s} = 7\,\text{TeV}$ are used later in section 4.15 for a comparison with the measurement performed in this thesis on the 2018 Run 2 data.

4.4 Data samples

The analysis uses the full data set collected in pp-collisions at $\sqrt{s} = 13\,\text{TeV}$ from 2018 which corresponds to an integrated luminosity of $\mathcal{L} = 2.1\,\text{fb}^{-1}$. Data are collected in the two polarities of the LHCb dipole's magnetic field *MagDown* and *MagUp*. Collected events of this data set have passed the NoBias trigger lines in HLT1 and HLT2, that serve as pass-through lines. This means that random events are selected to be stored without any selection requirements which allows for completely unbiased measurements. The default prescales for the NoBias trigger in HLT1 and HLT2 are 0.1 and 0.025. However, they have been loosened during the 2018 to speed up the collection of a calibration sample for the ECAL while running in magnet polarity *MagUp*. Therefore, the *MagUp* sample is much larger than the *MagDown* sample. The amount of events collected of the two polarities is not equal

but given by

$$N_{\text{events}}^{MagDown} = 23889958 \qquad \text{and} \qquad N_{\text{events}}^{MagUp} = 33974066. \tag{4.4}$$

The difference in size of the *MagDown* and *MagUp* datasets is later used to build weighted averages of the measurements in the two polarites to obtain the final result. K_S^0 candidates are build by combining two oppositely-charged reconstructed long (LL-reconstructed sample) or downstream (DD-reconstructed) tracks (see section 2.2.2 for the track type definitions), where the nominal mass of a charged pion was assigned to them. For Λ^0 candidates one track is given the proton mass instead of a pion mass. In both cases V^0 candidates are required to have an invariant mass within $50\,\text{MeV/c}^2$ of their nominal mass.

4.5 Simulation samples

Simulated Minimum bias events are used for efficiency calculations and studies of systematic uncertainties. They correspond to a total amount of 50 million events per magnet polarity. Two types of samples are produced running over the same simulated data set. The first is run through the full offline reconstruction as it is done for data and serves as the sample to calculate selection efficiencies. The second contains only the generator-level information which means that no tracks are reconstructed yet and only the simulated particles are part of the sample. By taking the ratio of reconstructed V^0 candidates from the first sample and simulated V^0 from the second sample, the efficiency of the reconstruction can be estimated. To know which of the reconstructed candidates are actual V^0 hadrons the simulation samples have to be truth-matched. The truth-matching strategy is explained in the following section.

4.6 Truth matching

A truth matching strategy is applied to simulated events to obtain a signal-only sample that can be used for the efficiency calculations as well as for the development of a candidate selection. For the truth matching each particle in the decay chains of the V^0 candidates is required to be assigned to the correct unique identification number (ID) from the Monte Carlo numbering scheme of the PDG [5], the `TRUEID`. Similarly, for the first three generations of ancestors of a particle the IDs are referred to as `MOTHER_ID`, `GD_MOTHER_ID`, `GD_GD_MOTHER_ID`. For prompt V^0 particles all of them are required to be 0, which stands for particles that directly originated from

the *pp*-collision. Prompt candidates are kept as signal for the truth matching. Figure 4.1 shows the frequency of different parent particles for $\Lambda^0/\bar{\Lambda}^0$ and K^0_S candidates in the two track type categories LL and DD. Apart from V^0 that are directly produced in the primary proton-proton collision, candidates originating from short-lived strong or electromagnetic decays are kept as signal as well, since they cannot be separated from promptly produced candidates in data. Furthermore,

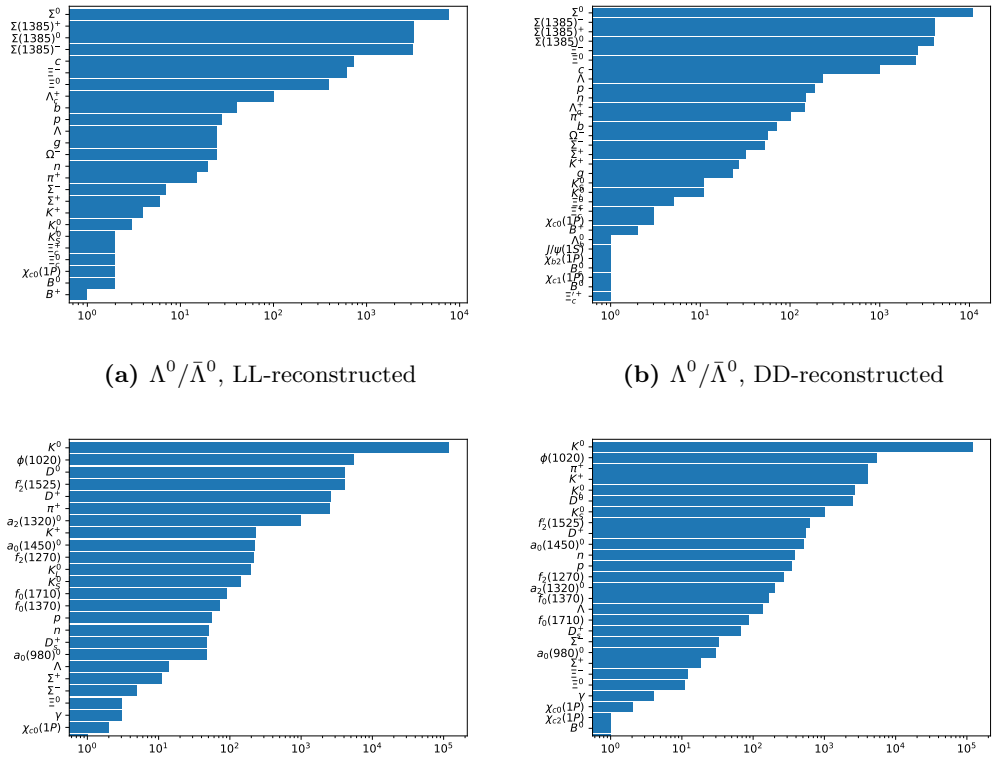

(a) $\Lambda^0/\bar{\Lambda}^0$, LL-reconstructed

(b) $\Lambda^0/\bar{\Lambda}^0$, DD-reconstructed

(c) K^0_S, LL-reconstructed

(d) K^0_S, DD-reconstructed

Figure 4.1: Frequency of different species of particles as parent particles to $\Lambda^0/\bar{\Lambda}^0$ and K^0_S in the two track type categories. All distributions are shown for 100000 simulated NoBias events where each particle is assigned to an unique identification number. Prompt V^0 particles are not shown. The x-axis is on a logarithmic scale.

there can be V^0 particles originating from weak decays of long-lived particles. These secondary contributions are a background to the prompt production, that needs to be estimated or suppressed during the signal extraction. Since decay products of weak decays have a larger displacement from the collision point, they can be suppressed by applying a selection to the Impact Parameter (IP) of the V^0 candidate

with respect to its associated PV. To investigate the separation between prompt and secondary V^0 candidates, an additional truth matching for secondary contributions is developed to obtain a sample consisting of V^0 hadrons coming only from weak decays.
For secondary $\Lambda^0/\bar{\Lambda}^0$ candidates the IDs for the truth matching are derived from Figure 4.1. It can be observed that the dominant long-lived contributions are coming from $\Xi^-(\to \Lambda^0\pi^-)$ and $\Xi^0(\to \Lambda^0\pi^0)$ hyperons. For K^0_S candidates there is no similar contribution. For all V^0 particles there is an additional small secondary contribution from charm decays. For Λ^0 these are originating from $\Lambda_c^+(\to \Lambda^0\pi^+, \to \Lambda^0\pi^+\pi^0, \to \Lambda^0\rho^+, \to \Lambda^0 3\pi)$ decays. For K^0_S candidates they are coming from D^0 or D^+ decays and are found to be a small effect. The suppression of the contributions from non-prompt weak decays is discussed in section 4.8.2. The truth matching strategy is summarised in Table 4.1.

Table 4.1: Unique identifiers from the PDG Monte Carlo numbering scheme [5] for the truth matching strategy applied to the decay chains of $K^0_S \to \pi^+\pi^-$ and $\Lambda^0 \to p\pi^-$ decays. For secondary V^0 contributions from weakly decaying hadrons a separate truth matching is developed. For all contributions charge conjugation is implied and the `TRUEID` is require to match to the one of the V^0 candidate. The `MOTHER_ID`, `GD_MOTHER_ID` and `GD_GD_MOTHER_ID` correspond to the IDs of the ancestors of the V^0 candidate.

	V^0	contribution	`MOTHER_ID`	`GD_MOTHER_ID`	`GD_GD_MOTHER_ID`
short-lived	Λ^0	$\Sigma^0 \to \Lambda^0\gamma$	3212	0	0
		$\Sigma^{*0} \to \Lambda^0\pi^0$	3214	0	0
		$\Sigma^{*\pm} \to \Lambda^0\pi^\pm$	3224	0	0
		$\Sigma^{*\pm} \to \Sigma^0(\to \Lambda^0\gamma)\pi^\pm$	3212	3224	0
	K^0_S	$K^*(892)^\pm \to K^0\pi^\pm$	311	313	0
		$K^*(892)^0 \to K^0\pi^0$	311	323	0
		$\phi(1020) \to K^0_S K^0_L$	333	0	0
		$f_2'(1525) \to K^0_S K^0_L$	335	0	0
secondary	Λ^0	$\Xi^0 \to \Lambda^0\pi^0$	3322	0	0
		$\Xi^- \to \Lambda^0\pi^-$	3312	0	0
		$\Lambda_c^+ \to \Lambda^0 X$	4122	4	0
	K^0_S	$D^{*0} \to D^0(\to K^0_S X)X$	421	423	4
		$D^{*+} \to D^0(\to K^0_S X)\pi^+$	421	413	4
		$D^{*+} \to D^+(\to K^0_S X)\pi^0$	411	413	4
		$D^+ \to K^0_S X$	411	4	0

4.7 Invariant mass fits

Fits to the invariant mass distributions of V^0 candidates are performed to measure signal yields in various steps of the analysis. All fits are performed as unbinned extended maximum-likelihood fits and make use of the same fitting model described in the following section. A fitting procedure consisting of five different steps is developed to make the fitting stable and flexible for all its applications in this analysis.

4.7.1 Fitting model

The fitting model used for the V^0 invariant mass distributions consists of two probability density functions (PDFs): one for the description of the signal mass peak and a second for the description of the background. The signal PDF parametrises the mass peaks of K^0_S and $\Lambda^0/\bar{\Lambda}^0$ candidates that is predominantly determined by a resolution function since the natural width of V^0 particles is negligibly small with respect to the detector's mass resolution. A well established parametrisation of the resolution function in LHCb is the double-sided Crystal Ball [134] function given by

$$f(x,\mu,\sigma,n_1,n_2,\alpha_1,\alpha_2) = \begin{cases} A_1(B_1 - \frac{x-\mu}{\sigma})^{-n_1}, & \text{for } \frac{x-\mu}{\sigma} < -\alpha_1 \\ \mathrm{e}^{-\frac{(x-\mu)^2}{2\sigma^2}}, & \text{for } -\alpha_1 < \frac{x-\mu}{\sigma} < \alpha_2 \\ A_2(B_2 - \frac{x-\mu}{\sigma})^{-n_2}, & \text{for } \frac{x-\mu}{\sigma} > \alpha_2 \end{cases} \tag{4.5}$$

with

$$A_i = \left(\frac{n_i}{|\alpha_i|}\right)^{n_i} \mathrm{e}^{-\frac{|\alpha_i|^2}{2}} \qquad \text{and} \qquad B_i = \frac{n_i}{|\alpha_i|} - |\alpha_i| \tag{4.6}$$

The double-sided Crystal Ball function uses a Gaussian distribution as its core, and two power-law functions for the tails, each characterised by the two tail parameters α_i and n_i. The parameter α_i defines how far from the mean value μ the transition from the Gaussian to the power-law tail is made. The parameter n_i is a free parameter of the power-law distribution. For the background PDF, a linear function is used. The PDF of the full fitting model is then given by the linear combination of the signal and background PDFs, each entering with the free multiplicative parameters N_{sig} and N_{bkg} for the signal and background yields.

4.7.2 Fitting procedure

The fitting procedure that performs the invariant mass fits of the V^0 candidates consists of five steps:

1. Fit the signal PDF to the truth-matched simulation sample to estimate the values of the fitting parameters, in order to have good starting values for the subsequent fit to data.
2. Fit the background PDF to the sidebands of the distribution on data to have an estimate for the background parameters.
3. Fit the full model to the data with fixed values of α_i and n_i to the ones obtained on simulation and fixed background parameters to estimate good starting values for μ and σ.
4. Fit the full model again with floating background parameters but fixed α_i and n_i.
5. Fit the full model again with all parameters floating. If the the average value of the pulls improves with respect to step 4 the fit parameters are taken from here, otherwise they are taken from step 4. This is decided based on the number of bins where the pull shows disagreement between data points and the fit larger than 3σ.

An example of the five steps is visualised in Figure 4.2. The fitting procedure is used for the fits in the optimisation of the $\mathcal{F}_{\text{IP}}$ selection in section 4.8.3, the invariant mass fits of the full p_{T} and y ranges in section 4.8.5 and the fits to the invariant mass distributions in the p_{T} and y bins from which the final signal yields for the production cross-section ratio measurement are extracted.

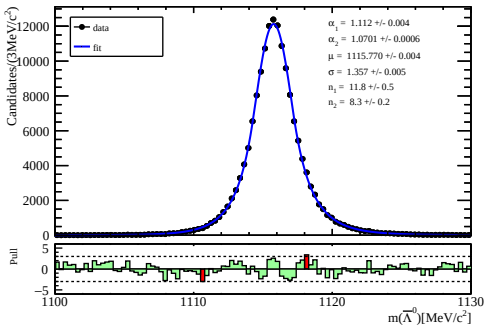

(a) Step 1

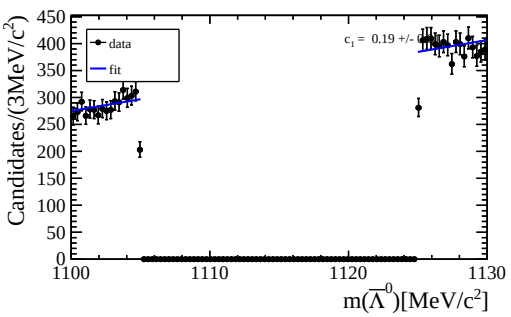

(b) Step 2

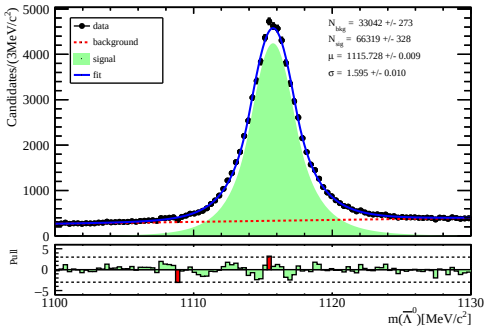

(c) Step 3

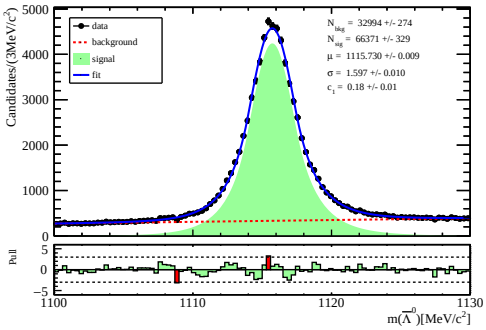

(d) Step 4

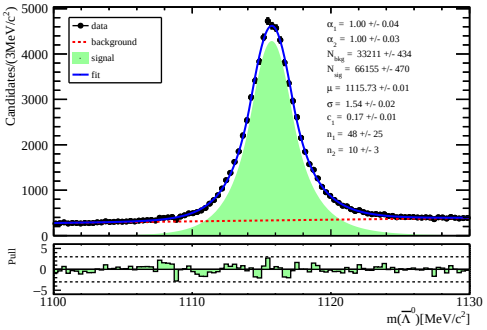

(e) Step 5

Figure 4.2: Invariant mass distributions of DD-reconstructed $\bar{\Lambda}^0$ hadrons with $3 < y < 3.5$ for the five steps of the fitting procedure. Step 1 is fitted on simulated events, whereas all other steps are performed on data.

4.8 Candidate selection

In contrast to data for regular LHCb analyses, the data from the NoBias trigger do not have any pre-selection applied online to the candidates. Therefore, the plots in Figure 4.3 show the bare output built of the tracks from the offline reconstruction, that were given mass hypotheses of pions and protons, and combined to build a common vertex to form $K^0_S \to \pi^+\pi^-$ and $\Lambda^0 \to p\pi^-/\bar{\Lambda}^0 \to \bar{p}\pi^+$ candidates. While

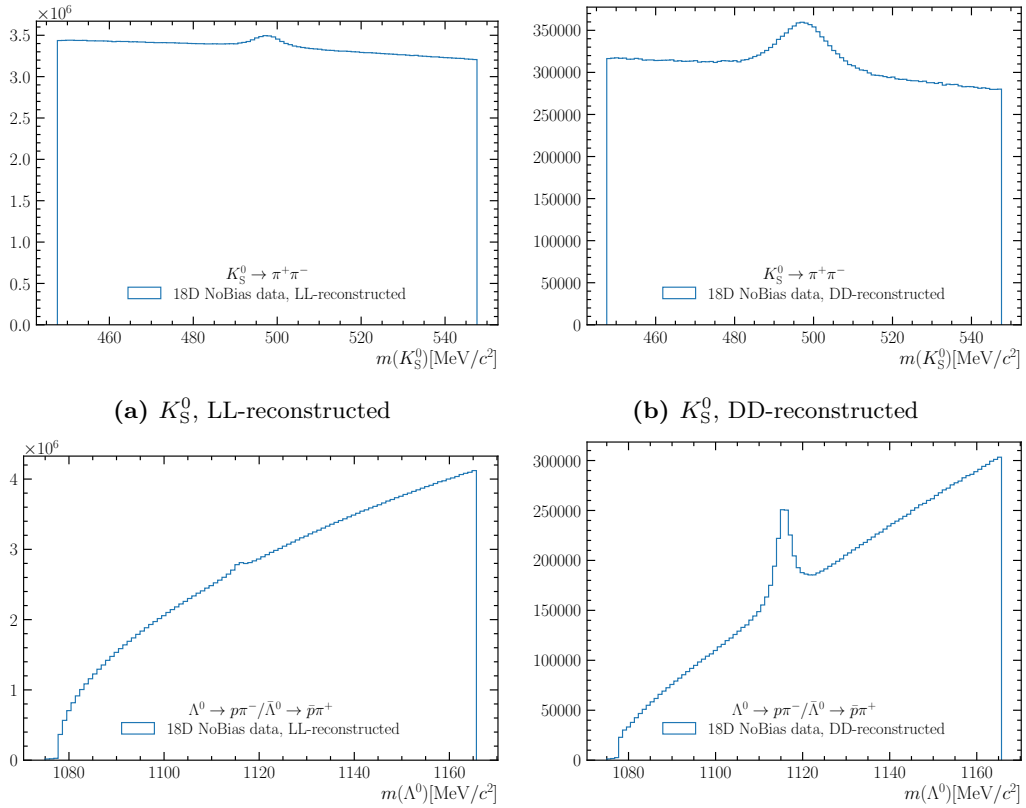

(a) K^0_S, LL-reconstructed

(b) K^0_S, DD-reconstructed

(c) Λ^0 & $\bar{\Lambda}^0$, LL-reconstructed

(d) Λ^0 & $\bar{\Lambda}^0$, DD-reconstructed

Figure 4.3: Invariant mass distributions for LL- and DD-reconstructed K^0_S and $\Lambda^0/\bar{\Lambda}^0$ hadrons directly plotted from the NoBias trigger output. No event selection is applied other than the invariant masses required to be within 50 MeV/c^2 of the nominal K^0_S or Λ^0 masses. All plots are shown for magnet polarity MagDown.

in the distribution of LL-reconstructed K^0_S candidates a hint of a peak at the nominal K^0_S mass is already visible, the Λ^0 is hidden behind the large amount of combinatorial

background coming from tracks produced in the *pp*-collision and pointing back to the interaction region. In the invariant mass distributions of the DD-reconstructed candidates peaks are both visible for K^0_S and Λ^0 as the combinatorial background is smaller due to a reduced amount of random tracks matching the displaced decay topology. The next sections describe the development of a candidate selection for the production cross-section ratio measurement of K^0_S and Λ^0 hadrons with early Run 3 data. Section 4.8.1 describes the search for a minimal set of variables, sections 4.8.4 and 4.8.2 the suppression of backgrounds from particle mis-identification and non-prompt V^0 decays. In section 4.8.3 the optimisation of IP-based selection is outlined.

4.8.1 Minimal selection for early Run 3 data

Studying the performance of the LHCb upgrade I detector and validating its simulation with early Run 3 data requires selections to be based on low-level variables that are easy to understand but resulting in a good signal to background ratio that allows to perform fits to the invariant masses of the V^0 candidates stably. Therefore, the IPs of the V^0 and its children particle are combined in section 4.8.3 to a single variable that is used for the candidate selection. The necessary statistical

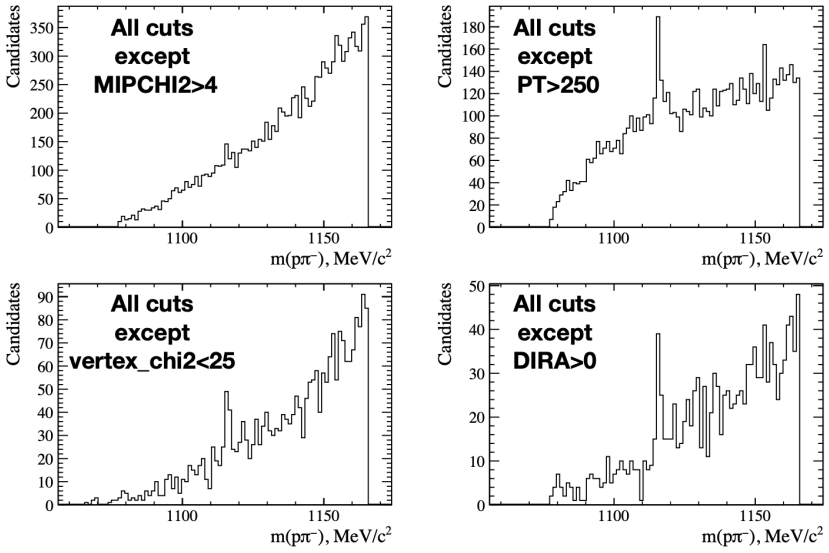

Figure 4.4: Invariant mass distributions of LL-reconstructed Λ^0 candidates from simulated Minimum Bias events with Run 3 conditions. Different selections using typical selection variables are applied each leaving out one of the variables. A Λ^0 peak is visible in all distributions except for the one not using a selection on the IP.

power needed for measuring the cross-section ratios can be easily recovered by taking data for a few days more or altering the prescale of the NoBias trigger. Typical selection variables for V^0 hadrons such as $\min(\chi^2_{\mathrm{IP}}(p, \pi^{\pm})) > 4$, $p_{\mathrm{T}}(V^0) > 250\,\mathrm{MeV/c}$, $\chi^2_{\mathrm{vtx}}(V^0) < 25$ and $\cos(\theta_{\mathrm{DIRA}}) > 0$ are studied on simulated events under Run 3 conditions to find a minimal selection. The χ^2_{IP} of a given track with respect to a given vertex is a measure of how likely it is for a track to have originated from a that vertex by looking at the difference of the χ^2 of the vertex fit with and without the track. For the selections developed, the IP/χ^2_{IP} are always considered with respect to the associated PV to V^0 candidate. The $\chi^2_{\mathrm{vtx}}(V^0)$ stands for the quality of the vertex fit of the V^0, *i.e.* how well the two tracks agree to come from a common vertex. The direction angle $\theta_{\mathrm{DIRA}}(V^0)$ is defined as the angle between momentum vector of the V^0 and the straight line connecting the vertex of the V^0 with its associated PV. An example of this study is shown in Figure 4.4 for LL-reconstructed Λ^0 candidates. For each distribution one of the variables is removed from the selection. Only in the one with the removed criterion on the $\min(\chi^2_{\mathrm{IP}}(p, \pi^{\pm}))$ no Λ^0 mass peak is visible. Instead of the χ^2_{IP}, the IP itself is looked at since the IP resolution and χ^2_{IP} need to be studied and compared to the simulated values to not introduce biases in the efficiency calculation, whereas the IP is more likely to be modelled correctly by the simulation. Nevertheless, potential residual biases from a mis-modelling of the IP distributions need to be studied on the first Run 3 data. The IP is found

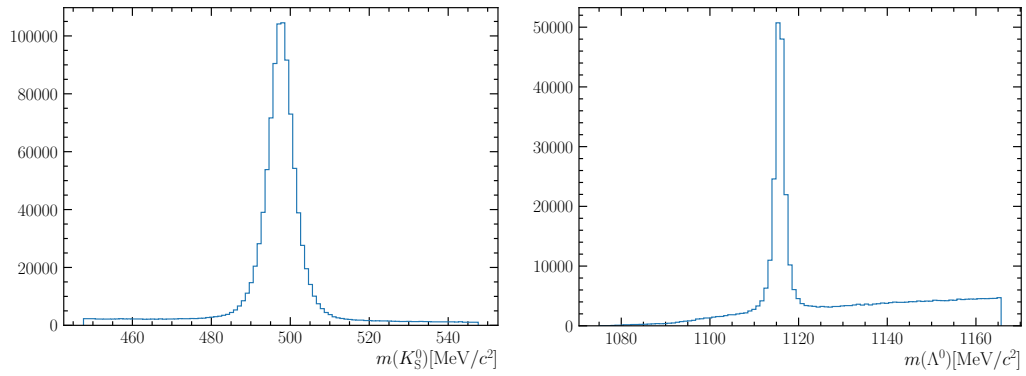

(a) K^0_{S} **(b)** $\Lambda^0/\bar{\Lambda}^0$

Figure 4.5: Invariant mass distributions of LL-reconstructed $V^0 = K^0_{\mathrm{S}}, \Lambda^0, \bar{\Lambda}^0$ candidates with a simple IP selection $(\mathrm{IP}(V^0) < 0.2, \mathrm{IP}(h^+) > 0.5, \mathrm{IP}(h^{(\prime)-}) > 0.5)$ applied. The plots are shown for the full *MagDown* data sample.

to be a powerful single variable to fully base the selection on. A simple selection $(\mathrm{IP}(V^0) < 0.2, \mathrm{IP}(h^+) > 0.5, \mathrm{IP}(h^{(\prime)-}) > 0.5)$ on the three IPs of a V^0 and its two children particle already demonstrates a strong suppression of the combinatorial background as can be seen from Figure 4.5. The power of an IP-based selection can

be seen by comparing Figure 4.5 to the distributions in Figure 4.3. An optimisation of the IP-based selection is discussed later in section 4.8.3.

4.8.2 Background from non-prompt decays

Apart from short-lived contributions to the production of V^0 hadrons that were discussed in section 4.6, there can also be long-lived contributions originating from weak decays. The dominant weak decay modes can be derived from the secondary contributions in Table 4.1. For both the K^0_S and $\Lambda^0/\bar{\Lambda}^0$ contributions from charm decays (D^0, D^+, Λ_c^+) are present. In the case of the $\Lambda^0/\bar{\Lambda}^0$ additional contributions from weakly decaying hyperons ($\Xi^- \to \Lambda^0\pi^-$, $\Xi^0 \to \Lambda^0\pi^0$) are dominating the background from secondary particles.
The two types of secondary contributions differ from each other in their lifetime as can be seen in Table 1.2. Moreover, the production cross-sections of hyperons are higher than the ones of charm hadrons. While the lifetimes of charm hadrons are smaller than the ones of the the V^0, the lifetimes of the Ξ^- and Ξ^0 hadrons are in the same order of magnitude as the one of the $\Lambda^0/\bar{\Lambda}^0$, which results in a more displaced decay vertex of the $\Lambda^0/\bar{\Lambda}^0$ than for $\Lambda^0/\bar{\Lambda}^0$ coming from charm decays. This is shown in the z_{vertex} distributions in the right column of Figure 4.6. As there is no contribution with such a displaced vertex in the case of the K^0_S, the production cross-section ratio $R(\bar{\Lambda}^0, K^0_S)$ is biased if no correction is applied for these non-prompt contributions. Furthermore, differences between the LL- and DD-reconstructed samples can be reduced by removing the contributions from non-promptly produced $\Lambda^0/\bar{\Lambda}^0$ hadrons. In addition, the choice of the model used to fit the invariant mass distributions of the V^0 candidates does not take into account contributions from non-prompt V^0, which could lead to instabilities if the non-prompt fraction is significantly large. Table 4.2 shows the fractions of all V^0 candidates that originated from the different weak decay modes.

Table 4.2: Fractions f_{LL} and f_{DD} of LL- and DD-reconstructed V^0 candidates that originated from non-prompt weak decays before the IP selection is applied.

V^0	non-prompt contribution	f_{LL}	f_{DD}
Λ^0	$\Xi^- \to \Lambda^0\pi^-$	1.7 %	5.2 %
	$\Xi^0 \to \Lambda^0\pi^0$	1.0 %	5.1 %
	$\Lambda_c^+ \to \Lambda^0 X$	0.2 %	0.2 %
	total	2.9 %	10.5 %
K^0_S	$D^{+,0} \to K^0_S X$	0.9 %	1.4 %

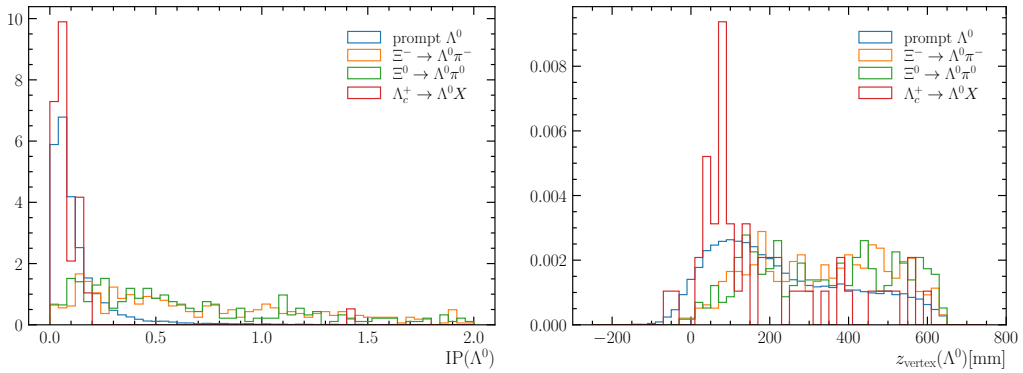

(a) IP(Λ^0), LL-reconstructed

(b) $z_{\text{vertex}}(\Lambda^0)$, LL-reconstructed

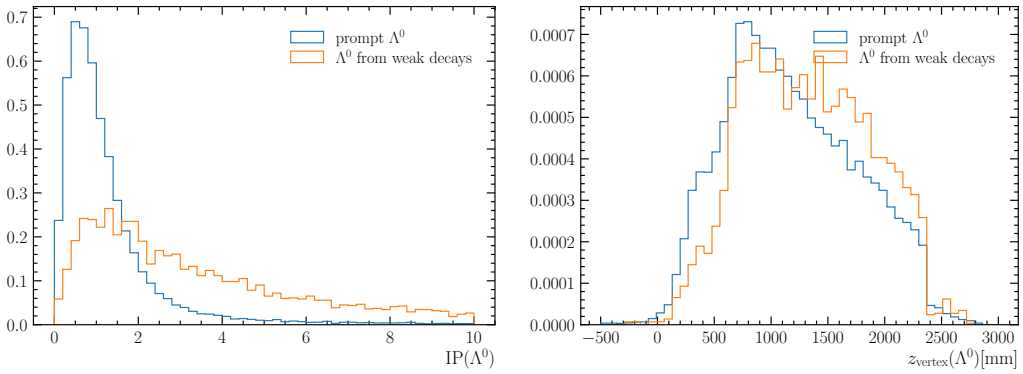

(c) IP(Λ^0), DD-reconstructed

(d) $z_{\text{vertex}}(\Lambda^0)$, DD-reconstructed

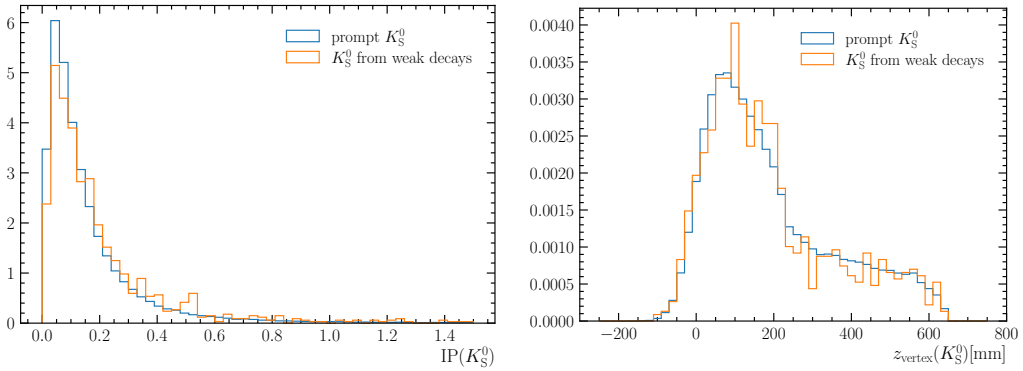

(e) IP(K_S^0), LL-reconstructed

(f) $z_{\text{vertex}}(K_S^0)$, LL-reconstructed

Figure 4.6: Comparisons of the IP(V^0) and decay vertex z-position $z_{\text{vertex}}(V^0)$ between prompt and non-prompt V^0 hadrons. For the LL-reconstructed Λ^0 the non-prompt candidates are further split into the contributing decay modes. Plots are shown for the full sample of simulated Minimum Bias events.

Figure 4.6 shows that a selection on the IP with respect to the associated PV can be used to suppress the contribution from hyperon decays for the Λ^0. Both the IP and z_{vertex} distributions show that prompt V^0 candidates are difficult to separate from the contributions from charm decays. Therefore, the IP selection is only performed for the Λ^0 and the charm contributions as well as the residual hyperon contributions are estimated on simulation and applied as correction to the final signal yields.
For the choice of the optimal cut point the Punzi *figure of merit* (FOM) [135]

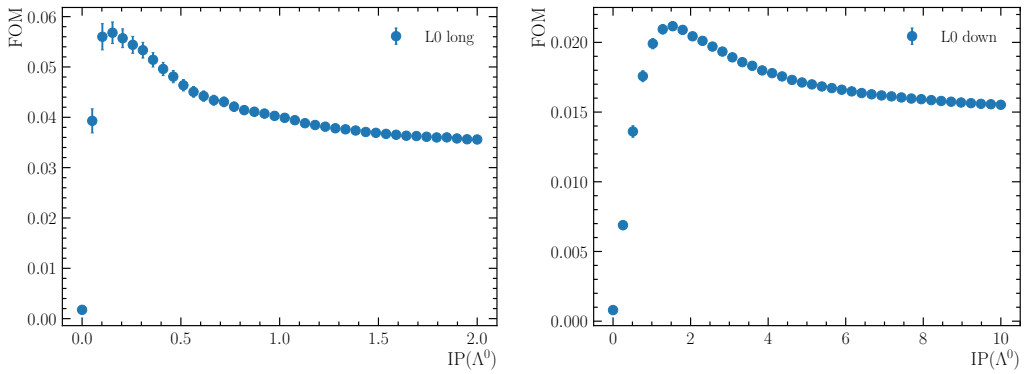

(a) LL-reconstructed **(b)** DD-reconstructed

Figure 4.7: Figure of merit for the suppression of the non-prompt contamination as a function of the cutting point on IP(Λ^0) for LL- and DD-reconstructed Λ^0 candidates. The maximum of each distribution is chosen as cut point.

$$\text{FOM} = \frac{\varepsilon_{\text{sel}}}{\frac{3}{2} + \sqrt{N_{\text{bkg}}^{\text{non-prompt}}}} \tag{4.7}$$

is evaluated as a scan of the cut point for the maximal IP. The number of non-prompt background candidates $N_{\text{bkg}}^{\text{non-prompt}}$ is obtained from simulation by counting the surviving candidates after each cutting point. The signal efficiency ε_{sel} for prompt Λ^0 is obtained from simulation by dividing the number of candidates after the cut and before the cut. The IP scans for the LL- and DD-reconstructed Λ^0 candidates are shown in Fig. 4.7. The ideal cut points for IP(Λ^0) are found to be 0.13 for the LL-reconstructed and 1.8 for the DD-reconstructed candidates. The remaining non-prompt contribution of weak decays is estimated per p_{T} and y in section 4.13.

4.8.3 Fisher discriminant

In order to obtain a more efficient selection based on the IP variables, the logarithms of the IPs of the V^0 and of its children particles are combined into a linear Fisher discriminant [136]

$$\mathcal{F}_{\mathrm{IP}}(V^0 \to h^+h^{(\prime)-}) = a\log_{10}(\mathrm{IP}(h^+)) + b\log_{10}(\mathrm{IP}(h^{(\prime)-})) + c\log_{10}(\mathrm{IP}(V^0)).$$

This variable is derived from the previous V^0 cross-section analyses by LHCb on Run 1 data [131] and the coefficients $a = b = 1$ and $c = -1$ are taken from there. For the optimisation of the cutting point with this variable two approaches can be followed to keep statistical and systematic uncertainties small in all bins of p_{T} and y:

1. Find an optimal cutting point for each individual bin where the binning is fixed in advance.
2. Determine the cutting point for the p_{T}- and y-integrated samples and choose binning in a way that the number of events is similar across all bins.

The second option is chosen for this analysis since its implementation is easier and it is more flexible for changing the binning if needed, *e.g.* to compare to other measurements, although the uncertainties might be sub-optimal in this scenario. The optimisation of the cutting point is performed by scanning the $\mathcal{F}_{\mathrm{IP}}$ variable for cutting points from > 1.0 to > 3.9 in steps of 0.1 and evaluating the Punzi figure of merit (FOM) [135]

$$\mathrm{FOM}(\varepsilon_{\mathrm{sel}}, N_{\mathrm{bkg}}) = \frac{\varepsilon_{\mathrm{sel}}}{\frac{3}{2} + \sqrt{N_{\mathrm{bkg}}}}, \tag{4.8}$$

where the selection efficiency $\varepsilon_{\mathrm{sel}}$ is evaluated on simulation and the number of background candidates N_{bkg} is obtained from a fit to invariant mass distribution after the $\mathcal{F}_{\mathrm{IP}}$ cut is applied. More details about efficiency calculations are given in section 4.12. The invariant mass fits are performed with the same model that is taken for the final invariant mass fit in the individual p_{T} and y bins. The description of the fitting model and procedure is done later in section 4.7. The optimisation is performed separately for K^0_{S} and $\Lambda^0/\bar{\Lambda}^0$ hadrons as well as for the two track type categories LL and DD but the same cut is chosen for the two magnet polarities. The result of the $\mathcal{F}_{\mathrm{IP}}$ scans are shown in Figure 4.8. An example of the invariant mass fits for the $\mathcal{F}_{\mathrm{IP}}$ scan is shown in Figure 4.9 for Λ^0 reconstructed with two long tracks. The full set of invariant mass fits can be found in the appendix. The cut points obtained from the $\mathcal{F}_{\mathrm{IP}}$ scans are shown in table 4.3. It can be seen that for both the K^0_{S} and the $\Lambda^0/\bar{\Lambda}^0$ a tighter cut point than for the long track sample is

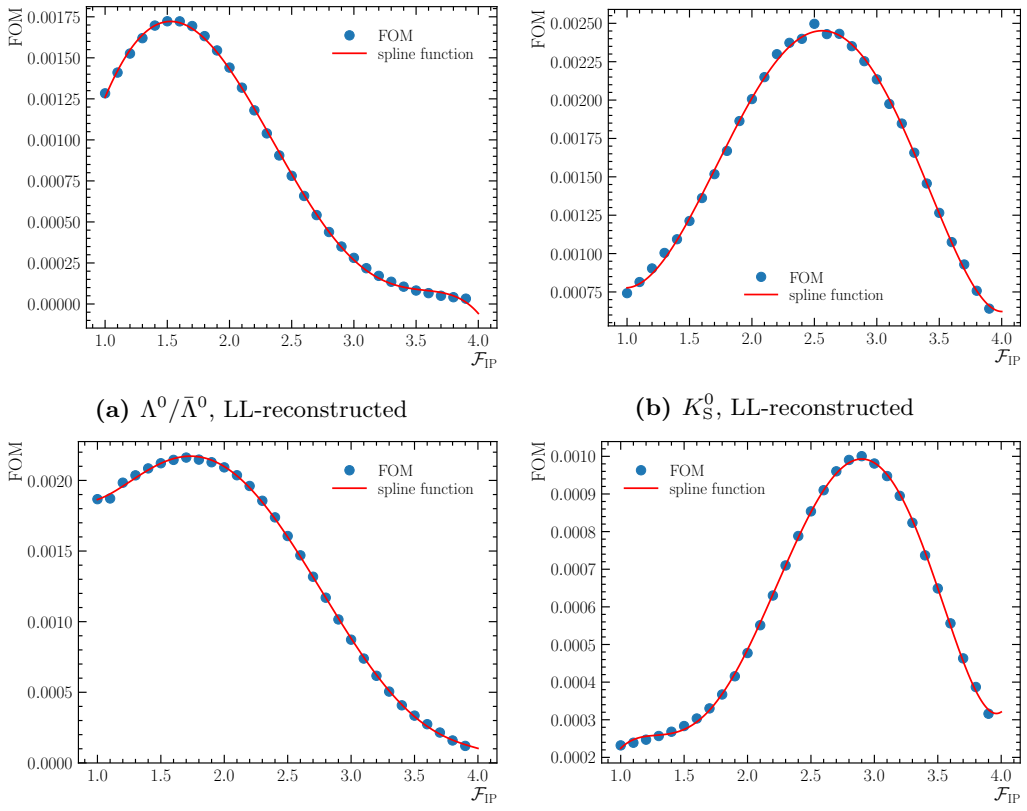

(a) $\Lambda^0/\bar{\Lambda}^0$, LL-reconstructed

(b) K^0_S, LL-reconstructed

(c) $\Lambda^0/\bar{\Lambda}^0$, DD-reconstructed

(d) K^0_S, DD-reconstructed

Figure 4.8: Figure of merit as a function of the cut point of the $\mathcal{F}_{\mathrm{IP}}$ variable for Λ^0 and K^0_S and the two track type categories. A spline function is used for smoothing out potential outliers due to instabilities in the invariant mass fits. The maximum of each spline function is taken as the optimal cut point.

favoured for the downstream track sample, because candidates in this topology have a larger flight distance and therefore the impact parameters of the V^0 children are more likely to have large impact parameters. Moreover, for K^0_S the cut is tighter than for Λ^0.

Table 4.3: Optimised cutting points for the $\mathcal{F}_{\text{IP}}$ variable for K^0_{S} and $\Lambda^0/\bar{\Lambda}^0$ in the two track type categories LL and DD.

V^0	LL	DD
K^0_{S}	2.6	2.9
$\Lambda^0/\bar{\Lambda}^0$	1.5	1.7

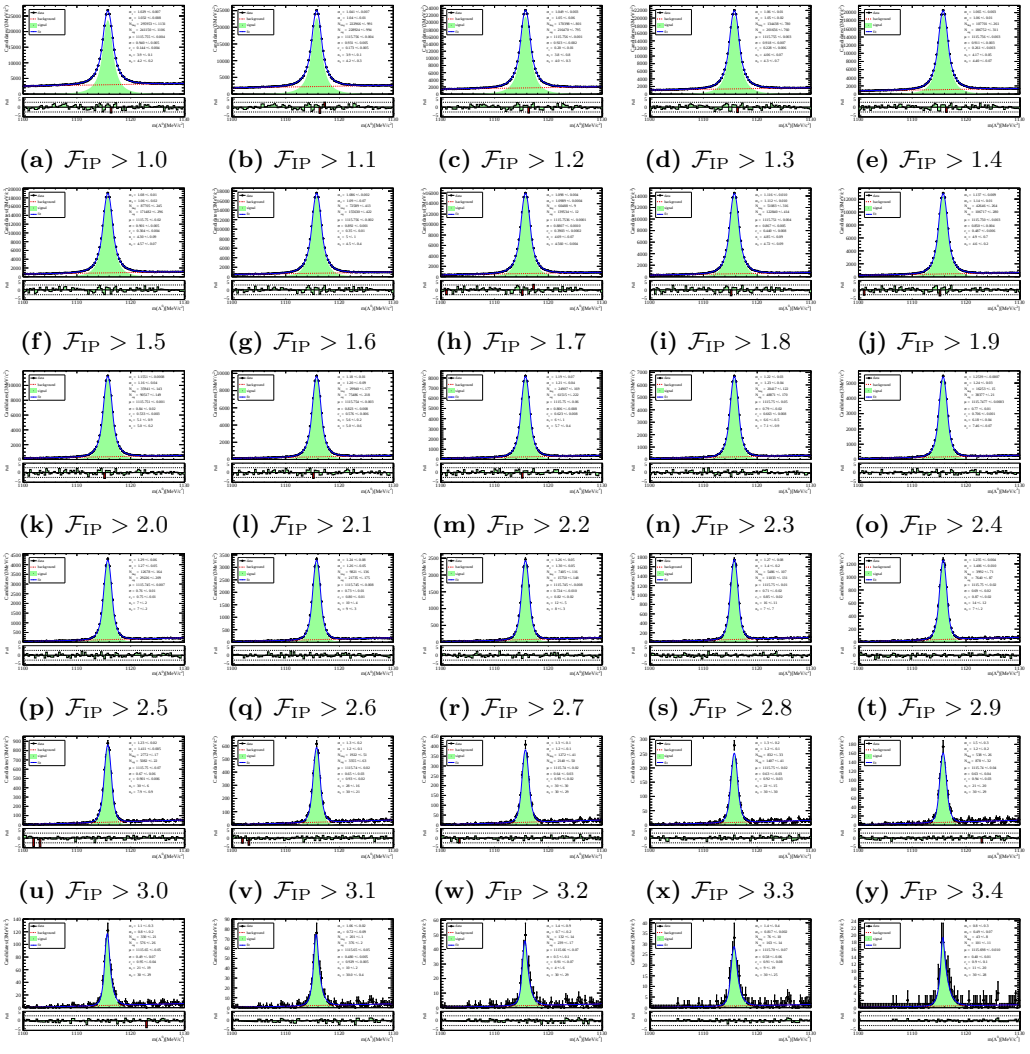

(a) $\mathcal{F}_{\text{IP}} > 1.0$ **(b)** $\mathcal{F}_{\text{IP}} > 1.1$ **(c)** $\mathcal{F}_{\text{IP}} > 1.2$ **(d)** $\mathcal{F}_{\text{IP}} > 1.3$ **(e)** $\mathcal{F}_{\text{IP}} > 1.4$

(f) $\mathcal{F}_{\text{IP}} > 1.5$ **(g)** $\mathcal{F}_{\text{IP}} > 1.6$ **(h)** $\mathcal{F}_{\text{IP}} > 1.7$ **(i)** $\mathcal{F}_{\text{IP}} > 1.8$ **(j)** $\mathcal{F}_{\text{IP}} > 1.9$

(k) $\mathcal{F}_{\text{IP}} > 2.0$ **(l)** $\mathcal{F}_{\text{IP}} > 2.1$ **(m)** $\mathcal{F}_{\text{IP}} > 2.2$ **(n)** $\mathcal{F}_{\text{IP}} > 2.3$ **(o)** $\mathcal{F}_{\text{IP}} > 2.4$

(p) $\mathcal{F}_{\text{IP}} > 2.5$ **(q)** $\mathcal{F}_{\text{IP}} > 2.6$ **(r)** $\mathcal{F}_{\text{IP}} > 2.7$ **(s)** $\mathcal{F}_{\text{IP}} > 2.8$ **(t)** $\mathcal{F}_{\text{IP}} > 2.9$

(u) $\mathcal{F}_{\text{IP}} > 3.0$ **(v)** $\mathcal{F}_{\text{IP}} > 3.1$ **(w)** $\mathcal{F}_{\text{IP}} > 3.2$ **(x)** $\mathcal{F}_{\text{IP}} > 3.3$ **(y)** $\mathcal{F}_{\text{IP}} > 3.4$

(z) $\mathcal{F}_{\text{IP}} > 3.5$ **(aa)** $\mathcal{F}_{\text{IP}} > 3.6$ **(ab)** $\mathcal{F}_{\text{IP}} > 3.7$ **(ac)** $\mathcal{F}_{\text{IP}} > 3.8$ **(ad)** $\mathcal{F}_{\text{IP}} > 3.9$

Figure 4.9: Mass fits to data of LL-reconstructed $\Lambda^0 \to p\pi^-/\bar{\Lambda}^0 \to \bar{p}\pi^+$ decays with all parameters floating for the $\mathcal{F}_{\text{IP}}$ scan.

4.8.4 Mis-identification vetoes

Apart from the non-prompt background from weak decays discussed in section 4.8.2 and the combinatorial background that is suppressed with the $\mathcal{F}_{\text{IP}}$ selection discussed in the previous section, there is another source of physics background arising from assigning the wrong mass hypothesis to the final state tracks. For example if the p mass is assigned to the π^+ in the $K^0_{\text{S}} \to \pi^+\pi^-$ decay, the candidate can be falsely reconstructed as a Λ^0. For most of these kind of mass swaps the thereby produced background does not peak under the Λ^0 mass peak. Potentially peaking backgrounds from wrongly assigned final state particle masses, can be identified by overlaps in an Armenteros-Podolanski plot [137]. It shows the p_{T} of

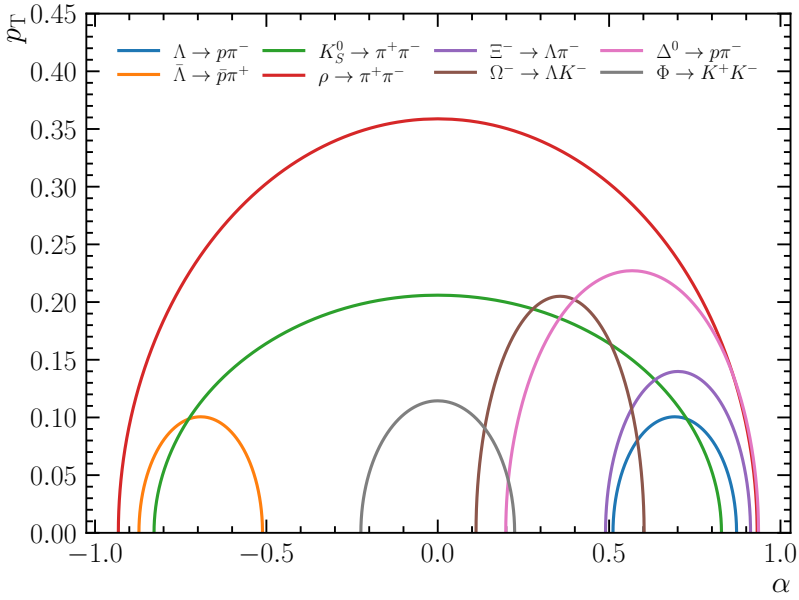

Figure 4.10: Armenteros-Podolanski plot for a selection of two-body decays. An overlap of $K^0_{\text{S}} \to \pi^+\pi^-$ decays with $\Lambda^0 \to p\pi^-$ and $\bar{\Lambda}^0 \to \bar{p}\pi^+$ can be seen.

one of the final state particles of a two-body decay as a function of the asymmetry α of the longitudinal momenta p_{L} of the two final-state particles. The p_{T} is defined with respect to the flight direction of the parent particle. The longitudinal momenta are the projection of the transverse momentum components on the direction of flight of the parent particle. As a result, two-body decays build an ellipse in the (p_{T}, α)-plane that can, when plotted for data, be used to identify them without knowing the masses of the final-state particles. More details about the representation of two-body decays in the Armenteros-Podolanski plot are given in Appendix C.

Figure 4.10 shows the Armenteros-Podolanski plot for a selection of two-body decays. It can be seen that the $K^0_S \to \pi^+\pi^-$ decays overlap with both the $\Lambda^0 \to p\pi^-$ and the $\bar{\Lambda}^0 \to \bar{p}\pi^+$ decays.[1] The distribution of the recalculated invariant mass

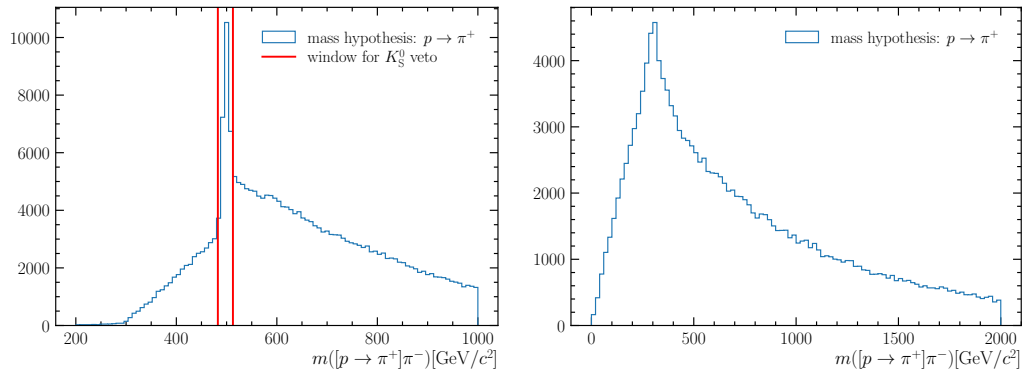

(a) LL-reconstructed **(b)** DD-reconstructed

Figure 4.11: Invariant mass distributions of $\Lambda^0/\bar{\Lambda}^0$ candidates with the mass hypothesis for the proton replaced with the nominal mass of the pion after the $\mathcal{F}_{\text{IP}}$ selection. A clear peak from $K^0_S \to \pi^+\pi^-$ decays is visible in the long track sample, whereas in the downstream track sample no peak at the K^0_S mass is present. The red vertical lines in the plot for the long track sample mark the $\pm 15\,\text{MeV/c}^2$ window around the nominal K^0_S mass that is used to veto background from misidentified $K^0_S \to \pi^+\pi^-$ decays.

$m([p \to \pi^+]\pi^-)$ of LL- and DD-reconstructed Λ^0 candidates after the IP selection is shown in Figure 4.11. Here, the mass hypothesis for the π^+/π^- is changed to the one of a $p/\bar{p}$. While for the LL-reconstructed sample a clear peak at the nominal K^0_S mass $m_{\text{PDG}}(K^0_S) = (497.611 \pm 0.010)\,\text{MeV/c}^2$ [5] is visible, for the DD-reconstructed no structure is visible. The lack of a peak in the DD-sample comes mostly from the smaller lifetime of K^0_S with respect to Λ^0 hadrons, the worse momentum resolution of downstream tracks and hence worse mass resolution, and the already applied IP selection. As a cross-check that no remaining peaking contribution is expected below the Λ^0 mass peak, the invariant mass distribution is plotted for simulated Λ^0 candidates that were truth-matched with the particle IDs of the K^0_S decay chain. No peaking $K^0_S \to \pi^+\pi^-$ contribution is observed for the LL- or DD-reconstructed samples. These are shown in the first row of plots in Figure 4.12 for LL- and DD-reconstructed Λ^0 candidates. To further reduce the background level, a veto selection for the LL-sample is applied, where the recalculated mass of the Λ^0 candidates is

[1] Further overlaps such as the depicted $\Xi^- \to \Lambda^0\pi^0$, $\Omega \to \Lambda^0 K^-$ and $\Delta \to p\pi^-$ are not relevant for this background study since they have a different decay topology or the final states have a neutral electric charge and would therefore not be reconstructed as tracks.

required to be $\pm 15\,\mathrm{MeV/c^2}$ away from $m_{\mathrm{PDG}}(K^0_{\mathrm{S}})$.
The same study is performed for $K^0_{\mathrm{S}} \to \pi^+\pi^-$ candidates where one of the pions could actually be a proton with wrongly assigned pion mass which would make in combination with the second pion a good $\Lambda^0/\bar{\Lambda}^0$ candidate. The second row of plots in Figure 4.12 shows the recalculated invariant mass distribution where for one of the pions the mass is replaced with the proton mass. No distinct peaking structures at the nominal Λ^0 mass $m_{\mathrm{PDG}}(\Lambda^0) = (1115.683 \pm 0.006)\,\mathrm{MeV/c^2}$ [5] are observed for both the LL- and DD-reconstructed decays. However, a small bump at about $2.2\,\mathrm{GeV/c^2}$ can be seen which comes from the second pion actually being a proton, while the first one was falsely given the proton mass. Since the bump is rather broad no veto is applied. The third row in Figure 4.12 shows the invariant K^0_{S} mass distribution where the decay chain is truth-matched to the one of $K^0_{\mathrm{S}} \to \pi^+\pi^-$ or $\Lambda^0 \to p\pi^-$. By this the choice of not applying a veto is justified as there is no peaking contribution below the K^0_{S} peak by misidentified $\Lambda^0 \to p\pi^-$ decays.

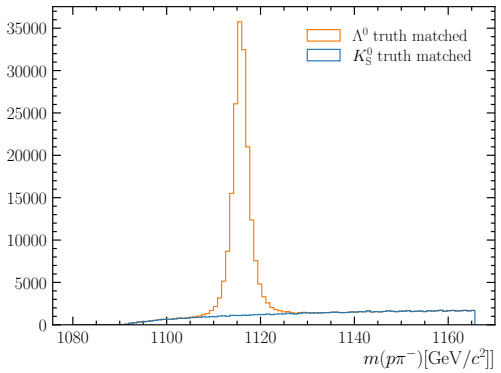

(a) truth-matched $m(p\pi^-)$, LL-reconstructed

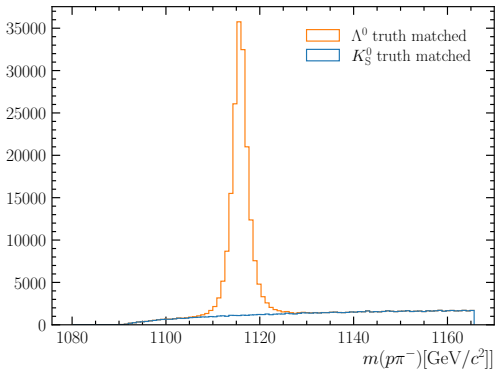

(b) truth-matched $m(p\pi^-)$, DD-reconstructed

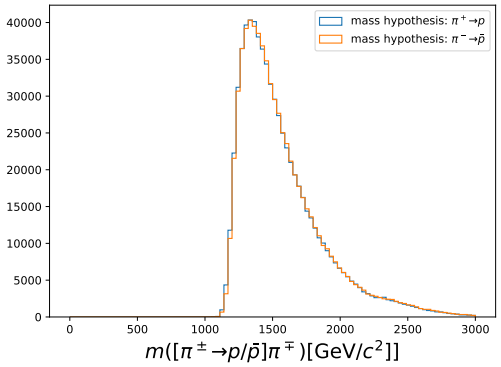

(c) $\pi^\pm \to p/\bar{p}$, LL-reconstructed

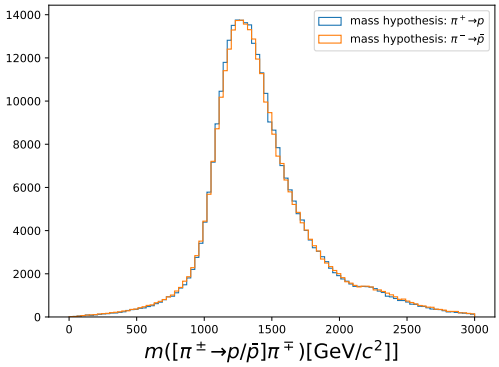

(d) $\pi^\pm \to p/\bar{p}$, DD-reconstructed

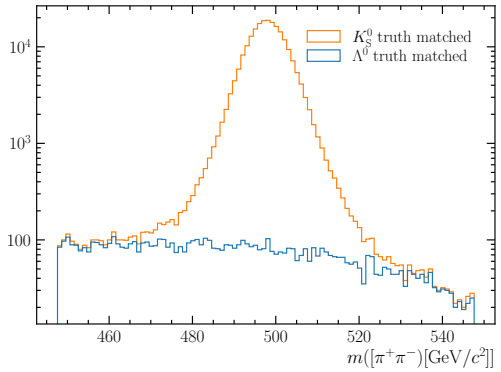

(e) truth-matched $m(\pi^+\pi^-)$, LL-reconstructed

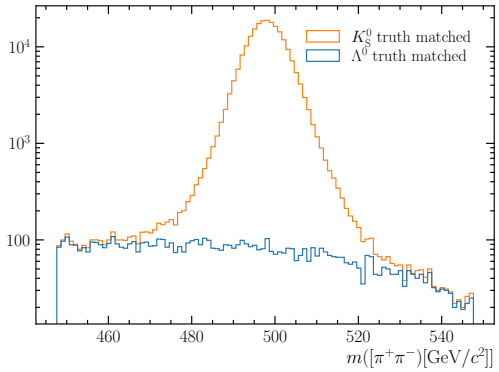

(f) truth-matched $m(\pi^+\pi^-)$, DD-reconstructed

Figure 4.12: Invariant mass distribution of (a) LL-reconstructed and (b) DD-reconstructed Λ^0 candidates from simulated Minimum Bias events where the candidates are truth-matched to the $\Lambda^0 \to p\pi^-$ (orange) and $K^0_S \to \pi^+\pi^-$ (blue) decay chains. For the K^0_S component no peaking structure is visible around the nominal Λ^0 mass. The $K^0_S \to \pi^+\pi^-$ contributes only to the combinatorial background. Figures (e) and (f) show the equivalent contribution of $\Lambda^0/\bar{\Lambda}^0$ decays to the $K^0_S \to \pi^+\pi^-$ candidates. Figures (c) and (d) show the invariant mass distributions of K^0_S candidates where one of the pion masses is replaced with the proton mass.

4.8.5 Bin-integrated mass fits

Invariant mass fits for the K^0_S and $\Lambda^0/\bar{\Lambda}^0$ in the full p_T and y ranges are performed after applying the IP selections and mis-identification vetoes by using the mass model and fitting procedure described earlier in section 4.7. They are shown in Figure 4.13. The signal yields N_{sig} for K^0_S and $\Lambda^0/\bar{\Lambda}^0$, obtained from the fits integrated in p_T

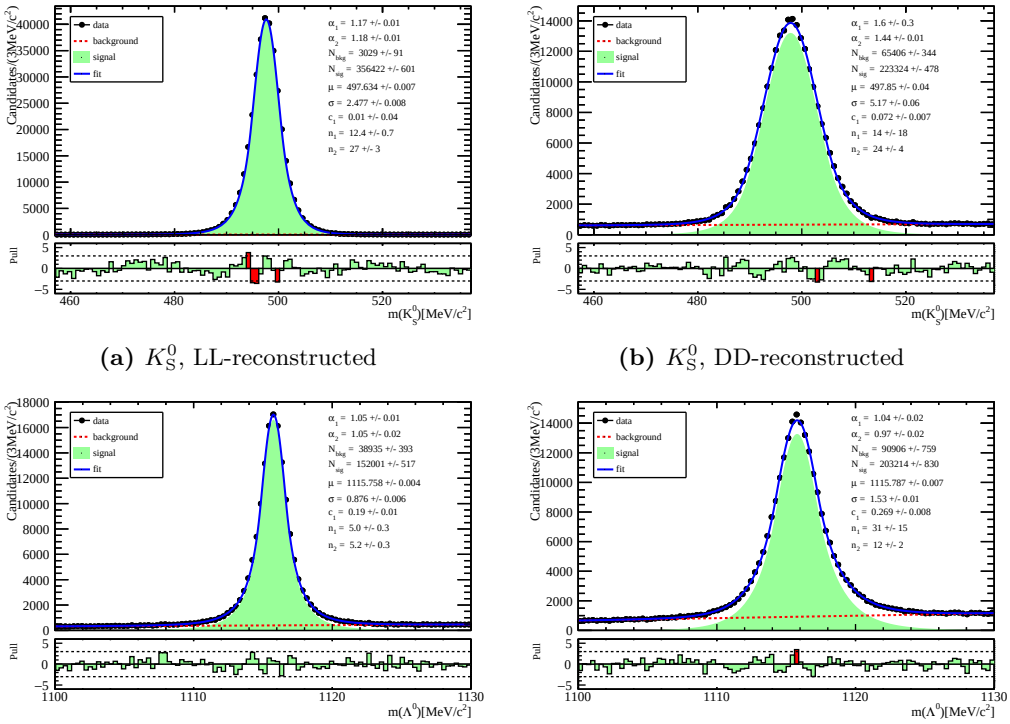

(a) K^0_S, LL-reconstructed

(b) K^0_S, DD-reconstructed

(c) $\Lambda^0/\bar{\Lambda}^0$, LL-reconstructed

(d) $\Lambda^0/\bar{\Lambda}^0$, DD-reconstructed

Figure 4.13: Invariant mass distributions of K^0_S and $\Lambda^0/\bar{\Lambda}^0$ reconstructed with two long tracks (LL) or two downstream tracks (DD) and $\mathcal{F}_{IP}$ selection applied. All plots are shown for magnet polarity *MagDown*.

and y after applying the IP selections and fitting the invariant mass distributions, are shown in Table 4.4.

Table 4.4: Signal yields for K^0_S and $\Lambda^0/\bar{\Lambda}^0$ integrated in p_T and y after applying the IP selection. All numbers are obtained from fits to invariant mass distribution for *MagDown*, *MagUp* and both polarities combined.

particle	track type	polarity	N_{sig}
K^0_S	LL	*MagDown*	$356\,422 \pm 601$
		MagUp	$661\,808 \pm 821$
		both	$1\,038\,083 \pm 1018$
	DD	*MagDown*	$223\,324 \pm 478$
		MagUp	$416\,349 \pm 732$
		both	$638\,119 \pm 912$
$\Lambda^0/\bar{\Lambda}^0$	LL	*MagDown*	$152\,001 \pm 517$
		MagUp	$281\,257 \pm 718$
		both	$432\,764 \pm 872$
	DD	*MagDown*	$203\,214 \pm 830$
		MagUp	$379\,516 \pm 929$
		both	$580\,545 \pm 614$

4.9 Crossing angle correction

As described in section 2.2.1 the small but non-vanishing crossing angle at the collision point differs among the two magnet polarities. As a consequence the distributions of kinematic quantities such as p_T and y are slightly biased, but in particular biased differently for *MagUp* and *MagDown*. In Figure 4.14 this is shown for the here investigated prompt $V^0 = K^0_S, \Lambda^0, \bar{\Lambda}^0$ hadrons by plotting their φ-angle distributions. Not only the different biases for the two magnet polarities make it relevant to correct for the crossing angle, but also if the measurement is being compared to other data sets or other experiments a bias of the cross-section by the crossing angle is undesirable. The correction of the crossing angle is performed by applying a Lorentz boost to the four-momentum of the V^0 into the centre-of-mass frame of the collision. After applying the correction the φ distributions are flat as can be seen from the blue distributions in Figure 4.14. Afterwards, the collision frame is rotated so that its z-axis coincides with the z-axis of the lab frame. In the following p_T and y correspond to their crossing angle corrected variables. Figure 4.15 shows the distributions of the p_T and y differences between crossing-angle corrected and uncorrected Λ^0 hadrons for the two magnet polarities.

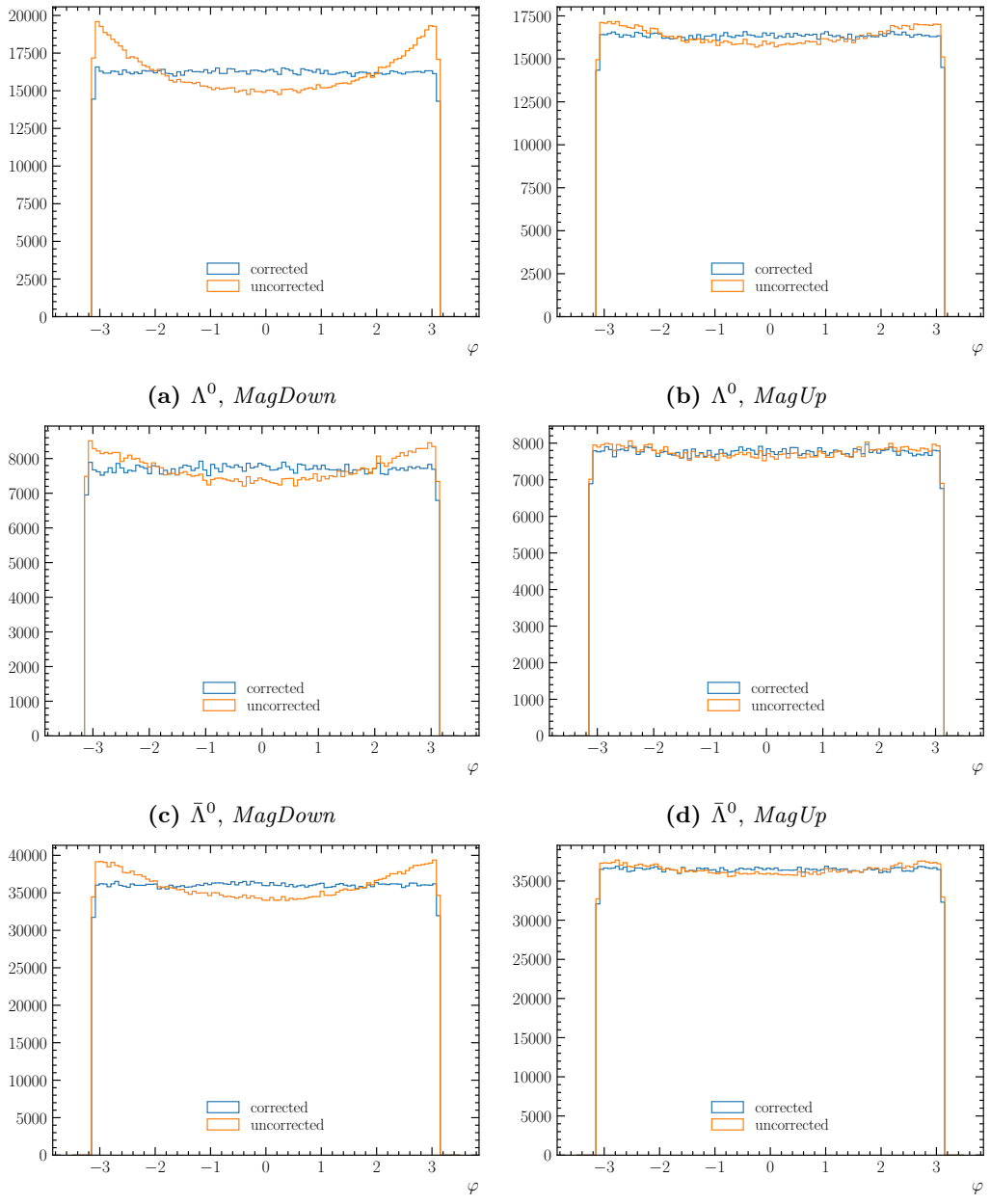

(a) Λ^0, *MagDown* **(b)** Λ^0, *MagUp*

(c) $\bar{\Lambda}^0$, *MagDown* **(d)** $\bar{\Lambda}^0$, *MagUp*

(e) K^0_S, *MagDown* **(f)** K^0_S, *MagUp*

Figure 4.14: Distribution of the φ-angle for truth-matched simulated promptly produced Λ^0, $\bar{\Lambda}^0$ and K^0_S hadrons before and after the crossing angle correction. For visualisation purposes plots show distributions for generator-level simulation without requiring the final state particles to be in the LHCb acceptance.

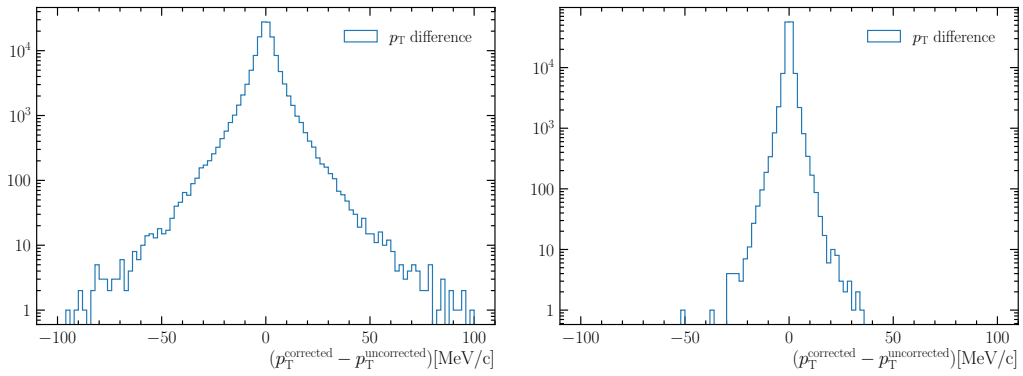

(a) p_T, *MagDown*

(b) p_T, *MagUp*

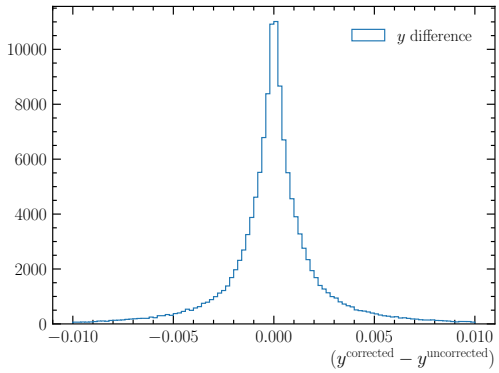

(c) y, *MagDown*

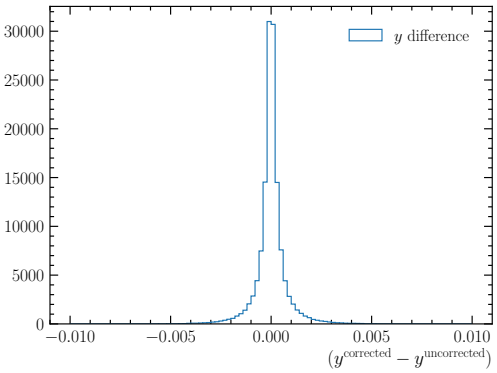

(d) y, *MagUp*

Figure 4.15: Differences of p_T and y between crossing-angle corrected and uncorrected Λ^0 hadrons. All distributions are plotted for simulated $\Lambda^0 \to p\pi^-$ decays within in the LHCb geometrical acceptance.

4.10 Binning

After the selection and the crossing angle correction is applied to the V^0 samples, the samples are split into p_{T} and y bins. The binning used for this measurement is the same as used for the Run 1 measurement at 7 TeV [131], so that the results can be easily compared. It is given by the following six bins in p_{T} and five bins in y:

$$\begin{aligned} p_{\mathrm{T}} \text{ in MeV}/c &: [150, 500], [500, 650], [650, 800], [800, 1000], [1000, 1200], [1200, 2500] \\ y &: [2, 2.5], [2.5, 3], [3, 3.5], [3.5, 4], [4, 4.5] \end{aligned}$$

An optimised binning based on equal amount of events per bin will be developed for the Run 3 data. The sample of $\Lambda^0/\bar{\Lambda}^0$ candidates is split into Λ^0 and $\bar{\Lambda}^0$ by the electric charges of the final state hadrons and the fits to invariant masses as well as the calculation of their efficiencies is performed separately.

4.11 Invariant mass fits

The invariant mass distributions in the different p_{T} and y bins are fitted to extract the signal yields for the production cross-section ratio measurements. The fitting model and procedure described in section 4.7 are used for the invariant mass fits. The fits are performed independently for the K^0_{S}, Λ^0 and $\bar{\Lambda}^0$ hadrons. They are done separately for all considered p_{T} and y bins, both magnet polarities and both track types categories. The Figures 4.16-4.19 show examples of the fourth/fifth step of the fitting procedure for LL-reconstructed K^0_{S} and $\bar{\Lambda}^0$ candidates in both the p_{T} and y bins for magnet polarity *MagDown*. The remaining fits of DD-reconstructed V^0 candidates and magnet polarity *MagUp* can be found in Appendix D.

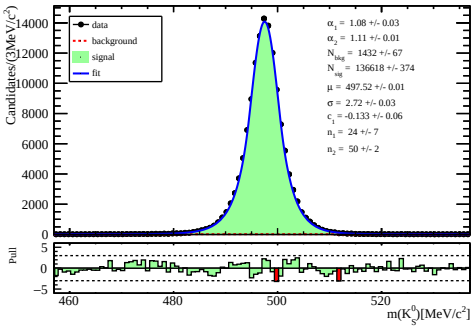

(a) $p_{\mathrm{T}} \in [150, 500]\,\mathrm{MeV}/c$

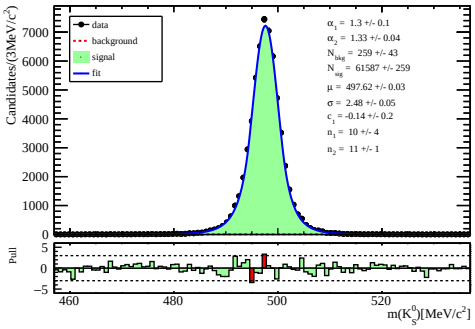

(b) $p_{\mathrm{T}} \in [500, 650]\,\mathrm{MeV}/c$

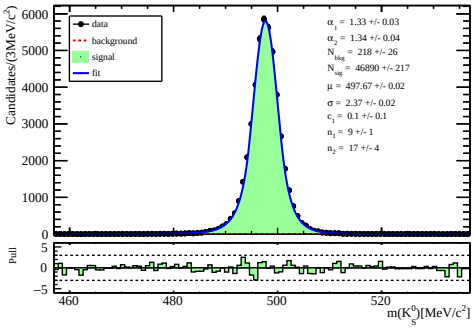

(c) $p_{\mathrm{T}} \in [650, 800]\,\mathrm{MeV}/c$

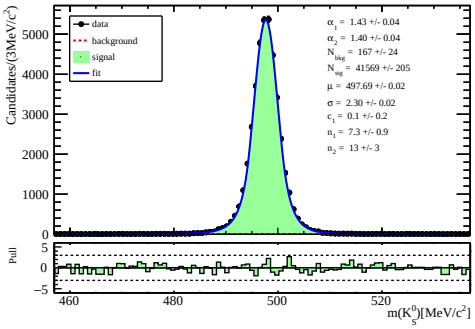

(d) $p_{\mathrm{T}} \in [800, 1000]\,\mathrm{MeV}/c$

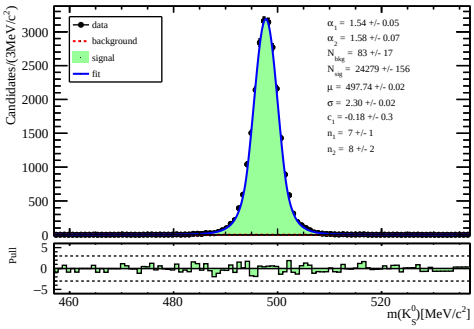

(e) $p_{\mathrm{T}} \in [1000, 1200]\,\mathrm{MeV}/c$

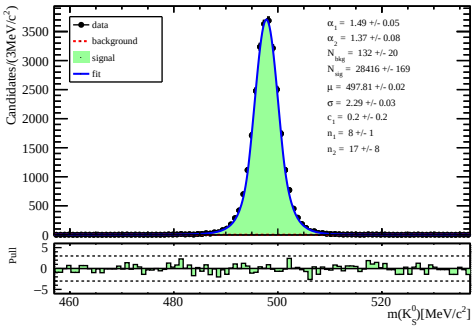

(f) $p_{\mathrm{T}} \in [1200, 2500]\,\mathrm{MeV}/c$

Figure 4.16: Invariant mass fits of LL-reconstructed K^0_{S} candidates in the different p_{T} bins. All plots are shown for the magnet polarity *MagDown*.

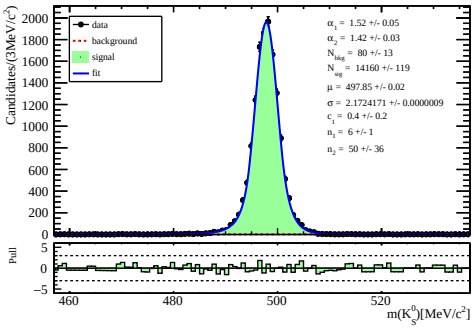

(a) $y \in [2, 2.5]$

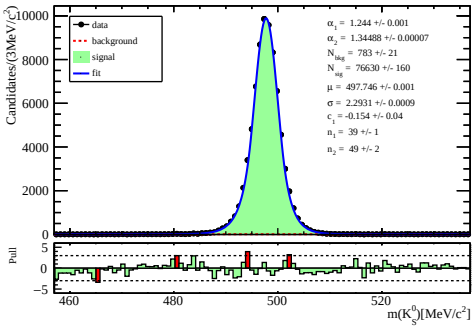

(b) $y \in [2.5, 3]$

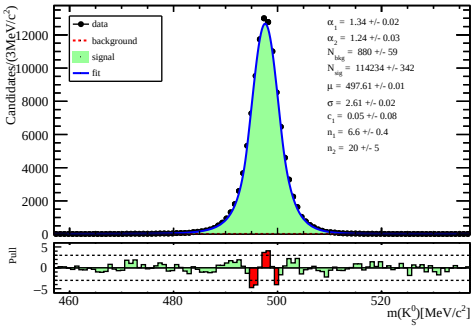

(c) $y \in [3, 3.5]$

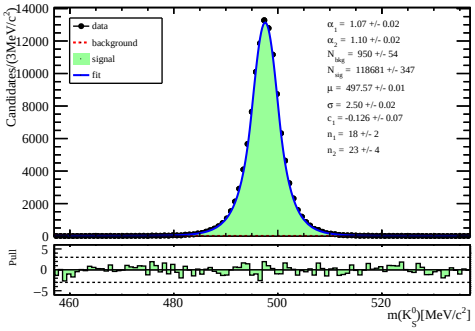

(d) $y \in [3.5, 4]$

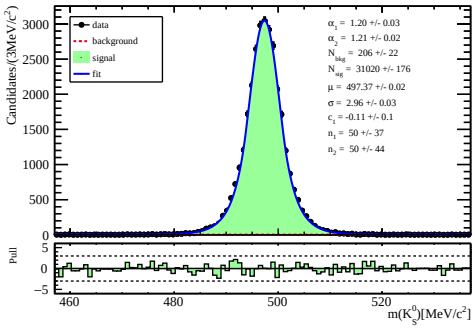

(e) $y \in [4, 4.5]$

Figure 4.17: Invariant mass fits of LL-reconstructed K^0_S candidates in the different y bins. All plots are shown for the magnet polarity *MagDown*.

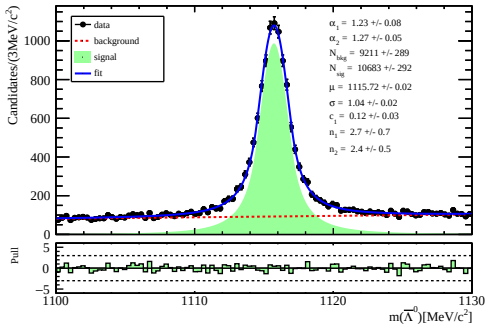

(a) $p_{\mathrm{T}} \in [150, 500]\,\mathrm{MeV}/c$

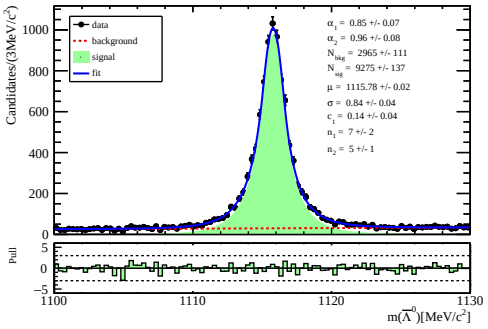

(b) $p_{\mathrm{T}} \in [500, 650]\,\mathrm{MeV}/c$

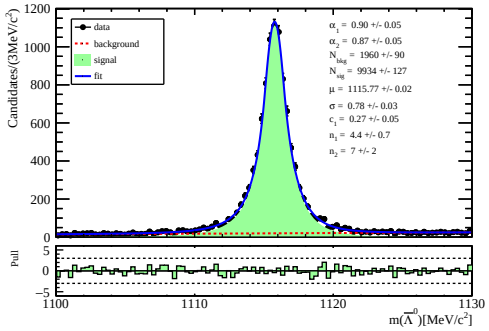

(c) $p_{\mathrm{T}} \in [650, 800]\,\mathrm{MeV}/c$

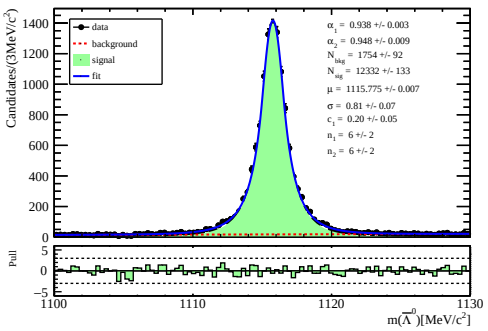

(d) $p_{\mathrm{T}} \in [800, 1000]\,\mathrm{MeV}/c$

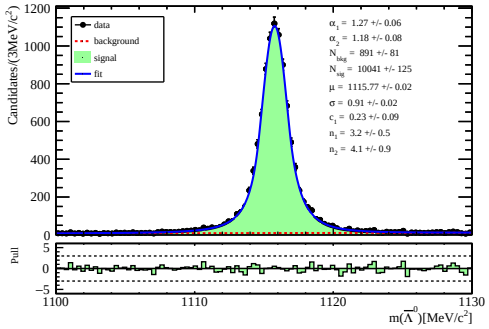

(e) $p_{\mathrm{T}} \in [1000, 1200]\,\mathrm{MeV}/c$

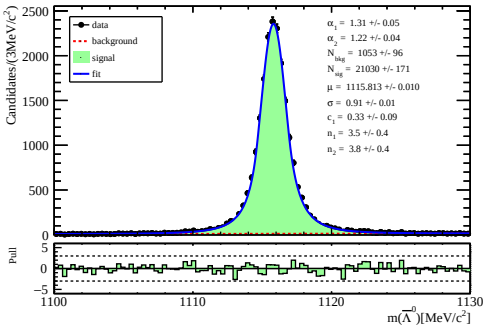

(f) $p_{\mathrm{T}} \in [1200, 2500]\,\mathrm{MeV}/c$

Figure 4.18: Invariant mass fits of LL-reconstructed $\bar{\Lambda}^0$ candidates in the different p_{T} bins. All plots are shown for the magnet polarity *MagDown*.

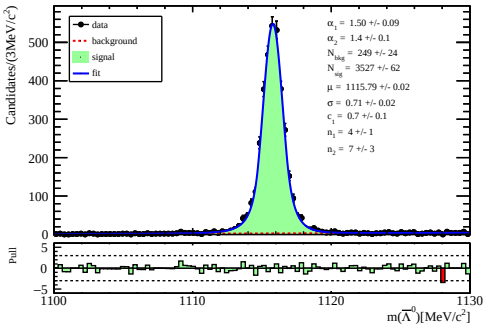

(a) $y \in [2, 2.5]$

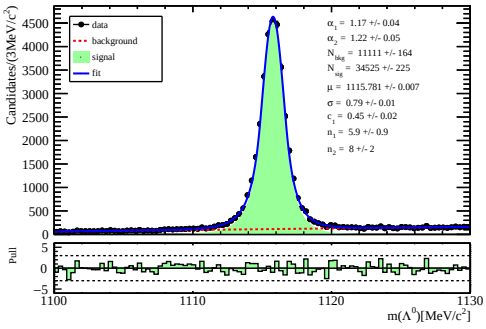

(b) $y \in [2.5, 3]$

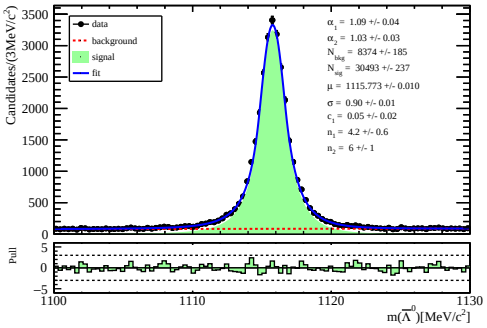

(c) $y \in [3, 3.5]$

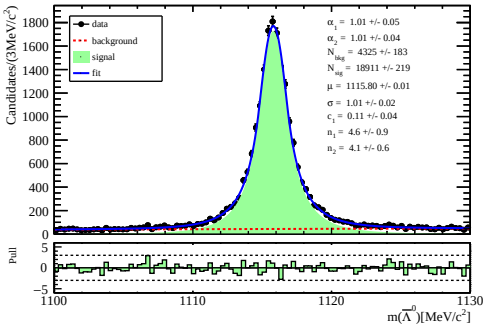

(d) $y \in [3.5, 4]$

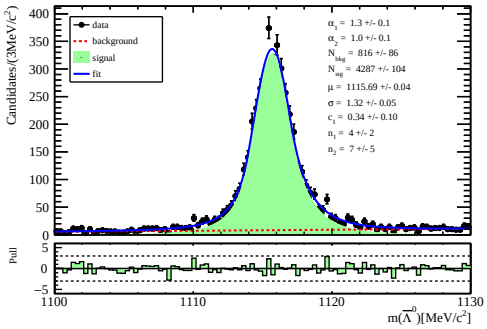

(e) $y \in [4, 4.5]$

Figure 4.19: Invariant mass fits of LL-reconstructed $\bar{\Lambda}^0$ candidates in the different y bins. All plots are shown for the magnet polarity *MagDown*.

4.12 Efficiency calculation

The efficiency calculation consists of several steps that account for the different parts of the detection and selection chain. These comprise the geometric acceptance, the reconstruction efficiency, the selection performed in the trigger system of LHCb and the candidate selection developed in section 4.8 to select K^0_S and Λ^0 decays. The different steps will be explained separately in the following sections.

4.12.1 Reconstruction efficiency

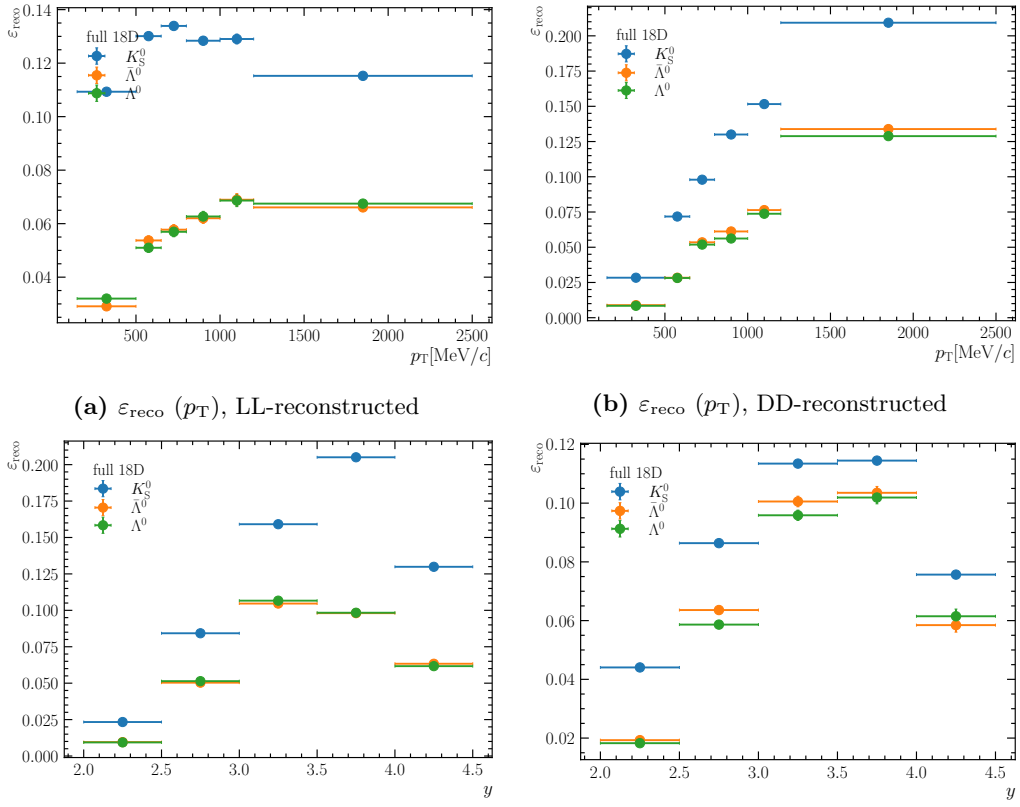

(a) $\varepsilon_{\text{reco}}$ (p_T), LL-reconstructed

(b) $\varepsilon_{\text{reco}}$ (p_T), DD-reconstructed

(c) $\varepsilon_{\text{reco}}$ (y), LL-reconstructed

(d) $\varepsilon_{\text{reco}}$ (y), DD-reconstructed

Figure 4.20: Reconstruction efficiencies $\varepsilon_{\text{reco}}$ for LL- and DD-reconstructed $V^0 = K^0_S, \Lambda^0, \bar{\Lambda}^0$ decays as a function of p_T and y. Plots are shown for magnet polarity *MagDown*.

Reconstruction efficiencies are calculated by comparing the number of generated V^0 candidates $N_{\text{generated}}$ taken from generator-level simulated samples and the reconstructed number $N_{\text{reconstructed}}$ taken from the simulation sample that was run through the offline reconstruction. It is given by

$$\varepsilon_{\text{reco}} = \frac{N_{\text{reconstructed}}}{N_{\text{generated}}}. \tag{4.9}$$

For the generator-level simulation the children particles of the V^0 are required to be in the LHCb acceptance, which is applied by requiring a pseudo-rapidity $2 < \eta < 5$. Figure 4.21 shows the obtained reconstruction efficiencies for LL-reconstructed and DD-reconstructed $V^0 = K^0_{\text{S}}, \Lambda^0, \bar{\Lambda}^0$ decays as a function of p_{T} and y.

4.12.2 Trigger and selection efficiency

The NoBias trigger lines that were used to record the data for the presented analysis do not apply any selection to the candidates so that the efficiency is 100 %.[2] However, the lines are prescaled so that only a fraction of events are randomly selected. Therefore, the trigger efficiency for the default prescale configuration is given by combining the prescales of HLT1 and HLT2 which results in

$$\varepsilon_{\text{trigger}} = \varepsilon_{\text{HLT1}} \cdot \varepsilon_{\text{HLT2}} = 0.01 \cdot 0.025 = 0.25\,\%. \tag{4.10}$$

However, the prescales have been changed for different data takings and fills of the LHC. Therefore, a more detailed study of the prescales need to be done in case the trigger efficiency is needed, *e.g.* for measuring the total cross-sections of the V^0 hadrons. The trigger efficiency is the same for $\Lambda^0/\bar{\Lambda}^0$ and K^0_{S} candidates and therefore cancels in the cross-section ratios. Signal selection efficiencies

$$\varepsilon_{\text{sel}} = \frac{N_{\text{after}}}{N_{\text{before}}} \tag{4.11}$$

are calculated on simulation by taking the ratio of the number of signal candidates before (N_{before}) and after (N_{after}) the selection is applied. The final selection efficiencies for the cross-section ratio measurements are calculated separately for each bin in p_{T} and y. The uncertainties on all calculated efficiencies are given by the binomial error

$$\Delta\varepsilon = \sqrt{\frac{\varepsilon(1-\varepsilon)}{N_{\text{before}}}}. \tag{4.12}$$

[2] Here, the denominator in the calculation of the trigger efficiency is the amount of reconstructible tracks with respect to the offline reconstruction. For Run 3 the trigger and reconstruction efficiencies cannot be factorised since the reconstruction is performed fully online.

The uncertainty on the efficiency is dominated by the size of the simulation sample. The obtained selection efficiencies are shown in Figure 4.20.

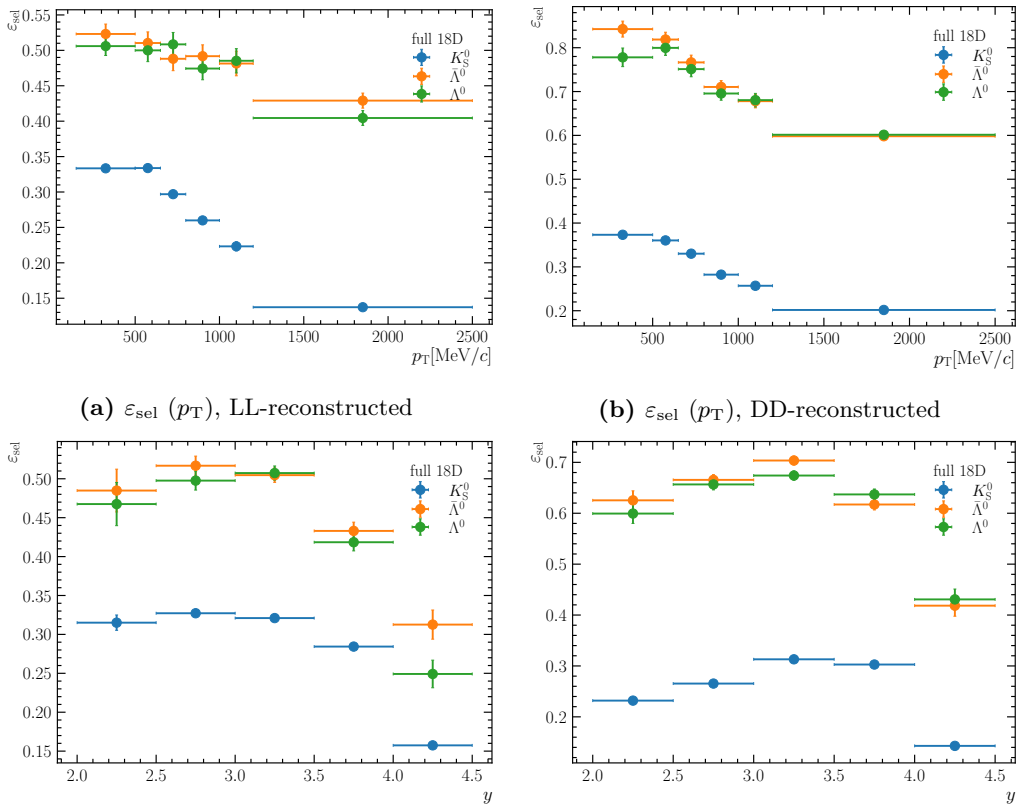

(a) ε_{sel} (p_{T}), LL-reconstructed

(b) ε_{sel} (p_{T}), DD-reconstructed

(c) ε_{sel} (y), LL-reconstructed

(d) ε_{sel} (y), DD-reconstructed

Figure 4.21: Selection efficiencies ε_{sel} for LL- and DD-reconstructed $V^0 = K^0_S, \Lambda^0, \bar{\Lambda}^0$ decays as a function of p_{T} and y. Plots are shown for magnet polarity *MagDown*.

4.13 Residual non-prompt contributions

As discussed in section 4.8.2 the suppression of non-prompt $V^0 = K^0_S, \Lambda^0, \bar{\Lambda}^0$ from weak decays of hyperons and charm hadrons is not perfect. Therefore, correction factors

$$f^{\text{non-prompt}}_{V^0}(p_T, y) = \frac{N^{\text{non-prompt}}_{V^0}(p_T, y)}{N^{\text{non-prompt}}_{V^0}(p_T, y) + N^{\text{prompt}}_{V^0}(p_T, y)}, \tag{4.13}$$

are calculated and applied to each p_T- and y-bin of the $R(\Lambda^0, K^0_S)$ cross-section ratio. For that, the number of prompt and non-prompt decays $N^{\text{non-prompt}}_{V^0}$ are counted on truth-matched simulation. Both magnet polarities are considered together. The estimated fractions as a function of p_T are shown in Figure 4.22 for K^0_S and $\Lambda^0/\bar{\Lambda}^0$ candidates. The results for DD-reconstructed V^0 candidates are more precise, because more background candidates remains after the IP selection performed in 4.8.2 with respect to the LL-reconstructed. When comparing Figure 4.22 to Table 4.2 it can be seen that the total non-prompt fractions for the $\Lambda^0/\bar{\Lambda}^0$ are reduced by about a factor of six for the LL-reconstructed decays and halved for the DD-reconstructed. For K^0_S candidates the fraction from Table 4.2 is only reduces by the cut on the $\mathcal{F}_{\text{IP}}$ and is shown for the p_T-bins in Figure 4.22. The splitting of the non-prompt $\Lambda^0/\bar{\Lambda}^0$ sample by contributing weak decays shows that the suppression of hyperon decays with the IP selection is more efficient than the one of charm decays since the fraction of $\Lambda^0/\bar{\Lambda}^0$ coming from Λ^+_c decays is reduced much less. This expected due to the much shorter lifetime of the Λ^+_c baryons. Therefore, they become more relevant for the residual non-prompt fraction for the LL-reconstructed $\Lambda^0/\bar{\Lambda}^0$ than for the DD-reconstructed.
Figure 4.23 shows the same residual non-prompt fractions as a function of y. Applying the residual non-prompt fractions as a correction to the $R(\bar{\Lambda}^0, K^0_S)$ ratio, equation 4.2 becomes

$$R(\bar{\Lambda}^0, K^0_S) = \frac{(1 - f^{\text{non-prompt}}_{\Lambda^0/\bar{\Lambda}^0}) N(\bar{\Lambda}^0 \to \bar{p}\pi^+) \varepsilon_{K^0_S \to \pi^+\pi^-} \mathcal{B}(K^0_S \to \pi^+\pi^-)}{(1 - f^{\text{non-prompt}}_{K^0_S}) N(K^0_S \to \pi^+\pi^-) \varepsilon_{\bar{\Lambda}^0 \to \bar{p}\pi^+} \mathcal{B}(\bar{\Lambda}^0 \to \bar{p}\pi^+)}. \tag{4.14}$$

No factor is applied for the ratio $R(\bar{\Lambda}^0, \Lambda^0)$ since the fractions are assumed to be equal for Λ^0 and $\bar{\Lambda}^0$ candidates.[3]

[3] This assumes that potential differences in the production of hyperons and anti-hyperons and in their branching fractions are negligible.

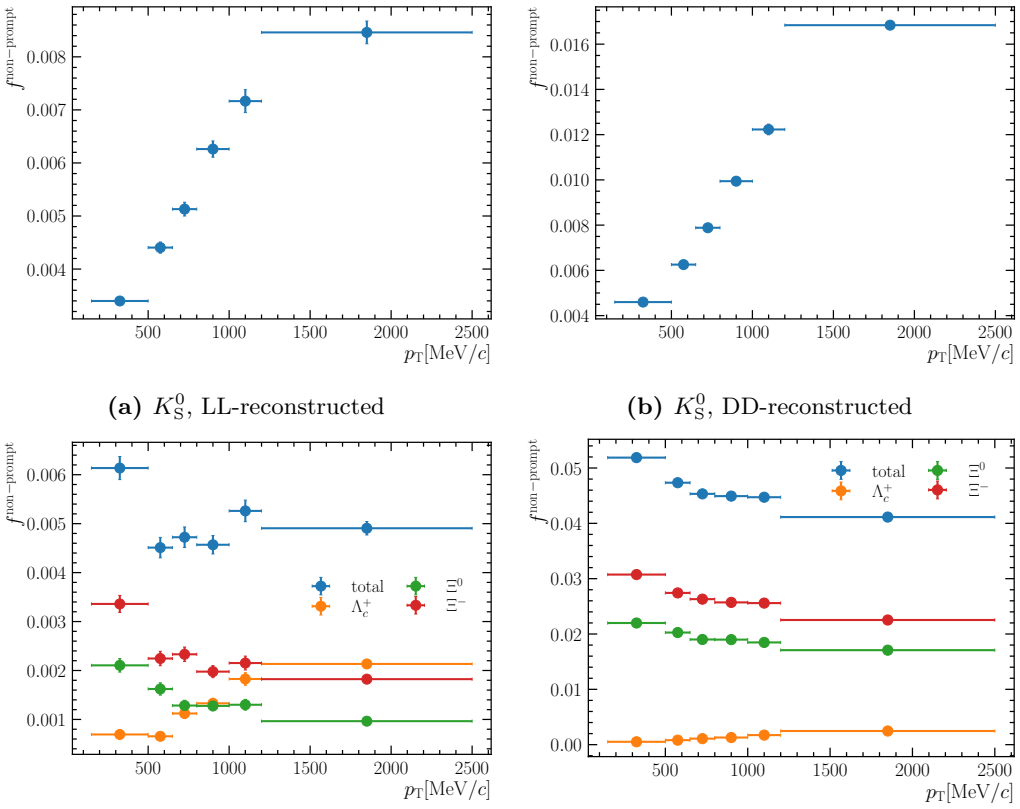

(a) K^0_{S}, LL-reconstructed

(b) K^0_{S}, DD-reconstructed

(c) $\Lambda^0/\bar{\Lambda}^0$, LL-reconstructed

(d) $\Lambda^0/\bar{\Lambda}^0$, DD-reconstructed

Figure 4.22: Residual non-prompt fractions $f^{\text{non-prompt}}$ as a function of p_{T} for LL- and DD-reconstructed K^0_{S} and $\Lambda^0/\bar{\Lambda}^0$ candidates. Values are estimated from truth-matched simulation. For the $\Lambda^0/\bar{\Lambda}^0$ candidates the fractions of the different contributing decays are shown.

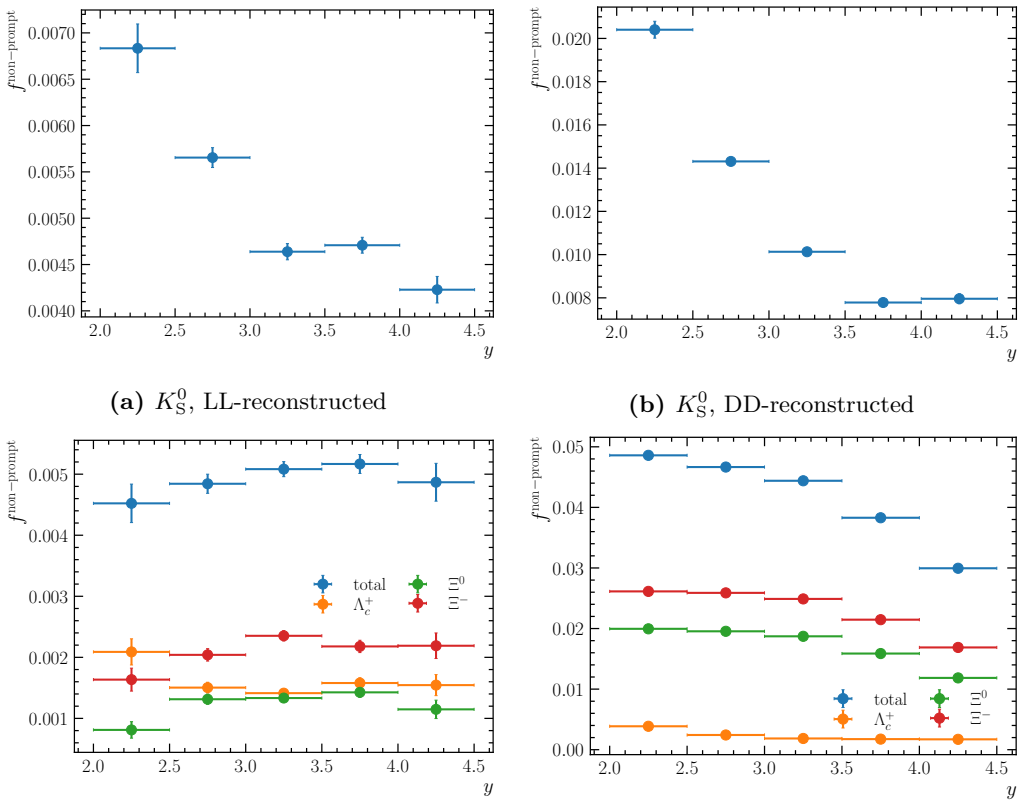

(a) K^0_S, LL-reconstructed

(b) K^0_S, DD-reconstructed

(c) $\Lambda^0/\bar{\Lambda}^0$, LL-reconstructed

(d) $\Lambda^0/\bar{\Lambda}^0$, DD-reconstructed

Figure 4.23: Residual non-prompt fractions $f^{\text{non-prompt}}$ as a function of y for LL- and DD-reconstructed K^0_S and $\Lambda^0/\bar{\Lambda}^0$ candidates. Values are estimated from truth-matched simulation. For the $\Lambda^0/\bar{\Lambda}^0$ candidates the fractions of the different contributing decays are shown.

4.14 Production cross-section ratios

The signal yields N_{sig} from the invariant mass fits in section 4.11, the reconstruction efficiencies $\varepsilon_{\text{reco}}$ and selection efficiencies ε_{sel} from section 4.12 as well as the residual non-prompt fractions $f^{\text{non-prompt}}$ from section 4.13 are combined according to equations 4.14 and 4.3 to build the production cross-section ratios $R(\bar{\Lambda}^0, K^0_{\text{S}})$ and $R(\bar{\Lambda}^0, \Lambda^0)$. The branching fractions $\mathcal{B}(K^0_{\text{S}} \to \pi^+\pi^-) = 0.6920 \pm 0.0005$ and $\mathcal{B}(\bar{\Lambda}^0 \to \bar{p}\pi^+) = 0.639 \pm 0.005$ are taken from Ref. [5]. For the final ratios the weighted average

$$R = \frac{N^{MagDown}_{\text{events}} R^{MagDown} + N^{MagUp}_{\text{events}} R^{MagUp}}{N^{MagDown}_{\text{events}} + N^{MagUp}_{\text{events}}} \tag{4.15}$$

of the results $R^{MagDown}$ and R^{MagUp} for the two magnet polarities is built by weighting to their fractions of events in the dataset. Here, $N^{MagDown}_{\text{events}}$ and $N^{MagUp}_{\text{events}}$ are the total numbers of events in the full 2018 NoBias dataset that are listed in section 4.4. The results for the $R(\bar{\Lambda}^0, K^0_{\text{S}})$ as function of p_{T} and y in the LL and DD track type categories are shown in Figure 4.24. It can be observed that the production of $\bar{\Lambda}^0$ hadrons is suppressed with respect to K^0_{S} hadrons and the suppression is increasing for low p_{T} and high y. Slight differences between $R(\bar{\Lambda}^0, K^0_{\text{S}})$ from the LL-reconstructed and DD-reconstructed candidates are observed that are assumed to originate from additional non-prompt contributions from $V^0 = K^0_{\text{S}}, \Lambda^0, \bar{\Lambda}^0$ created in material interactions. For the DD-sample a larger contribution is expected as more detector material is traversed. This is also suggested by the truth matching plots in Figure 4.1 where the fraction of $V^0 = K^0_{\text{S}}, \Lambda^0, \bar{\Lambda}^0$ having a $\pi^{\pm}$ or $p/\bar{p}$ as parent particle for the K^0_{S} and the $\Lambda^0/\bar{\Lambda}^0$ is larger in the DD-samples. A precise estimation of the contribution from material interactions has to be performed to better understand the differences between the measured production cross-section ratio $R(\bar{\Lambda}^0, K^0_{\text{S}})$ of the LL- and DD-reconstructed production. Moreover, the systematic uncertainties of the measurement need to be estimated. Figure 4.25 shows the ratio $R(\bar{\Lambda}^0, \Lambda^0)$ as a function of p_{T} and y for the LL- and DD-reconstructed Λ^0 and $\bar{\Lambda}^0$ candidates. A trend towards a slight suppression of $\bar{\Lambda}^0$ to Λ^0 hadrons can be observed in all bins. However, the ratio is also well compatible with $R(\bar{\Lambda}^0, \Lambda^0) = 1$, which means that Λ^0 and $\bar{\Lambda}^0$ hadrons are produced in equal amounts. A dedicated study of the differences in detection efficiency of Λ^0 and $\bar{\Lambda}^0$ as well as a precise estimation of the systematic uncertainties of the measurement need to be performed to make more conclusive statements.

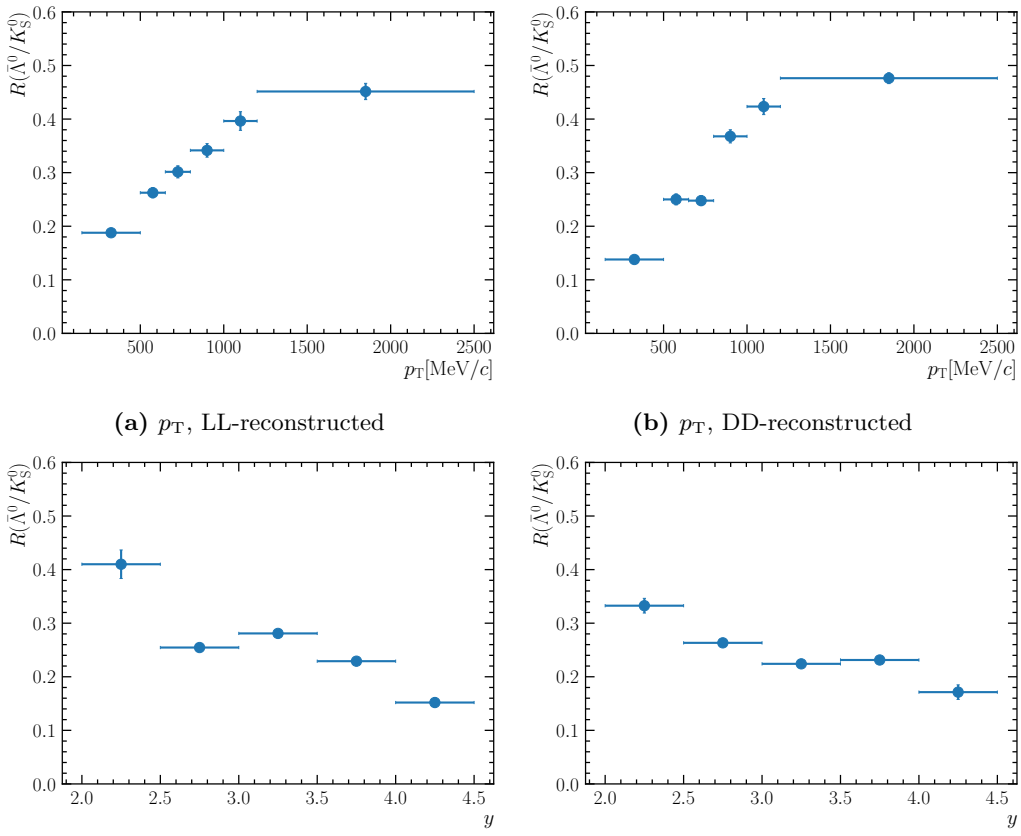

(a) p_T, LL-reconstructed

(b) p_T, DD-reconstructed

(c) y, LL-reconstructed

(d) y, DD-reconstructed

Figure 4.24: Averaged value of $R(\bar{\Lambda}^0, K^0_S)$ as a function of p_T and y for LL- and DD-reconstructed V^0 decays. The error bars include only statistical uncertainties.

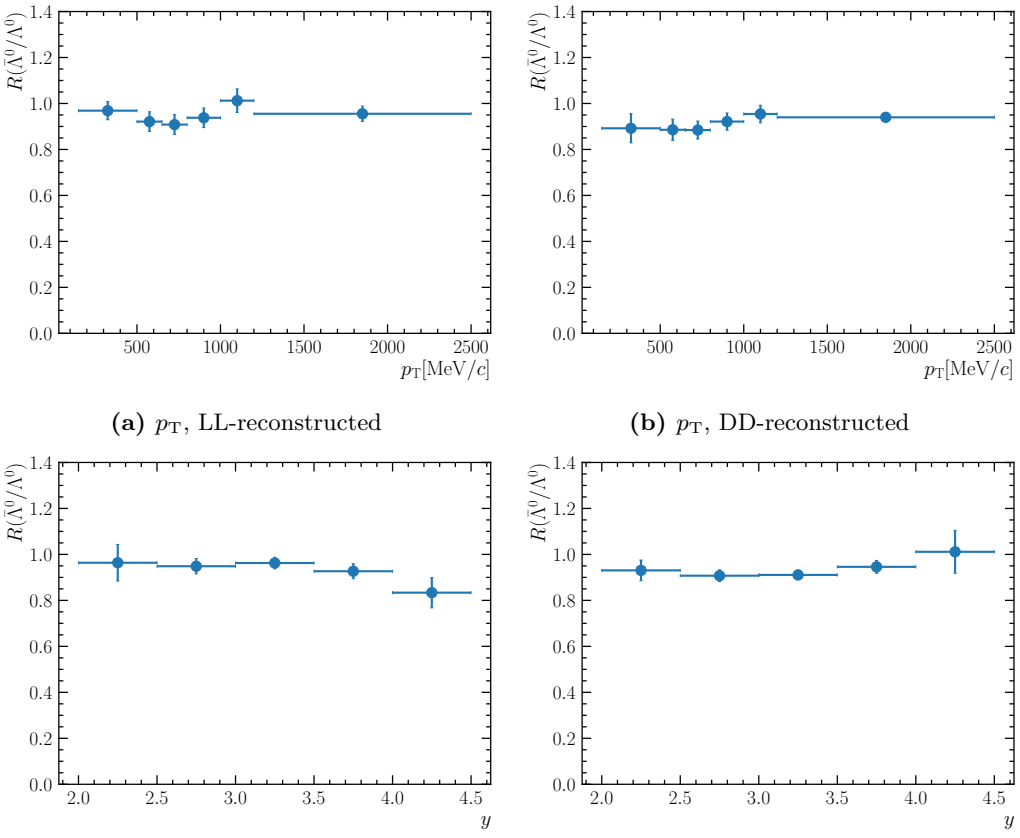

(a) p_T, LL-reconstructed

(b) p_T, DD-reconstructed

(c) y, LL-reconstructed

(d) y, DD-reconstructed

Figure 4.25: Averaged value of $R(\bar{\Lambda}^0, \Lambda^0)$ as a function of p_T and y for LL- and DD-reconstructed V^0 decays. The error bars include only statistical uncertainties.

4.15 Conclusions and outlook

A minimal selection for V^0 candidates based on the IPs of the V^0 hadrons and their decay products has been developed on the full 2018 Run 2 NoBias pp-collision data sample in preparation for an measurement of the production cross-section ratios $R(\bar{\Lambda}^0, K^0_S)$ and $R(\bar{\Lambda}^0, \Lambda^0)$ on early data taken in Run 3. The decay products of the V^0 candidates are reconstructed as two long tracks or two downstream tracks. In addition, the measurement of the $R(\bar{\Lambda}^0, K^0_S)$ and $R(\bar{\Lambda}^0, \Lambda^0)$ at $\sqrt{s} = 13\,\text{TeV}$ has been performed in bins of p_T and y on the Run 2 data set and can be taken as a cross-check once Run 3 data is available. For that, a fitting procedure has been developed to extract signal yields from the invariant mass distributions of all $V^0 = K^0_S, \Lambda^0, \bar{\Lambda}^0$ in all p_T and y bins, track type categories and magnet polarities separately. Reconstruction and selection efficiencies have been calculated on simulation samples. Finally, the amount of background from non-prompt $V^0 = K^0_S, \Lambda^0, \bar{\Lambda}^0$ hadrons coming from hyperon or charm decays has been calculated on simulation and has been applied as a correction to the signal yield. Figure 4.26 shows a comparison between the measured ratio $R(\bar{\Lambda}^0, K^0_S)$, averaged between the magnet polarities, on Run 2 data and Run 1 pp-collision data at $\sqrt{s} = 7\,\text{TeV}$ from a previous LHCb measurement [131] for LL-reconstructed K^0_S and $\bar{\Lambda}^0$ hadrons. A good agreement between the two results can be observed in all p_T bins. However, the slope in the dependence clearly differs. To conclusively interpret whether this observed trend results from

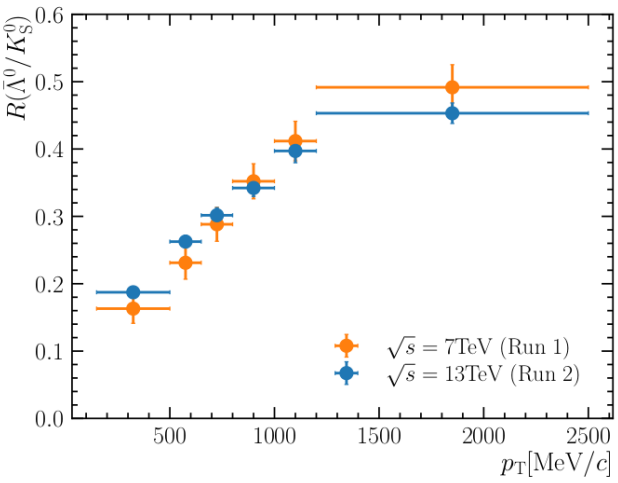

Figure 4.26: Comparison of the ratio $R(\bar{\Lambda}^0, K^0_S)$ between Run 1 and Run 2 data.

the increased centre-of-mass energy, the next steps in this analysis need to study potential residual non-prompt contributions from material interactions and the

systematic uncertainties of the measurement have to be estimated. The slight difference between the measurement on LL-reconstructed and DD-reconstructed V^0 candidates indicates a non-prompt contribution from material interactions.
For the Run 3 measurement the performance of the selection has to be evaluated on real data once it is available. Furthermore, the positions and widths of the V^0 mass peaks can be used to study potential residual mis-alignments of the tracking system that could lead to shifts in the mass peak positions, as well as worse momentum and hence mass peak resolutions. Once a precise measurement of the integrated luminosity $\mathcal{L}$ is available, the measurement can be extended to measure also the total V^0 production cross-sections by using equation 4.1. For that a precise study on the data-simulation agreement of tracking efficiencies needs to performed. Furthermore, the trigger selection efficiency, *i.e.* the prescales for the NoBias trigger, need to be taken into account.

Chapter 5

Summary - Résumé - Zusammenfassung

5.1 Summary

The LHCb experiment at CERN is currently undergoing the first major upgrade (LHCb Upgrade I) [104, 105] of its detector to operate at a five times higher instantaneous luminosity of $\mathcal{L} = 2 \times 10^{33}\,\mathrm{cm}^{-2}\mathrm{s}^{-1}$ during the next data taking period (Run 3). It will be equipped with a new set of tracking detectors to match the conditions of a higher track multiplicity and an increased radiation damage. This includes a new silicon-pixel Vertex Locator (VELO) enclosing the collision region at a distance of 5.1 mm to reconstruct primary and decay vertices of b and c hadrons, a small silicon-strip tracker (UT) upstream of the LHCb dipole magnet as well as three large-area Scintillating Fibre Tracker (SciFi) stations with four layers each downstream of the magnet. Another major change for the LHCb Upgrade I is the upgrade of the trigger system, where the removal of the formerly used Level-0 (L0) hardware trigger not only requires a full detector read-out at the collision rate of 40 MHz but also a complete re-design of the software-based high-level trigger (HLT) to be able to cope with a higher demanded throughput of data of 30 MHz. The first stage of the upgraded trigger system (HLT1) performs a partial event reconstruction and selection and is for the first time fully implemented to run on about 200 Graphics Processing Units (GPU) cards of type NVIDIA RTX A5000 at the beginning of Run 3.
The delay in the installation of the UT required the development of alternative track reconstruction algorithms for HLT1 to the so far baseline algorithm [116], the *forward tracking*. An adaption of the *Seeding & Matching* algorithms used for HLT2

[124] has been developed for HLT1 as part of this thesis.
The Seeding is a standalone reconstruction of track segments in the SciFi that consist of two separate algorithms performing the pattern recognition in the xz-plane, in which the tracks are bent on a parabola-like trajectory by the magnetic field, and the yz-plane where no magnetic field is present so that tracks can be modeled as straight lines. The seeding in the xz-plane builds two- and three-hit combinations from hits in three out of the six SciFi x-layers, in which fibres are aligned vertically. The parabola from the three-hit combinations is then extrapolated to the remaining x-layers to look for at least two additional hits. The seeds found in the xz-plane are used to predict hit positions in the remaining six SciFi layers, the u- and v-layers, that are tilted by $\pm 5^\circ$ with respect to the x-layers. Due to the tilted geometry many fibres in the stereo layers can have the same x-position, so that a large search window in the slope t_y has to opened for hits in the first considered stereo layer. Assuming that the track originated from (0,0,0) the t_y from the straight line to the first hit can be extrapolated to the next layer and a more refined search window in t_y can be defined for the second hit. This procedure is then iterated for all hits in the remaining layers by using the t_y from the already found hits. SciFi seeds with at least ten found hits are accepted.
After the seeding in the SciFi, a matching algorithm attempts to find pairs of SciFi seeds and VELO tracks that originated from the same particle. By matching these track segments, so-called long tracks are reconstructed. Long tracks come from particles that have traversed and left signals in all tracking detectors of LHCb, whereas so-called downstream tracks originate from particles that decay downstream of the VELO and therefore only leave signals in the UT and SciFi.
The performance of the *Seeding & Matching* is evaluated and found to have compatible tracking efficiency with the forward tracking with $> 90\,\%$ for long tracks from B decays over a large p/p_{T} range. In addition, a strong improvement in the tracking efficiency for low-p/p_{T}, as can be seen in the left figure below, is obtained. The total ghost rate is found at a level of about $10\,\%$ which is about twice as high as for the *forward tracking* and mostly related to the lack from additional hits in the UT. The throughput of the HLT1 algorithm sequence including the *Seeding & Matching* is measured to be around 170 kHz per NVIDIA RTX A5000 GPU card. Running this HLT1 sequence on about 200 of such GPU cards matches well with the required throughput of 30 MHz. The *Seeding & Matching* is now used as the new baseline track reconstruction algorithm for HLT1 and currently being commissioned on the first data of Run 3.
To ensure the recording of high-quality data for physics analyses the performance of the upgraded detector needs to be studied in detail with the early data of Run 3. For this purpose, a measurement of production cross-section ratios of the promptly-produced, i.e. directly in the pp-collision at $\sqrt{s} = 13\,\mathrm{TeV}$, $V^0 = K^0_{\mathrm{S}}, \Lambda^0, \bar{\Lambda}^0$ hadrons is prepared for the first data from Run 3 as part of this thesis. An analysis framework

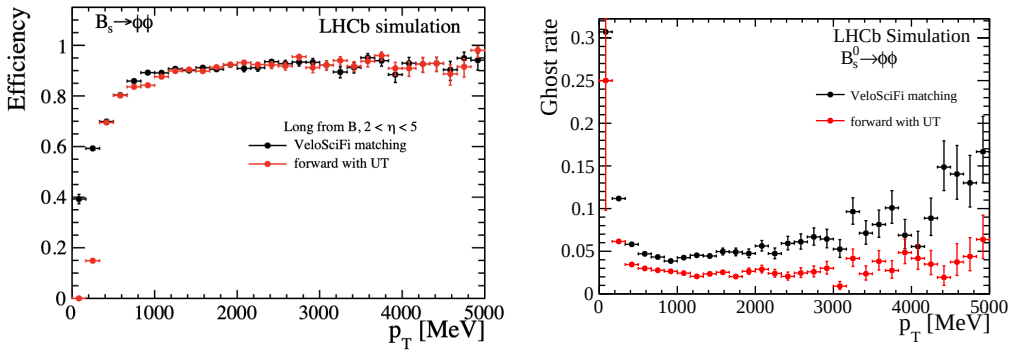

Comparison of the track reconstruction efficiency and the ghost rate as a function of p between the *Seeding & Matching* and the *forward tracking* in HLT1.

measuring the ratios

$$R(\bar{\Lambda}^0, K_S^0) = \frac{\sigma(pp \to \bar{\Lambda}^0 X)}{\sigma(pp \to K_S^0 X)} \quad \text{and} \quad R(\bar{\Lambda}^0, \Lambda^0) = \frac{\sigma(pp \to \bar{\Lambda}^0 X)}{\sigma(pp \to \Lambda^0 X)}$$

as a function of p_T and y is developed with the full 2018 LHCb data set recorded during Run 2. V^0 decays are very suitable for a measurement on very early data since the production cross-sections are huge and their decay channels $K_S^0 \to \pi^+\pi^-$, $\Lambda^0 \to p\pi^-$ and $\bar{\Lambda}^0 \to \bar{p}\pi^+$ have large branching fractions and are easy to reconstruct. The results obtained for the Run 2 data will then be used as a reference once the first physics data in Run 3 is recorded. For the Run 2 measurement V^0 decays are

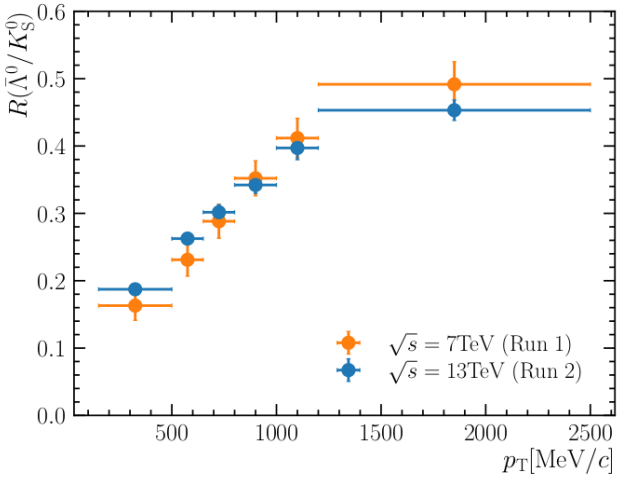

Comparison of the ratio $R(\bar{\Lambda}^0, K_S^0)$ between Run 1 and Run 2 data.

reconstructed in two track type categories, where the final state hadrons are either both long (LL-reconstructed) or downstream tracks (DD-reconstructed). An impact parameter (IP)-based selection with minimal amount of variables is developed for selecting V^0 decays in Run 3. The IP's of the V^0 and its decay products are combined into a single variable $\mathcal{F}_{\text{IP}}$ for which an optimal cut point is determined separately for K^0_{S} and $\Lambda^0/\bar{\Lambda}^0$ decays and for the two track type categories. Backgrounds from non-prompt V^0 hadrons coming from hyperonic or charm decays are suppressed by an additional selection on the IP of the V^0 and their residual fraction is estimated on simulation. Invariant mass fits are performed in all p_{T} and y bins to extract signal yields. The reconstruction and selection efficiencies for each bin are estimated on simulation. The obtained ratio $R(\bar{\Lambda}^0, K^0_{\text{S}})$ shows a suppression of $\bar{\Lambda}^0$ with respect to K^0_{S} hadrons and its p_{T} dependence agrees well with previously measured ratios on Run 1 data [131] as can be seen in the figure above. The ratio $R(\bar{\Lambda}^0, \Lambda^0)$ is found slightly below 1, which favours a production of Λ^0 over $\bar{\Lambda}^0$ hadrons. For the next steps of this analysis the systematic uncertainties of the ratio measurements need to be determined as well as a study of potential non-prompt contributions from material interaction has to be performed. Furthermore, for $R(\bar{\Lambda}^0, \Lambda^0)$ differences in the detection efficiency of p and $\bar{p}$ needs to be studied.

5.2 Résumé

L'expérience LHCb au CERN est en train d'effectuer un majeur upgrade (LHCb Upgrade I) [104, 105] de son détecteur afin de fonctionner à une luminosité instantanée cinq fois plus élevée de $\mathcal{L} = 2 \times 10^{33}\,\text{cm}^{-2}\text{s}^{-1}$ pendant la prochaine période de prise de données (Run 3). Il sera équipé d'un nouvel ensemble de trajectographes pour s'adapter aux conditions d'une multiplicité de traces plus élevée et d'un rayonnement accru. Il s'agit notamment d'un nouveau Vertex Locator (VELO) à pixels en silicium entourant la région de collision à une distance de 5.1 mm pour reconstruire les sommets primaires et de désintégration des hadrons b et c, d'un petit suiveur à bandes de silicium en amont (UT) de l'aimant dipôle de LHCb ainsi que de trois stations à fibres scintillantes (SciFi) de grande surface avec quatre couches chacune en aval de l'aimant. La mise à ajour du système de trigger constitue un autre changement majeur dans le cadre du premier upgrade de LHCb. En effet, la suppression du hardware trigger (L0), utilisé jusqu'à présent, nécessite non seulement une lecture complète du détecteur au taux de collision de 40 MHz, mais aussi une reconception complète du trigger de haut niveau (HLT) basé sur le software, afin de pouvoir faire face à un débit de données de 30 MHz. La première étape du système de trigger (HLT1) effectue une reconstruction et sélection partielles des événements et est pour

la première fois entièrement mise en œuvre pour fonctionner sur environ 200 cartes graphique (GPU) NVIDIA RTX A5000 au début du Run 3.
Le retard dans l'installation du UT a nécessité le développement d'algorithmes de reconstruction alternatifs à l'algorithme de base pour HLT1 [116], le *forward tracking*. Une adaptation des algorithmes *Seeding & Matching* utilisés pour HLT2 [124] a été développée pour HLT1 dans le cadre de cette thèse.
Le seeding est une reconstruction autonome des segments de trace dans le SciFi qui consiste en deux algorithmes distincts effectuant premièrement la reconnaissance des trajectoires dans le plan xz dans lequel les traces sont courbées de manière parabolique par le champ magnétique, et le plan yz dans lequel aucun champ magnétique n'est présent de sorte que les traces peuvent être modélisées comme des lignes droites. Le seeding dans le plan xz construit des combinaisons à deux et trois hits à partir de trois sur les six layers du SciFi x avec des fibres alignées verticalement. La parabole des combinaisons à trois hits est ensuite extrapolée aux layers x restantes pour rechercher au moins deux hits supplémentaires. Les seeds trouves dans le plan xz sont ensuite utilisées pour prédire la position dans les six layers du SciFi restantes, les layers u- et v, qui sont inclinées de $\pm 5°$ par rapport aux layers x. En raison de cette l'inclinaison, plusieurs fibres dans les layers stéréo peuvent avoir la même position x, de sorte qu'il faut partir de plusieurs traces puisqu'aucune information y n'est présente. En supposant que la trace commence en (0,0,0), la pente t_y de la ligne droite jusqu'au premier hit peut être extrapolée au layer suivant et une fenêtre de recherche plus petite en t_y peut être définie pour la deuxième hit. Cette procédure est ensuite itérée pour tous les résultats dans les layers restantes en utilisant les t_y des hits déjà trouvés. Les seeds SciFi avec au moins dix hits trouvées sont acceptées. Après le seeding dans le SciFi, un algorithme d'appariement cherche à trouver des paires de seeds SciFi et de traces VELO qui proviennent de la même particule. En faisant correspondre ces segments de trajectoire, les traces dites longues sont reconstruites. Les traces longues proviennent de particules qui ont traversé et laissé un signal sur tous les détecteurs de tracking de LHCb, tandis que les traces dites downstream proviennent de particules qui se désintègrent en aval du VELO et ne laissent donc des signaux que dans l'UT et le SciFi.

Les performances du *Seeding & Matching* sont évaluées et il s'avère que l'efficacité du tracking est compatible avec l'algorithme de forward avec $> 90\,\%$ pour les longues traces des désintégrations B sur un large range de p/p_{T}. De plus, une forte amélioration de l'efficacité de tracking pour les faibles p/p_{T} est visible sur la figure de gauche ci-dessous. Le taux de ghost total est d'environ $10\,\%$, ce qui est environ deux fois plus élevé que pour le forward et est principalement lié à l'absence des hits supplémentaires dans l'UT. Le débit de la séquence de l'algorithme HLT1, y compris le *Seeding & Matching*, est mesuré à environ 170 kHz par carte GPU NVIDIA RTX A5000. L'exécution de HLT1 sur environ 200 de ces cartes GPU correspond donc bien au débit requis de 30 MHz. Le *Seeding & Matching* est maintenant utilisé

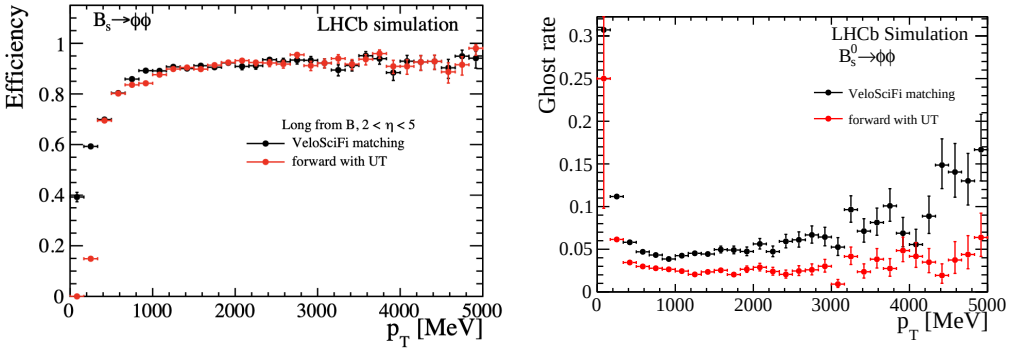

Comparaison de l'efficacité de la reconstruction des traces et le ghost rate en fonction de p_T entre le *Seeding & Matching* et le *forward tracking* dans HLT1.

comme nouvel algorithme de reconstruction de traces de référence pour HLT1 et est actuellement mis en service sur les premières données du Run 3.
Pour garantir l'enregistrement de données de physique de haute qualité pour les analyses de physique les performances du détecteur amélioré doivent être étudiées en détail avec les premières données du Run 3. À cette fin, une mesure des rapports de sections efficaces de production des $V^0 = K^0_S, \Lambda^0, \bar{\Lambda}^0$ promptement produits, c'est-à-dire directement dans la collision pp à $\sqrt{s} = 13\,\text{TeV}$, est préparée pour les premières données du Run 3 dans le cadre de cette thèse. Un cadre d'analyse mesurant les rapports

$$R(\bar{\Lambda}^0, K^0_S) = \frac{\sigma(pp \to \bar{\Lambda}^0 X)}{\sigma(pp \to K^0_S X)} \qquad \text{et} \qquad R(\bar{\Lambda}^0, \Lambda^0) = \frac{\sigma(pp \to \bar{\Lambda}^0 X)}{\sigma(pp \to \Lambda^0 X)}$$

en fonction de p_T et de y est développé avec l'ensemble des données 2018 du LHCb enregistrées au cours du Run 2. Les désintégrations V^0 sont très appropriées pour une mesure sur des premières données car la section efficace de production est énorme et leurs canaux de désintégration $K^0_S \to \pi^+\pi^-$, $\Lambda^0 \to p\pi^-$ et $\bar{\Lambda}^0 \to \bar{p}\pi^+$ ont de grandes fractions de branchement et sont faciles à reconstruire. Les résultats obtenus pour les données du Run 2 seront ensuite utilisés comme référence lorsque les premières données de physique du Run 3 seront enregistrées. Pour la mesure du Run 2, les désintégrations V^0 sont reconstruites dans deux catégories de types de traces, où les hadrons de l'état final sont soit des traces longues (LL-reconstruit) soit des traces downstream (DD-reconstruit). Une sélection basée sur les paramètres d'impact (IP) avec un nombre minimal de variables est développée pour sélectionner les désintégrations V^0 dans le Run 3. Les IP du V^0 et de ses produits de désintégration sont combinés en une seule variable $\mathcal{F}_{\text{IP}}$ pour laquelle un point de coupure optimal est déterminé séparément pour les désintégrations K^0_S et $\Lambda^0/\bar{\Lambda}^0$ et pour les deux catégories de type de trace. Les particules provenant d'hadrons V^0 non-prompts

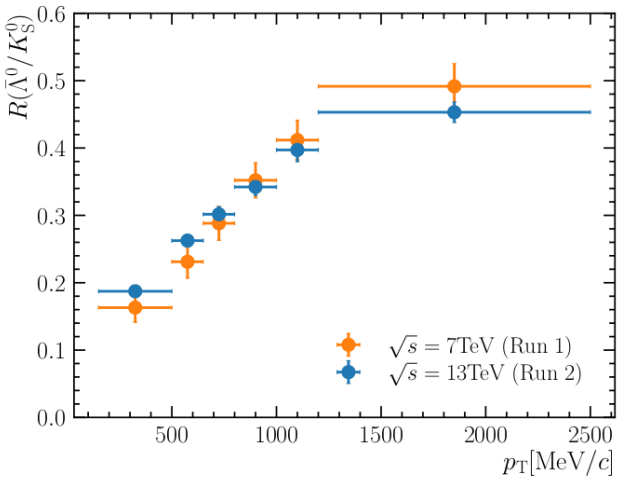

Comparaison du ratio $R(\bar{\Lambda}^0, K^0_S)$ entre les données du Run 1 et du Run 2.

issus de désintégrations hyperoniques ou de charme sont supprimés par une sélection supplémentaire sur l'IP du V^0 et leur fraction résiduelle est estimée par simulation. Des ajustements de masse invariante sont effectués dans toutes les tranches de p_T et de y pour extraire les efficacité de selection du signal. Les efficacités de reconstruction et de sélection pour chaque bin kinematique sont estimées par simulation. Le rapport obtenu $R(\bar{\Lambda}^0, K^0_S)$ montre une suppression de $\bar{\Lambda}^0$ par rapport aux hadrons K^0_S et sa dépendance p_T s'accorde bien avec les rapports précédemment mesurés sur les données de Run 1 [131] comme on peut le voir sur la figure au-dessous. Le rapport $R(\bar{\Lambda}^0, \Lambda^0)$ est légèrement inférieur à 1, ce qui favorise la production de Λ^0 par rapport aux hadrons $\bar{\Lambda}^0$. Pour les prochaines étapes de cette analyse, les incertitudes systématiques des mesures du rapport doivent être déterminées et une étude des contributions potentielles non-prompt provenant de l'interaction avec la matière doit être réalisée. Successivement, pour $R(\bar{\Lambda}^0, \Lambda^0)$, les différences entre l'efficacité de détection de p et de $\bar{p}$ doivent être étudiées.

5.3 Zusammenfassung

Das LHCb-Experiment am CERN durchläuft derzeit das erste große Upgrade (LHCb Upgrade I) [104, 105] seines Detektors, um während der nächsten Datennahmeperiode (Run 3) Daten mit einer verfünffachten instantanen Luminosität $\mathcal{L} = 2 \times 10^{33}\,\mathrm{cm}^{-2}\mathrm{s}^{-1}$ nehmen zu können. Dafür wird LHCb mit einem vollständig

neuen Satz an Spurfindungsdetektoren ausgestattet, um sich an die Bedingungen einer höheren Spurmultiplizität und erhöhter Strahlungsschäden anzupassen. Dazu gehört ein neuer Siliziumpixel Vertex Locator (VELO), der die Kollisionsregion in einem Abstand von 5.1 mm umschließt, um primäre und Zerfallsvertizes von b- und c-Hadronen zu rekonstruieren, ein Siliziumstreifen-Detektor (UT) vor dem LHCb Dipolmagneten sowie drei großflächige Spurfindungsstationen mit je vier Lagen szintillierender Fasern (SciFi) hinter dem Magneten. Desweiteren absolviert auch das Triggersystem des LHCb-Experiments ein größeres Upgrade, bei dem das Entfernen des früher verwendeten Level-0 (L0) Hardware-Triggers nicht nur ein vollständiges Auslesen des Detektors bei einer Kollisionsrate von 40 MHz erfordert, sondern auch eine komplette Neugestaltung des Software-basierten High-Level-Triggers (HLT), um den resultierenden notwendigen Datendurchsatz von 30 MHz bewältigen zu können. Die erste Stufe des Triggersystems (HLT1) führt eine Teilrekonstruktion und Selektion der Kollisionsereignisse durch und ist zum ersten Mal vollständig implementiert für die Anwendung auf $\mathcal{O}(200)$ Graphikkarten (GPUs) des Typs NVIDIA RTX A5000 zu Beginn von Run 3. Verzögerungen in der Installation des UT-Detektors haben die Entwicklung alternativer Spurrekonstruktionsalgorithmen zu dem bisher verwendenten *forward tracking* für HLT1 erfordert. Die *Seeding & Matching*-Algorithmen [124], die für HLT2 entwickelt wurden, wurden im Rahmen dieser Arbeit für die Anwendung in HLT1 angepasst. Das Seeding ist eine eigenständige Rekonstruktion von Spursegmenten im SciFi-Detektor, die aus zwei separaten Algorithmen besteht. Diese führen eine Mustererkennung in der xz-Ebene, in der die Teilchenspuren durch das Magnetfeld auf eine parabel-förmige Bahn abgelenkt werden, und der yz-Ebene, in der kein Magnetfeld vorhanden ist und Spuren als linear angenommen werden können, durch. Das Seeding in der xz-Ebene bildet Kombinationen aus zwei und drei Detektorhits in drei von den sechs vertikal ausgerichteten x-Lagen des SciFi-Detektors. Eine Extrapolation der Parabel, geformt durch die drei Hits, zu den übrigen x-Lagen wird danach verwendet um nach mindestens zwei zusätzlichen Hits zu suchen. Die in der xz-Ebene gefundenen Seeds werden dann zur Vorhersage der Hit-Positionen in den verbleibenden sechs SciFi-Lagen, den u und v-Lagen, verwendet, die gegenüber den x-Lagen um $\pm 5^\circ$ geneigt sind. Aufgrund der gekippten Geometrie können viele Fasern in den u/v-Ebenen die gleiche x-Position haben, so dass für die erste brtrachtete Lage ein breites Suchfenster in der Steigung t_y für potentiell passende Hits betrachtet werden muss da keine y-Information vorhanden ist. Unter der Annahme, dass die Teilchenspur von (0,0,0) ausging, kann die Steigung t_y der Geraden zum ersten Hit auf die nächste Lage extrapoliert und ein verfeinertes Suchfenster in t_y für den zweiten Hit definiert werden. Dieses Verfahren wird dann für alle Hits in den verbleibenden Lagen iteriert, indem die t_y der bereits gefundenen Hits verwendet werden. SciFi-Seeds mit mindestens zehn gefundenen Hits werden akzeptiert. Nach dem SciFi-Seeding versucht ein Matching-Algorithmus, Paare von SciFi-Seeds und VELO-Spuren zu finden, die vom selben Teilchen stammen. Durch

den Kombination dieser Spursegmente werden so genannte *long tracks* rekonstruiert. Long tracks stammen von Teilchen, die alle Spurfindungsdetektoren von LHCb durchquert und dort Signale hinterlassen haben, während so genannte downstream tracks von Teilchen stammen, die hinter dem VELO zerfallen und daher nur Signale im UT und SciFi hinterlassen.
Die Performance des *Seeding & Matching* zeigt, dass die Spurfindungseffizienz von $> 90\,\%$ mit der des *forward tracking* für long tracks aus B-Zerfällen über einen großen p/p_{T}-Bereich kompatibel ist. Darüber hinaus ist eine starke Verbesserung der Spurfindungseffizienz für niedrige p/p_{T}-Werte zu verzeichnen, wie in der linken Abbildung unten zu sehen ist. Die totale *ghost rate* liegt bei $10\,\%$, was etwa doppelt

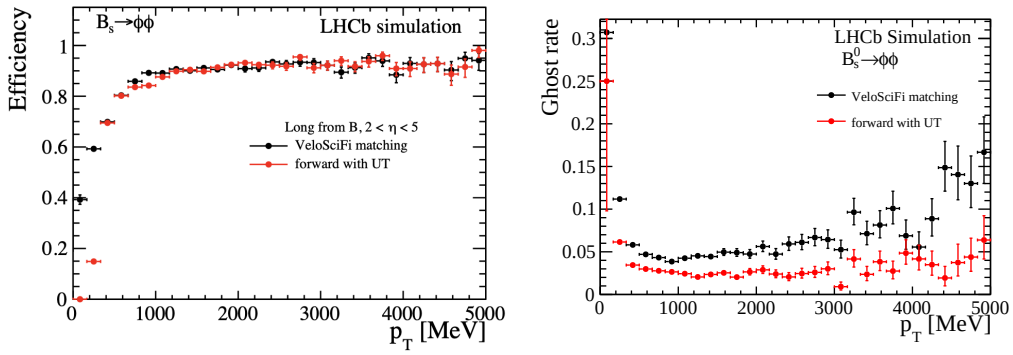

Vergleich der Spurfindungseffizienz und der ghost rate als Funktion von p_{T} und y zwischen dem *Seeding & Matching* und dem *forward tracking* in HLT1.

so hoch ist wie beim *forward tracking* und hauptsächlich auf das Fehlen zusätzlicher Hits im UT zurückzuführen ist. Der Datendurchsatz der HLT1-Algorithmus-Sequenz einschließlich des *Seeding & Matching* wird mit etwa 170 kHz pro NVIDIA RTX A5000 GPU-Karte gemessen. Die Ausführung von HLT1 auf etwa 200 solcher GPU-Karten entspricht daher gut dem erforderten Durchsatz von 30 MHz. Das *Seeding & Matching* wird nun als neuer Hauptalgorithmus für die Rekonstruktion von Spuren für HLT1 verwendet und wird derzeit mit den ersten Run 3-Daten in Betrieb genommen.
Um die Aufnahme von qualitativ hochwertigen Daten für Physik-Analysen zu gewährleisten muss die Performance des LHCb Upgrade I-Detektors mit Hilfe der ersten Daten von Run 3 ausführlich untersucht werden. Zu diesem Zweck wurde im Rahmen dieser Arbeit eine Messung der Produktionswirkungsquerschnittsverhältnisse von prompt-erzeugten, d.h. direkt in der pp-Kollision bei $\sqrt{s} = 13\,\mathrm{TeV}$, $V^0 = K^0_{\mathrm{S}}, \Lambda^0, \bar{\Lambda}^0$-Hadronen für die ersten Daten von Run 3 vorbereitet. Ein Analyse-

Framework zur Messung der Verhältnisse

$$R(\bar{\Lambda}^0, K^0_S) = \frac{\sigma(pp \to \bar{\Lambda}^0 X)}{\sigma(pp \to K^0_S X)} \qquad \text{and} \qquad R(\bar{\Lambda}^0, \Lambda^0) = \frac{\sigma(pp \to \bar{\Lambda}^0 X)}{\sigma(pp \to \Lambda^0 X)}$$

als Funktion von p_T und y wird mit dem gesamten 2018er LHCb-Datensatz entwickelt, der während Run 2 aufgezeichnet wurde. V^0-Zerfälle eignen sich sehr gut für eine Messung an sehr frühen Daten, da der Produktionswirkungsquerschnitt sehr groß ist, die Zerfallskanäle $K^0_S \to \pi^+\pi^-$, $\Lambda^0 \to p\pi^-$ und $\bar{\Lambda}^0 \to \bar{p}\pi^+$ große Verzweigungsverhältnisse haben und leicht zu rekonstruieren sind. Die für die Run 2-Daten erzielten Ergebnisse werden dann als Referenz verwendet, sobald die ersten Daten für Physik-Analysen in Run 3 aufgezeichnet werden. Für die Messung in Run 2

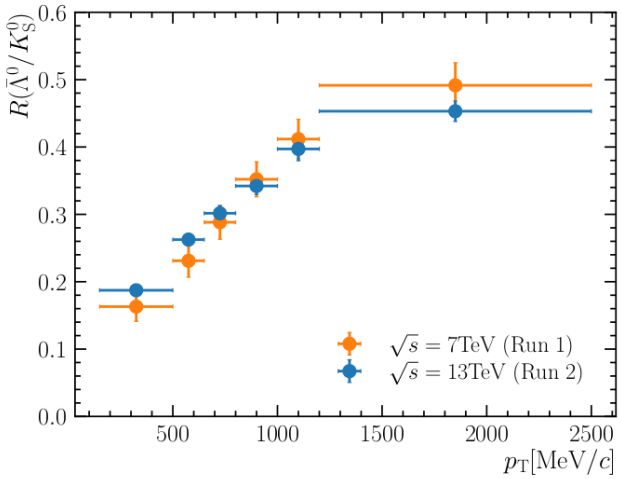

Vergleich des Verhältnisses $R(\bar{\Lambda}^0, K^0_S)$ zwischen Run 1 und Run 2-Daten.

werden V^0-Zerfälle in zwei Spurtypen rekonstruiert, wobei die Endzustandshadronen entweder long (LL-rekonstruiert) oder downstream tracks (DD-rekonstruiert) sind. Für die Run 3-Selektion der V^0-Zerfälle wurde eine auf Stoßparametern (IP) basierende Selektion mit einer minimalen Anzahl von Variablen entwickelt. Die IPs vom V^0 und seinen Zerfallsprodukten werden zu einer einzigen Variablen $\mathcal{F}_{\text{IP}}$ zusammengesetzt, für die ein optimaler Schnittpunkt separat für K^0_S- und $\Lambda^0/\bar{\Lambda}^0$-Zerfälle und für die beiden Spurtypkategorien bestimmt wird. Untergründe von nicht-prompten V^0-Hadronen, die von hyperonischen oder charm-Zerfällen stammen, werden durch eine zusätzliche Selektion des IP der V^0-Hadronen unterdrückt und ihr Restanteil wird mit Hilfe von simulierten Daten abgeschätzt. In allen p_T- und y-Bins werden Fits an die Verteilung der invarianten Masse durchgeführt, um die Anzahl an Signalereignissen zu ermitteln. Die Rekonstruktions- und Selektionseffizienzen für jeden Bin werden mit Hilfe von simulierten Daten geschätzt. Das erhaltene

Verhältnis $R(\bar{\Lambda}^0, K^0_S)$ zeigt eine Unterdrückung von $\bar{\Lambda}^0$ im Vergleich zu K^0_S-Hadronen, und seine p_T-Abhängigkeit stimmt gut mit zuvor gemessenen Verhältnissen auf Run 1-Daten [131] überein, wie in der Abbildung oben zu sehen ist. Das Verhältnis $R(\bar{\Lambda}^0, \Lambda^0)$ liegt knapp unter 1, was für eine erhöhte Produktion von Λ^0- gegenüber $\bar{\Lambda}^0$-Hadronen spricht. Als nächste Schritte dieser Analyse müssen die systematischen Unsicherheiten der Verhältnismessungen bestimmt und eine Studie über mögliche nicht-prompte Beiträge aus Wechselwirkungen mit dem Detektormaterial durchgeführt werden. Darüber hinaus müssen für $R(\bar{\Lambda}^0, \Lambda^0)$ Unterschiede in der Detektion von p und $\bar{p}$ untersucht werden.

Appendices

A Kalman filter

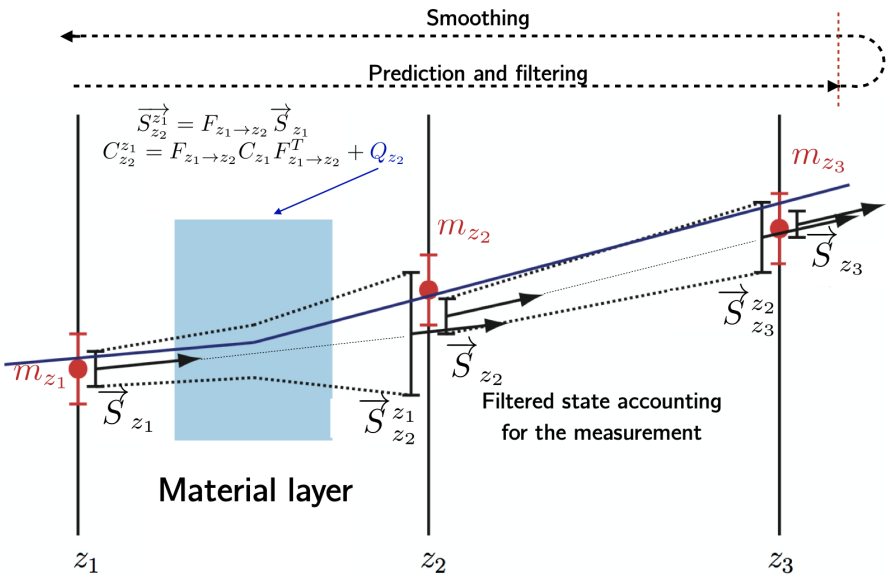

Figure A1: Working principle of a Kalman filter. $\vec{S}^{z_i}_{z_j}$ denotes the predicted state vector at z_j obtained with the propagation matrix $F_{z_i \to z_j}$ and the filtered state vector from $\vec{S}_{z_i}$ at z_i. The measurements at the different detector layers at z_i are given by m_{z_i}. Finally the Kalman filter is run in reversed order for smoothing the Kalman filter. Taken from Ref. [113].

The starting point of a Kalman filter is initialized with a track state seed (state vector $\vec{S}_{z_0}$ and covariance matrix C_{z_0}) that was previously found by the pattern recognition. Every iteration of the Kalman filter moves from one plane at z_i to

the next plane at z_j using a *prediction* and a *filtering step*. An example for two iterations is shown in Figure A1. The prediction step transforms the found state vector $\vec{S}_{z_i}$ in the layer at z_i into a predicted state vector $\vec{S}_{z_j}^{z_i}$ in the layer at z_j using the transport matrix $F_{z_i \to z_j}$ using

$$\vec{S}_{z_j}^{z_i} = F_{z_i \to z_j} \vec{S}_{z_i} \tag{1}$$

The transport matrix contains the information about the underlying track model that is used for the fit. The covariance matrix C_{z_i} is transformed by

$$C_{z_j}^{z_i} = F_{z_i \to z_j} C_{z_i} F_{z_i \to z_j}^T + Q_{z_j}, \tag{2}$$

where Q_{z_j} is an additional noise matrix that takes into account multiple Coulomb scattering and energy losses from material interactions of the particle in the material that is between z_i and z_j. The filtering step is comparing a measurement m_{z_j} with covariance matrix V_{z_j} at z_j to the predicted state vector by building the residual

$$r_{z_j}^{z_i} = m_{z_j} - H_{z_j} \vec{S}_{z_j}^{z_i} \tag{3}$$

and its error

$$R_{z_j}^{z_i} = V_{z_j} + H_{z_j} C_{z_j}^{z_i} H_{z_j}^T, \tag{4}$$

with H_{z_j} being another matrix projecting the state vector into the measurement plane. Therefore, H_{z_j} is trivial if the z-position of the track state and the measurement plane are identical. In order to obtain the best estimate for the track state vector at z_j the residual and its error are used to build a χ^2 function which is minimized. This results in

$$\vec{S}_{z_j} = \vec{S}_{z_j}^{z_i} + K_{z_j} r_{z_j}^{z_i} \tag{5}$$

$$C_{z_j} = (1 - H_{z_j} K_{z_j}) C_{z_j}^{z_i} \tag{6}$$

being the best estimates for the state vector and its covariance matrix at z_j. Here K_{z_j} corresponds to the gain matrix of the Kalman filter given by

$$K_{z_j} C_{z_j}^{z_i} H_{z_j}^T (R_{z_j}^{z_i})^{-1}. \tag{7}$$

The residuals of the filtered track state are then given by

$$r_{z_j} = (1 - H_{z_j} K_{z_j}) r_{z_j}^{z_i} \tag{8}$$

$$R_{z_j} = (1 - H_{z_j} K_{z_j}) R_{z_j}^{z_i} \tag{9}$$

The final quality of the track fit with the Kalman filter is given by

$$\chi^2 = \sum_{i=0}^{n_{\text{Hits}}^{\text{accepted}}} \frac{r_i}{R_i}, \tag{10}$$

where $n_{\text{Hits}}^{\text{accepted}}$ is number of kept hits of the track. Hits can be removed if the individual χ_i^2 contribution exceeds a predefined threshold and they are likely to be outliers that were falsely added to the track candidate by the pattern recognition. The χ^2 is then used as track quality parameter to decide whether the track candidate is a real track. An additional step that can be made to improve the parameter estimation of the Kalman filter is a smoothing step. Here, after the Kalman filter is applied once it is repeated in the reversed order using the final track state as initial seed.

B Scintillating fibres

The fibres used for the SciFi tracker are composed of a core and two thin (each $< 3\,\%$ of the total fibre diameter) claddings. The core is made of a doped polystyrene plastic scintillator[1] to create photons from traversing ionizing particles whereas the two claddings (poly(methyl methacrylate) and a fluorinated polymer) with decreasing refractive indices ensure the guidance of the produced light via internal reflection towards the end of the fibre where the SiPMs or mirrors are located. Table B1 lists the refractive indices of the materials used in the core and the claddings of the fibre. Figure 2.33a shows the structure of the fibre schematically.

Table B1: Refractive indices n of the materials used for the scintillating fibres as well as there fraction d/d_{fibre} of the total diameter $d_{\text{fibre}} = 250\,\mu\text{m}$ of the fibre. Data taken from Ref. [138].

Fibre component	Material	n	d/d_{fibre}
Scintillating core	Polystyrene	1.59	94 %
Inner cladding	Poly(methyl methacrylate)	1.49	3 %
Outer cladding	Fluorinated polymer	1.52	3 %

The chemical structure of polystyrene contains a benzene ring that enables valence electrons to form a conjugated π-orbital, which allows them to be de-localized from their initial C atom so that they can be excited when particles traverse the fibre.

[1] Scintillators of type SCSF-78MJ produced by the company Kuraray are used [138].

Figure B1 shows schematically the states of the excitation spectra of the singlet and triplet states of polystyrene. An electron in the ground state S needs a few eV to go up to an excited singlet state S^* or S^{**}. Each state can have additional vibrational modes that are depicted as thinner solid lines. S^{**}-states rapidly ($< 10^{-11}$ s) decay

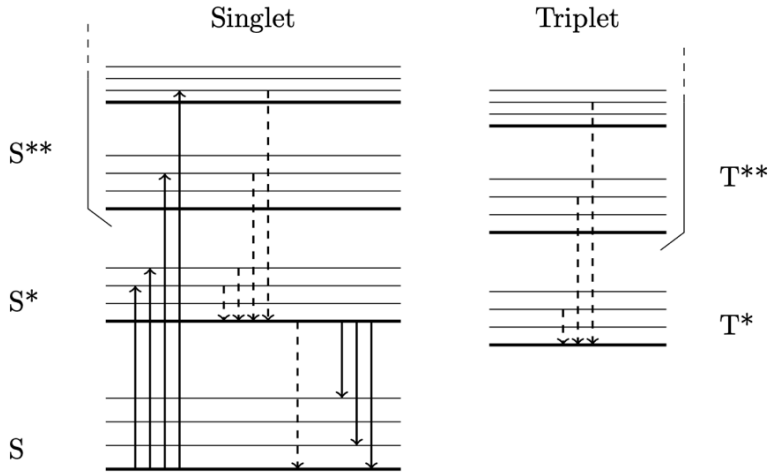

Figure B1: Excitation spectra of singlet and triplet quantum states in polystyrene. For each state the splitting into vibrational modes is depicted as thin solid lines, whereas the lowest state is shown as a thicker line. Radiative transitions are drawn as solid arrow lines, radition-less transitions as dashed arrow line. Taken from Ref. [114].

non-radiatively into the lowest S^* state by internal degradation processes [139]. Here, the released energy is converted into vibrational phonons. Transitions from the lowest S^* to the vibrational levels of the ground state occur via the emission of fluorescent photons (scintillation light) with decay times between 1 ns and 80 ns [139]. Since the energy needed for a vibrational excitation is higher than the energy releases during the photon emission, the scintillator is transparent to its own scintillation light. Apart from the singlet states excited electrons can also populate triplet (e.g. T^*, T^{**}) states. The direct excitation to these states from the ground states is heavily suppressed. However, $S^{**} \rightarrow T^{**}$ transitions can occur. Like for singlet states the highly excited states decay rapidly and radiation-less to the lowest triplet states. Direct transitions from T^* to S are rules out by the selection rules. Instead, they decay via the triplet annihilation process $T^* + T^* \rightarrow S^* + S +$ phonons which can lead to a delayed emission of scintillation light from the subsequent $S^* \rightarrow S$ transitions.
A minimal ionizing particle (MIP) has an energy deposition in polystyrene of around 200 keV/mm, so there can be plenty of excited electrons. However, the scintillator

quantum efficiency defined as the energy emitted as photons by the energy initially deposed by the ionizing particles is only around 5 % so that the initial light yield is not high enough too reach the SiPMs due to several effects causing transmission losses.
For this reason the scintillator is doped with a dye (p-Therphenyl) that helps to increase the light yield output via non-radiative dipole-dipole interactions, also known as the Förster transfer [140]. This only works if the average distance of an excitation centre to a molecule of the dopant is a few nm which is achieved by doping with a concentration of 1 %. A second dopant tetraphenyl butadiene (TPB) at a low concentration of about 0.05 % is used as a wavelength shifter to shift the emission spectrum into the sensitive area of the SiPMs. The fast emission processes of the two chosen dopants enable to fulfill the tight timing requirements to the SciFi of a sub-25 ns read-out. They are also preferred over a single dopant that directly emits in the sensitive spectrum of the SiPM as they do not suffer much from self-absorption, so that the scintillation light yield can be kept high. Figure B2 shows the spectra of the absorption and emission as a function of the wavelength λ for the scintillator and the dopants.

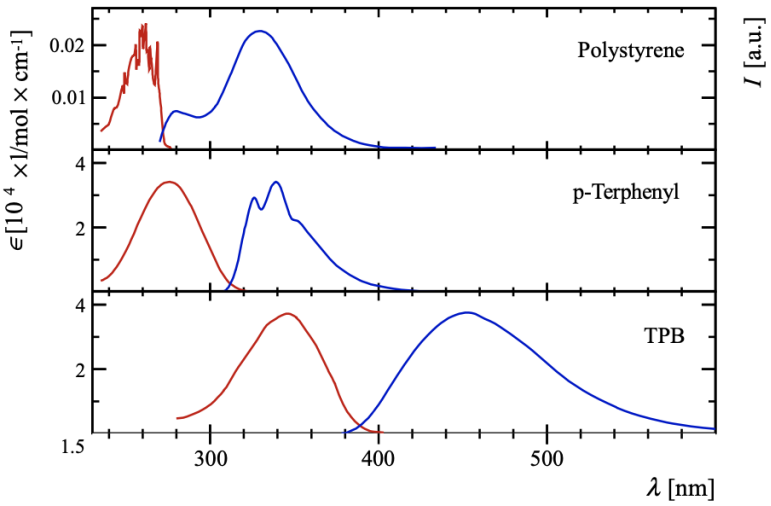

Figure B2: Absorption and emission spectra of the polystyrene scintillator and the p-Terphenyl and TPB dopants. Adapted from Ref. [112].

C Armenteros-Podolanski plot

The Armenteros-Podolanski plot [137] is a kinematical representation of two-body that build ellipses in the plane spanned by the asymmetry α of longitudinal momenta of the two decay products and their transverse momentum p_{T}. It can be used to discriminate different two-body decays in data without making assumptions of the masses of the decay products or the parent particle. For the derivation of the characteristic ellipsis that represents a two-body decay like $V^0 \to h^+h^{(\prime)-}$ in an Armenteros-Podolanski plot the decay has to be looked at not only in the laboratory frame but also in the center-of-mass frame of the V^0. Figure C1 depicts the representations of the decay in the two reference frames. The momentum of a decay product in the center-of-mass frame is given by

$$\begin{aligned} p^* = \frac{1}{4m(V^0)^2}\Big[&m(V^0)^4 + m(h^+)^4 + m(h^{(\prime)-})^4 \\ &- 2m(V^0)^2(m(h^+)^2 + m(h^{(\prime)-})^2) - 2m(h^+)^2m(h^{(\prime)-})^2\Big] \end{aligned} \tag{11}$$

The here used p_{T} of one of the final state hadrons h^+ or $h^{(\prime)-}$ is defined with

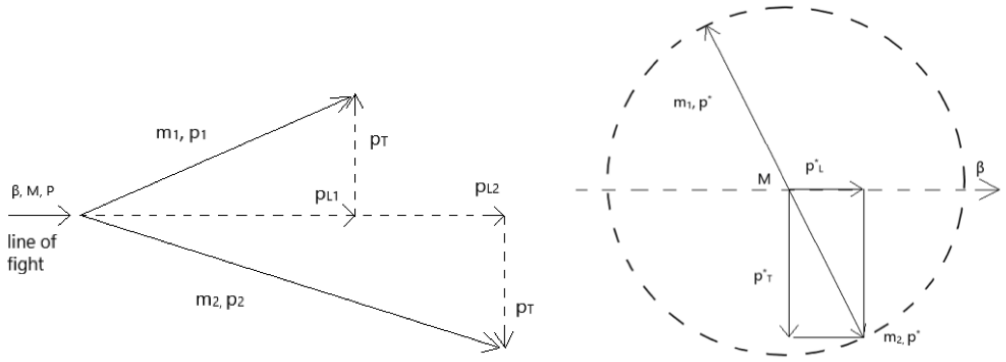

(a) lab frame **(b)** center-of-mass frame

Figure C1: Kinematic representations of a V^0 decay in the laboratory frame and the center-of-mass frame. Taken from Ref. [141].

respect to the flight direction of the V^0. Due to momentum conservation it is identical for both particles ($p_{\mathrm{T}}(h^+) = p_{\mathrm{T}}(h^{(\prime)-}) = p_{\mathrm{T}}$). Furthermore, it is invariant under a Lorentz boost of strength $\beta = \vec{\beta}(V^0)$ to the center-of-mass frame of the V^0 ($p_{\mathrm{T}} = p^*_{\mathrm{T}}$). The longitudinal momentum p_{L} is then defined as the projection of the momentum vector onto the flight direction of the V^0. They can also be expressed

as

$$p_{\mathrm{L}} = p_{\mathrm{L}}^{*} = \pm p^{*}\cos(\theta) \qquad \text{and} \qquad p_{\mathrm{T}} = p_{\mathrm{T}}^{*} = p^{*}\sin(\theta), \tag{12}$$

where the decay angle θ is the angle between flight direction of the V^0 and the momentum p^* of the final state hadron in the V^0 rest frame. The asymmetry of the longitudinal momentum is defined as

$$\alpha = \frac{p_{\mathrm{L}}(h^{+}) - p_{\mathrm{L}}(h^{(\prime)-})}{p_{\mathrm{L}}(h^{+}) + p_{\mathrm{L}}(h^{(\prime)-})} = \frac{2p^{*}}{\beta}\cos(\theta) + \frac{m(h^{+})^2 - m(h^{(\prime)-})^2}{m(V^0)^2}. \tag{13}$$

Combining this with $p_{\mathrm{T}}^{*} = p^{*}\sin(\theta)$ an ellipse for the $V^0 \to h^{+}h^{(\prime)-}$ decay in the Armenteros-Podolanski plane (α, p_{T}) can be constructed as

$$\frac{\alpha - \alpha_0}{r_\alpha^2} + \frac{p_{\mathrm{T}}^2}{(p^{*})^2} = 1 \tag{14}$$

where the center of the ellipse $(\alpha_0, 0)$ and the semi-axes $(r_\alpha, r_{p_{\mathrm{T}}})$ are given by

$$(\alpha_0, 0) = \left(\frac{m(h^{+})^2 - m(h^{(\prime)-})^2}{m(V^0)^2}\right) \qquad \text{and} \qquad (r_\alpha, r_{p_{\mathrm{T}}}) = \left(\frac{2p^{*}}{m(V^0)}, p^{*}\right). \tag{15}$$

Table C1 shows the corresponding values for $K_{\mathrm{S}}^0 \to \pi^{+}\pi^{-}$ and $\Lambda^0 \to p\pi^{-}$ decays.

Table C1: Values for the parameters of the ellipses of $K_{\mathrm{S}}^0 \to \pi^{+}\pi^{-}$ and $\Lambda^0 \to p\pi^{-}/\bar{\Lambda}^0 \to \bar{p}\pi^{+}$ decays in the Armenteros-Podolanski plot.

decay	p^* in GeV	α_0	r_α
$K_{\mathrm{S}}^0 \to \pi^{+}\pi^{-}$	0.206	0	0.827
$\Lambda^0 \to p\pi^{-}$/ $\bar{\Lambda}^0 \to \bar{p}\pi^{+}$	0.101	$\pm$0.691	0.181

D Results of the invariant mass fits for the strange hadron candidates

The fits to the invariant masses of V^0 candidates in the various p_{T} and y bins have been described in section 4.7 and 4.11 and have been performed to extract the signal yields $N_{\mathrm{sig}}(V^0)$ that go into the construction of the ratio $R(\bar{\Lambda}^0, K_{\mathrm{S}}^0)$ and $R(\bar{\Lambda}^0, \Lambda^0)$. This appendix gives the complete overview about all invariant mass fits and the extracted yields. The tables D1 and D2 summarize all extracted yields for LL-

and DD-reconstructed K^0_S, Λ^0 and $\bar{\Lambda}^0$ candidates. The sections D.1-D.5 show the corresponding fits to invariant masses. Step four or five of the fitting procedure are shown depending on the stability of the fitting model and procedure in the given bin and from which step the signal yield was extracted.

Table D1: Signal yields $N_{\text{sig}}(V^0)$ extracted from the fits to the invariant mass distributions of the LL-reconstructed $V^0 = K^0_S, \Lambda^0, \bar{\Lambda}^0$ candidates.

polarity	bin	$N_{\text{sig}}(K^0_S)$	$N_{\text{sig}}(\bar{\Lambda}^0)$	$N_{\text{sig}}(\Lambda^0)$
MagDown	$p_T \in [150, 500]$ MeV	$136\,618 \pm 374$	$10\,683 \pm 292$	$10\,446 \pm 130$
	$p_T \in [500, 650]$ MeV	$61\,587 \pm 259$	9275 ± 137	9718 ± 143
	$p_T \in [650, 800]$ MeV	$46\,890 \pm 217$	9934 ± 127	$10\,268 \pm 126$
	$p_T \in [800, 1000]$ MeV	$41\,569 \pm 205$	$12\,332 \pm 133$	$12\,806 \pm 132$
	$p_T \in [1000, 1200]$ MeV	$24\,279 \pm 156$	$10\,041 \pm 125$	$10\,672 \pm 124$
	$p_T \in [1200, 2500]$ MeV	$28\,416 \pm 169$	$21\,030 \pm 171$	$22\,284 \pm 173$
	$y \in [2, 2.5]$	$14\,160 \pm 119$	3527 ± 62	3606 ± 61
	$y \in [2.5, 3]$	$76\,630 \pm 160$	$34\,525 \pm 225$	$17\,501 \pm 153$
	$y \in [3, 3.5]$	$114\,234 \pm 342$	$30\,493 \pm 237$	$31\,972 \pm 237$
	$y \in [3.5, 4]$	$118\,681 \pm 347$	$18\,911 \pm 219$	$19\,911 \pm 223$
	$y \in [4, 4.5]$	$31\,020 \pm 176$	4287 ± 104	4464 ± 74
MagUp	$p_T \in [150, 500]$ MeV	$252\,335 \pm 507$	$16\,628 \pm 228$	$20\,064 \pm 28$
	$p_T \in [500, 650]$ MeV	$113\,881 \pm 338$	$16\,584 \pm 175$	$18\,184 \pm 151$
	$p_T \in [650, 800]$ MeV	$87\,014 \pm 298$	$17\,892 \pm 174$	$19\,685 \pm 152$
	$p_T \in [800, 1000]$ MeV	$77\,718 \pm 280$	$22\,312 \pm 184$	$24\,716 \pm 204$
	$p_T \in [1000, 1200]$ MeV	$45\,351 \pm 213$	$17\,960 \pm 163$	$19\,790 \pm 148$
	$p_T \in [1200, 2500]$ MeV	$54\,375 \pm 234$	$37\,914 \pm 223$	$41\,687 \pm 225$
	$y \in [2, 2.5]$	$27\,171 \pm 165$	6313 ± 81	6951 ± 86
	$y \in [2.5, 3]$	$141\,963 \pm 379$	$63\,734 \pm 294$	$33\,255 \pm 213$
	$y \in [3, 3.5]$	$213\,284 \pm 466$	$54\,639 \pm 258$	$60\,525 \pm 319$
	$y \in [3.5, 4]$	$218\,443 \pm 467$	$33\,588 \pm 183$	$37\,708 \pm 295$
	$y \in [4, 4.5]$	$57\,684 \pm 242$	7400 ± 79	8609 ± 134

Table D2: Signal yields $N_{\mathrm{sig}}(V^0)$ extracted from the fits to the invariant mass distributions of the DD-reconstructed $V^0 = K^0_{\mathrm{S}}, \Lambda^0, \bar{\Lambda}^0$ candidates.

polarity	bin	$N_{\mathrm{sig}}(K^0_{\mathrm{S}})$	$N_{\mathrm{sig}}(\bar{\Lambda}^0)$	$N_{\mathrm{sig}}(\Lambda^0)$
MagDown	$p_{\mathrm{T}} \in [150, 500]$ MeV	$30\,035 \pm 225$	3023 ± 188	3898 ± 66
	$p_{\mathrm{T}} \in [500, 650]$ MeV	$27\,978 \pm 126$	5582 ± 326	6146 ± 112
	$p_{\mathrm{T}} \in [650, 800]$ MeV	$28\,990 \pm 187$	7985 ± 188	8905 ± 282
	$p_{\mathrm{T}} \in [800, 1000]$ MeV	$34\,568 \pm 327$	$13\,338 \pm 185$	$14\,190 \pm 215$
	$p_{\mathrm{T}} \in [1000, 1200]$ MeV	$27\,615 \pm 186$	$13\,993 \pm 195$	$14\,462 \pm 164$
	$p_{\mathrm{T}} \in [1200, 2500]$ MeV	$63\,390 \pm 266$	$46\,434 \pm 352$	$47\,772 \pm 216$
	$y \in [2, 2.5]$	$20\,468 \pm 161$	9077 ± 109	9399 ± 125
	$y \in [2.5, 3]$	$65\,304 \pm 986$	$29\,384 \pm 207$	$31\,111 \pm 212$
	$y \in [3, 3.5]$	$78\,953 \pm 322$	$35\,902 \pm 286$	$38\,187 \pm 248$
	$y \in [3.5, 4]$	$48\,350 \pm 264$	$20\,348 \pm 256$	$22\,156 \pm 470$
	$y \in [4, 4.5]$	$10\,886 \pm 110$	3913 ± 93	3925 ± 117
MagUp	$p_{\mathrm{T}} \in [150, 500]$ MeV	$55\,361 \pm 589$	5888 ± 337	6210 ± 352
	$p_{\mathrm{T}} \in [500, 650]$ MeV	$27\,978 \pm 126$	$10\,153 \pm 213$	$11\,398 \pm 278$
	$p_{\mathrm{T}} \in [650, 800]$ MeV	$54\,238 \pm 273$	$15\,541 \pm 247$	$16\,700 \pm 167$
	$p_{\mathrm{T}} \in [800, 1000]$ MeV	$64\,518 \pm 270$	$25\,249 \pm 195$	$26\,887 \pm 234$
	$p_{\mathrm{T}} \in [1000, 1200]$ MeV	$50\,421 \pm 237$	$25\,208 \pm 236$	$28\,121 \pm 200$
	$p_{\mathrm{T}} \in [1200, 2500]$ MeV	$117\,323 \pm 352$	$83\,316 \pm 439$	$91\,127 \pm 348$
	$y \in [2, 2.5]$	$38\,356 \pm 222$	$16\,501 \pm 146$	$17\,673 \pm 150$
	$y \in [2.5, 3]$	$119\,460 \pm 410$	$53\,623 \pm 296$	$58\,165 \pm 298$
	$y \in [3, 3.5]$	$145\,618 \pm 566$	$66\,155 \pm 470$	$71\,871 \pm 484$
	$y \in [3.5, 4]$	$90\,442 \pm 358$	$37\,833 \pm 380$	$41\,683 \pm 226$
	$y \in [4, 4.5]$	$20\,035 \pm 154$	6595 ± 172	7674 ± 163

D.1 K^0_S - *MagDown*

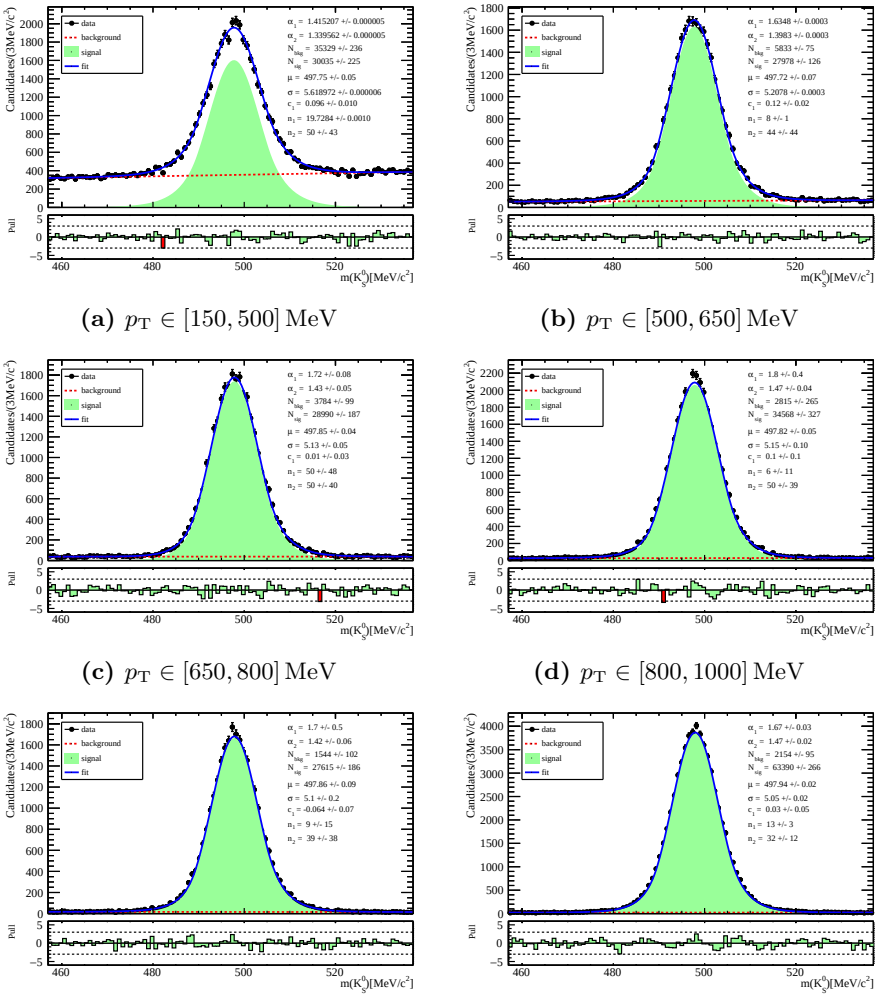

(a) $p_T \in [150, 500]$ MeV **(b)** $p_T \in [500, 650]$ MeV

(c) $p_T \in [650, 800]$ MeV **(d)** $p_T \in [800, 1000]$ MeV

(e) $p_T \in [1000, 1200]$ MeV **(f)** $p_T \in [1200, 2500]$ MeV

Figure D1: Invariant mass fits of DD-reconstructed K^0_S candidates in the different p_T bins. All plots are shown for the magnet polarity *MagDown*.

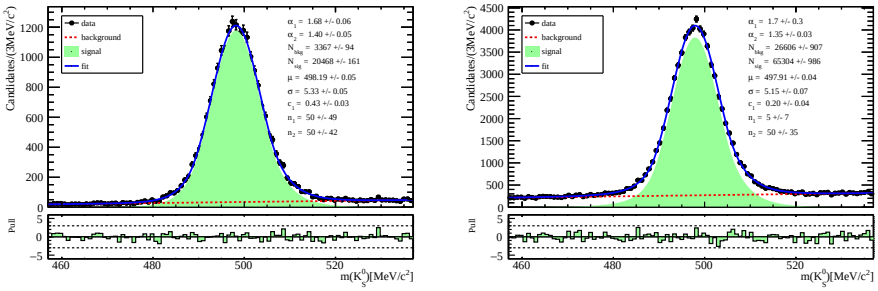

(a) $y \in [2, 2.5]$ **(b)** $y \in [2.5, 3]$

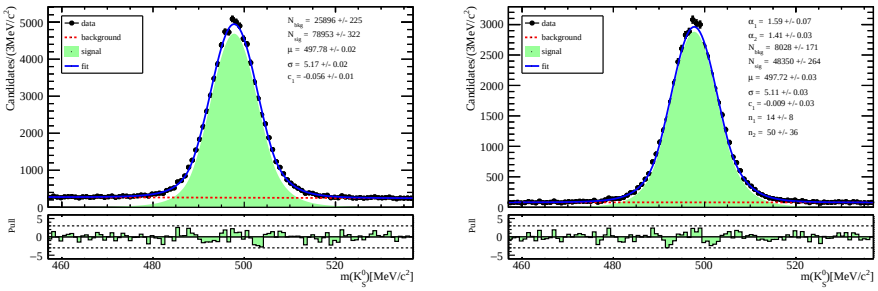

(c) $y \in [3, 3.5]$ **(d)** $y \in [3.5, 4]$

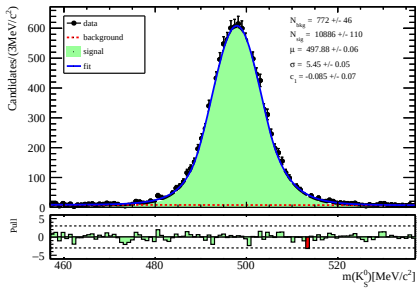

(e) $y \in [4, 4.5]$

Figure D2: Invariant mass fits of DD-reconstructed K^0_S candidates in the different y bins. All plots are shown for the magnet polarity *MagDown*.

D.2 K_S^0 - *MagUp*

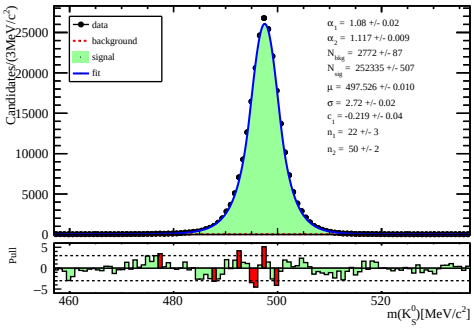

(a) $p_{\mathrm{T}} \in [150, 500]\,\mathrm{MeV}$

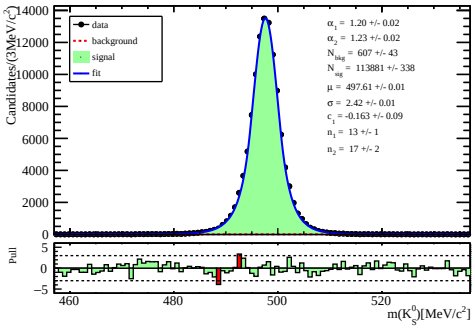

(b) $p_{\mathrm{T}} \in [500, 650]\,\mathrm{MeV}$

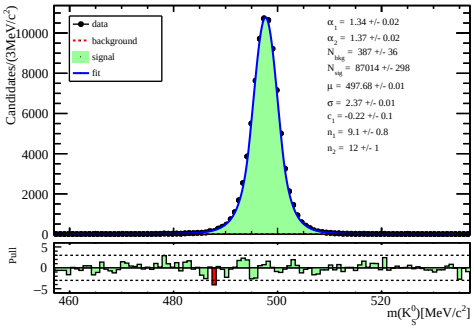

(c) $p_{\mathrm{T}} \in [650, 800]\,\mathrm{MeV}$

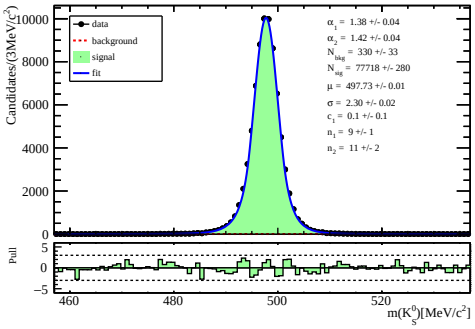

(d) $p_{\mathrm{T}} \in [800, 1000]\,\mathrm{MeV}$

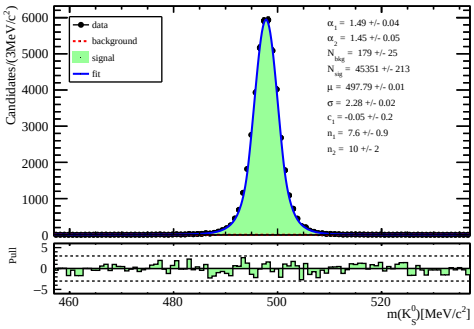

(e) $p_{\mathrm{T}} \in [1000, 1200]\,\mathrm{MeV}$

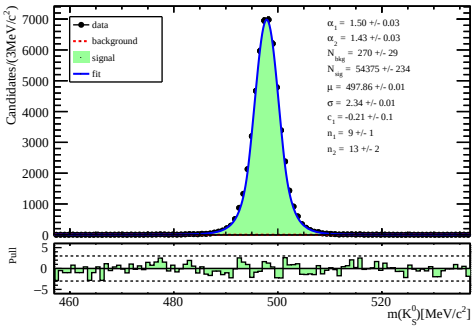

(f) $p_{\mathrm{T}} \in [1200, 2500]\,\mathrm{MeV}$

Figure D3: Invariant mass fits of LL-reconstructed K^0_{S} candidates in the different p_{T} bins. All plots are shown for the magnet polarity *MagUp*.

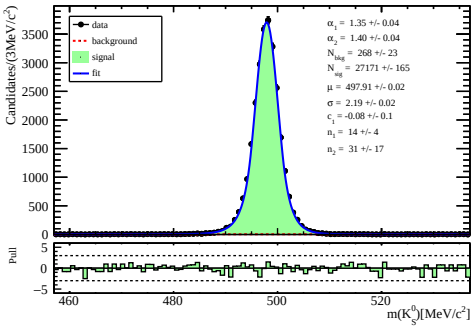

(a) $y \in [2, 2.5]$

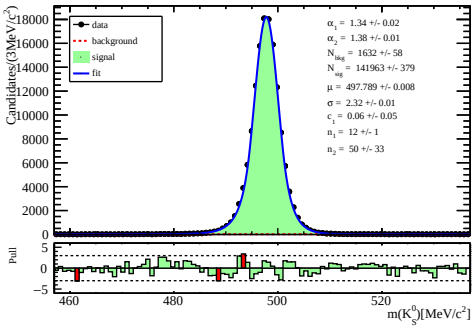

(b) $y \in [2.5, 3]$

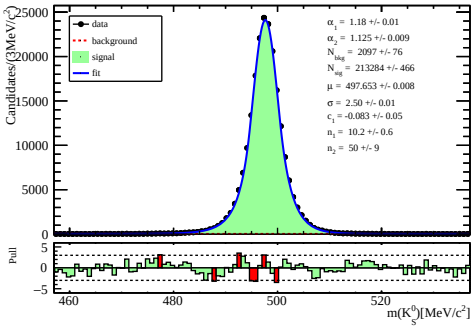

(c) $y \in [3, 3.5]$

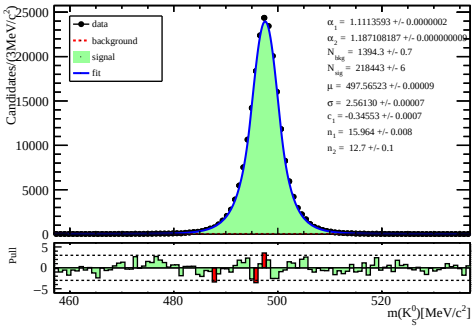

(d) $y \in [3.5, 4]$

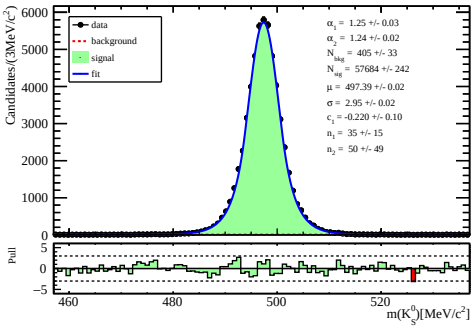

(e) $y \in [4, 4.5]$

Figure D4: Invariant mass fits of LL-reconstructed K^0_S candidates in the different y bins. All plots are shown for the magnet polarity *MagUp*.

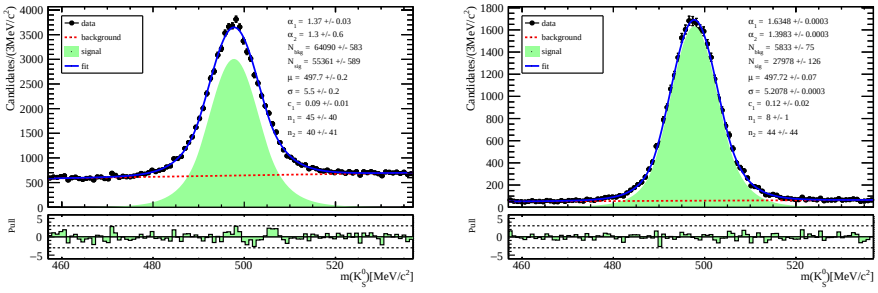

(a) $p_{\mathrm{T}} \in [150, 500]\,\mathrm{MeV}$

(b) $p_{\mathrm{T}} \in [500, 650]\,\mathrm{MeV}$

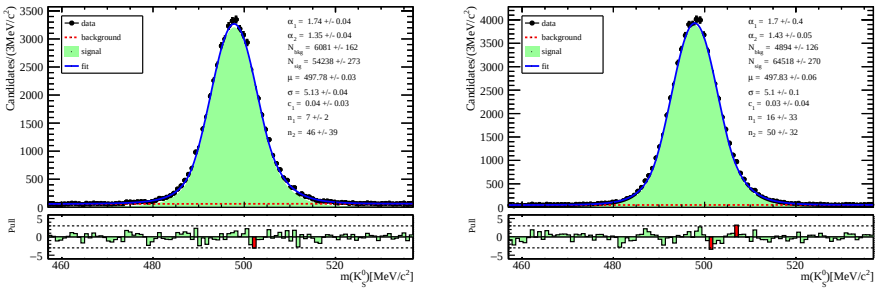

(c) $p_{\mathrm{T}} \in [650, 800]\,\mathrm{MeV}$

(d) $p_{\mathrm{T}} \in [800, 1000]\,\mathrm{MeV}$

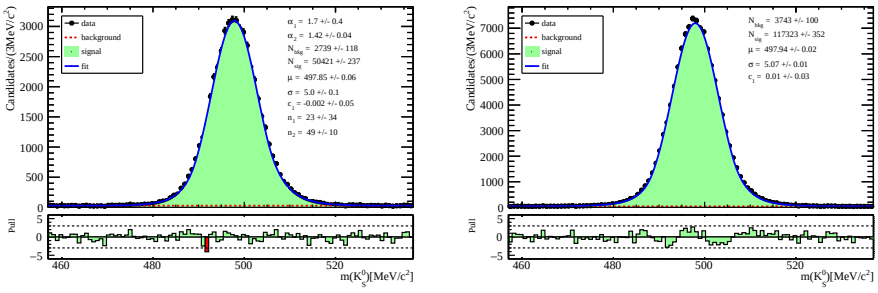

(e) $p_{\mathrm{T}} \in [1000, 1200]\,\mathrm{MeV}$

(f) $p_{\mathrm{T}} \in [1200, 2500]\,\mathrm{MeV}$

Figure D5: Invariant mass fits of DD-reconstructed K^0_{S} candidates in the different p_{T} bins. All plots are shown for the magnet polarity *MagUp*.

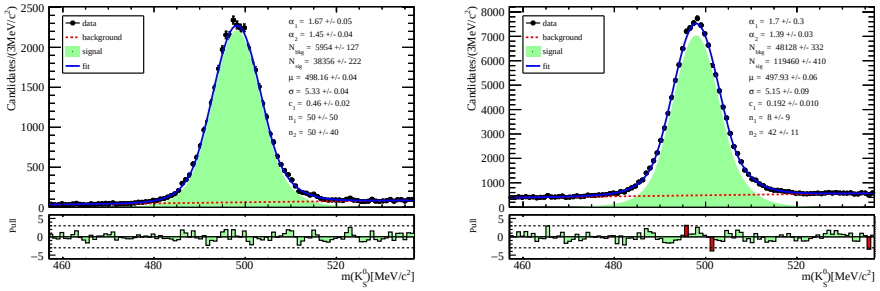

(a) $y \in [2, 2.5]$

(b) $y \in [2.5, 3]$

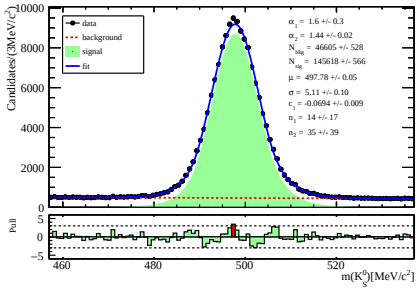

(c) $y \in [3, 3.5]$

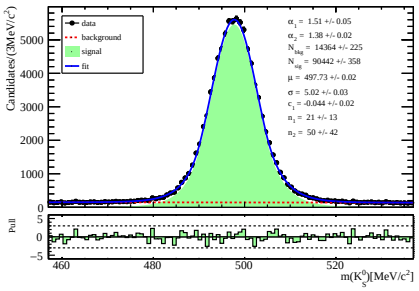

(d) $y \in [3.5, 4]$

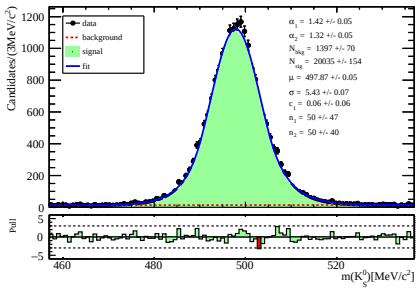

(e) $y \in [4, 4.5]$

Figure D6: Invariant mass fits of DD-reconstructed K^0_S candidates in the different y bins. All plots are shown for the magnet polarity *MagUp*.

D.3 Λ^0- *MagDown*

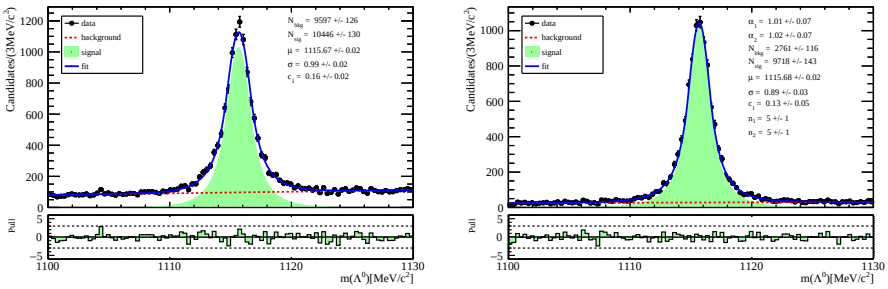

(a) $p_{\mathrm{T}} \in [150, 500]\,\mathrm{MeV}$

(b) $p_{\mathrm{T}} \in [500, 650]\,\mathrm{MeV}$

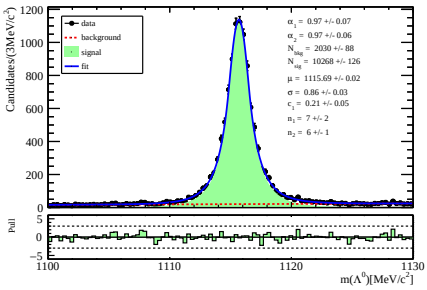

(c) $p_{\mathrm{T}} \in [650, 800]\,\mathrm{MeV}$

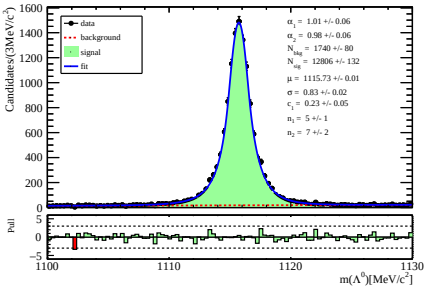

(d) $p_{\mathrm{T}} \in [800, 1000]\,\mathrm{MeV}$

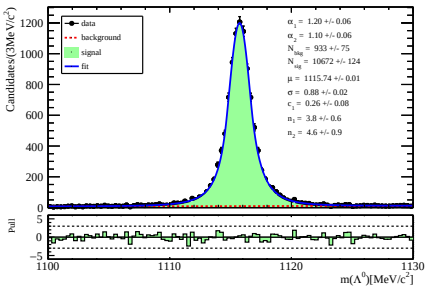

(e) $p_{\mathrm{T}} \in [1000, 1200]\,\mathrm{MeV}$

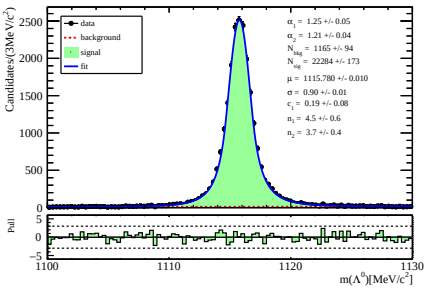

(f) $p_{\mathrm{T}} \in [1200, 2500]\,\mathrm{MeV}$

Figure D7: Invariant mass fits of LL-reconstructed Λ^0 candidates in the different p_{T} bins. All plots are shown for the magnet polarity *MagDown*.

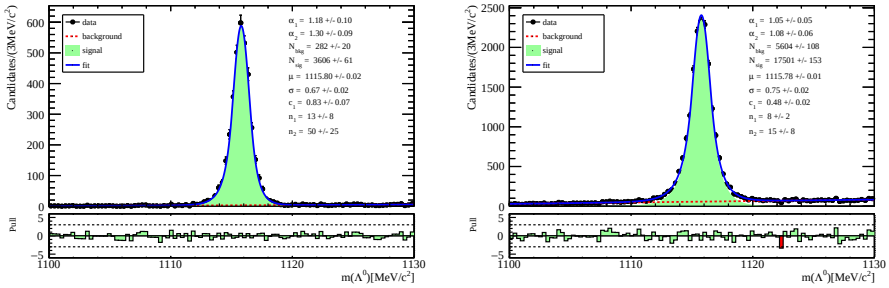

(a) $y \in [2, 2.5]$

(b) $y \in [2.5, 3]$

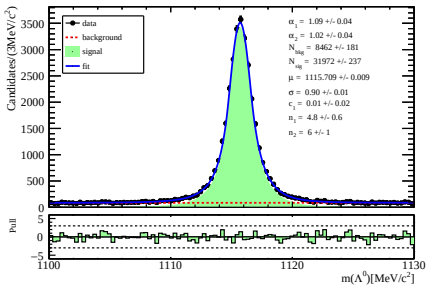

(c) $y \in [3, 3.5]$

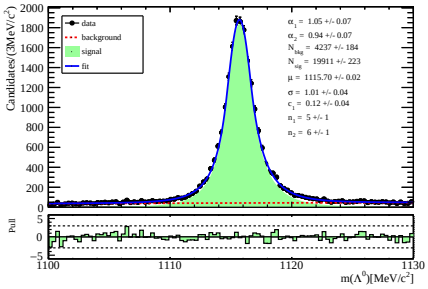

(d) $y \in [3.5, 4]$

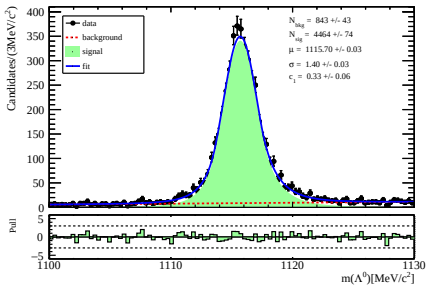

(e) $y \in [4, 4.5]$

Figure D8: Invariant mass fits of LL-reconstructed Λ^0 candidates in the different y bins. All plots are shown for the magnet polarity *MagDown*.

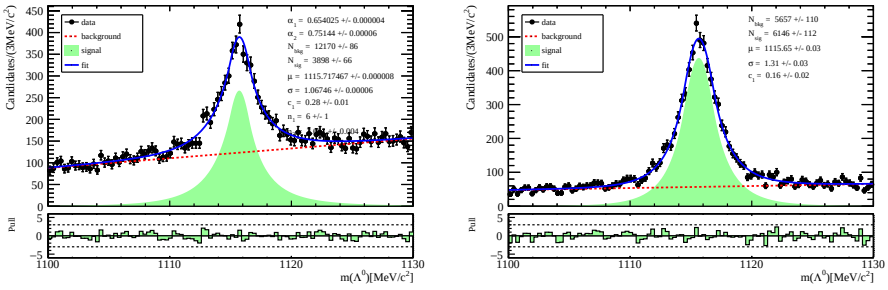

(a) $p_{\mathrm{T}} \in [150, 500]\,\mathrm{MeV}$

(b) $p_{\mathrm{T}} \in [500, 650]\,\mathrm{MeV}$

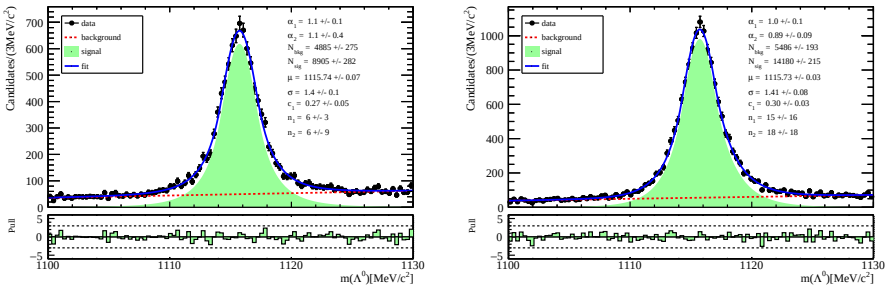

(c) $p_{\mathrm{T}} \in [650, 800]\,\mathrm{MeV}$

(d) $p_{\mathrm{T}} \in [800, 1000]\,\mathrm{MeV}$

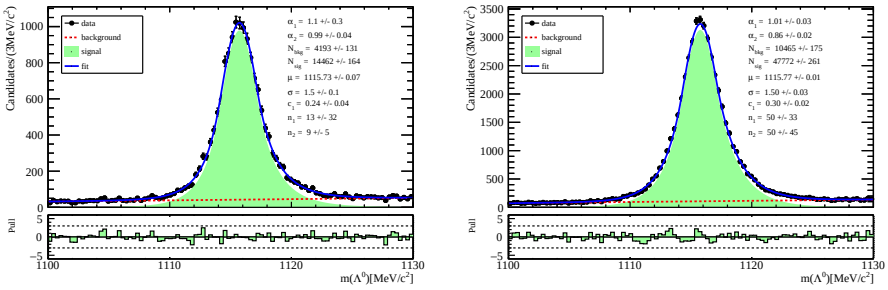

(e) $p_{\mathrm{T}} \in [1000, 1200]\,\mathrm{MeV}$

(f) $p_{\mathrm{T}} \in [1200, 2500]\,\mathrm{MeV}$

Figure D9: Invariant mass fits of DD-reconstructed Λ^0 candidates in the different p_{T} bins. All plots are shown for the magnet polarity *MagDown*.

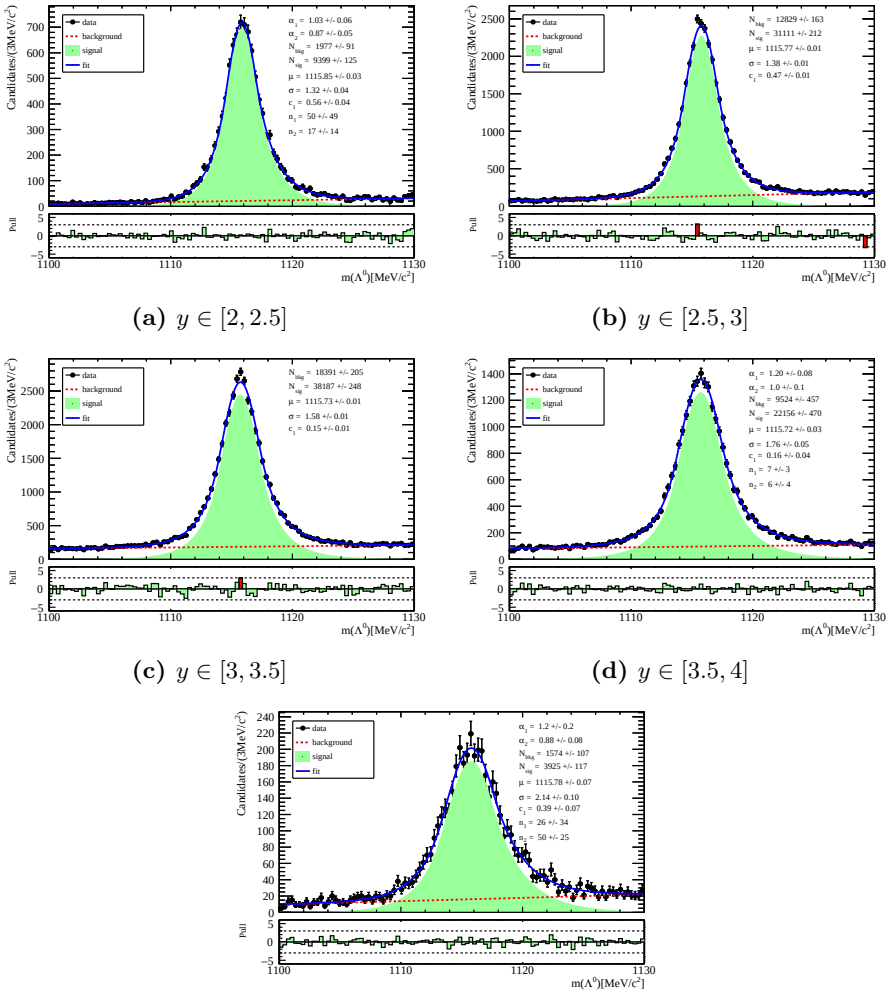

(a) $y \in [2, 2.5]$ **(b)** $y \in [2.5, 3]$

(c) $y \in [3, 3.5]$ **(d)** $y \in [3.5, 4]$

(e) $y \in [4, 4.5]$

Figure D10: Invariant mass fits of DD-reconstructed Λ^0 candidates in the different y bins. All plots are shown for the magnet polarity *MagDown*.

D.4 Λ^0- *MagUp*

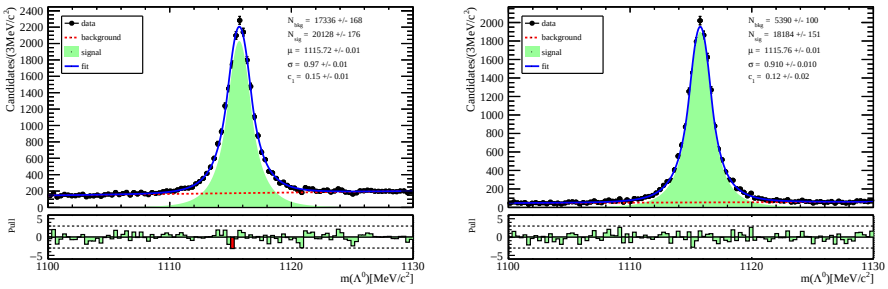

(a) $p_{\mathrm{T}} \in [150, 500]\,\mathrm{MeV}$ **(b)** $p_{\mathrm{T}} \in [500, 650]\,\mathrm{MeV}$

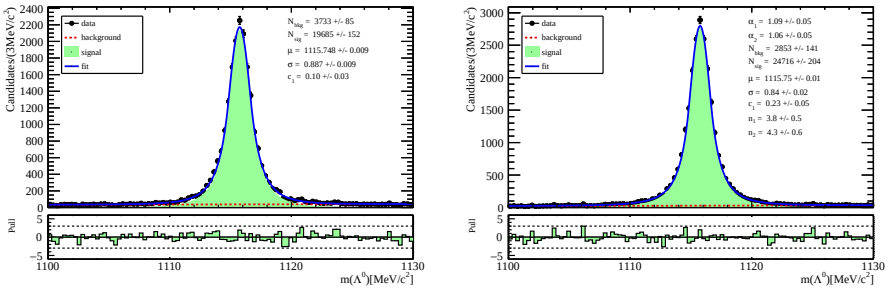

(c) $p_{\mathrm{T}} \in [650, 800]\,\mathrm{MeV}$ **(d)** $p_{\mathrm{T}} \in [800, 1000]\,\mathrm{MeV}$

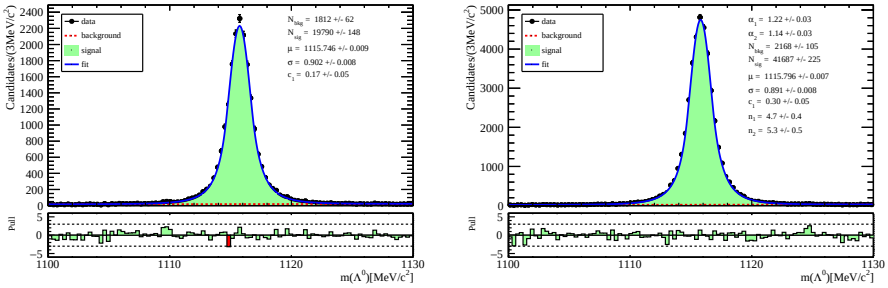

(e) $p_{\mathrm{T}} \in [1000, 1200]\,\mathrm{MeV}$ **(f)** $p_{\mathrm{T}} \in [1200, 2500]\,\mathrm{MeV}$

Figure D11: Invariant mass fits of LL-reconstructed Λ^0 candidates in the different p_{T} bins. All plots are shown for the magnet polarity *MagUp*.

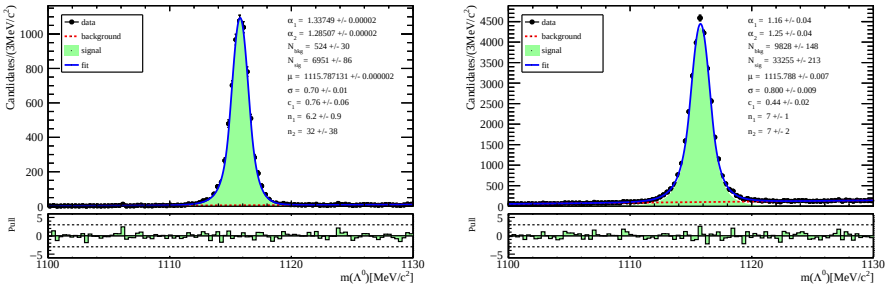

(a) $y \in [2, 2.5]$

(b) $y \in [2.5, 3]$

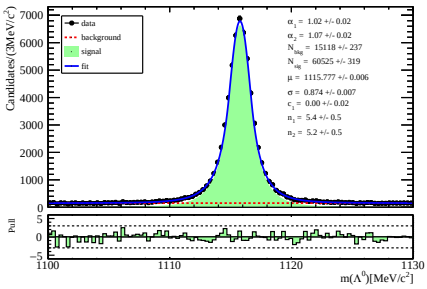

(c) $y \in [3, 3.5]$

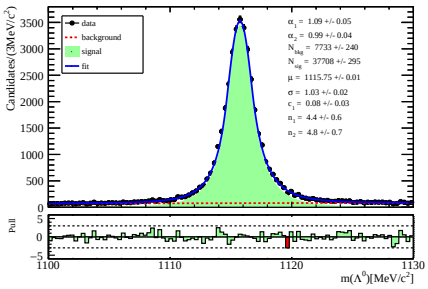

(d) $y \in [3.5, 4]$

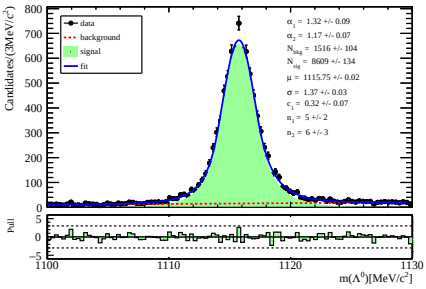

(e) $y \in [4, 4.5]$

Figure D12: Invariant mass fits of LL-reconstructed Λ^0 candidates in the different y bins. All plots are shown for the magnet polarity *MagUp*.

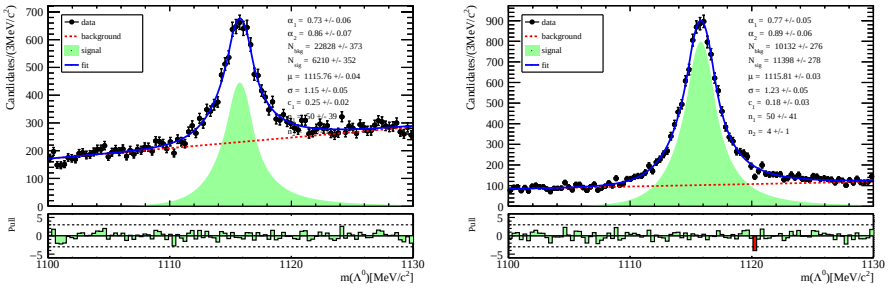

(a) $p_{\mathrm{T}} \in [150, 500]\,\mathrm{MeV}$ **(b)** $p_{\mathrm{T}} \in [500, 650]\,\mathrm{MeV}$

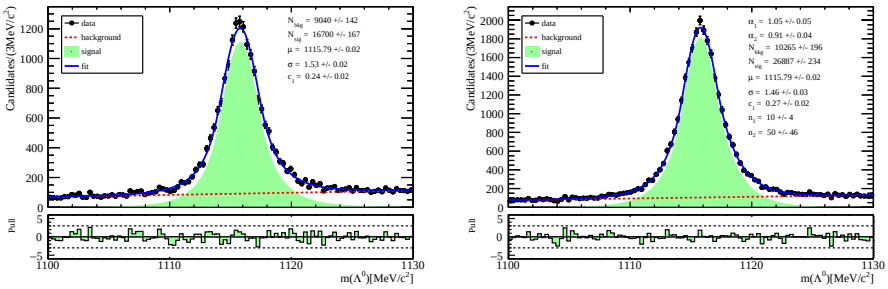

(c) $p_{\mathrm{T}} \in [650, 800]\,\mathrm{MeV}$ **(d)** $p_{\mathrm{T}} \in [800, 1000]\,\mathrm{MeV}$

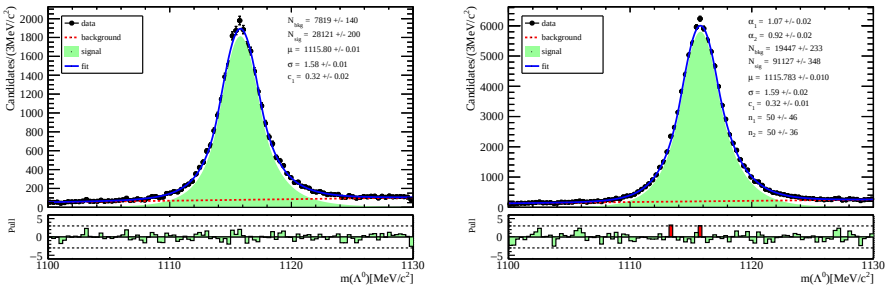

(e) $p_{\mathrm{T}} \in [1000, 1200]\,\mathrm{MeV}$ **(f)** $p_{\mathrm{T}} \in [1200, 2500]\,\mathrm{MeV}$

Figure D13: Invariant mass fits of DD-reconstructed Λ^0 candidates in the different p_{T} bins. All plots are shown for the magnet polarity *MagUp*.

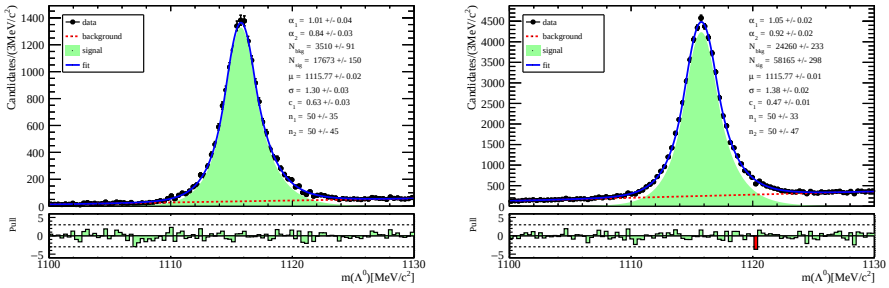

(a) $y \in [2, 2.5]$

(b) $y \in [2.5, 3]$

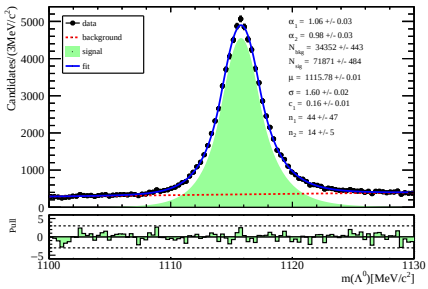

(c) $y \in [3, 3.5]$

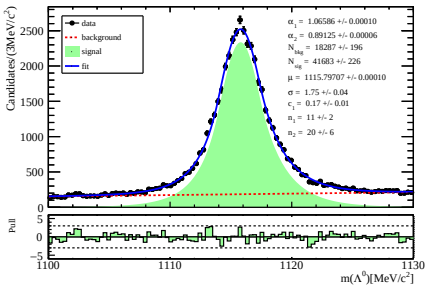

(d) $y \in [3.5, 4]$

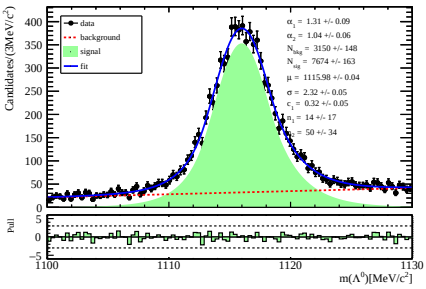

(e) $y \in [4, 4.5]$

Figure D14: Invariant mass fits of DD-reconstructed Λ^0 candidates in the different y bins. All plots are shown for the magnet polarity *MagUp*.

D.5 $\bar{\Lambda}^0$- *MagDown*

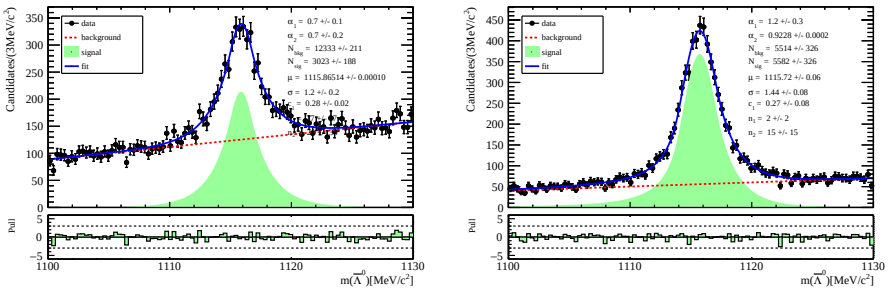

(a) $p_{\mathrm{T}} \in [150, 500]\,\mathrm{MeV}$ **(b)** $p_{\mathrm{T}} \in [500, 650]\,\mathrm{MeV}$

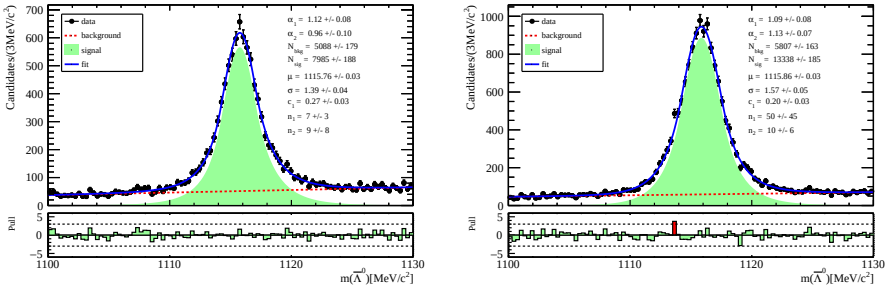

(c) $p_{\mathrm{T}} \in [650, 800]\,\mathrm{MeV}$ **(d)** $p_{\mathrm{T}} \in [800, 1000]\,\mathrm{MeV}$

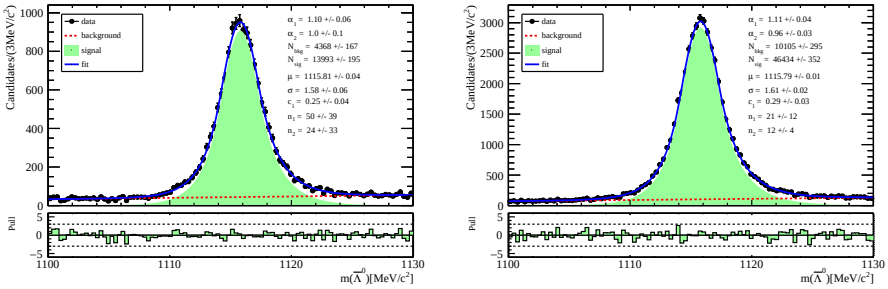

(e) $p_{\mathrm{T}} \in [1000, 1200]\,\mathrm{MeV}$ **(f)** $p_{\mathrm{T}} \in [1200, 2500]\,\mathrm{MeV}$

Figure D15: Invariant mass fits of DD-reconstructed $\bar{\Lambda}^0$ candidates in the different p_{T} bins. All plots are shown for the magnet polarity *MagDown*.

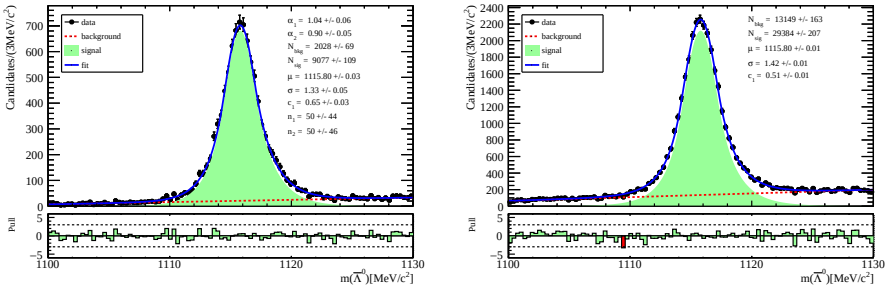

(a) $y \in [2, 2.5]$ **(b)** $y \in [2.5, 3]$

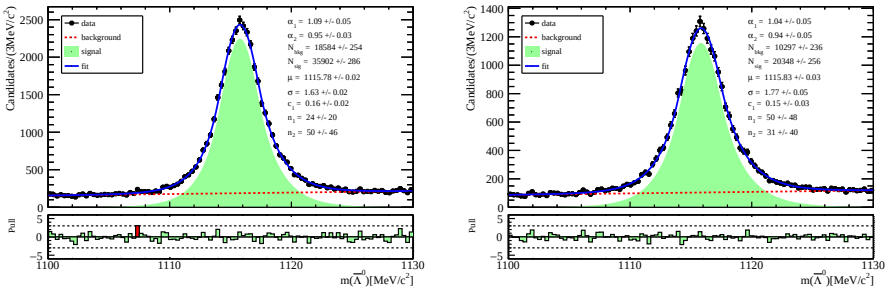

(c) $y \in [3, 3.5]$ **(d)** $y \in [3.5, 4]$

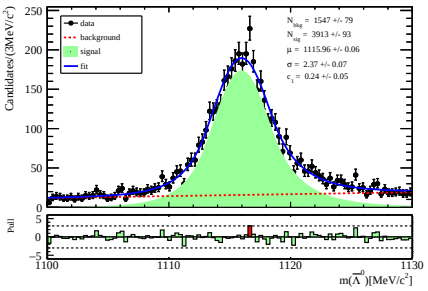

(e) $y \in [4, 4.5]$

Figure D16: Invariant mass fits of DD-reconstructed $\bar{\Lambda}^0$ candidates in the different y bins. All plots are shown for the magnet polarity *MagDown*.

D.6 $\bar{\Lambda}^0$- *MagUp*

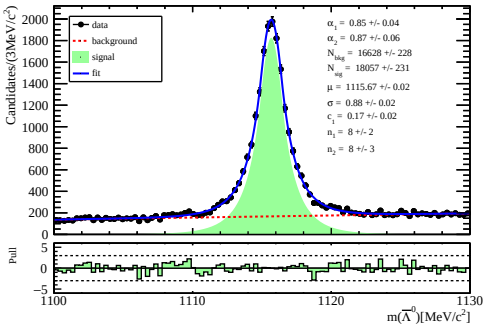

(a) $p_{\mathrm{T}} \in [150, 500]\,\mathrm{MeV}$

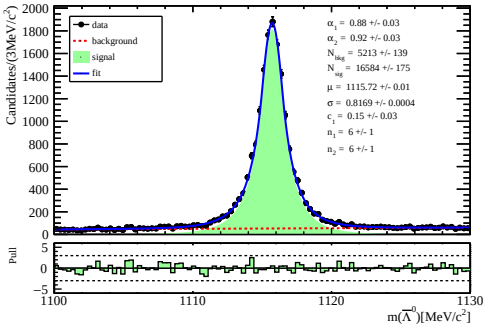

(b) $p_{\mathrm{T}} \in [500, 650]\,\mathrm{MeV}$

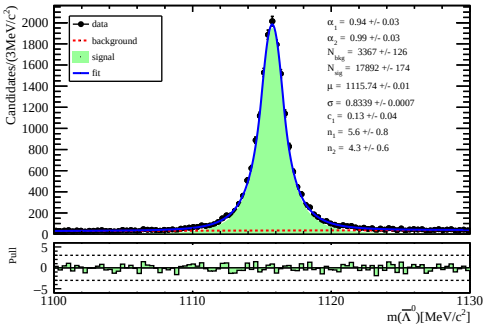

(c) $p_{\mathrm{T}} \in [650, 800]\,\mathrm{MeV}$

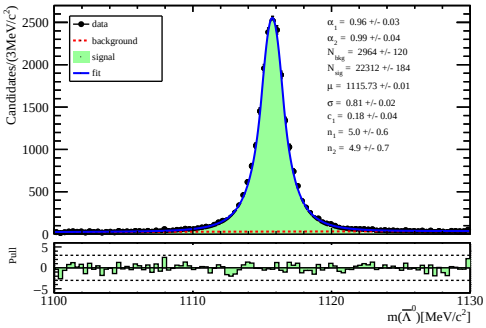

(d) $p_{\mathrm{T}} \in [800, 1000]\,\mathrm{MeV}$

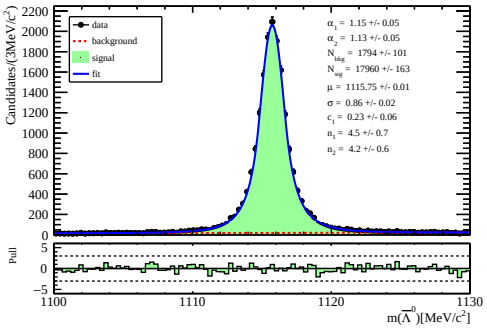

(e) $p_{\mathrm{T}} \in [1000, 1200]\,\mathrm{MeV}$

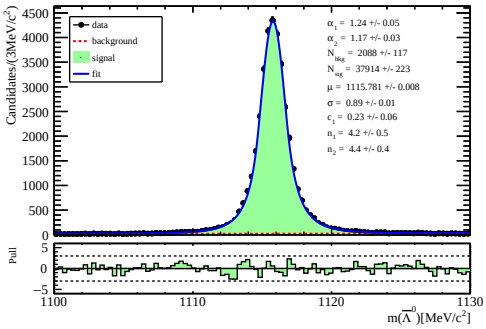

(f) $p_{\mathrm{T}} \in [1200, 2500]\,\mathrm{MeV}$

Figure D17: Invariant mass fits of LL-reconstructed $\bar{\Lambda}^0$ candidates in the different p_{T} bins. All plots are shown for the magnet polarity *MagUp*.

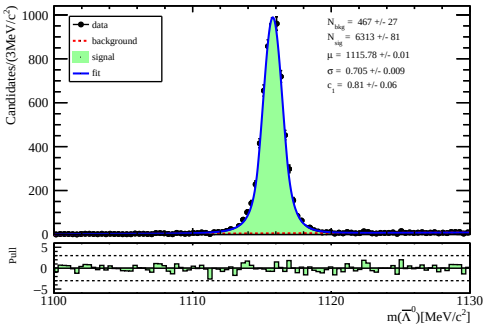

(a) $y \in [2, 2.5]$

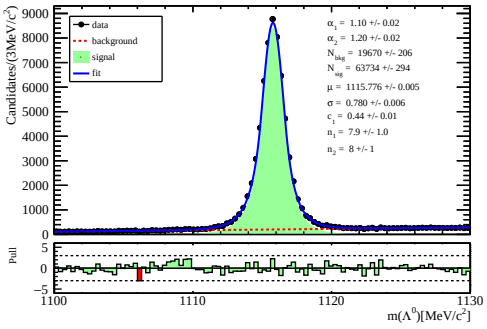

(b) $y \in [2.5, 3]$

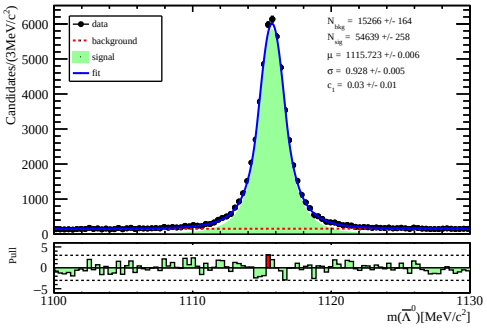

(c) $y \in [3, 3.5]$

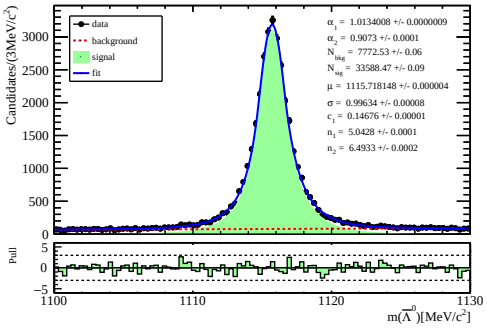

(d) $y \in [3.5, 4]$

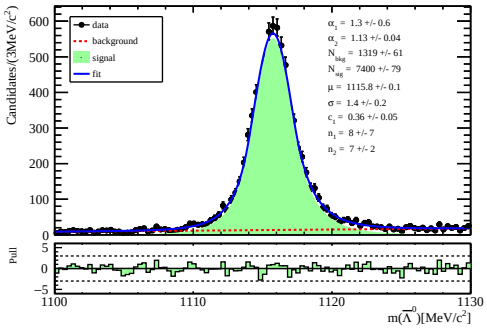

(e) $y \in [4, 4.5]$

Figure D18: Invariant mass fits of LL-reconstructed $\bar{\Lambda}^0$ candidates in the different y bins. All plots are shown for the magnet polarity *MagUp*.

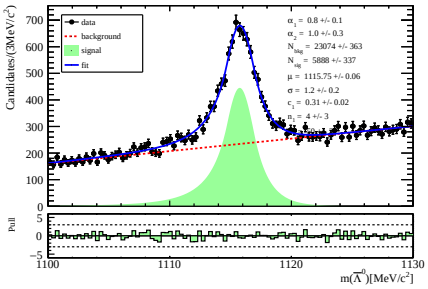

(a) $p_{\mathrm{T}} \in [150, 500]\,\mathrm{MeV}$

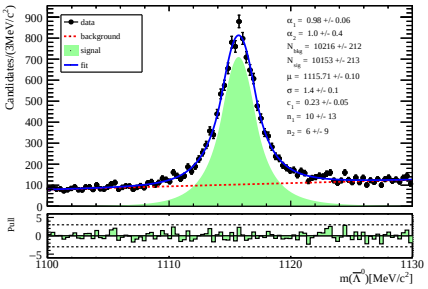

(b) $p_{\mathrm{T}} \in [500, 650]\,\mathrm{MeV}$

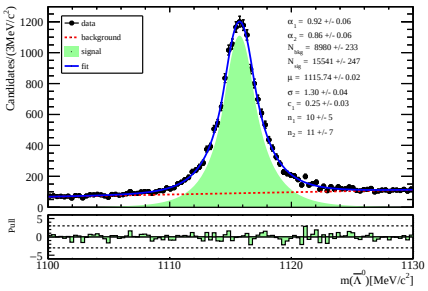

(c) $p_{\mathrm{T}} \in [650, 800]\,\mathrm{MeV}$

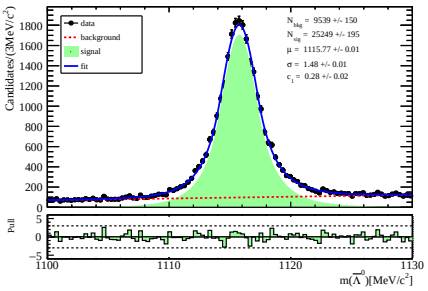

(d) $p_{\mathrm{T}} \in [800, 1000]\,\mathrm{MeV}$

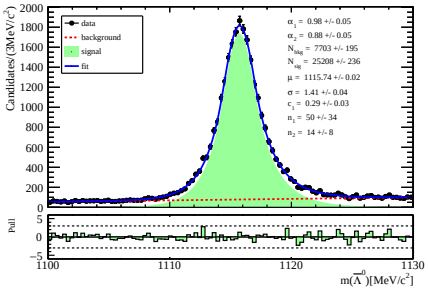

(e) $p_{\mathrm{T}} \in [1000, 1200]\,\mathrm{MeV}$

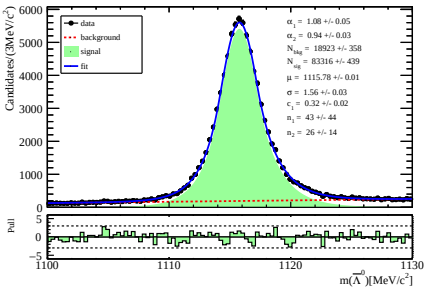

(f) $p_{\mathrm{T}} \in [1200, 2500]\,\mathrm{MeV}$

Figure D19: Invariant mass fits of DD-reconstructed $\bar{\Lambda}^0$ candidates in the different p_{T} bins. All plots are shown for the magnet polarity *MagUp*.

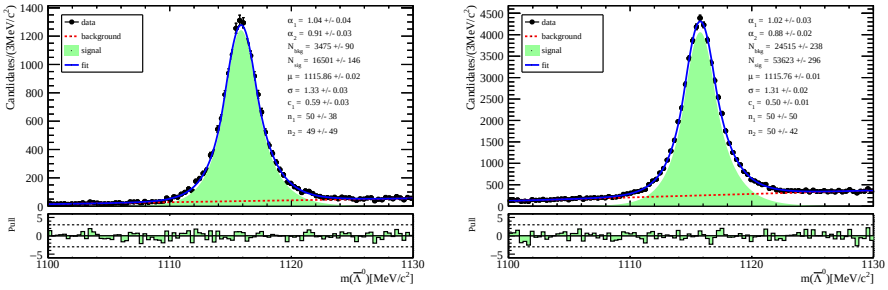

(a) $y \in [2, 2.5]$ **(b)** $y \in [2.5, 3]$

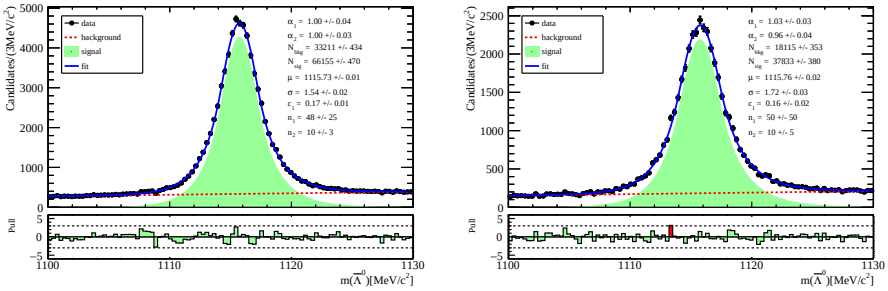

(c) $y \in [3, 3.5]$ **(d)** $y \in [3.5, 4]$

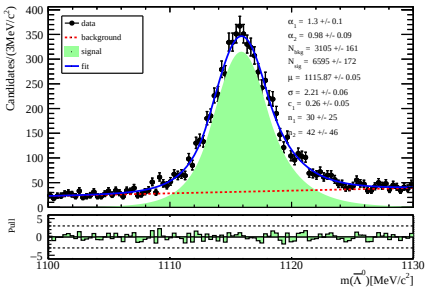

(e) $y \in [4, 4.5]$

Figure D20: Invariant mass fits of DD-reconstructed $\bar{\Lambda}^0$ candidates in the different y bins. All plots are shown for the magnet polarity *MagUp*.

Bibliography

[1] D. J. Griffiths, *Introduction to elementary particles; 2nd rev. version*, Physics textbook, New York, NY: Wiley, 2008.

[2] M. Thomson, *Modern particle physics*, New York: Cambridge University Press, 2013.

[3] M. E. Peskin and D. V. Schroeder, *An Introduction to quantum field theory*, Reading, USA: Addison-Wesley, 1995.

[4] M. D. Schwartz, *Quantum Field Theory and the Standard Model*, Cambridge University Press, 2014.

[5] Particle Data Group, R. L. Workman et al., *Review of Particle Physics*, PTEP 2022 (2022), p. 083C01.

[6] SNO Collaboration, Q. R. Ahmad et al., *Measurement of the rate of* $\nu_e + d \rightarrow p + p + e^-$ *interactions produced by* ^8B *solar neutrinos at the Sudbury Neutrino Observatory*, Phys. Rev. Lett. 87 (2001), p. 071301, arXiv: `nucl-ex/0106015`.

[7] P. Dirac and R. Fowler, *The quantum theory of the electron*, Proc. R. Soc. Lond. A 117 (1928).

[8] M. Gell-Mann, *The Eightfold Way: A Theory of strong interaction symmetry* (1961).

[9] Y. Ne'eman, *Derivation of strong interactions from a gauge invariance*, Nucl. Phys. 26 (1961), ed. by R. Ruffini and Y. Verbin, pp. 222–229.

[10] H. Fritzsch, M. Gell-Mann, and H. Leutwyler, *Advantages of the Color Octet Gluon Picture*, Phys. Lett. B 47 (1973), pp. 365–368.

[11] D. J. Gross and F. Wilczek, *Ultraviolet Behavior of Nonabelian Gauge Theories*, Phys. Rev. Lett. 30 (1973), ed. by J. C. Taylor, pp. 1343–1346.

[12] H. D. Politzer, *Reliable Perturbative Results for Strong Interactions?* Phys. Rev. Lett. 30 (1973), ed. by J. C. Taylor, pp. 1346–1349.

[13] M. Gell-Mann, *A Schematic Model of Baryons and Mesons*, Phys. Lett. 8 (1964), pp. 214–215.

[14] Belle Collaboration, S. K. Choi et al., *Observation of a narrow charmonium-like state in exclusive $B^{\pm} \to K^{\pm}\pi^{+}\pi^{-}J/\psi$ decays*, Phys. Rev. Lett. 91 (2003), p. 262001, arXiv: hep-ex/0309032.

[15] LHCb Collaboration, R. Aaij et al., *Observation of $J/\psi p$ Resonances Consistent with Pentaquark States in $\Lambda_b^0 \to J/\psi K^{-} p$ Decays*, Phys. Rev. Lett. 115 (2015), p. 072001, arXiv: 1507.03414 [hep-ex].

[16] LHCb Collaboration, R. Aaij et al., *Observation of a narrow pentaquark state, $P_c(4312)^{+}$, and of two-peak structure of the $P_c(4450)^{+}$*, Phys. Rev. Lett. 122.22 (2019), p. 222001, arXiv: 1904.03947 [hep-ex].

[17] P. Koppenburg, *List of hadrons observed at the LHC* (2021).

[18] S. Weinberg, *A Model of Leptons*, Phys. Rev. Lett. 19 (1967), pp. 1264–1266.

[19] S. L. Glashow, *Partial Symmetries of Weak Interactions*, Nucl. Phys. 22 (1961), pp. 579–588.

[20] A. Salam and J. C. Ward, *Weak and electromagnetic interactions*, Nuovo Cim. 11 (1959), pp. 568–577.

[21] K. Nishijima, *Charge Independence Theory of V Particles*, Prog. Theor. Phys. 13.3 (1955), pp. 285–304.

[22] M. Gell-Mann, *The interpretation of the new particles as displaced charge multiplets*, Nuovo Cim. 4.S2 (1956), pp. 848–866.

[23] P. W. Higgs, *Broken Symmetries and the Masses of Gauge Bosons*, Phys. Rev. Lett. 13 (1964), ed. by J. C. Taylor, pp. 508–509.

[24] ATLAS Collaboration, G. Aad et al., *Observation of a new particle in the search for the Standard Model Higgs boson with the ATLAS detector at the LHC*, Phys. Lett. B 716 (2012), pp. 1–29, arXiv: 1207.7214 [hep-ex].

[25] CMS Collaboration, A. M. Sirunyan et al., *Observation of Higgs boson decay to bottom quarks*, Phys. Rev. Lett. 121.12 (2018), p. 121801, arXiv: 1808.08242 [hep-ex].

[26] N. Cabibbo, *Unitary Symmetry and Leptonic Decays*, Phys. Rev. Lett. 10 (1963), pp. 531–533.

[27] M. Kobayashi and T. Maskawa, *CP Violation in the Renormalizable Theory of Weak Interaction*, Prog. Theor. Phys. 49 (1973), pp. 652–657.

[28] R. N. Cahn, *The Eighteen arbitrary parameters of the standard model in your everyday life*, Rev. Mod. Phys. 68 (1996), pp. 951–960.

[29] L. Canetti et al., *Matter and Antimatter in the Universe*, New J. Phys. 14 (2012), p. 095012, arXiv: 1204.4186 [hep-ph].

[30] R. D. Peccei and H. R. Quinn, *Constraints Imposed by CP Conservation in the Presence of Instantons*, Phys. Rev. D 16 (1977), pp. 1791–1797.

[31] E. Corbelli and P. Salucci, *The Extended Rotation Curve and the Dark Matter Halo of M33*, Mon. Not. Roy. Astron. Soc. 311 (2000), pp. 441–447, arXiv: astro-ph/9909252.

[32] LHCb Collaboration, R. Aaij et al., *Differential branching fractions and isospin asymmetries of $B \to K^{(*)}\mu^+\mu^-$ decays*, JHEP 06 (2014), p. 133, arXiv: 1403.8044 [hep-ex].

[33] LHCb Collaboration, R. Aaij et al., *Angular analysis and differential branching fraction of the decay $B_s^0 \to \phi\mu^+\mu^-$*, JHEP 09 (2015), p. 179, arXiv: 1506.08777 [hep-ex].

[34] LHCb Collaboration, R. Aaij et al., *Measurements of the S-wave fraction in $B^0 \to K^+\pi^-\mu^+\mu^-$ decays and the $B^0 \to K^*(892)^0\mu^+\mu^-$ differential branching fraction*, JHEP 11 (2016), [Erratum: JHEP 04, 142 (2017)], p. 047, arXiv: 1606.04731 [hep-ex].

[35] LHCb Collaboration, Roel Aaij et al., *Measurement of CP-Averaged Observables in the $B^0 \to K^{*0}\mu^+\mu^-$ Decay*, Phys. Rev. Lett. 125.1 (2020), p. 011802, arXiv: 2003.04831 [hep-ex].

[36] LHCb Collaboration, R. Aaij et al., *Tests of lepton universality using $B^0 \to K_S^0\ell^+\ell^-$ and $B^+ \to K^{*+}\ell^+\ell^-$ decays*, Phys. Rev. Lett. 128.19 (2022), p. 191802, arXiv: 2110.09501 [hep-ex].

[37] LHCb Collaboration, R. Aaij et al., *Test of lepton universality in beauty-quark decays*, Nature Phys. 18.3 (2022), pp. 277–282, arXiv: 2103.11769 [hep-ex].

[38] LHCb Collaboration, R. Aaij et al., *Test of lepton universality with $\Lambda_b^0 \to pK^-\ell^+\ell^-$ decays*, JHEP 05 (2020), p. 040, arXiv: 1912.08139 [hep-ex].

[39] LHCb Collaboration, R. Aaij et al., *Test of lepton universality with $B^0 \to K^{*0}\ell^+\ell^-$ decays*, JHEP 08 (2017), p. 055, arXiv: 1705.05802 [hep-ex].

[40] BaBar Collaboration, J. P. Lees et al., *Evidence for an excess of $\bar{B} \to D^{(*)}\tau^-\bar{\nu}_\tau$ decays*, Phys. Rev. Lett. 109 (2012), p. 101802, arXiv: 1205.5442 [hep-ex].

[41] BaBar Collaboration, J. P. Lees et al., *Measurement of an Excess of $\bar{B} \to D^{(*)}\tau^-\bar{\nu}_\tau$ Decays and Implications for Charged Higgs Bosons*, Phys. Rev. D 88.7 (2013), p. 072012, arXiv: 1303.0571 [hep-ex].

[42] Belle Collaboration, M. Huschle et al., *Measurement of the branching ratio of $\bar{B} \to D^{(*)}\tau^-\bar{\nu}_\tau$ relative to $\bar{B} \to D^{(*)}\ell^-\bar{\nu}_\ell$ decays with hadronic tagging at Belle*, Phys. Rev. D 92.7 (2015), p. 072014, arXiv: 1507.03233 [hep-ex].

[43] Belle Collaboration, S. Hirose et al., *Measurement of the τ lepton polarization and $R(D^*)$ in the decay $\bar{B} \to D^*\tau^-\bar{\nu}_\tau$ with one-prong hadronic τ decays at Belle*, Phys. Rev. D 97.1 (2018), p. 012004, arXiv: 1709.00129 [hep-ex].

[44] Belle Collaboration, G. Caria et al., *Measurement of $\mathcal{R}(D)$ and $\mathcal{R}(D^*)$ with a semileptonic tagging method*, Phys. Rev. Lett. 124.16 (2020), p. 161803, arXiv: 1910.05864 [hep-ex].

[45] LHCb Collaboration, R. Aaij et al., *Measurement of the ratio of the $B^0 \to D^{*-}\tau^+\nu_\tau$ and $B^0 \to D^{*-}\mu^+\nu_\mu$ branching fractions using three-prong τ-lepton decays*, Phys. Rev. Lett. 120.17 (2018), p. 171802, arXiv: 1708.08856 [hep-ex].

[46] LHCb Collaboration, R. Aaij et al., *Test of Lepton Flavor Universality by the measurement of the $B^0 \to D^{*-}\tau^+\nu_\tau$ branching fraction using three-prong τ decays*, Phys. Rev. D 97.7 (2018), p. 072013, arXiv: 1711.02505 [hep-ex].

[47] Muon g-2 Collaboration, B. Abi et al., *Measurement of the Positive Muon Anomalous Magnetic Moment to 0.46 ppm*, Phys. Rev. Lett. 126.14 (2021), p. 141801, arXiv: 2104.03281 [hep-ex].

[48] LHCb Collaboration, R. Aaij et al., *Measurements of prompt charm production cross-sections in pp collisions at $\sqrt{s} = 13$ TeV*, JHEP 03 (2016), [Erratum: JHEP 09, 013 (2016), Erratum: JHEP 05, 074 (2017)], p. 159, arXiv: 1510.01707 [hep-ex].

[49] LHCb Collaboration, R. Aaij et al., *Measurement of the b-quark production cross-section in 7 and 13 TeV pp collisions*, Phys. Rev. Lett. 118.5 (2017), [Erratum: Phys.Rev.Lett. 119, 169901 (2017)], p. 052002, arXiv: 1612.05140 [hep-ex].

[50] NA48 Collaboration, V. Fanti et al., *The Beam and detector for the NA48 neutral kaon CP violation experiment at CERN*, Nucl. Instrum. Methods Phys. Res., A 574 (2007), 433–471. 57 p.

[51] NA62 Collaboration, E. Cortina Gil et al., *The Beam and detector of the NA62 experiment at CERN*, JINST 12.05 (2017), P05025, arXiv: 1703.08501 [physics.ins-det].

[52] KOTO Collaboration, T. Yamanaka, *The J-PARC KOTO experiment*, PTEP 2012 (2012), 02B006.

[53] LHCb Collaboration, R. Aaij et al., *Constraints on the $K^0_S \to \mu^+\mu^-$ Branching Fraction*, Phys. Rev. Lett. 125.23 (2020), p. 231801, arXiv: 2001.10354 [hep-ex].

[54] *Search for $K^0_{S(L)} \to \mu^+\mu^-\mu^+\mu^-$ decays at LHCb* (2022), arXiv: 2212.04977 [hep-ex].

[55] LHCb Collaboration, R. Aaij et al., *Evidence for the rare decay $\Sigma^+ \to p\mu^+\mu^-$*, Phys. Rev. Lett. 120.22 (2018), p. 221803, arXiv: 1712.08606 [hep-ex].

[56] A. A. Alves et al., *Prospects for Measurements with Strange Hadrons at LHCb*, JHEP 05 (2019), p. 048, arXiv: 1808.03477 [hep-ex].

[57] E. Mobs, *The CERN accelerator complex. Complexe des accélérateurs du CERN* (2016).

[58] L. Evans and P. Bryant, *LHC Machine*, Journal of Instrumentation 3.08 (2008), S08001–S08001.

[59] E. Keil, *The Large Hadron Collider LHC*, eConf C960625 (1996), OPS010.

[60] ATLAS Collaboration, G. Aad et al., *The ATLAS Experiment at the CERN Large Hadron Collider*, JINST 3 (2008), S08003.

[61] CMS Collaboration, S. Chatrchyan et al., *The CMS Experiment at the CERN LHC*, JINST 3 (2008), S08004.

[62] ALICE Collaboration, K. Aamodt et al., *The ALICE experiment at the CERN LHC*, JINST 3 (2008), S08002.

[63] LHCb Collaboration, A. A. Alves et al., *The LHCb Detector at the LHC*, JINST 3 (2008), Also published by CERN Geneva in 2010, S08005.

[64] A. D. Martin et al., *Parton distributions for the LHC*, Eur. Phys. J. C 63 (2009), pp. 189–285, arXiv: 0901.0002 [hep-ph].

[65] LHCb Collaboration, C. Elsässer, *$\bar{b}b$ production angle plots*, URL: https://lhcb.web.cern.ch/lhcb/speakersbureau/html/bb%5C_ProductionAngles.html.

[66] LHCb Collaboration, R. Aaij et al., *LHCb Detector Performance*, Int. J. Mod. Phys. A 30.07 (2015), p. 1530022, arXiv: 1412.6352 [hep-ex].

[67] LHCb Collaboration, LHCb Collaboration, *LHCb Performance Plots*, URL: https://lbgroups.cern.ch/online/%20OperationsPlots/index.htm..

[68] W. Herr, W. Meddahi, and Y. Papaphilippou, *How do we have to operate the LHCb spectrometer magnet?* Tech. rep., Geneva: CERN, 2008.

[69] R. Aaij et al., *Performance of the LHCb Vertex Locator*, JINST 9 (2014), P09007, arXiv: 1405.7808 [physics.ins-det].

[70] LHCb Collaboration, *LHCb Silicon Tracker - Material for Publications*, URL: https://www.physik.uzh.ch/groups/lhcb/public/material/.

[71] LHCb Collaboration, LHCb Collaboration, *LHCb inner tracker: Technical Design Report*, tech. rep., 2002.

[72] LHCb Outer Tracker Group, R. Arink et al., *Performance of the LHCb Outer Tracker*, JINST 9.01 (2014), P01002, arXiv: 1311.3893 [physics.ins-det].

[73] LHCb Outer Tracker Group, Ph. d'Argent et al., *Improved performance of the LHCb Outer Tracker in LHC Run 2*, JINST 12.11 (2017), P11016, arXiv: 1708.00819 [physics.ins-det].

[74] O. Callot, *FastVelo, a fast and efficient pattern recognition package for the Velo*, tech. rep., LHCb, Geneva: CERN, 2011.

[75] Y. Amhis et al., *Description and performance studies of the Forward Tracking for a scintilating fibre detector at LHCb*, tech. rep., Geneva: CERN, 2014.

[76] M. Benayoun and O. Callot, *The forward tracking, an optical model method*, tech. rep., revised version number 1 submitted on 2002-02-22 17:19:02, Geneva: CERN, 2002.

[77] O. Callot and S. Hansmann-Menzemer, *The Forward Tracking: Algorithm and Performance Studies*, tech. rep., Geneva: CERN, 2007.

[78] P. V. C. Hough, *Machine Analysis of Bubble Chamber Pictures*, Conf. Proc. C 590914 (1959), pp. 554–558.

[79] P. V. C. Hough, *Method and means for recognizing complex patterns*, (1962).

[80] R. O. Duda and P. E. Hart, *Use of the Hough transformation to detect lines and curves in pictures*, Commun. ACM 15.1 (1972), pp. 11–15.

[81] D. H. Ballard, *Generalizing the Hough transform to detect arbitrary shapes*, Pattern Recognition 13.2 (1981), pp. 111–122.

[82] E. E. Bowen et al., *VeloTT tracking for LHCb Run II*, tech. rep., Geneva: CERN, 2016.

[83] O. Callot and M. Schiller, *PatSeeding: A Standalone Track Reconstruction Algorithm*, tech. rep., Geneva: CERN, 2008.

[84] O. Callot, *Downstream Pattern Recognition*, tech. rep., Geneva: CERN, 2007.

[85] S. Stahl and S. Hansmann-Menzemer, *Update on Downstream Tracking*, tech. rep., Geneva: CERN, 2009.

[86] R. E. Kalman, *A New Approach to Linear Filtering and Prediction Problems*, Journal of Basic Engineering 82.1 (1960), pp. 35–45.

[87] P. Billoir, *Track fitting with multiple scattering: A new method*, Nuclear Instruments and Methods in Physics Research 225.2 (1984), pp. 352–366.

[88] R. Frühwirth, *Application of Kalman filtering to track and vertex fitting*, Nuclear Instruments and Methods in Physics Research Section A: Accelerators, Spectrometers, Detectors and Associated Equipment 262.2 (1987), pp. 444–450.

[89] LHCb RICH Group, M. Adinolfi et al., *Performance of the LHCb RICH detector at the LHC*, Eur. Phys. J. C 73 (2013), p. 2431, arXiv: 1211.6759 [physics.ins-det].

[90] E. Dall'Occo, *Search for heavy neutrinos and characterisation of silicon sensors for the VELO upgrade*.

[91] P. Robbe, *Generators, Calorimeter Trigger and J/ψ production at LHCb*.

[92] P. Perret and X. Vilasis-Cardona, *Performance of the LHCb calorimeters during the period 2010-2012*, J. Phys.: Conf. Ser. 587 (2014), see LHCb-TALK-2014-236, 012012. 6 p.

[93] A. A. Alves et al., *Performance of the LHCb muon system*, JINST 8 (2013), P02022, arXiv: 1211.1346 [physics.ins-det].

[94] F. Archilli et al., *Performance of the Muon Identification at LHCb*, JINST 8 (2013), P10020, arXiv: 1306.0249 [physics.ins-det].

[95] C. Ilgner et al., *The Beam Conditions Monitor of the LHCb Experiment* (2010), arXiv: 1001.2487 [physics.ins-det].

[96] C. Barschel, *Precision luminosity measurement at LHCb with beam-gas imaging*, PhD thesis, 2014.

[97] LHCb Collaboration, R. Aaij et al., *Prompt K^0_S production in pp collisions at $\sqrt{s} = 0.9\,\text{TeV}$*, Phys. Lett. B693 (2010), p. 69, arXiv: 1008.3105 [hep-ex].

[98] LHCb Collaboration, R. Aaij et al., *Precision luminosity measurements at LHCb*, JINST 9.12 (2014), P12005, arXiv: 1410.0149 [hep-ex].

[99] LHCb Collaboration, R. Aaij et al., *Design and performance of the LHCb trigger and full real-time reconstruction in Run 2 of the LHC*, JINST 14.04 (2019), P04013, arXiv: 1812.10790 [hep-ex].

[100] R. Aaij et al., *Tesla : an application for real-time data analysis in High Energy Physics*, Comput. Phys. Commun. 208 (2016), pp. 35–42, arXiv: 1604.05596 [physics.ins-det].

[101] S. Borghi, *Novel real-time alignment and calibration of the LHCb detector and its performance*, Nuclear Instruments and Methods in Physics Research Section A: Accelerators, Spectrometers, Detectors and Associated Equipment 845 (2017), Proceedings of the Vienna Conference on Instrumentation 2016, pp. 560–564.

[102] R. Aaij et al., *A comprehensive real-time analysis model at the LHCb experiment*, JINST 14.04 (2019), P04006, arXiv: 1903.01360 [hep-ex].

[103] S. Tolk et al., *Data driven trigger efficiency determination at LHCb*, tech. rep., Geneva: CERN, 2014.

[104] LHCb Collaboration, *Letter of Intent for the LHCb Upgrade*, tech. rep., Geneva: CERN, 2011.

[105] LHCb Collaboration, I. Bediaga et al., *Framework TDR for the LHCb Upgrade: Technical Design Report*, tech. rep., 2012.

[106] T. Poikela et al., *VeloPix: the pixel ASIC for the LHCb upgrade*, JINST 10 (2015), p. C01057.

[107] D. H. Cámpora Pérez et al., *Search by triplet: An efficient local track reconstruction algorithm for parallel architectures*, J. Comput. Sci. 54 (2022), p. 101422, arXiv: 2207.03936.

[108] LHCb Collaboration, *LHCb VELO Upgrade Technical Design Report*, tech. rep., 2013.

[109] P. Collins et al., *Microchannel Cooling for the LHCb VELO Upgrade I. Microchannel Cooling for the LHCb VELO Upgrade I*, tech. rep., 31 pages, 27 figures, Geneva: CERN, 2021, arXiv: 2112.12763.

[110] E. Jans, *Operational aspects of the VELO cooling system of LHCb*, PoS Vertex2013 (2014), PoS(Vertex 2013)038, 038. 10 p.

[111] G. Aglieri Rinella et al., *The NA62 GigaTracKer: a low mass high intensity beam 4D tracker with 65 ps time resolution on tracks*, JINST 14 (2019), P07010, arXiv: 1904.12837 [physics.ins-det].

[112] LHCb Collaboration, *LHCb Tracker Upgrade Technical Design Report*, tech. rep., 2014.

[113] R. Quagliani, *Study of double charm B decays with the LHCb experiment at CERN and track reconstruction for the LHCb upgrade*, Presented 06 Oct 2017, 2017.

[114] M. Deckenhoff, *Scintillating Fibre and Silicon Photomultiplier Studies for the LHCb upgrade*, Presented 23 Feb 2016, 2015.

[115] S. Esen et al., *Clustering and rawbank decoding for the SciFi detector*, tech. rep., 2018.

[116] R. Aaij et al., *Allen: A high level trigger on GPUs for LHCb*, Comput. Softw. Big Sci. 4.1 (2020), p. 7, arXiv: 1912.09161 [physics.ins-det].

[117] LHCb Collaboration, *RTA and DPA dataflow diagrams for Run 1, Run 2, and the upgraded LHCb detector* (2020).

[118] LHCb Collaboration, *LHCb Upgrade GPU High Level Trigger Technical Design Report*, tech. rep., Geneva: CERN, 2020.

[119] C. Bozzi, *LHCb Computing Resource usage in 2018*, tech. rep., Geneva: CERN, 2019.

[120] Niklas Nolte, *A Selection Framework for LHCb's Upgrade Trigger*, PhD thesis, 2020.

[121] LHCb Collaboration, *LHCb PID Upgrade Technical Design Report*, tech. rep., 2013.

[122] LHCb Collaboration, *LHCb SMOG Upgrade*, tech. rep., Geneva: CERN, 2019.

[123] LHCb Collaboration, *LHCb PLUME: Probe for LUminosity MEasurement*, tech. rep., Geneva: CERN, 2021.

[124] S. Aiola et al., *Hybrid seeding: A standalone track reconstruction algorithm for scintillating fibre tracker at LHCb*, Comput. Phys. Commun. 260 (2021), p. 107713, arXiv: 2007.02591.

[125] P. A. Günther, *LHCb's Forward Tracking algorithm for the Run 3 CPU-based online track-reconstruction sequence* (2022), arXiv: 2207.12965 [physics.ins-det].

[126] A. Scarabotto, *Tracking on GPU at LHCb's fully software trigger* (2022).

[127] LHCb Collaboration, *Standalone track reconstruction and matching algorithms for the GPU-based High Level Trigger at LHCb* (2022).

[128] A. Kachanovich et al., *Higgs portal to dark matter and $B \to K^{(*)}$ decays*, Eur. Phys. J. C 80.7 (2020), p. 669, arXiv: 2003.01788 [hep-ph].

[129] A. Oyanguren et al., *Effect of the High Level Trigger for detecting Long-Lived Particles at LHCb*, Frontiers in Big Data 5 (2022).

[130] J. Albrecht et al., *The Muon Puzzle in cosmic-ray induced air showers and its connection to the Large Hadron Collider*, Astrophys. Space Sci. 367.3 (2022), p. 27, arXiv: 2105.06148 [astro-ph.HE].

[131] LHCb Collaboration, R. Aaij et al., *Measurement of V^0 production ratios in pp collisions at $\sqrt{s} = 0.9$ and 7 TeV*, JHEP 08 (2011), p. 034, arXiv: 1107.0882 [hep-ex].

[132] ALICE Collaboration, S. Acharya et al., *Production of light-flavor hadrons in pp collisions at $\sqrt{s} = 7$ and $\sqrt{s} = 13$ TeV*, Eur. Phys. J. C 81.3 (2021), p. 256, arXiv: 2005.11120 [nucl-ex].

[133] ALICE Collaboration, S. Acharya et al., *Multiplicity dependence of (multi-)strange hadron production in proton-proton collisions at $\sqrt{s} = 13$ TeV*, Eur. Phys. J. C 80.2 (2020), p. 167, arXiv: 1908.01861 [nucl-ex].

[134] J. E. Gaiser, *Charmonium Spectroscopy From Radiative Decays of the J/ψ and ψ'*, PhD thesis, 1982.

[135] G. Punzi, *Sensitivity of searches for new signals and its optimization*, eConf C030908 (2003), ed. by L. Lyons, R. P. Mount, and R. Reitmeyer, MODT002, arXiv: physics/0308063.

[136] R. A. Fisher, *The use of multiple measurements in taxonomic problems*, Annals Eugen. 7 (1936), pp. 179–188.

[137] R. Armenteros and J. Podolankski, *III. Analysis of V-events*, The London, Edinburgh, and Dublin Philosophical Magazine and Journal of Science 45.13 (1954).

[138] Kuraray, *Kuraray home webpage*, URL: `http://kuraraypsf.jp/psf/index.html`.

[139] F.D. Brooks, *Development of organic scintillators*, Nuclear Instruments and Methods 162.1 (1979), pp. 477–505.

[140] T. Förster, *Zwischenmolekulare Energiewanderung und Fluoreszenz*, Annalen der Physik 437.1-2 (1948), pp. 55–75, eprint: `https://onlinelibrary.wiley.com/doi/pdf/10.1002/andp.19484370105`.

[141] P. Baladrón Rodrıguez et al., *Calibration of the momentum scale of a particle physics detector using the Armenteros-Podolanski plot*, JINST 16.06 (2021), P06036, arXiv: `2012.03620 [physics.ins-det]`.

Acknowledgements

During the past years, and especially during the time of my PhD, there have been a large amount of people that supported me and my work directly or indirectly, that I would like to thank here.
First, I want to thank Johannes for supervising the various theses that I wrote in the last five years. You convinced me to join the LHCb group in Dortmund for my bachelor thesis and to stay there for many more years. You also supported me with all my spin-off projects from what the Dortmund group normally does and planned career steps with me, especially with this co-tutelle.
Special thanks to Vava, for your supervision of my thesis, introducing me to the RTA world and building a team spirit in the RECEPT and RTA groups during the Zoom era. Thanks for your life advices, funny stories, our shared passion for bureaucracy and delicious guacamole. I would like to thank both of you again for making this co-tutelle, even if it took two years to set it up, working, for helping me develop as a scientist, for enabling me to stay at CERN for a period of my PhD and giving me freedom and flexibility in my research projects and working places. The combination of all of this clearly boosted my learning process and personal well-being.
I want to thank my referees Carla Göbel and Vincenzo Vagnoni and Delphine Hardin for being on my thesis jury and Kevin Kröninger for being on the jury after already reviewing my bachelor and master theses.
I want to thank Bernhard Spaan for significantly contributed to my understanding of particle physics through his various lectures and who I was always happy to discuss with. Special thanks to Alessandro, Christina for becoming close friends, nice housemates and supportive colleagues. I had a great time with you in Paris and at CERN. Thanks also to my other CERN housemates Luana, Pablo and Liam. Special thanks to Louis who helped me a lot in understanding how the LHCb tracking and especially the Seeding works. Thanks also for sharing amazing quiz nights in Geneva. I would like to thank Marianna, Dorothea, Anja, Janina, Fra, Lorenzo, Gaia, Guilia, Felicia, Chiara, Giorgia, Renaud, Tommaso and many other

people at CERN to make the time there very enjoyable both inside and outside of LHCb. Thanks to one of my oldest LHCb friends from Summer Student times in 2018, Lera, for fun times at CERN and organising the Starterkit Run 3 Starterkit together. I would like to thank Vitalii and Elena in particular, for teaching me a lot of LHCb physics and discussing all the questions I had over the last years. Thanks to Eva and Yasmine for being excellent EMTF conveners and giving me career advice. I would also like to thank Yasmine for being such a creative and inspiring LHCb colleague. Thanks to Jacques and Fra for following the progress of my work during my time at LPNHE. I would like to thank Alex and Maik for being amazing office mates. I would like to thank the EMTF, RTA and QEE working groups that supported my work with fruitful discussions.
I want to thank the rest of my LHCb colleagues for making this collaboration an outstanding particle physics experiment, a nice working environment and awesome barbecues. Thanks to all the people at LPNHE that supported me in the last years and becoming good friends. Thanks to the Dortmund LHCb group for accompanying my bachelor, master and PhD projects. I would like to thank the Ecole Doctorale and all people that were involved in the administrative procedure of this cotutelle. I want to thank my family for supporting me. Finally, I want to thank Emma for always being there for me and motivating me through these 3 years.